PROGRAMA DE DOCTORADO EN INGENIERÍA INDUSTRIAL

TESIS DOCTORAL:

Miller Cycle and Exhaust Gas Recirculation for a Naturally Aspirated Lean-burn Gas Engine

Presentada por Denis Neher para optar al grado de
Doctor/a por la Universidad de Valladolid

Dirigida por:
Dr. Blanca Giménez Olavarría
&
Dr.-Ing. Maurice Kettner

UVa
Secretaría Administrativa. Escuela de Doctorado. Casa del Estudiante. C/ Real de Burgos s/n. 47011-Valladolid. ESPAÑA
Tfno.: + 34 983 184343; + 34 983 423908; + 34 983 186471 - **Fax** 983 186397 - **E-mail**: seccion.tercer.ciclo@uva.es

Universidad de Valladolid

DOCTORAL THESIS

Miller Cycle and Exhaust Gas Recirculation for a Naturally Aspirated Lean-burn Gas Engine

Presented by:

Denis Neher, M.Sc.

Directed by:

Dr. Blanca Giménez Olavarría

&

Prof. Dr.-Ing. Maurice Kettner

Valladolid & Karlsruhe

Date of Defence: 4th December 2017

EXAMINING BOARD

President: Dr. Francisco Vicente Tinaut Fluixá

Secretary: Dr. Juan José Hernández Adrover

Speaker: Prof. Dr.-Ing. Ulrich Spicher

Acknowledgments

Abstract

Motivated by tightening emission standards for small natural gas driven cogeneration gas engines, this thesis explores an alternative working process that extends the prevailing lean-burn operation with Miller cycle and cooled exhaust gas recirculation (EGR). The combination of these well-established means is expected to improve the trade-off between engine efficiency, NO_x emissions and indicated mean effective pressure (IMEP) of a naturally aspirated gas engine.

Preliminary experiments on the combustion of varying mixture composition under quiescent flow conditions were conducted using a constant volume combustion chamber. Evaluating the measured pressure trace reveals how relative air-fuel ratio, exhaust gas concentration, pressure and temperature of the unburnt zone affect laminar burning velocity and temperature of the burnt zone. Subsequently, the effect of replacing a part of excess air with exhaust gas on the performance of the baseline engine (Otto valve timing) was studied. After first trials centred on the trade-off between engine efficiency and NO_x emissions at constant IMEP, the potential to increase IMEP at constant NO_x emissions was assessed.

A representative comparison between both approaches to realise a Miller working cycle, namely early and late intake valve closing, is a core element of this work. The effective compression ratio of the baseline engine, as criteria for comparability, was maintained constant by adjusting the geometrical compression ratio. To this end, a method was applied that accounts for the effects of gas dynamics, such as ram effect and reverse flow. A detailed model of the test bed engine was built using one-dimensional engine simulation software. The model predicts realistic engine behaviour and enabled analysing the influence of intake valve closing on engine performance. Fundamental differences between early and late Miller cycle could be explored and configurations of same expansion/compression ratio for experimental engine testing determined. Using the same piston design for both configurations, ensures identical squish and area to volume ratio, thus favouring comparability. 3D CFD gas exchange calculations were conducted to gain a deeper insight into the influence of intake valve closing on charge motion and homogenisation. The numerical results help explaining different combustion characteristics of both Miller configurations in experimental engine testing.

Comprehensive series of measurements were carried out in engine operation with Miller valve timing and varying EGR rate. The main focus was put on the potential that the working process offers in improving the trade-off between engine efficiency and NO_x emissions at constant IMEP of the baseline engine's reference operating point.

Resumen

Debido al endurecimiento de los estándares de emisiones para sistemas de microcogeneración con motor de combustión interna de gas natural, esta tesis estudia un proceso de trabajo alternativo que extiende la operación con mezclas pobre con ciclo de Miller y recirculación de gases de escape refrigerados (EGR). Se espera que la combinación de estos medios mejore el conflicto de objetivos entre la eficiencia del motor, las emisiones de NO_x y la presión media indicada (IMEP) de un motor de gas de aspiración natural.

Se llevaron a cabo experimentos preliminares sobre la combustión de mezclas variables bajo condiciones de flujo quedas utilizando una cámara de combustión de volumen constante. El análisis de la curva de presión muestra cómo el dosado, la concentración de EGR, la presión y la temperatura de la zona no quemada afectan a la velocidad de combustión laminar y la temperatura de la zona quemada. Posteriormente, se estudió el efecto de EGR refrigerado sobre el comportamiento del motor de serie (ciclo Otto) que sólo opera con con mezclas pobres. Mientras primeros ensayos se centraron en el conflicto entre la eficiencia del motor y las emisiones de NO_x a IMEP constante, después se evaluó el potencial de aumentar IMEP a NO_x constantes.

Una comparación representativa entre ambos enfoques para realizar un ciclo de de Miller, es decir, con momentos de apartura de la válvula de admisión más avanzados o retrasados, es un elemento central de esta tesis. La relación de compresión efectiva del motor de serie se mantuvo constante ajustando la relación de compresión geométrica, como criterio de comparabilidad. Con este fin, se aplicó un nuevo método para calcular la relación de compresión efectiva que considera los efectos de la dinámica del gas, tales como el efecto del ram y el flujo inverso. Para simular el comportamiento del motor y analizar la influencia del momento de cierre de la válvula de admisión al rendimiento del motor, un modelo detallado del banco de ensayos fue diseñado usando un programa de simulación 1D. Esto permitió determinar las diferencias fundamentales entre ambas estrategias Miller y elegir configuraciones de misma relación de expansión/compresión para realizar ensayos de motor. El hecho que se utilizó el mismo diseño de pistón para ambas configuraciones, favorece la compatibilidad de resultados. Se realizaron cálculos CFD (Computational Fluid Dynamics) en 3D del cambio de gases para analizar la influencia del momento de cierre de la válvula de admisión al movimiento de carga y al grado de homogeneización de la mezcla. Los resultados numéricos ayudan a explicar las diferentes características de combustión de ambas configuraciones de Miller en los ensayos experimentales.

Finalmente se realizaron series de ensayos con configuración Miller variando la tasa de EGR. Se prestó especial atención en determinar el potencial de mejorar el conflicto de objetivos entre la eficiencia del motor y las emisiones de NO_x a IMEP constante del punto de referencia del motor de serie.

Kurzfassung

Vor dem Hintergrund zukünftig schärferer Emissionsgrenzwerte für erdgasbetriebene Klein-Blockheizkraftwerke wurde im Rahmen dieser Arbeit ein alternatives Brennverfahren untersucht, das den weit verbreiteten homogenen Magerbetrieb um Miller-Steuerzeiten und gekühlte Abgasrückführung (AGR) erweitert. Die Kombination dieser etablierten Einzelmaßnahmen soll zur Entschärfung des Zielkonflikts zwischen Wirkungsgrad, NO_x-Emissionen und Mitteldruck bei gemischansaugenden Gasmotoren beitragen.

Für eine isolierte Betrachtung des Einflusses der Gemischzusammensetzung auf die Verbrennung unter strömungsberuhigten Bedingungen wurden Versuche mit einer Verbrennungsbombe durchgeführt. Durch Analyse des gemessenen Druckverlaufs konnten Rückschlüsse auf die laminare Brenngeschwindigkeit und die Temperatur der verbrannten Zone in Abhängigkeit von Luftverhältnis, Abgaskonzentration, Druck und Temperatur der unverbrannten Zone gezogen werden. Im nächsten Schritt wurde die Auswirkung gekühlter AGR auf das Betriebsverhalten des magerbetriebenen Serienmotors (Otto-Steuerzeiten) analysiert. Dabei wurde ein Teil der überschüssigen Luft durch Abgas ersetzt mit dem Ziel die Wärmekapazität des Gemischs anzuheben. Während zunächst unter Beibehaltung des indizierten Mitteldrucks der Fokus auf dem Zielkonflikt zwischen Wirkungsgrad und NO_x-Emissionen lag, wurde nachfolgend das Potenzial zur NO_x-neutralen Anhebung des Mitteldrucks bewertet.

Der repräsentative Vergleich zwischen den beiden Ansätzen, über die ein Miller-Arbeitsprozess realisiert werden kann, frühes und spätes Einlassschließen, bildet einer der Kernpunkte dieser Arbeit. Dabei wurde unter Berücksichtigung gasdynamischer Effekte, wie Rückströmen und Nachladeeffekt, das effektive Verdichtungsverhältnis mit einer geeigneten Methode entsprechend der Serienkonfiguration angeglichen, indem das geometrische Verdichtungsverhältnis angehoben wurde. Die Erstellung eines Modells des Versuchsträgers für die eindimensionale Motorprozessrechnung ermöglichte den Einfluss des Einlassventilschließens auf den Motorbetrieb realitätsnah nachzubilden. Ferner konnten grundlegende Unterschiede beider Miller-Strategien beleuchtet und Konfigurationen zur Umsetzung am ausgeführten Motor bestimmt werden. Diese verfügen über das gleiche Expansions-Kompressions-Verhältnis, sodass ein einheitlicher Kolben für die experimentellen Untersuchungen, die zunächst im homogenen Magerbetrieb erfolgten, verwendet werden konnte. Mögliche Unterschiede in der Verbrennung sind daher allein der veränderten Steuerzeiten geschuldet, was Ergebnisse von 3D-CFD-Berechnungen der Zylinderinnenströmung belegen.

Im nächsten Schritt erfolgten Untersuchungen im Motorbetrieb mit den bestimmten Miller-Konfigurationen und variierender AGR-Rate. Dabei wurden insbesondere das Potenzial sowie die Grenzen zur Verbesserung des Zielkonflikts zwischen Wirkungsgrad und NO_x-Emissionen bei konstantem indiziertem Mitteldruck im Vergleich zum Serienbrennverfahren beleuchtet.

Contents

Abbreviations and Symbols

Abbreviations

	Description
0D/ 1D / 3D	zero/ one/ three dimensional
ABB	Asea Brown Boveri
ABDC	After BDC
AGHG	Anthropogenic greenhouse gas emissions
Ar	Argon
AVL	Anstalt für Verbrennungskraftmaschinen List
BBDC	Before bottom dead centre
BDC	Bottom dead centre
BTDC	Before top dead centre
C2H2	Ethyne
C_3H_8	Propane
CAD	Computer Aided Design
CFD	Computational Fluid Dynamics
CH_4	Methane
CHP	Combined heat and power
CO	Carbon monoxide
CO_2	Carbon dioxide
CVCC	Constant volume combustion chamber
EES	Engineering equation solver
EGR	Exhaust gas recirculation
EVC	Exhaust valve closing
EVO	Exhaust valve opening
HCCI	Homogeneous charge compression ignition
HCHO	Formaldehyde
HCN	Hydrogen cyanide
HHV	Higher heating value
HO_2	Hydroperoxyl radical
HSI	Hot surface ignition

ICE	Internal combustion engine
IVC	Intake valve closing
IVO	Inlet valve opening
MAN	Maschinenfabrik Augsburg-Nürnberg
MBT	Maximum brake torque
N_2O	Nitrous oxide
NG	Natural gas
NH_3	Ammonia
NO	Nitric oxide
NO_2	Nitrogen dioxide
NO_x	Nitrogen oxide
NSC	NO_x storage catalyst
O_2	Oxygen
OP	Operating point
PGI	Prechamber gas ignition
PI	Proportional-integral
$ROHR_g$	Gross rate of heat release
$ROHR_n$	Net rate of heat release
ROP	Reference operating point
SCR	Selective catalytic reduction
SOC	Start of combustion
TDC	Top dead centre
TWC	Three way catalyst
UAS	University of Applied Sciences
UVa	Universidad de Valladolid

Latin Symbols

	Unit	Description
u	[-]	Vibe parameter
A/V ratio	[1/mm]	Surface area to volume ratio
A_l	$[m^2]$	Area of laminar flame front
A_t	$[m^2]$	Area of turbulent flame front

BMEP	[bar]	Brake mean effective pressure
c	[-]	Coefficient for calculating laminar burning velocity
C_1	[-]	Constant of Woschni model
C_2	[-]	Constant of Woschni model
CA50	[°CA ATDC]	Combustion phasing
CA5-CA90	[°CA]	Burn duration
C_D	[-]	Flow coefficient
COV_{IMEP}	[%]	Coefficient of variation in IMEP
c_p	[kJ/kg K]	Specific heat capacity at constant pressure
C_S	[-]	Swirl coefficient
C_{Sq}	[-]	Squish ratio
c_v	[kJ/kg K]	Specific heat capacity at constant volume
D	[-]	Dilution ratio
d	[-]	Coefficient for calculating laminar burning velocity
D_B	[mm]	Piston bowl diameter
D_{cyl}	[mm]	Cylinder bore diameter
dm_b/dt	[kg/s]	Mass burning rate
ECR	[-]	Expansion/compression ratio of the idealised cycle
ECR_y	[-]	Effective expansion/compression ratio of the actual cycle
FCR	[-]	Fuel conversion ratio
FMEP	[bar]	Friction mean effective pressure
h	[J/kg]	Specific enthalpy
IMEP	[bar]	Indicated mean effective pressure
$IMEP_g$	[bar]	Gross indicated mean effective pressure
ISFC	[g/kWh]	Indicated specific fuel consumption
$ISFC_g$	[g/kWh]	Gross indicated specific fuel consumption
$ISFC_{ideal}$	[g/kWh]	Indicated specific fuel consumption of the ideal engine
$ISFC_p$	[g/kWh]	Pumping indicated specific fuel consumption
IT	[°CA ATDC]	Ignition timing
IT-CA5	[°CA]	Burning delay
k	[m²/s²]	Specific TKE energy of the turbulent fluctuations

k_i	[cm³/mol s]	Rate constant of reaction i
LHV	[MJ/kg]	Lower heating value
LHV_i	[kJ/mol]	Lower heating value of the species i
m	[-]	Form parameter of Vibe function
M	[Nm]	Torque
m	[kg]	Mass
m_{charg}	[mg]	Mass of in-cylinder charge
$\dot{m}_{air}$	[kg/h]	Mass flow of air
$\dot{m}_{EGR}$	[kg/h]	Mass flow of EGR
M_{eg}	[g/mol]	Molar mass of exhaust gas
$\dot{m}_{NG}$	[kg/h]	Mass flow of natural gas
n	[rev/min]	Engine speed
n	[-]	Polytropic exponent
n_{air}	[-]	Number of moles of air
$n_{air\,stoich}$	[-]	Number of moles of air required for stoichiometric combustion
n_{EGR}	[-]	Number of moles of exhaust gas recirculated
n_{fuel}	[-]	Number of moles of fuel
p_0	[bar]	Initial pressure
p_{air}	[bar]	Pressure of air entering the gas path
p_{amb}	[bar]	Ambient pressure
p_{boost}	[bar]	Boost pressure
p_{cyl}	[bar]	In-cylinder pressure
P_{el}	[W]	Electric power
p_{IVC}	[bar]	In-cylinder pressure at IVC
p_m	[bar]	In-cylinder pressure of motored engine
p_{max}	[bar]	Peak pressure of in-cylinder charge
PMEP	[bar]	Pumping mean effective pressure
p_{SOC}	[bar]	In-cylinder pressure at start of combustion
q	[J/kg]	Specific heat
Q	[J]	Heat
q_{max}	[kJ/mol]	Theoretical specific heat released

Q_n	[J]	Net heat
q_{unb}	[kJ/mol]	Unreleased specific heat
Q_{wall}	[J]	Wall heat losses
R^2	[-]	Coefficient of determination
R_{air}	[J/kg K]	Gas constant of air
r_c	[-]	Compression ratio of air-standard Otto cycle
$r_{c,c}$	[-]	Effective compression ratio of the idealised cycle
$r_{c,Miller}$	[-]	Compression ratio of air-standard Miller cycle
$r_{c,eff}$	[-]	Effective compression ratio of the actual cycle
r_e	[-]	Expansion ratio of the air-standard Otto cycle
$r_{e,Miller}$	[-]	Expansion ratio of the air-standard Miller cycle
r_{geo}	[-]	Geometrical compression ratio
rg_{res}	[%]	Volumetric residual gas fraction
r_i	[mol/cm³ s]	Reaction rate of reaction i
r_u	[kg/m³]	Density of unburnt mixture
s_l	[m/s]	Laminar burning velocity
s_t	[m/s]	Turbulent burning velocity
t	[s]	Time
T_0	[K]	Initial temperature
T_{air}	[°C]	Temperature of air entering the gas path
$T_{b,max}$	[K]	Peak temperature of burnt zone
T_{cyl}	[K]	In-cylinder temperature
T_{EGR}	[°C]	Temperature of exhaust gas recirculated
T_{exh}	[°C]	Exhaust gas temperature
T_{intake}	[°C]	Intake port temperature
T_{IVC}	[K]	Mean in-cylinder temperature at IVC
TKE	[m²/s²]	Turbulent kinetic energy
T_{max}	[K]	Peak temperature of in-cylinder charge
T_{SOC}	[K]	In-cylinder temperature at start of combustion
T_u	[K]	Temperature of unburnt zone
u	[J/kg]	Specific internal energy

U	[J]	Internal energy
u	[m/s]	Velocity of a turbulent flow
$\bar{u}$	[m/s]	Mean component of velocity
u'	[m/s]	Fluctuating component of velocity
v	[cm³/kg]	Specific volume
V	[cm³]	Volume
$\dot{V}_{air}$	[m³/h]	Volume flow of air
V_{BDC}	[cm³]	Volume at BDC
$V_{BDC,eff}$	[cm³]	Volume at the effective BDC
V_d	[cm³]	Displacement volume
$\dot{V}_{EGR}$	[m³/h]	Volume flow of exhaust gas recirculated
V_{IVC}	[cm³]	Cylinder volume at inlet valve closing
$\dot{V}_{NG}$	[m³/h]	Volume flow of natural gas
v_p	[m/s]	Instantaneous piston velocity
v_{pm}	[m/s]	Mean piston velocity
$\dot{V}_{ref}$	[m³/h]	Reference volume flow
v_{sq}	[m/s]	Theoretical squish velocity
V_{TDC}	[cm³]	Volume at BDC
$\dot{W}$	[J/s]	Change in volume work
w	[m/s]	Characteristic velocity
$W_{comp,loss}$	[J]	Losses in compression
$W_{compression}$	[J]	Work required for compression
$W_{expansion}$	[J]	Work obtained from expansion
W_i	[J]	Indicated cycle work
$x(\alpha)$	[-]	Cumulative normalised heat of Vibe function
x_{EGR}	[%]	EGR rate
x_i	[-]	Mole fraction of the species i
z	[mm]	Distance between squish surface and cylinder roof

Greek Symbols

	Unit	Description
α	°CA	Crank angle
α_{SOC}	°CA	Start of combustion
β	[-]	Ratio of actual to equilibrium NO concentration
γ	[-]	Ratio of the specific heat capacities
$\Delta\alpha_{BD}$	°CA	Burn duration of Vibe function
$\Delta ISFC_{comb}$	g/kWh	Loss in ISFC due to imperfect combustion
ΔT	[K]	Temperature rise
δ	%	Deviation
η_{ideal}	%	Efficiency of the ideal engine
η_{th}	%	Thermal efficiency
λ	[-]	Relative air-fuel ratio of the combustion
ρ_{EGR}	[kg/m³]	Density of exhaust gas recirculated
ρ_i	[kg/m³]	Partial density of species i
ρ_N	kg/m³	Norm density
σ_{CA50}	°CA	Standard variation of combustion phasing
ϕ	[-]	Fuel-air equivalence ratio

1 Introduction

Growing energy demand coupled with rising importance of reducing greenhouse emissions worldwide increase the need for highly efficient energy systems that convert primary fuels into the energy form desired. In 2010, CO_2 emitted from fossil fuel combustion was responsible for about 65 % of the global anthropogenic greenhouse gas emissions (AGHG). With 25 %, electricity and heat production pose the majority of the AGHG, closely followed by agriculture, forestry, other land use (24 %) and the industry sector (21 %) [63]. The reduction of the annual CO_2 emissions to avoid a climate change is therefore of utmost interest. In 2011, for instance, the European Union released the low-carbon roadmap that claims a 80-95 % CO_2 reduction by 2050 relative to 1990 levels [42]. Even more ambitious are the targets defined by the United Nations Framework Convention on Climate Change in 2015. One of its main objectives is to prevent the global average temperature from increasing by 2 °C respective to pre-industrial levels [164].

1.1 Background and Motivation

The simultaneous use of heat and power allows cogeneration systems, also known as combined heat and power units (CHP), to achieve overall efficiencies of over 90 %. In Denmark, Finland, Russia and Latvia, 30-50 % of the generated electrical power was achieved through cogeneration units in 2008 [67]. Mostly, natural gas (NG) is used as fuel, which holds a clear advantage regarding CO_2 emissions over other fossil energy carriers including petrol, Diesel or coal, solely due to its molecular structure. Figure 1-1 (left) shows the increasing net electrical energy generated by NG-operated cogeneration plants with an electrical power output (P_{el}) up to 1 MW_{el} in Germany between 2004 and 2014. The target of the

1

German government is to further enhance the overall generated P_{el} from cogeneration up to 110 TWh until 2020 and 120 TWh until 2025, respectively [21]. This would correspond to 20.1 % [22] of the total German net electrical energy generation in 2016.

The emission legislations imposed differ significantly worldwide, even within certain countries such as Switzerland or Japan, depending on electrical power generated or thermal energy input required. In Germany, cogeneration manufacturers in the small power range orient themselves to emission standards according to TA Luft 2002 (Technical Instruction on Air Quality Control) [19]. It obliges large gas engines with a thermal input of 1 MW and above to meet dry NO_x emissions as low as 500 mg/m$_N^3$ at 5 % O_2 (approx. 200 ppm). The significant rise of installed systems over the past years leads to progressively stringent emission standards. In 2018, a Europe-wide tightening will take place that applies to NG driven cogeneration engines with a generated electrical power of $P_{el} = 50$ kW and less [43]. The NO_x limit of 240 mg/kWh at 0 % O_2 is related to thermal energy input (higher heating value HHV) and amounts approximately to the half of the present value given by TA Luft 2002 (i.e. approx. 100 ppm).

In the small power sector of 50 kW$_{el}$ and less, naturally aspirated gas engines usually operate with external mixture formation that prepares either a lean or a stoichiometric air-fuel mixture. The latter requires a three-way-catalyst (TWC) in order to reduce tail pipe emissions such as hydrocarbons (HC), carbon monoxide (CO) and nitrogen oxide (NO_x). In lean-burn operation, an oxidation catalyst converts HC and CO emissions, while low combustion temperature ensures low raw NO_x emissions. This is not only realised through lean mixture but also by retarded ignition timing, leading to a thermodynamically unfavourable combustion phasing (CA50). Since combustion temperatures and thus wall heat losses drop with leaning, the engine still reaches relatively high thermal efficiency, yet it operates with relative air-fuel ratios beyond the efficiency optimum.

Figure 1-1 (right) shows schematically the challenge that naturally aspirated lean-burn cogeneration engines are facing when the aim is to comply with future emission limits. Despite being capable of meeting them through further mixture dilution, thermal efficiency decreases as a result of prolonged combustion and increasing cycle-by-cycle variations. The falling fuel fraction leads to lower indicated mean effective pressure (IMEP) that, in turn, reduces engine power at constant engine speed. The relative losses caused by friction increase, thus deteriorating the engine's brake efficiency. For this reason, developers of naturally aspirated cogeneration engines are forced to account for alternative means that ensure low NO_x emissions and high engine efficiency without losses in engine power. The approach taken in this work combines lean-burn operation, Miller cycle and cooled exhaust gas recirculation (EGR) for a naturally aspirated gas engine, which is henceforth denoted as Lean-Miller-EGR working process.
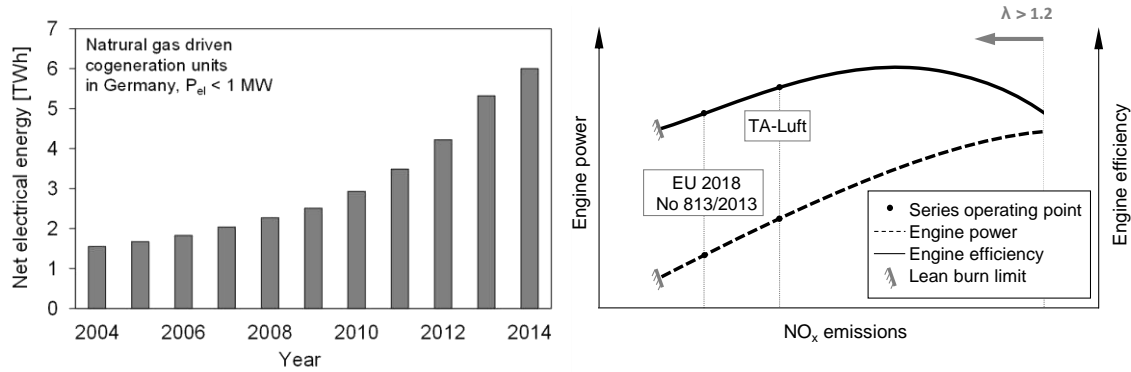
Figure 1-1: Net electrical energy generated through natural gas operating cogeneration units of an electrical power output of $P_{el} < 1$ MW$_{el}$ between 2004 and 2014 in Germany (left) according to [146]; Trade-off between engine efficiency, engine power and NO$_x$ emissions (schematically) (right)

Miller cycle, realised by either advancing or retarding the intake valve closing and adjusted compression ratio, increases the ratio between expansion and compression work. Thermal efficiency increases but the modified valve timing diminishes charging efficiency, thus causing losses in engine power at same relative air-fuel ratio. This could be counteracted by running the engine with a richer mixture but raw NO$_x$ emissions would increase drastically due to rising combustion temperatures. In order to enhance engine power without increasing raw NO$_x$, the mixture's heat capacity needs to be increased. While turbocharged engines manage this by simply enhancing the mass of the in-cylinder charge, this work follows an alternative mixture configuration based on exhaust gas recirculation (EGR) where some of the excess-air is directly replaced by exhaust gas. Due to the high amount of H$_2$O and CO$_2$, exhaust gas has a significantly higher heat capacity than air. Therefore, substituting a part of excess air holds out the prospect of allowing the engine to generate power and NO$_x$ emissions of the baseline configuration, while the Miller cycle is expected to ensure high engine efficiency. Alternatively, the engine could operate at same engine power and efficiency but lower NO$_x$ emissions.

The Lean-Miller-EGR working process was investigated as a part of a research project that involved partners from industry, such as the manufacturer of the cogeneration engine used in this work, SenerTec Kraft-Wärme-Energiesysteme GmbH. From the manufacturer's perspective, holding engine power and engine speed constant was essential, leading to an almost constant friction mean effective pressure (FMEP) and a linear correlation between engine brake power and indicated mean effective pressure IMEP. The trade-off described in Figure 1-1 (right) can therefore be seen as one between indicated fuel consumption (ISFC) and NO$_x$ emissions at constant IMEP. For this reason, it was expedient to carry out the majority of the trials at the IMEP of the reference operating point.

1.2 Objective

The core objective of this work is to analyse the Lean-Miller-EGR working process as an

alternative to the prevailing lean-burn concept with Otto valve timing regarding fuel consumption, combustion process, gas exchange characteristics and exhaust gas emissions for a naturally aspirated gas engine. In order to meet this objective, the following sub-objectives were defined:

- Experimental study on the influence of exhaust gas concentration and air-fuel ratio on laminar burning velocity and combustion temperature.
- Study of EGR in lean-burn operation with conventional Otto valve timing to either improve the ISFC-NO_x trade-off at constant IMEP or to increase IMEP at constant NO_x emissions.
- Determination of a method that allows calculating the effective compression ratio of different engine configurations by considering the effects of gas dynamics.
- Evaluation of the fundamental differences between early and late Miller valve timing of both same effective compression ratio and expansion/compression ratio in lean-burn engine operation.
- Analysis of the effect of cooled EGR on engine operation with early and late Miller valve timing with particular focus on the ISFC-NO_x trade-off at constant IMEP compared to the conventional Otto setup of the baseline engine.

1.3 Methodology

The thesis presented is divided into eight chapters. The second chapter covers a comprehensive literature study, including the fundamentals of combustion, exhaust gas emissions and lean-burn operation. Miller cycle and exhaust gas recirculation (EGR), as major means of this work, are explored more in detail.

In Chapter 3, relevant parameters for studying the Lean-Miller-EGR working process are addressed and results of 0D calculations assuming an ideal gas exchange analysed. With respect to actual engine operation, a method to determine the effective compression ratio in due consideration of gas dynamic effects is presented.

Chapter 4 details the experimental and numerical setup used in this work, including a constant volume combustion chamber (CVCC) and two single-cylinder test bed engines. The results from engine I primarily served to validate a detailed 1D CFD (Computational Fluid Dynamics) engine model created in this thesis, while engine II was used for experimental trials (Chapter 7). Detailed CAD data of the intake and exhaust port as well as the combustion chamber allowed creating a gas exchange 3D CFD model.

Chapter 5 elaborates on a 1D CFD study of varying Miller valve timing at constant effective compression ratio. After analysing air-diluted engine operation, the effect of EGR as a second diluent is evaluated. Based on the results, early and late Miller configurations that not only exhibit the same effective compression ratio but also the same expansion/compression ratio are selected for subsequent engine trials.

The realisation of the determined early and late Miller configurations is subject of Chapter 6. It involves the simulation-assisted design of the valve train and the increase of the compression ratio by modifying piston geometry.

At the beginning of Chapter 7, experimental results from the CVCC are presented. The influence of mixture dilution, either achieved through air or additional exhaust gas, is analysed with particular attention on laminar burning velocity and combustion temperature. After, the effect of cooled EGR on engine operation with baseline valve timing is studied at almost constant intake port temperature to avoid that thermal influences could distort the interpretation of the results. While the first analysis focuses on the ISFC-NO_x trade-off at constant IMEP, the second shows the potential to increase IMEP at constant NO_x emissions. Subsequently, engine testing with early and late Miller valve timing and with increased compression ratio in air-diluted engine operation is explored. Characteristic combustion parameters are evaluated using data from 3D CFD calculations. Eventually, the influence of EGR for both Miller designs is studied and compared to the lean operated baseline engine.

Chapter 8 summarises the findings of this work and suggests actions to take in the future development of the working process.

The results presented stem from a publicly funded research project, whose results were partly published before in [101–106].

2 Fundamentals and State of the Art

Efficiency and emissions of an internal combustion engine (ICE) are mainly driven by the combustion itself. It is therefore crucial for the outcome of the alternative working process investigated in this work. After briefly describing the fundamentals of combustion and formation of the most important emissions, the single means applied in this work, i.e. lean-burn operation, Miller cycle and exhaust gas recirculation (EGR), are subject of this chapter.

2.1 Combustion

The combustion process describes the exothermic conversion of chemically bonded energy into heat. In complete combustion, a hydrocarbon fuel C_xH_y reacts with oxygen O_2 to form carbon dioxide CO_2 and water vapour H_2O as described by the following chemical equation:

$$C_xH_y + \left(x + \frac{y}{4}\right)(O_2 + 3.773\,N_2) \rightarrow xCO_2 + \frac{y}{4}H_2O + 3.773\left(x + \frac{y}{4}\right)N_2 \qquad (2\text{-}1)$$
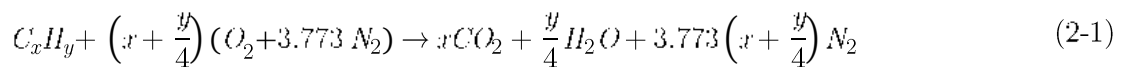
Air, as oxygen source, primarily contains nitrogen N_2 ($N_2/O_2 \approx 0.7905/0.2095$ (volumetric)) and is therefore found to a large extent in the exhaust gas. For a combustion with excess air, exhaust gas also includes O_2, whereas a lack of O_2 results in unburnt hydrocarbons and CO. The relative air-fuel ratio λ or its inverse, the fuel-air equivalence ratio ϕ, are commonly used parameters to describe the ratio of moles of O_2 available for combustion n_{O2} and the fuel-dependent number of moles of O_2 required for a stoichiometric combustion $n_{O2,stoich}$ or vice versa:

$$\lambda = \phi^{-1} = \frac{n_{O2}}{n_{O2,stoich}} \qquad (2\text{-}2)$$

7

Stoichiometric combustion takes place at $\lambda = 1.0$, while $\lambda > 1.0$ and $\lambda < 1.0$ defines combustion of lean and rich mixtures, respectively. The relative air-fuel ratio strongly influences both combustion temperature and the laminar burning velocity, thus affecting engine performance and emissions significantly. For engine cycle analysis and simulation, the initial combustion temperature is described by the adiabatic flame temperature calculated by applying the first law of thermodynamics [29, 169]. It results from a complete combustion with no shaft work or heat transfer to the surroundings and represents the maximum temperature of a combustion process at constant pressure or constant volume. Figure 2-1 (left) shows the adiabatic flame temperature at constant pressure as function of the fuel-air equivalence ratio for different fuels at standard conditions for temperature and pressure. Since there is more dissociation, i.e. endothermic reactions, for hydrocarbon-air mixtures on the lean side, peaking of adiabatic flame temperature occur for rich mixtures [77].

When discussing the influence of mixture composition on flame propagation of a premixed combustion within a reciprocating combustion engine, it is important to distinguish between laminar and turbulent burning velocity. The laminar burning velocity s_l is defined as the velocity, at which unburnt gas of the premixed mixture propagates through the flame front and is transformed to products under laminar flow conditions [57, 156]. The laminar burning velocity, in literature also often termed as laminar flame speed or velocity [116], only depends on composition, temperature and pressure of the mixture. It can be determined experimentally using constant volume combustion chambers (CVCC) or laminar flow burners, occasionally equipped with optical metrology. Alternatively, numerical codes, containing comprehensive reaction kinetic mechanisms, allow for its calculation [124]. The influence of mixture dilution achieved either through air or exhaust gas on laminar burning velocity of air-methane or air-exhaust-gas-methane mixtures was subject of several works, all pointing out that increasing dilution slows down combustion [14, 24, 34, 50, 83, 122, 124, 176]. Witt and Griebel [176] compared numerical results obtained using GRI-Mech 3.0 mechanism to experimental work of others for lean air-methane mixtures and derived the empirical correlations given by Eq. (2-3)

$$s_l = c \cdot p^{-d} \tag{2-3}$$

where p stand for pressure and c and d are coefficients that depend on the temperature of the unburnt zone and the relative air-fuel ratio (see Annex A.1). Lämmle [74] extended this correlation by the findings of Liao et al. [79], who studied the effect of volumetric residual gas concentrations rg_{vol} up to $30\,\%$ on both lean and rich combustion ($0.7 < \phi < 1.2$) of natural gas with a volumetric methane fraction of $96.16\,\%$:

$$s_l = c \cdot p^{-d} \left(5.4825 \cdot rg_{vol}^2 - 4.1988 \cdot rg_{vol} + 0.9952\right) \tag{2-4}$$

In spark-ignited ICE, flame kernel growth is initially determined by a laminar burning velocity. As the flame front increases in size, it becomes sensitive to the eddies of the turbulent flow field inside the combustion chamber [117]. The eddies wrinkle and distort

the flame front, leading to a turbulent combustion with a larger flame area shown in Figure 2-1 (right).
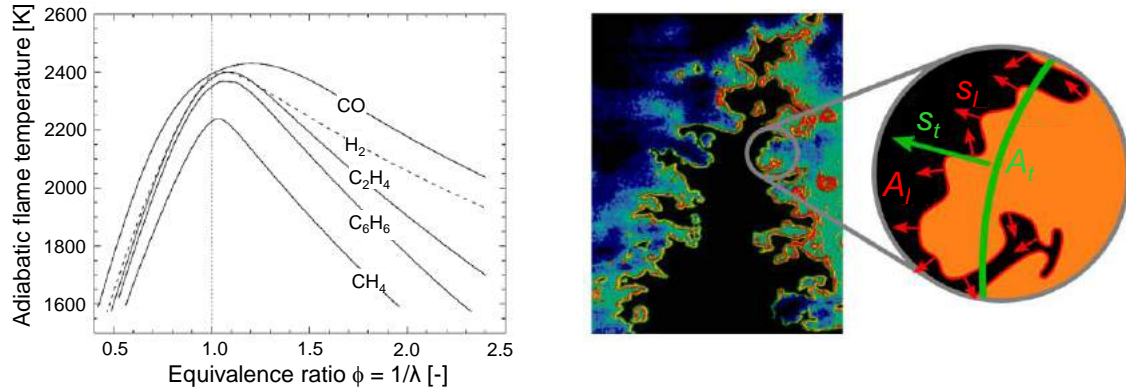
Figure 2-1: Adiabatic flame temperature over fuel-air equivalence ratio of different fuels according to [77] (left) and shape of a turbulent flame front according to [124] (right)

According to the approach of Damköhler [30], the flame front propagates with a turbulent burning velocity s_t that is related to the turbulent area A_t, the laminar burning velocity s_l and its area A_l:

$$s_t = s_l \cdot \frac{A_l}{A_t}$$

(2-5)

Damköhler suggests to calculate the turbulent burning velocity as the sum of the laminar burning velocity and the root mean square of the turbulent fluctuation velocity u':

$$s_t = s_l + u'$$

(2-6)

Equation (2-6) describes the proportional behaviour between the turbulent burning velocity and the turbulent fluctuation velocity. This is true until the time required for chemical reactions to occur gain importance, thus reducing the increase in turbulent burning velocity [115]. Nevertheless, burning velocity in engine operation still reaches values several times higher than the laminar burning velocity [57].

2.2 Exhaust Gas Emissions

Equation (2-1) represents a very simplified approach to describe the combustion process, since, in fact, numerous reactions take place. These result in intermediate products that either take part in further reactions or remain in the exhaust gas as consequence of incomplete combustion caused by insufficient amount of O_2 molecules or reactions that take place too slow to achieve chemical equilibrium. As a result, the exhaust gas contains far more components than calculated from ideal combustion, including pollutants such as carbon monoxide (CO), nitrogen oxide (NO_x), unburnt hydrocarbons (HC) and particulates. While the last is negligible for gas engines due to external mixture preparation [88], NO_x, HC and

CO emissions highly depend on the relative air-fuel ratio λ as shown in Figure 2-2.
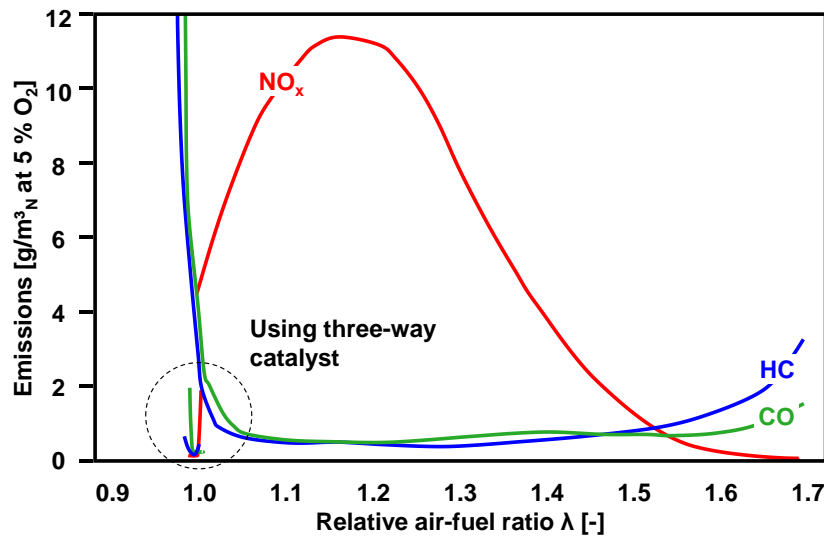
Figure 2-2: NOx, HC and CO emissions over air-fuel ratio of a gas engine based on [3]

Although pollutants form merely a small part of the exhaust gas (approximately 1 % for a petrol engine), they pose a threat to human health and the environment [88]. The emitted CO_2 is not considered as a pollutant, in spite of its contribution to global warming [88]. This arises from the fact that it represents no direct threat to human's health and occurs in the course of complete oxidation of any hydrocarbon. Hence, it can only be reduced by either improving engine fuel consumption or using an alternative combustible of a lower ratio between CO_2 and lower heating value (LHV) [88]. In the following, the formation of the main exhaust gas components of gas engines is described. For a more detailed explanation on engine emissions, the author refers to literature [27, 88, 90, 96, 169]

2.2.1 Nitrogen Oxides NOx

Nitrogen oxides (NO_x) react in the atmosphere with water vapour and solar radiation to cause ground ozone and a part of acid rain [29]. In stoichiometric or moderate lean burn operation, the emitted NO_x is mainly composed of nitric oxide (NO) that entirely oxidises to nitrogen dioxide NO_2 under ambient conditions. The four widely accepted mechanisms to describe the NO formation, namely thermal, prompt, fuel and N_2O mechanism, are briefly addressed in the following:

Thermal NO
Thermal NO is formed behind the flame front in the hot burnt gas mainly from atmospheric nitrogen [90]. Zeldovich described a 2-step reaction mechanism for the first time in 1946, which Lavoie extended in 1970. It shows that free oxygen radicals and high OH concentration are vital to the oxidation process, following to

$$O + N_2 \overset{k_1}{\longleftrightarrow} NO + N \qquad\qquad\qquad\qquad (2\text{-}7)$$

$$N + O_2 \overset{k_2}{\longleftrightarrow} NO + O \tag{2-8}$$

$$N + OH \overset{k_3}{\longleftrightarrow} NO + H \tag{2-9}$$
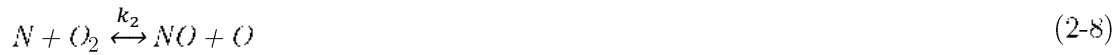
where k_1 to k_3 are the experimentally determined rate constants of the forward and reverse reactions. The forward reaction plays a predominant role over the reverse reaction due to lower temperature in the later part of the combustion. The reactions take place very slowly, causing a "freezing" of the NO concentration. In literature, different values are found for the forward rate constant, all showing that reaction (2-7) is significantly slower than (2-8) and (2-9). Due to the triple bond of the N_2 molecule, reaction (2-7) requires a high activation energy and only proceeds quickly at high temperatures. It is therefore crucial for thermal NO formation, whose name suggests its high temperature dependency. A temperature rise from 2000 to 2500 K, for example, increases the amount of NO by a factor of approximately 50 [88].

Prompt NO

The prompt NO mechanism, postulated by Fenimore in 1979, describes rapid NO formation in the flame front [90]. Owing to its low activation energy, it occurs at temperatures of about 1000 K [88]. The mechanism is much more complex than the one of thermal NO, as it is coupled to the CH radical that undergoes various reactions. The CH radical reacts with N_2 to form hydrogen cyanide (HCN) and N, and eventually oxidises to NO. However, ethyne (C_2H_2), as precursor of the CH radical, is only formed in the flame front under rich conditions, thus prompt NO plays a minor role in homogenous lean combustion.

NO formed via Nitrous Oxide

NO from nitrous oxide N_2O mechanism gains in importance for lean mixtures, where thermal NO decreases due to lower combustion temperature. Furthermore, lean conditions suppress the formation of CH radicals and, in turn, the one of prompt NO. The mechanism occurs at high pressures, as in the case of lean Otto or modern Diesel engines, and is hardly affected by low temperatures. It is presumably the main source of NO in HCCI engine operation under lean conditions [88].

NO from Fuel Nitrogen

This reaction mechanism is negligible for engine operation with hydrocarbon fuels but plays a relevant role for coal or coal-derived fuels that contain a considerable amount $(0.5 - 2.0$ % by weight) of chemically bonded nitrogen [90]. The nitrogen-containing compounds evaporate during the gasification to convert over multiple reactions to precursors of NO formation such as HCN and NH_3 [88].

Reactions to NO_2

The NO fraction found in the exhaust gas of ICE is usually predominant to that of NO_2. However, at low combustion temperatures, prevailing in combustion of highly diluted mixtures, the ratio between NO_2 and NO can increase notably due to following reactions:

$$NO + HO_2 \leftrightarrow NO_2 + OH \tag{2-10}$$

$$NO + OH \leftrightarrow NO_2 + H \tag{2-11}$$

$$NO + O_2 \leftrightarrow NO_2 + O \tag{2-12}$$

While reaction (2-10) gives the conversion from NO to NO_2 at low temperatures and high HO_2 concentrations, reaction (2-11) accounts for the decomposition of NO_2 at high temperatures. The main NO_2 source for low combustion temperature working processes is likely found in reaction (2-12). It describes the NO_2 conversion at low temperature, which cannot react again to NO, owing to the slow combustion and the lack of oxygen caused by poor homogenisation [88]. Hence, not only low temperatures but also high oxygen levels support high NO_2/NO ratios [110].

2.2.2 Carbon Monoxide CO

The combustion of hydrocarbons is accompanied by the formation of carbon monoxide CO, which is favoured by high temperature and pressure. It is oxidised to CO_2 relatively late in the combustion process and represents about 45 % of the fuel's heat release [88]. While the concentration of OH radicals promotes the oxidation, dissociation of CO_2 increases the thermal decay of the oxidation products of reaction (2-13) [36].

$$CO + OH \leftrightarrow CO_2 + H \tag{2-13}$$

In rich combustion, both unburnt fuel caused by the lack of oxygen and pronounced dissociation as high temperatures contribute to high CO emissions [29]. Dissociation is also the source for CO emissions under stoichiometric and lean conditions, for which theoretically, CO would entirely oxidise to CO_2. For very lean mixtures, low combustion temperatures and incomplete combustion close to the cylinder walls reduce the temperature-dependent reaction rate of reaction (2-13). As a result of the slower oxidation of CO to CO_2, the CO fraction increases [88].

2.2.3 Hydrocarbons HC and Formaldehyde HCHO

Hydrocarbons (HC) originate from areas that cannot be reached by the flame, leading to combustion that takes place incompletely or not at all. HC consist of numerous species, of which some react in the atmosphere with NO_2 to form smog in the presence of sunlight [26, 29]. Peak HC emissions occur under cold conditions that hinder their oxidation and, in the case of liquid fuels, their evaporation process. With the mixture type being decisive for their formation, note that the following description is confined to conventional Otto engines running with homogeneous mixtures [27, 88]. The main source of HC emissions are crevices, followed by flame and wall quenching effects as secondary sources. Crevices are narrow regions connected to the main combustion chamber that the mixture can enter or escape but the flame cannot propagate into since it is extinguished by the cold walls. The crevice

volume, including piston top-land, spark plug thread, valve seat and head gasket crevice, usually amounts to 1 to 2 % of the clearance volume. The gas density in the crevices is several times higher than that in the bulk, as the cold cylinder walls cool it down rapidly. For this reason, the affected mass is significantly higher than the volume initially indicates. Cheng [27] argues that crevices cause 38 % of HC emissions in petrol operation, with the piston-ring-liner region representing the predominant crevice HC source. For lean-burn gas engines, Bauer and Wachtmeister [8] found the crevice region to be responsible for 70 to 90 % of HC emissions. Lean mixtures close to their burn limit are furthermore affected by flame quenching effects, extinguishing the flame prematurely before it reaches the cylinder wall [8, 27]. Another HC source is wall quenching that describes the effect where a flame extinguishes shortly before the cylinder wall, resulting in a thin layer of unburnt air-fuel mixture adjacent to the wall [27]. Most of the unburnt fuel fraction diffuses into the flame and converts to products rapidly, thus contributing only little to HC emissions [96]. Another small HC source that gains relevance for aging engines represents exhaust valve leakage [27].

Next to HC emissions, Bauer and Wachtmeister analysed in [8] also the formation of Formaldehyde (HCHO) in lean-burn gas combustion. HCHO is an intermediate product of the methane oxidation process that occurs in the cold flame region at temperatures of 400 to 800 K and oxidises quickly at 1200 K and above [8]. The authors claim incomplete combustion and partial burning to be decisive for HCHO emissions and thus sharing the same sources as HC emissions. Emissions from the piston top-land crevice volume showed differing behaviour for varying ignition timing and air-fuel ratio, whereas a strong correlation between both HCHO and HC caused from other sources became evident [8].

For petrol operation, HC and HCHO emissions emerge from oil layers, liquid fuel and deposits, which, however, are either negligibly small or non-existent for lean natural gas operation [96].

2.3 Homogeneous Lean-burn Operation

The majority of stationary gas engines operate with lean air-fuel mixture to profit from low combustion temperatures that lead to low raw NO_x emissions, prolong engine lifetime due to lower thermal load and benefit efficiency partly caused by reduced wall heat losses. A further advantage arises from the higher ratio of the specific heat capacities γ, which is, beside the compression ratio r_c the only parameter that determines the thermal efficiency η_{th} of the air-standard Otto cycle:

$$\eta_{th} = 1 - \frac{1}{r_c^{\gamma-1}} \qquad (2-14)$$

The air-standard cycle assumes a constant ratio of the specific heat capacities and is not to be confused with the ideal engine cycle, which indeed features the consideration of the

temperature-dependent mixture properties and furthermore dissociation. The ideal engine's efficiency $\eta_{id,al}$ as function of the relative air-fuel ratio λ and the compression ratio is shown in Figure 2-3 (left). Increasing λ from 1.0 to 1.6 for a compression ratio of $r_c = 13.0$ lifts thermal efficiency from 50.3 to 54.3 %, while a stoichiometric operated engine would require a compression ratio over 18:1 to achieve the same benefit. In response to the higher temperature level at the end of the compression stroke, however, knocking tendency, peak combustion pressure and NO_x emissions would increase. Depending on the application, either one of these effects restrict the compression ratio. Leaning, on the other hand, is primarily limited by increasing combustion instability [120], whose root cause is spatial mixture inhomogeneity as reported by Gorenflo [47]. Besides, increasing mixture dilution prolongs burning delay and burn duration as a result of falling laminar burning velocities, as shown in Figure 2-3 (right).
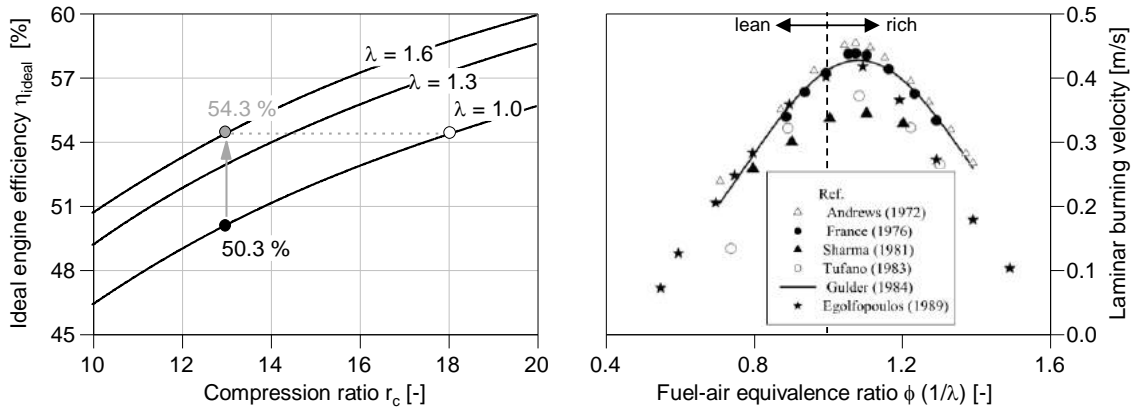
Figure 2-3: Efficiency of the ideal engine over compression ratio for varying relative air-fuel ratio (left); Laminar burning velocity over fuel-air equivalence ratio (right) [24]

Mixture density and temperature, residual gas fraction and flow conditions in the spark region govern the inflammation process within the prechamber [68] and, in turn, the formation of the flame jets to induce the main combustion. Fresh mixture enters the unscavenged prechamber during the compression stroke, causing a reduction of the residual gas fraction. This first leads either to a lower or constant temperature, in the case mixing balances the temperature rise caused by the compression as reported in [129]. In the further course of the compression stroke, both mixture temperature and pressure increase while density decreases. Turbulent kinetic energy (TKE) inside the prechamber also rises over crank angle until it peaks shortly before TDC [100, 129]. From this it follows that very early ignition timings lead to unfavourable ignition conditions and reduce the efficacy of the prechamber due to smaller flame jet size, while retarded combustion has the opposing effect. However, optimal ignition conditions are difficult to generalise since the prechamber design, defined by, amongst others, the volume, the number of orifices and their orientation, is often specifically adjusted to the engine's specifications.

Prechamber spark plugs are frequently used in small lean-burn cogeneration engines to

overcome the disadvantages of extended burn durations and higher cycle-by-cycle variations. The prechamber decouples the flow conditions at the vicinity of the spark from the ones of the main combustion chamber. After the exhaust and intake stroke, the prechamber is only filled with exhaust gas from the former cycle. In the course of the compression stroke, air-fuel mixture enters the prechamber through tangentially arranged orifices, leading to good homogenisation with the exhaust gas. Due to a high degree of turbulence within the prechamber, a stable and rapid inflammation takes place, causing a fast heat release and significant pressure rise. The pressure difference to the main combustion chamber produces flame jets that penetrate into the main combustion chamber with a pressure difference of 1 to 3 bar for prechamber volumes between 1 to 2 % of the volume at TDC [165]. The intense and wide mixture inflammation as well as additional turbulence generated in the main combustion chamber decrease burning delay and cycle-by-cycle variations [3, 65, 68], allowing small gas engines to operate at $\lambda = 1.5 - 1.7$. Since large gas engines run at lower engine speeds than those in the small power range, they experience lower wall heat losses due to the smaller surface area to volume ratio (A/V). In response to higher process temperature as well as prolonged time for NO_x formation, the relative air-fuel ratio to achieve acceptable NO_x emissions increases. The increased burn duration due to leaning and longer flame distance limit the use of unscavenged prechamber spark plugs to cylinder bore diameters of smaller than 250 mm [3]. Therefore, large gas engines are equipped with scavenged prechambers that benefit from a nearly stoichiometric air-fuel mixture realised through fuel injection into the prechamber during compression stroke. The increased mixture strength intensifies the flame jets significantly and facilitates the ignition of very lean mixtures in the main combustion chamber of $\lambda \approx 2.0$ [65].

Figure 2-4 (left) shows the cumulated released heat over crank angle at constant relative air-fuel ratio of $\lambda = 1.4$ and a constant ignition timing of a naturally aspirated gas engine operated with standard and unscavenged prechamber spark plug [151]. Combustion initiated by the prechamber takes place notably faster, indicated by a shorter burn duration of 4.2 °CA and advanced combustion phasing of about 10 °CA. For trials at MBT spark timing (maximum brake torque), the misfire limit is shifted slightly, while combustion stability is substantially improved as COV_{IMEP} plotted over λ in Figure 2-4 (right) shows.

With the ignition concept being decisive for combustion stability, alternative approaches, including, laser, plasma, microwave, corona or performance gas ignition (PGI), were and are studied by others [49]. A thorough review of prechamber initiated combustion is given in [160]. Another innovative concept is hot surface ignition (HSI), which is also subject of research work at Karlsruhe UAS [139]. Further means to improve the lean-burn capability of an engine aim at intensifying charge motion, leading to accelerated combustion and higher combustion stability [68, 120, 132].
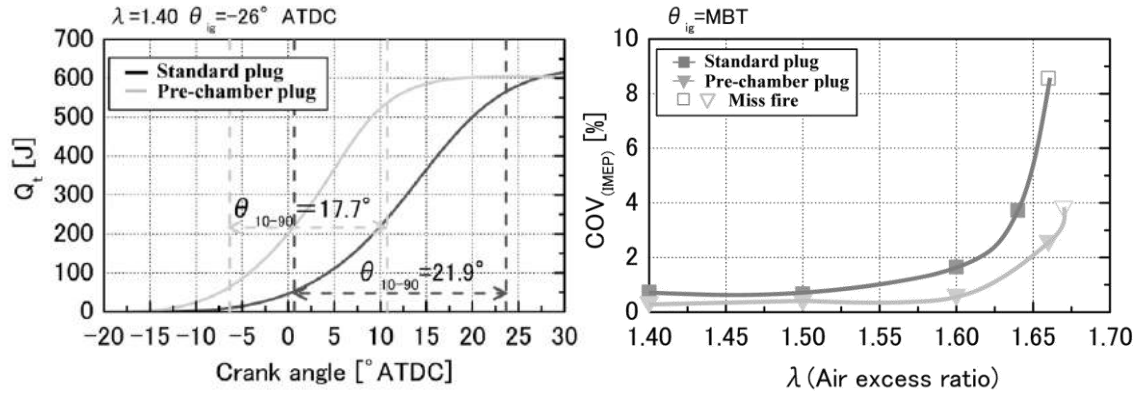
Figure 2-4: Cumulative heat release (left) and COV_IMEP (right) over relative air-fuel ratio at MBI spark timing [151]

High levels of mixture dilution through air can improve the engine's thermal efficiency but decreasing fuel concentration requires a larger in-cylinder mass for achieving the same IMEP. Part load applications manage this by simply de-throttling, while turbocharged engines enhance in-cylinder filling by increasing boost pressure. In the case of a naturally aspirated engine, leaning is detrimental to IMEP. Consequently, thermal efficiency might improve but at the expense of brake efficiency due to the lower IMEP/FMEP ratio.

2.4 Miller Cycle

The intake valve of a conventional engine closes shortly after bottom dead centre (BDC), in order to take advantage of gas dynamic effects that favour engine breathing. Closing the intake valve earlier or later, on the other hand, might be attractive for multiple reasons as it can:

- increase engine efficiency
- reduce NO_x emissions
- mitigate the knocking tendency
- reduce pumping work in part load operation
- improve aftertreatment
- reduce the engine's thermal load
- increase rated power

2.4.1 Background and Denomination of Miller Cycle

Early and late intake valve closing (IVC) (see Figure 2-5) was firstly described in the patents and publications of Ralph Miller [91–94], released from 1947 to 1957, and is accordingly often denoted as Miller cycle. Miller increased the charging pressure and used an intercooler to provide sufficient mass of in-cylinder charge at favourable thermodynamic conditions. For early IVC, the trapped charge within the cylinder expands after closing the intake valve before BDC, i.e. during the intake stroke, leading to similar pressure but lower

temperature at the beginning of the compression than that of ordinary supercharged combustion engines [92]. A similar effect is achieved for late IVC, however, as opposed to an intermediate expansion, a part of the mixture is discharged during the compression stroke.
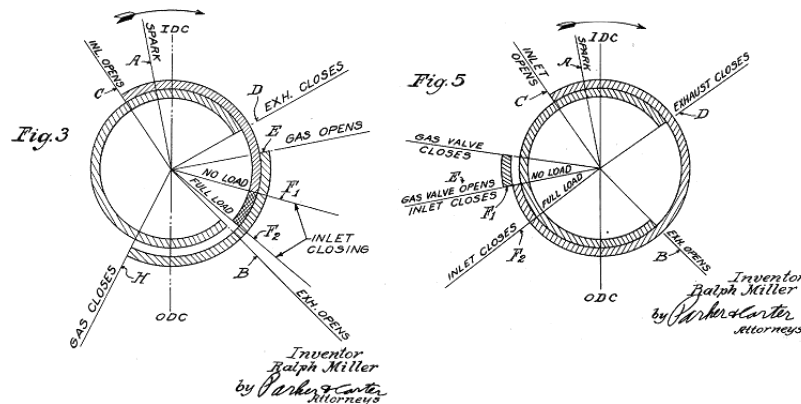

Figure 2-5: Early (left) and late (right) intake valve closing [93]

The process, also named '*low temperature supercharging*', allows the engine to operate at higher power without increasing thermal load on engine components. A mechanical device is used to vary intake valve timing in engine operation with respect to engine load. In [94], Miller discusses results of this working process in large gas engines and a Diesel engine. The latter operates with IVC for highest charging efficiency – i.e. IVC after BDC – from half-load down to ensure reliable ignition conditions. For higher loads, intake valve closing is advanced and boost pressure increased to maintain the compression end pressure constant. At same thermal load, the benefit in brake mean effective pressure (BMEP) over a conventional supercharged engine amounts to 22.1 % and 34.3 %, respectively. Contrary to the Diesel engine, the gas engines, discussed in [94], operated at constant air-fuel ratio and varying early intake valve closing, regardless of engine load. As a result of the consistently higher expansion to compression ratio, decreasing exhaust heat losses enable an indicated efficiency up to 50 %. Latest IVC of about 55 °CA before bottom dead centre BBDC is set at 85 % load, while in full load the engine needs to slightly advance IVC to avoid knocking at maximum boost pressure. Decreasing boost pressure and advancing IVC allow the engine to operate at lower load. Since the regulation of load occurs at constant air-fuel ratio, it is similar to that of nowadays automotive Otto engines equipped with unthrottled load control by the means of variable valve timing [37]. In [93], Miller addresses the benefit of applying early or late intake valve closing also for a naturally aspirated engine. In response to a reduced effective compression ratio, knocking tendency decreases while maintaining a high expansion ratio.

Overexpansion is one of the major features of the Miller cycle. Its basic idea goes back to the work of James Atkinson, who patented a 4-stroke gas engine with a specific crank train design in 1887 (see Figure 2-6). Its key component is an additional linkage (E), connecting

the connecting rod (C), the crankshaft (F) and a further linkage (H) with one another. While the crankshaft experiences a continuous rotational motion, the linkage (H), which is attached on the other end to a fixed centre, rotates back and forth. This entails expansion and exhaust strokes that are longer than the intake and compression strokes [2]. Very recent work shows that weight and friction pose the main challenges when realising such an engine configuration [114].

J. ATKINSON.
GAS ENGINE.
No. 367,496.   Patented Aug. 2, 1887.
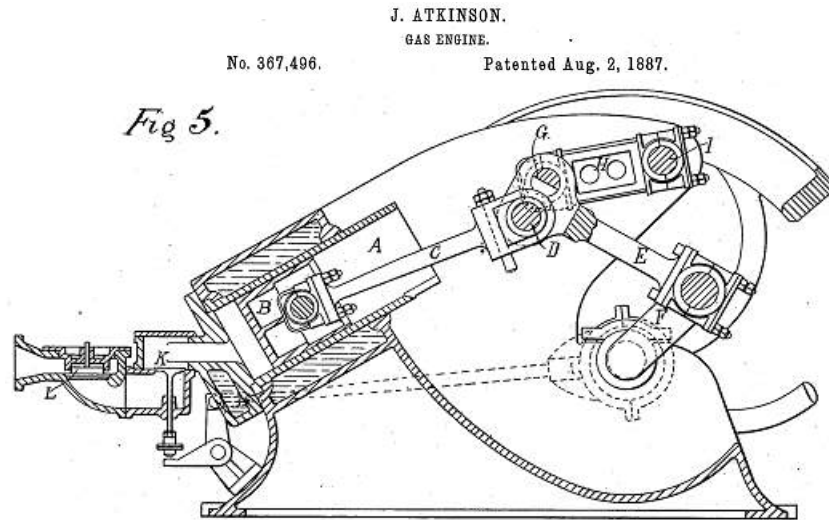
Figure 2-6: Cut-view through Atkinson's extended expansion engine [2]

A working process with an extended expansion realised over the crank train is named after its inventor Atkinson cycle. This term is, however, often used to describe late intake valve closing even if Atkinson never mentioned to adjust the valve event. Hence, it is somehow unclear why late intake valve closing is associated with Atkinson cycle in literature. A possible explanation is given in [141], presuming that a paper of Luria et al. [81], published in 1982, is the origin of this discrepancy. The authors in [81] introduce the name '*Otto-Atkinson engine*' for a configuration that retards intake valve closing in correspondence to the load.

Table 2-1 shows the different definitions that have been established over the years to describe IVC before or after BDC as early/late Miller, Miller/Atkinson valve timing or cycle or early/late IVC.

Table 2-1: Denomination of Miller cycle found in literature

Miller with IVC before BDC	Miller with IVC after BDC	Source
Early Miller	Late Miller	[41, 45, 46, 51, 126, 131, 141, 153, 154]
Miller valve timing / cycle	Atkinson valve timing / cycle	[40, 56, 61, 127, 136, 142, 166, 168, 178, 179]
Early IVC	Late IVC	[37, 38, 54, 95, 175]

2.4.2 Cycle Parameters and Geometrical Relations

The air-standard Otto cycle opens and closes the intake and exhaust valve at bottom dead centre (BDC) and top dead centre (TDC), respectively. Consequently, compression and expansion occur over the whole piston stroke from BDC to TDC and vice versa. Advancing or retarding intake valve closing (IVC), reduces the effective compression ratio, thus lowering the pressure level at the end of the compression stroke, as shown in Figure 2-7 (left). IVC before BDC leads to an intermediate expansion from IVC to BDC with a start of the compression stroke below ambient pressure. Retarded IVC, on the other hand, features a gas exchange that takes place beyond BDC, where mixture exits the cylinder isobarically until meeting IVC. Once the intake valve has closed (at $1_b'$), both early and late Miller show coherent pressure traces. The effective compression ratio and engine efficiency decrease to the same extent for both valve timings. For this reason, this work no longer distinguishes between early and late Miller approaches in idealised cycle considerations.
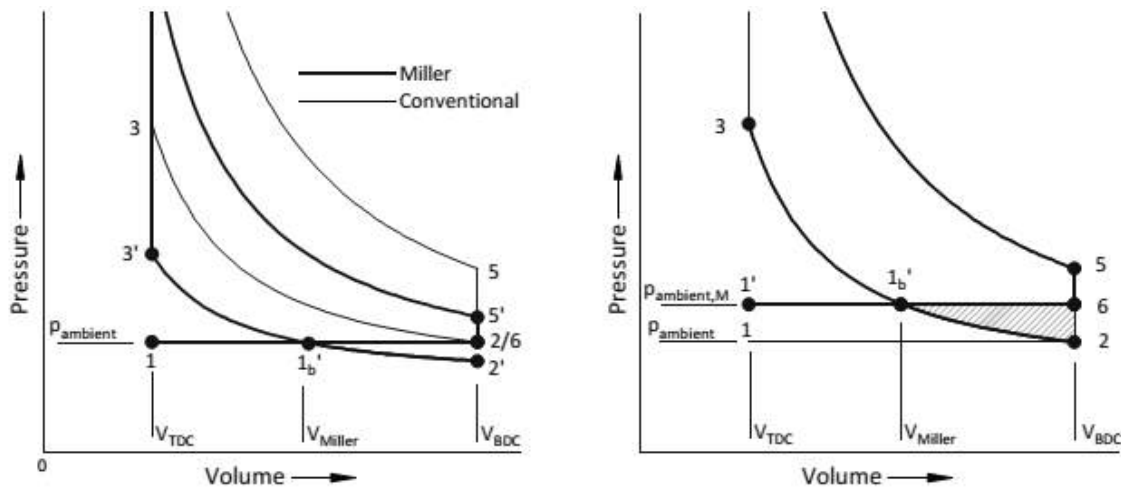
Figure 2-7: Air-standard Otto and Miller cycle at same geometrical compression ratio [141]

Unless the effective compression ratio is adjusted to its initial value, the cycle experiences a loss in engine efficiency. The drawback, highlighted as shaded area, becomes clear when superimposing the high-pressure phase of both Miller and Otto cycle in Figure 2-7 (right). It assumes that thermodynamic ambient conditions of the Miller cycle equal the ones inside the cylinder of the Otto configuration at the volume Miller closes its intake valve. As a result of the same mass, the same heat is added to the cycle, leading to coherent pressure traces until Miller cycle opens the exhaust valve at BDC and gas exchange occurs at a higher pressure level. The hatched area below displays the loss in work that occurs without adjusting the effective compression ratio as IVC is modified.

Assuming equal ambient conditions for both cycles, leads to a mass of in-cylinder charge that is proportional to the volume at IVC (see Figure 2-8). At constant relative air-fuel ratio, the added heat Q only depends on the charging efficiency. The charging efficiency describes the ratio between the actual in-cylinder mass and the theoretical in-cylinder mass

when assuming that the displacement volume is filled with mixture under ambient conditions [57]. The isobaric gas exchange at ambient pressure level of the air-standard engine cycle leads to highest charging efficiency for IVC at BDC (i.e. ideal Otto cycle). With V_{BDC} and V_{TDC} being the volumes at BDC and TDC, respectively, the compression ratio r_c and expansion ratio r_e of the ideal Otto cycle solely depend on cylinder geometry. Both parameters match each other and can also be denoted as geometrical compression and geometrical expansion ratio r_{geo} as given in Eq. (2-15):

$$r_c = r_e = r_{geo} = \frac{V_{BDC}}{V_{TDC}} \tag{2-15}$$

The compression of the air-standard Miller cycle, on the other hand, effectively commences during the compression stroke at the volume for which IVC occurs, $V_{IVC,Miller}$. To achieve same temperature and pressure at the end of the compression stroke, the effective compression ratio is to be adjusted. To this end, V_{TDC} is reduced, becoming $V_{TDC,Miller}$ so that the compression ratio $r_{c,Miller}$ follows to:

$$r_{c,Miller} = \frac{V_{IVC,Miller}}{V_{TDC,Miller}} \tag{2-16}$$

V_{BDC} is altered by the same value as V_{TDC} and hence renamed to $V_{TDC,Miller}$. Shifting the ordinate of Miller cycle correspondingly, sharpens the understanding of the geometrical relations (see Figure 2-8, left). Since exhaust valve opening (EVO) still occurs at BDC, the expansion ratio $r_{e,Miller}$ is analogously defined to the Otto cycle over the ratio between both dead volumes given by Eq. (2-17):

$$r_{e,Miller} = \frac{V_{BDC,Miller}}{V_{TDC,Miller}} = r_{geo,Miller} \tag{2-17}$$

The ratio between the expansion ratio and the compression ratio is also known as expansion/compression ratio ECR or Miller degree [141], being a characteristic parameter of Miller valve timing [57, 84]:

$$ECR = \frac{r_{e,Miller}}{r_{c,Miller}} = \frac{r_{geo,Miller}}{r_{c,Miller}} = \frac{r_e}{r_c} = \frac{r_{geo}}{r_c} \tag{2-18}$$

For the Otto cycle it applies that $ECR = 1.0$ as $r_e = r_{geo} = r_c$, while Miller cycle reaches $ECR > 1.0$ with $r_{e,Miller} = r_{geo,Miller} > r_{c,Miller}$. The benefit in engine efficiency caused by $ECR > 1.0$, shown as green area, arises from the increased ratio of expansion to compression work. This can be emphasised by referring the cycles to the specific volume v shown in Figure 2-8 (right). Although same specific heats q are added to both cycles, the Miller configuration yields a benefit (depicted as green region) in specific work caused by an extended expansion. Nevertheless, overall cycle work suffers since the loss in expansion work outweighs the benefit in compression work due to less heat Q added (see Figure 2-8, left).
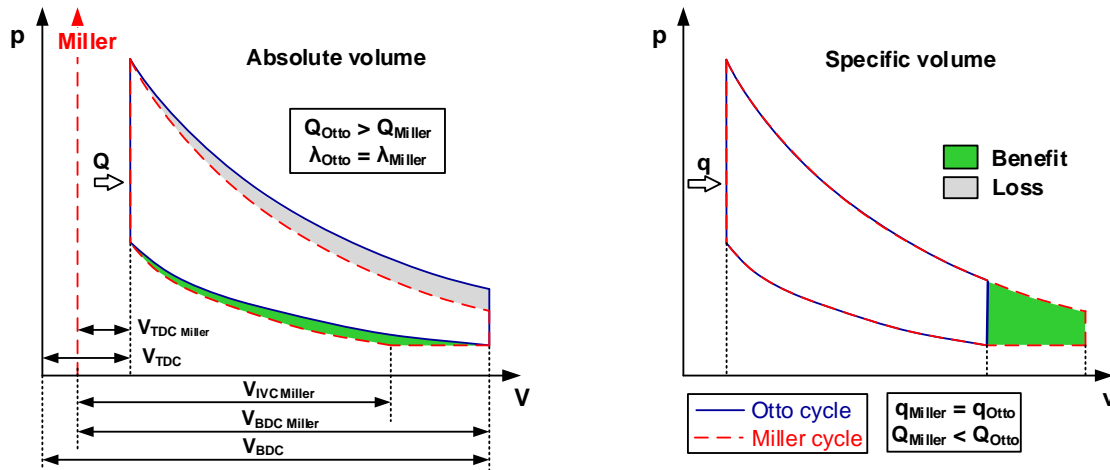
Figure 2-8: Ideal Otto and Miller cycle in the p-V diagram referred to absolute (left) and specific volume (right) (schematically)

The compression ratio, as a driving parameter for engine efficiency (cf. Eq. (2-14)), is limited in actual engine operation by peak combustion pressure, NO_x emissions or knocking combustion. While these restrict the expansion ratio of an engine configuration that operates with Otto valve timing, the Miller cycle enables an expansion ratio that is higher than the effective compression ratio. As a result, engine efficiency increases without exceeding the critical parameters that limit the effective compression ratio. However, the falling in-cylinder mass that reduces engine power at same air-fuel ratio for a naturally aspirated ICE poses the major challenge to also experience a benefit in brake efficiency.

2.4.3 Miller Cycle in Research and Field Operation

The reason to implement Miller cycle varies with respect to the application, the ICE type and the parameter to be optimised. In stationary gas and Diesel engines the major motivation is to improve the trade-off between NO_x emissions and brake specific fuel consumption (BSFC). For automotive Otto engines, on the other hand, the focus lies on lowering fuel consumption or knocking tendency. Depending on the ICE type (naturally aspirated or turbocharged), operation mode (full or part load) and valve train design (fixed or variable valve timing), operating parameters (air-fuel ratio, charging pressure) and engine design (compression ratio, gas path, turbocharger) need to be modified to realise an efficient Miller cycle. The modifications to be made and their effects differ from one another and might improve the target variable but at the same time deteriorate another one. In this context, the ensuing sections give an overview of the different applications in which Miller cycle is found in literature.

2.4.3.1 Miller Cycle for Stationary Gas Engines

The loss in charging efficiency is likely the reason why Miller valve timing is rarely applied to naturally aspirated gas engines. The use of a turbocharger and intercooler would allow compensating the losses in charging efficiency and lead to lower initial process temperature

but same pressure. However, the tailpipe pressure pulsations hinder the use of turbochargers in single-cylinder engines, while using a supercharger is viable, but would significantly increase system costs.

Naturally Aspirated Stationary Gas Engines

Mikalsen et al. [89] conducted a theoretical and numerical study on Miller cycle for a small naturally aspirated cogeneration Otto engine with a displacement volume of 117 cm^3. Starting from the datum configuration with a relatively low compression ratio of 6:1 and an engine speed of 3000 rev/min, the geometrical compression ratio was increased for a constant mean piston velocity by adjusting both piston stroke and engine speed. 3D CFD calculations of the high-pressure loop were carried out with stoichiometric mixture and ignition timings for optimum engine efficiency. Expansion/compression ratios up to 1.6 were analysed, increasing indicated efficiency by over 15 % at the expense of losses in engine power of approximately 30 %. In the case of a lean-burn engines, losses in power can be compensated by reducing the relative air-fuel ratio λ. The rising engine-out NO_x emissions require either engine after-treatment or the increase of the mixture's heat capacity as presented in [103, 105]. The authors conducted a numerical and experimental study for a naturally aspirated lean-burn cogeneration engine with the target to optimise the intake path design for highest charging efficiency. Compared to the baseline configuration, early Miller valve timing decreased NO_x emissions by 30 % for same electrical efficiency and power [105].

The alternative to optimising the intake path is to start from a large engine size that allows for sufficient in-cylinder charge despite Miller valve timing. To the author's knowledge, Yanmar Co., Ltd. is the only manufacturer that follows this approach on naturally aspirated cogeneration engines, for which low power densities are acceptable. The rated power output ranges from 5 kW up to 25 kW in lean-burn, and amounts to 35 kW in stoichiometric operation. The smallest configuration is a 3-cylinder engine with a displacement volume of 900 cm^3 and a cylinder bore of 68 mm [99].

Turbocharged Stationary Gas Engines

Saito et al. [131] realised Miller valve timing for a turbocharged intercooled 23.7 litre 6-cylinder gas engine, operating with a prechamber spark plug. The baseline intake valve closing of 46 °CA after bottom dead centre (ABDC) was retarded to 80 and 100 °CA ABDC, respectively, leading to a lower effective compression ratio at same charging pressure. NO_x emissions decrease thanks to reduced peak combustion temperature and pressure while BMEP is maintained at 10.9 bar by adjusting charging pressure. Both Miller configurations improved the trade-off between BSFC and NO_x emissions, enabling for lowest emissions within that work. Owing to the reduced temperature and pressure level, a decreasing knocking tendency offers potential to further increase the geometrical compression ratio from 13.1 to 15.0 for IVC = 80 °CA ABDC. Figure 2-9 plots brake thermal efficiency

against relative air-fuel ratio λ for the baseline engine ($r_{g,o} = 13.1$) and late Miller configuration ($r_{g,o} = 15.0$) at constant BMEP $= 10.9$ bar. It can be seen that the required charging pressure is higher for Miller cycle at same λ due to the reverse flow that takes place during the compression stroke. The Miller configuration increases efficiency up to 1 %-point close to the knock limit and therefore at relatively high NO_x emissions, while the potential to reduce NO_x emissions for same brake thermal efficiency decreases.
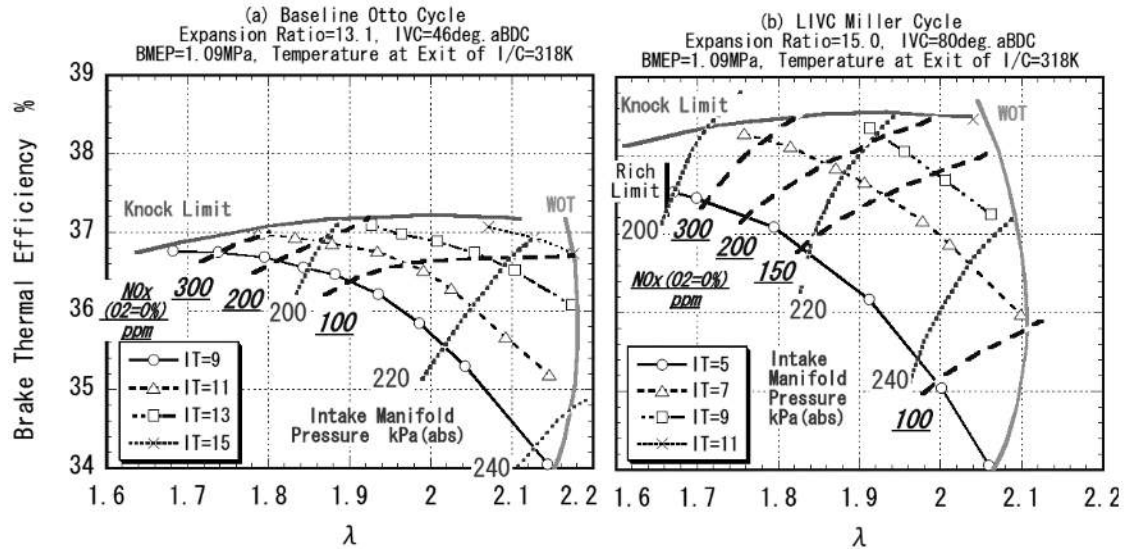

Figure 2-9: Comparison between Otto (left) and late Miller cycle (right) at n = 1500 rev/min [131]

Fukuzwa et al. [46] and Endo et al. [41] describe the development of lean-burn Miller cycle gas engines that operate in a power range from 280 to 1100 kW and at engine speeds of 1200, 1500 and 1800 rev/min. The displacement volume amounts to 4.1 litre/cylinder and the no. of cylinders varies between 6, 12 and 16. Encouraged by the lack of mass-produced turbochargers that give sufficient boost pressure at low flow rates by the time the work was performed, the authors developed a new turbocharger specifically for the valve timing selected. The authors found that a Miller configuration with a geometrical compression ratio of $r_{g,o} = 15.0$ holds a clear advantage in efficiency over conventional lean-burn or stoichiometric operating engines. However, aftertreatment with selective catalytic reduction (SCR) is required to achieve NO_x emissions of 150 ppm and below.

Wülfert et al. [178, 179] analysed early and late Miller valve timing for a single-cylinder research engine with a displacement volume of 4.77 litres, a compression ratio of 13:1 and a constant engine speed of 1500 rev/min. Early Miller valve timing reduces thermal load of the combustion chamber, allowing for higher engine power due to lower knocking tendency. At same engine power, realised by adjusting charging pressure, thermal load of the combustion chamber and NO_x emissions decrease significantly. Fuel consumption, on the contrary, increases due to higher HC emissions and cycle-by-cycle variations. Besides, rising exhaust gas temperature augments the thermal load of the turbocharger. Late Miller cycle shows the opposing trend, where lower fuel consumption is achieved at the expense of NO_x

emissions. The authors argue that the benefit in efficiency arises reportedly from fewer pumping losses.

Fuchs et al. [45] address the ongoing development of a turbocharged and intercooled large-bore natural gas engine of the 1-2 MW segment that already operates with late Miller cycle. One of the keys to higher engine power and efficiency at constant NO_x emissions of 250 mg/m$_N^3$ (at 5 % O_2) and below, was the incorporation of a second turbocharger stage that enables pressure ratios higher than 5 bar. To keep the peak temperature of the unburnt zone, which served as indicator for knocking tendency, constant, intake valve closing needed to be further retarded. Together with an adjusted geometrical compression ratio BMEP increases from 20 to 22 bar. Depending on intake manifold design, the reverse flow that takes place during the compression stroke deteriorates the temperature distribution within the intake manifold. As result, significant variations in temperature and combustion occur across the cylinders and limit further retarding of IVC. Early Miller valve timing, on the other hand, experiences no reverse flow during the compression stroke and allows the engine to operate at same peak temperature of the unburnt zone but a pressure level that is about 8 bar higher than that of the late Miller configuration. Compared to the datum configuration, BMEP increases up to 24 bar and engine efficiency enhances by 0.5 to 1.0 %-points at same NO_x emissions. The benefit is partly attributable to a new prechamber spark ignition system that allows the engine to operate with advanced combustion phasing and lower cycle-by-cycle variations in peak combustion pressure and IMEP.

Behrens et al. [9] realised early Miller valve timing for a slow running (1000 rev/min) 16-cylinder gas engine of 3.6 MW generated brake power. Starting from the baseline compression ratio of 10:1 that is unsusceptible to knocking, an increase to 12:1 leads to a similar methane number required as the one of the baseline engine at same IMEP. The Miller configuration increases engine efficiency from 40.4 to 42.5 % at BMEP = 16 bar and NO_x emissions below 500 mg/m$_N^3$ (TA-Luft).

Miller cycle combined with two-stage turbocharging is also implemented in the largest gas engines of 10 MW and above. Böckhoff et al. describe in [12] the continuous development of the largest MAN gas engine that achieves a brake efficiency over 51 % at BMEP = 22.5 bar. According to Trapp et al. [161], the 20-cylinder Jenbacher J920 engine operates even at higher BMEP of 24 bar and reaches an electrical efficiency of 50.0 %.

2.4.3.2 Miller Cycle in Petrol Engines

In the automotive sector, Otto engines mostly operate with stoichiometric mixture and are therefore quantity-controlled, often realised using throttle valve. The losses in part load operation, mainly arising during the pumping loop, can be decreased by implementing variable valve timing. The mass of air is then controlled by adjusting intake valve closing and throttling (if still required) in correspondence with the required load. The effect of IVC in part load operation is shown in Figure 2-10. It can be clearly seen that advancing or

retarding IVC leads to a smaller pumping loop, thus reducing the pumping losses.
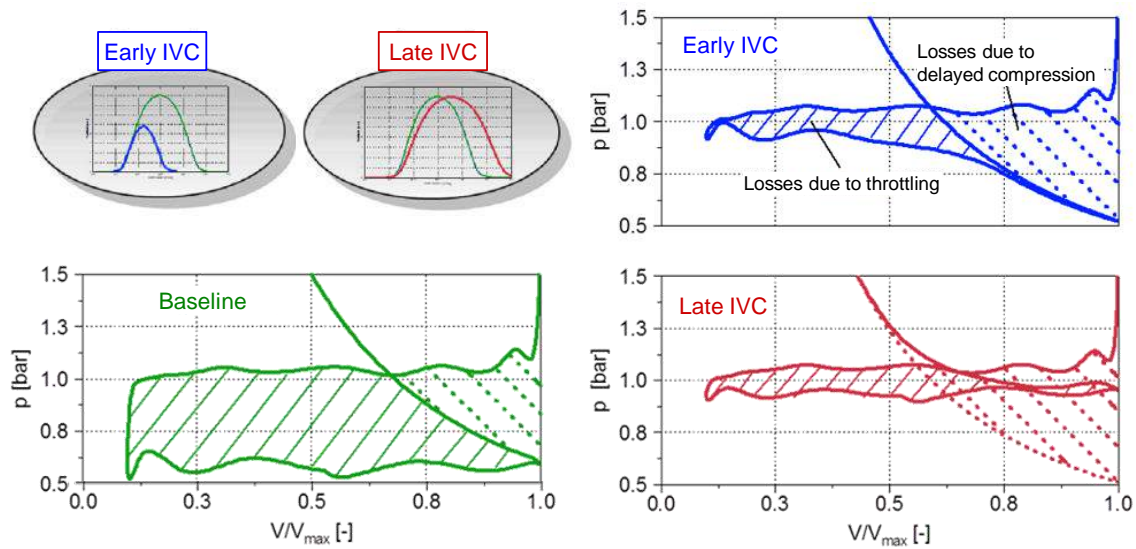

Figure 2-10: Comparison of different part load strategies using variable valve timing (according to [40])

With respect to possible rated engine power, it is of vital importance whether the engine operates naturally aspirated or super-/turbocharged. Engines for transient operating conditions are usually equipped with cam switching (primarily two-stage) or fully variable valve train systems. The latter provides the highest degree of flexibility and is therefore already incorporated in a large number of series production engines [52].

Naturally Aspirated Petrol Engines

Miller cycle is mostly found in naturally aspirated Otto engines of hybrid electrical vehicles, for which the reduced brake torque caused by worsened engine breathing can be increased again by engaging an electrical motor. Examples for recently introduced models are Lexus RX450h, Toyota Prius and Mercedes S 400 hybrid, all featuring high compression ratios between 11.7 and 13.0 [59], realised through late Miller cycle combined with an EGR system. For the Mercedes S 400 hybrid engine (M 272 E35), retarding intake valve closing by 30 °CA as well as modifying the cylinder head to increase in-cylinder charge motion, enables an increase of the compression ratio from 10.7 to 11.7 [59]. The brake torque of the Miller configuration is lower than that of the baseline engine up to speeds of approximately 5700 rev/min. For engine speeds above, the rising ram effect occurring for late intake valve closing lifts the brake torque to higher values than the baseline engine. Besides, the electrical motor overcompensates for the losses in brake torque over the whole engine speed range. In conjunction with a high expansion ratio and reduced pumping losses, fuel consumption can be reduced by 9 % at BMEP = 2 bar and n = 2000 rev/min.

Likewise to hybrid engines, late Miller valve timing and high compression ratios recently gained popularity to purely ICE driven vehicles. In 2011, Mazda presented the Skyactiv-G engine that operates with late IVC, reducing pumping losses by 20 % and allowing for a compression ratio of 14:1 to achieve high engine efficiency [48]. In 2014, Daihatsu, Mazda

and Toyota introduced naturally aspirated engines that operate with Miller cycle with the aim of lowering knocking tendency (Daihatsu) and reducing pumping losses (Mazda and Toyota). The Miller valve timings enable engine designs with high compression ratios that range from 11.5 and 13.5 [64].

Ries et al. [40] studied the influence of different valve timing strategies (IVC at -88 °, 0 and 75 °CA ABDC) as mean to lower pumping losses in part load operation for a single-cylinder engine (bore/stroke = 77/88 mm) operating at constant IMEP = 2.8 bar, n = 2000 rev/min and CA50 = 8 °CA ATDC. Starting from neutral valve timing (IVC at BDC), the pumping mean effective pressure (PMEP) can be reduced by about 9 % for late and 49 % for early Miller valve timing. The lower gross IMEP (IMEP$_g$) required to keep IMEP constant reduces the wall heat losses. Because the modified valve timings alter charge motion (will be addressed in 2.4.4), both configurations experience disadvantages in combustion delay and duration due to a reduced level of turbulence. This effect occurs to a higher extent for early Miller valve timing, yet it holds with a plus of 1.4 %-points in indicated efficiency a larger advantage over the neutral configuration than the late Miller strategy (0.8 %-points).

Turbocharged Petrol Engines

The fact that in 2015 and 2016 numerous car manufactures released turbocharged engines operating with Miller cycle, underlines its potential to improve engine efficiency [17, 18, 64]. Next to reduced losses in part load, it enables lower knocking tendency in full load operation, owing to a decreased temperature level of in-cylinder charge. Flierl et al. [44], for example, applied a fully variable intake valve train to a naturally aspirated 2.0 litre Otto engine, for which intake valve lift and spread were varied during engine operation for three different exhaust valve spreads. Reduced pumping work of 35 % in part load operation (BMEP = 2 bar, n = 2000 rev/min) causes savings in BSFC of 13 %.

Elsner et al. [40] analysed the potential to reduce the losses in part load operation by varying intake valve closing for a 1.4 litre four-cylinder turbocharged Otto engine with direct injection. In low part load at BMEP = 1 bar and n = 2000 rev/min, early IVC decreases BSFC by 12 % and late IVC by 7 % compared to baseline valve timing. The authors claim that early IVC is superior to late IVC due to lower friction losses with decreasing valve lift and the higher benefit in dethrottling. Beside the reduced pumping losses, closing IVC before or after BDC lowers the effective compression ratio, decreasing in-cylinder pressure and temperature during the compression stroke, as shown in Figure 2-11. The increase of boost pressure through the turbocharger compensates for the lack of mass caused by modified valve timing. Together with an intercooler that ensures low mixture temperatures, the high-pressure loop begins, for both early and late IVC, at same mass but lower charge temperature and pressure. As a result of decreasing knocking tendency, the engine can operate with more favourable combustion phasing in full load operation. At BMEP = 29 bar and n = 1500 rev/min (low end torque), it could be advanced by 4 °CA

for early IVC and 2-3 °CA for late IVC. BSFC decreases by 12 % at BMEP = 23 bar and n = 5000 rev/min (rated engine power), caused by earlier CA50 and less enriching required for component protection. The benefit is again smaller for late IVC, arising from the reverse flow into the intake section that leads to higher mixture temperature.
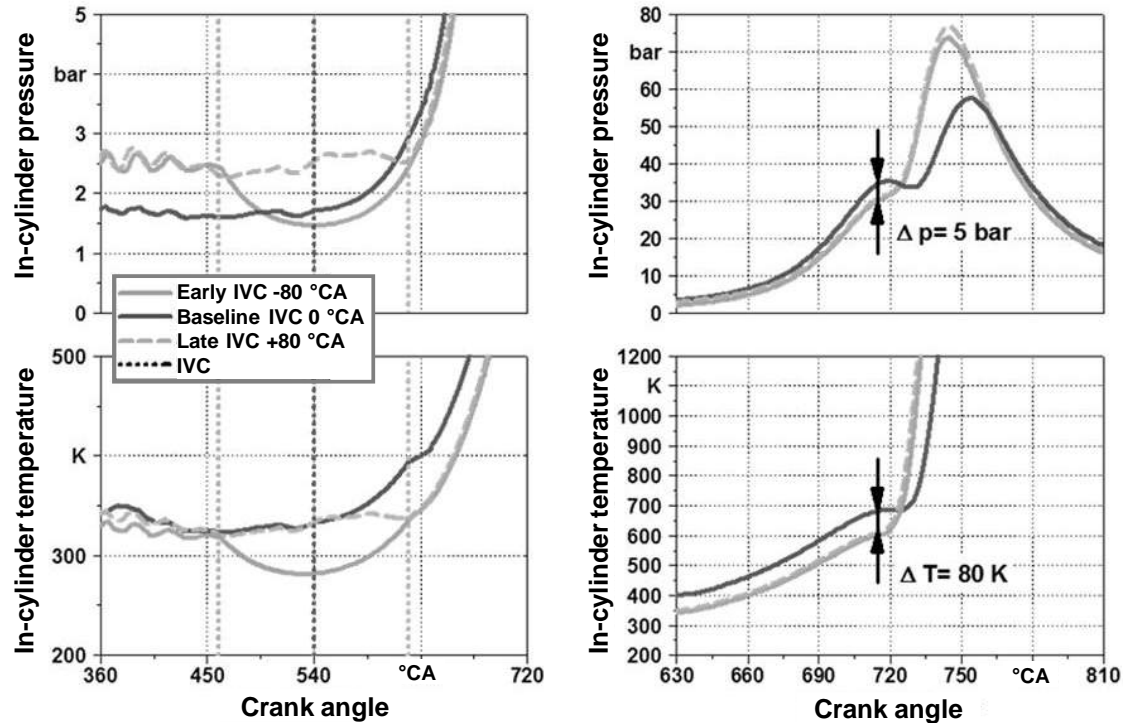

Figure 2-11: Influence of IVC on in-cylinder pressure (top) and temperature (bottom) in knock-limited full load operation [40]

Schutting et al. [141] conducted a study on knocking combustion for a gasoline engine operating with stoichiometric mixture that shows the potential of advancing CA50 (termed as MFB 50%) by applying Miller cycle without mentioning whether IVC occurs before or after BDC (see Figure 2-12). Knocking combustion forces the baseline engine with a compression ratio of $r_{g,c} = 15$ to operate at late combustion phasing of CA50 = 15 °CA, for which it reaches higher efficiency than the configuration with Miller valve timing. When increasing relative boost pressure to 0.1 bar, both engine setups reach similar efficiency in spite of different CA50 of 10 °CA for Miller and 18 °CA for the baseline valve timing. With rising boost pressure, both configurations need to retard CA50 to avoid knocking combustion. While the baseline requires for a boost pressure of 0.2 bar a combustion phasing beyond 20 °CA ATDC, the Miller setup is able to operate with a boost pressure of 0.4 bar at CA50 = 18 °CA, leading to an increase in indicated efficiency of approximately 0.7 %-points. The authors mention that a part of the benefit must be ascribed to lower pumping losses, as the boost pressure was provided externally.
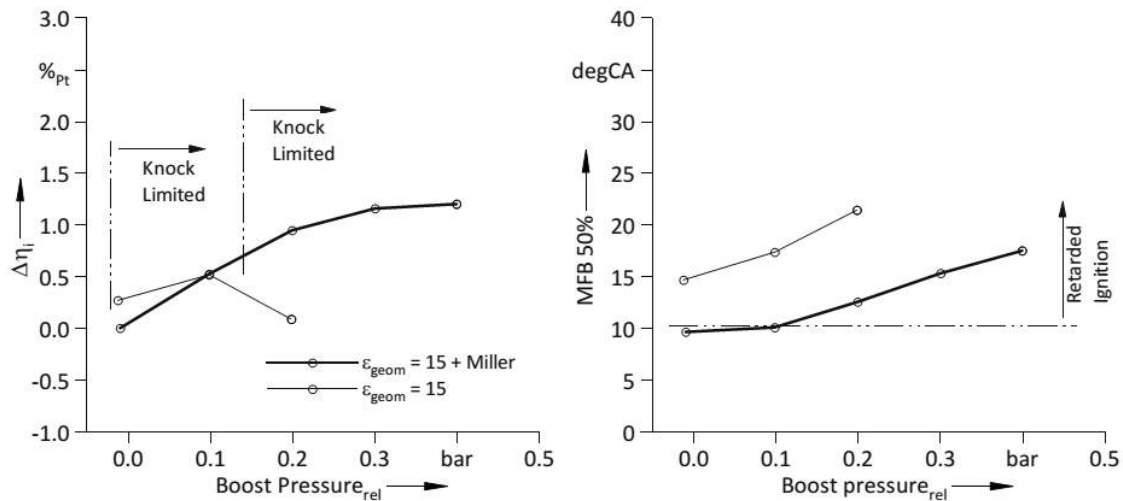
Figure 2-12: Indicated efficiency (left) and combustion phasing (right) as function of boost pressure [141]

According to [17, 18], Volkswagen and Audi also make use of the potential of Miller valve timing to reduce the knocking tendency that allows for engine designs with high compression ratios, as seen in recently launched passenger cars.

2.4.3.3 Miller Cycle in Diesel Engines

Early Miller cycle was widely introduced in Diesel marine applications to improve the BSFC-NO_x trade-off [37], whereas for passenger vehicles, external EGR appears to be more promising method unless throttling is required for hot aftertreatment.

In [158], a 6 litre marine Diesel engine was equipped with two-stage turbocharging and Miller valve timing, increasing rated engine power from 560 to 640 kW while NO_x emissions decrease by 40 % at slightly better fuel consumption.

Schutting et al. [142] carried out a comprehensive numerical and experimental study on a single-cylinder research engine (automotive application) that reveals that modifying intake valve closing reduces NO_x emissions by 36 % for almost same ISFC (at IMEP = 12 bar, n = 2000 rev/min). Early Miller outperforms late Miller valve timing due to the lower temperature level. Nevertheless, in a comparison to baseline valve timing combined with external EGR, early Miller valve timing holds disadvantages in terms of particulates, NO_x and CO emissions at same ISFC. Theißl et al. [153] also compared Miller valve timing to conventional valve timing with cooled EGR for a 12.4 litre heavy-duty engine running at 1200 rev/min. The early Miller configuration decreases fuel consumption by 3 % in full load and 3.2 % in part load operation compared with the baseline engine at same NO_x emissions of 9 g/kWh. The benefit in fuel consumption with external EGR amounts to 5 % and additionally allows reducing NO_x down to 7 g/kWh at full load. The reason to still incorporate Miller cycle into Diesel engines, as opposed to cooled EGR, lies in lower costs, complexity and engine wear [153].

SCR systems, as a widely used means to reduce NO_x emissions of Diesel engines, require

exhaust gas temperatures of 200 °C to achieve sufficient conversion rates [153]. At low loads, this can be managed through air or exhaust flaps that reduce the engine's charging efficiency. The decreasing in-cylinder mass leads to higher combustion and exhaust gas temperatures. The increasing pumping loss is similar to part load Otto operation realised through air throttling. Applying Miller valve timing not only lowers the pumping losses by 20 % but also reduces NO_x emissions due to its cooling effect. The reduced temperature and pressure level at the beginning of combustion, however, are detrimental to the engine's cold start behaviour [153].

2.4.3.4 Summary

The findings from the literature survey presented show the numerous effects Miller cycle exerts. While stationary gas engines, whether naturally aspirated or turbocharged, feature permanent Miller valve timing, the automotive sector profits from variable valve timing. The crucial advantage of turbo- or supercharged to naturally aspirated engines is the possibility of partly outsourcing the compression into the intake port. In conjunction with an intercooler, same in-cylinder pressure at lower temperature of the unburnt zone and therefore higher knock resistance can be achieved [45]. Table 2-2 summarises the applications in which Miller cycle is implemented, including the respective motivation.

Table 2-2: Overview for the use of Miller cycle

Fuel	Application	Induction type	λ	Load	Motivation
Gas	Stationary	Naturally aspirated	> 1 / 1	Full load	Improve efficiency, Improve BSFC-NO_x trade-off
Gas	Stationary	Turbocharged	> 1	Full load	Improve BSFC-NO_x trade-off, reduce knocking, lower thermal load
Petrol	Automotive	Naturally aspirated	1	Part / full load	Reduce Pumping losses, reduce knocking, improve efficiency
Petrol	Automotive	Turbo-/supercharged	1	Lower part load	Reduce Pumping losses, reduce knocking, improve efficiency
Diesel	Automotive, maritime	Turbocharged	> 1	Part load	Reduce Pumping losses, improve aftertreatment

2.4.4 Influence of Valve Timing on In-cylinder Flow

Literature proves that intake valve timing strongly influences charge motion, thus being decisive for the combustion process [23, 40, 46, 95, 127, 136, 142, 178, 179]. In-cylinder flow chiefly consists of large flow structure such as swirl and tumble and small scale turbulence. Swirl describes the rotational motion within the cylinder about its long axis, while tumble is the vortex motion perpendicular to the cylinder axis [29]. Although swirl can decay slightly during engine cycle due to interactions with the cylinder wall, its flow structure mostly persists until combustion begins [23]. This is particularly true for rotationally symmetrical combustion chambers. Tumble, on the other hand, breaks up into small scale

turbulence almost entirely as the piston approaches TDC during the compression stroke [3].

The velocity of a turbulent flow u can be separated into a mean $\bar{u}$ and a fluctuating component u':

$$u\ (x,t) = \ \bar{u}\ (x,t) + u'(x,t) \tag{2-19}$$

The root mean square of u' describes the magnitude of the turbulent fluctuations, also known as the turbulence intensity. With the assumption of isotropic homogeneous turbulence, the values of all three directions of u' are the same and the specific turbulent kinetic energy (TKE) of the turbulent fluctuations k can be written as follows:

$$k = \frac{3}{2} \cdot u'^{\,2} \tag{2-20}$$

Since experimental analysis of engine flow behaviour is fairly complex as well as cost and time expensive, 3D CFD (Computational Fluid Dynamics) simulation is mostly used instead.

The works conducted in [127, 136] report that both early and late Miller valve timing decrease the turbulent kinetic energy compared to the baseline that closes at BDC or shortly after. The effect is larger for early Miller cycle, primarily caused by a lower tumble level due to a reduced maximum valve lift and a longer dissipation time. Both works identify intake valve masking as effective means to increase turbulence for early Miller even beyond values of the late Miller valve timing.

Wülfert et al. [178, 179] analysed the influence of different valve lift curves on charge motion for same mass of in-cylinder achieved by adjusting charging pressure. Figure 2-13 shows left the investigated valve lift curves and right the traces of TKE calculated using 3D CFD simulation. The baseline and late Miller (referred to as Atkinson) configuration reach their maximum in TKE between 110 and 130 °CA, while both early Miller setups peak significantly earlier. The Miller 2 design shows the highest TKE at the beginning of the intake stroke as it shows the largest mass flow. However, the short opening duration avoids taking advantage of the initial benefit. Miller 1 reveals the highest peak in TKE of all configurations that occurs around 100 °CA. After the peak, TKE decreases across all valve timings due to viscous dissipation. The Miller strategies, Miller 1, Atkinson 1 and Atkinson 2 reach similar values at TDC, while Miller 2 and the baseline configuration exhibit a lower turbulence level. A high turbulence level can compensate for drawbacks in combustion as in the following explained for the Miller 1 configuration: The reduced process temperature level caused by the Miller 1 valve timing is detrimental to both burning delay and laminar burning velocity. An increase of TKE, on the other hand, promotes a turbulent flame front that increases the turbulent burning velocity inside the cylinder. As a result, the Miller 1 setup achieves a similar rate of heat release as the baseline configuration despite lower process temperatures.
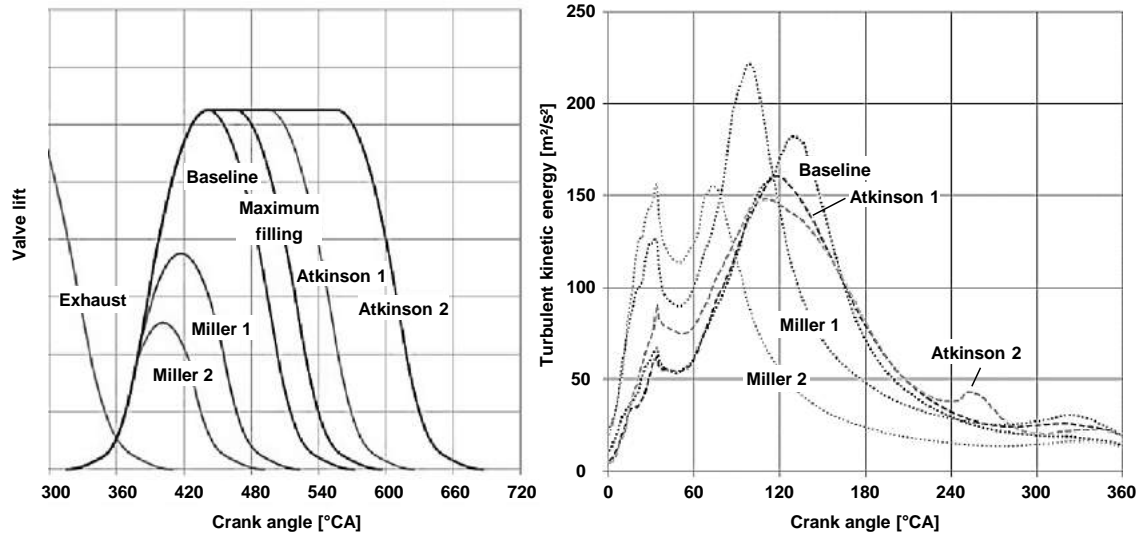
Figure 2-13: Valve lift curves investigated (left) and turbulent kinetic energy over crank angle at same charge mass (right) according to [179]

Schutting et al. [142] analysed turbulence and velocity inside the cylinder of a Diesel engine equipped with neutral and Miller valve timing of constant maximum valve lift. Late Miller (IVC = 75 °CA ABDC) and neutral (IVC at BDC) valve timing showed similar TKE and flow velocity, while early Miller cycle (IVC = 55 °CA BBDC) was detrimental to either parameters.

2.4.5 Effective Compression Ratio

As formulated in Section 2.4.2, the effective compression ratio of an idealised engine cycle can be expressed by the ratio between the volume at IVC and TDC:

$$r_{c,IVC} = \frac{V_{IVC}}{V_{TDC}} \tag{2-21}$$

Unlike the air-standard Otto cycle, which exhibits IVC at BDC, the actual Otto engine closes the intake valve after BDC to take advantage of the effects of gas dynamics regarding charging efficiency. An arriving pressure wave shortly before the intake valve closes, for example, can significantly increase the mixture flow into the cylinder even beyond BDC (i.e. during the compression stroke). In the case of a naturally aspirated engine, this effect, also known as ram effect [11, 57], can be maximised through a specific design of the gas path, leading to highest charging efficiency for a given engine speed. As the amplitudes of the intake pressure pulsations increase with engine speed, intake valve timing needs to be retarded to achieve highest charging efficiency. However, decreasing the engine speed for the same intake valve closing again, would lead to a reverse flow during the compression stroke due to smaller amplitudes of the pressure pulsation on the intake side. Given that the effective compression ratio correlates with the charging efficiency at constant geometrical compression ratio, engine speed plays an important role. From these considerations,

it becomes clear that the effective compression ratio is more sensitive to decreasing engine speeds for late Miller valve timing as these not only reduce the ram effect but also cause a pronounced reverse flow. For early Miller, on the other hand, the effective compression ratio diminishes more with increasing engine speeds, owing to the reduced time for the mixture to be aspirated [61]. Furthermore, it is not possible to take advantage of a pronounced ram effect for such an intake valve closing.

Various works address the influence of intake valve closing on the effective compression ratio quantitatively without or only vaguely explaining its definition [35, 55, 75, 131, 137]. Others simply apply the definition of the ideal cycle given by Eq. (2-21) [51, 98, 168]. However, based on the findings in literature, it is of vital importance to consider the effects of gas dynamics when determining the effective compression ratio of an actual engine cycle $r_{c,eff}$ [54, 70]. Different authors have assessed $r_{c,eff}$ through a variety of methods that mostly centre on finding a so-called effective BDC volume $V_{BDC,eff}$ that replaces V_{IVC} of Eq. (2-21), leading to:

$$r_{c,eff} = \frac{V_{BDC,eff}}{V_{TDC}}$$

(2-22)

A prevalent approach (cf. [54, 69, 70, 97, 148]) to determine $V_{BDC,eff}$, introduced by He et al. [53], is based on a polytropic change of state starting from IVC. Applying a linear fit to the compression process in the log(p)-log(V) diagram (see Figure 2-14, left), gives a constant polytropic exponent n. The effective volume is then found at the cylinder volume where the extrapolated pressure reaches the mean pressure value of the intake manifold (termed as IMP within the diagram). Zhang et al. used a similar method [180], yet the polytropic exponent is determined from the measured pressure signal and the volume between ignition timing and IVC. The pressure at BDC serves as threshold for backward calculation.

Koehler et al. [70] also analysed alternative reference values to determine $V_{BDC,eff}$, including the mean intake pressure over the whole cycle (720 °CA) and the one during the span the intake valve is open (from IVO to IVC). The results shown in Figure 2-14 (right) as function of IVC were obtained from 1D CFD calculations of a motored four-cylinder Diesel engine at an engine speed of 4000 rev/min. It further depicts the in-cylinder peak pressure p_{max}, an appropriate indicator when comparing different methods for determining $r_{c,eff}$, as shown by the authors in [70]. It is interesting to note that the correlation between $r_{c,eff}$ and p_{max} is significantly stronger when using the mean intake pressure of the entire cycle. This is particularly true for IVC after BDC as both parameters, $r_{c,eff}$ and p_{max}, peak at same IVC. The values of $r_{c,eff}$ calculated from the mean pressure during intake valve opening are consistently higher due to the lower pressure level as the mixture is aspirated. Both the mean intake pressure over the entire cycle and the one from IVO to IVC approach one

another with shortening intake valve opening. Therefore, the difference between both approaches is reduced as IVC is advanced.
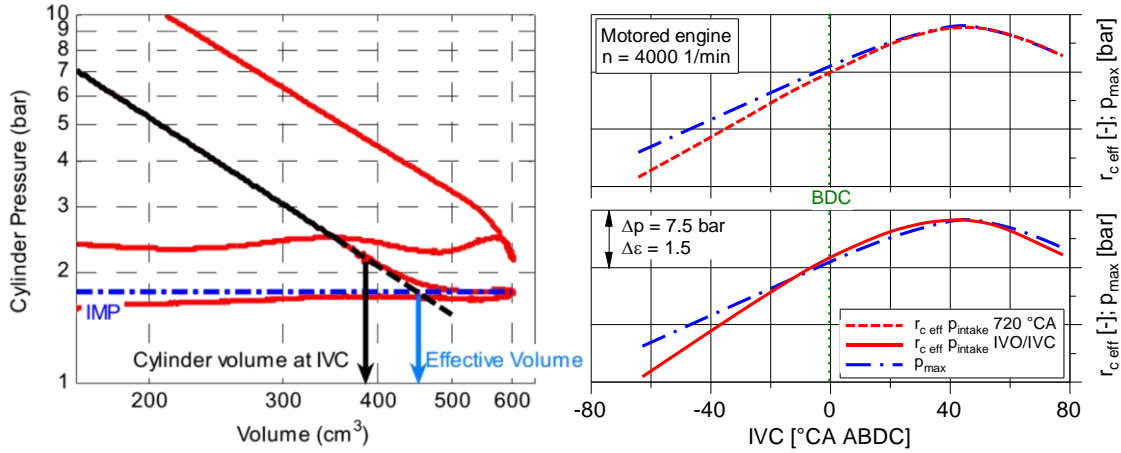

Figure 2-14: Polytropic calculation to the volume in the effective BDC [53] (left) and effective compression ratio as function of intake valve closing for different reference values in motored engine operation based on [70] (right)

The authors in [70] further analysed an approach to calculate $r_{c\,eff}$ over the relationship between compression and charging pressure for a natural gas engine operating with Miller cycle is rather briefly described by Endo [41] and Fukuzawa [46]. Based on the information given in [41, 46], it is assumed that $r_{c\,eff}$ is calculated in motored engine operation by applying an isentropic change of state as formulated in Eq. (2-23)

$$r_{c\,eff} = \left(\frac{p_{max}}{p_{boost}}\right)^{\frac{1}{\gamma}}$$ (2-23)

where p_{max} is the peak compression pressure, p_{boost} the boost pressure and γ the ratio of the specific heat capacity of the mixture.

Löbbert [80] analysed part load operation using a fully variable valve train as alternative to a conventional throttle for a four-cylinder automotive engine. In order to account for the decreasing initial pressure of the cycle defined at V_{BDC}, the author defines $V_{BDC\,eff}$ at the intersection of pressure trace during exhaust and compression stroke as shown in Figure 2-15 (left).

Saunders et al. [134] suggest an adiabatic compression from 1 bar to the measured peak pressure level in motored operation. However, the result represents rather an estimated than an accurately determined value.

Figure 2-15 (right) shows a selection of the aforementioned approaches to determine $r_{c\,eff}$ in motored engine operation at constant engine speed for varying intake valve closing [70]. The shift of the maximum in $r_{c\,eff}$ relative to that of p_{max} when assuming $V_{BDC\,eff} = V_{IVC}$

emphasises the lack of accuracy when applying Eq. (2-21) to real engine operation. Conversely, the methods of He and Endo and Fukuzawa show much stronger correlation between p_{max} and $r_{c\,eff}$.
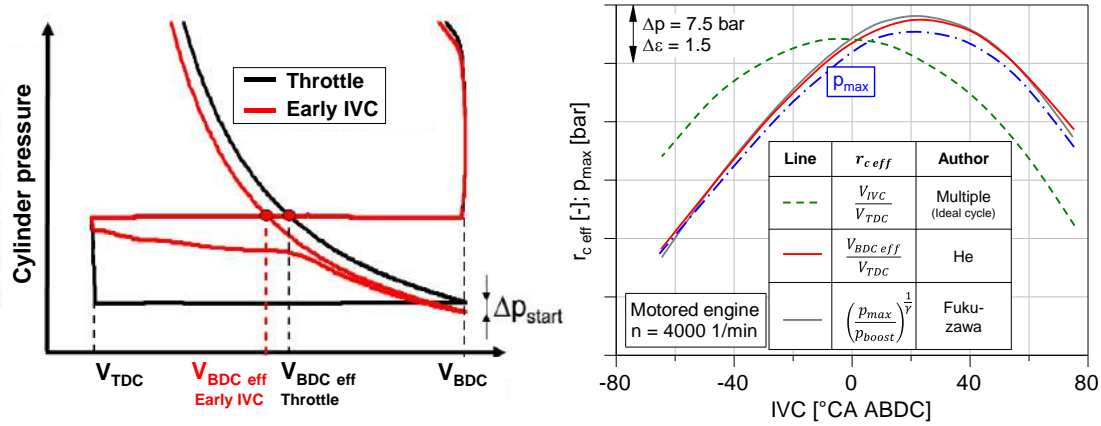

Figure 2-15: Approach of Löbbert to determine $r_{c\,eff}$ according to [80] (left); Effective compression ratio calculated by applying different approaches and p_{max} over IVC in simulated motored engine operation based on [70] (right)

2.5 External Exhaust Gas Recirculation

External exhaust gas recirculation (EGR) poses an established means to dilute the air-fuel mixture. It is found in various applications with different intentions, depending on the fuel and mixture strategy, as seen in Table 2-3. The amount of exhaust gas recycled is usually given by the EGR rate x_{EGR}. It is the ratio between the mass flow of exhaust gas recirculated $\dot{m}_{EGR}$ and the total mass flow aspirated, consisting of exhaust gas $\dot{m}_{EGR}$, air $\dot{m}_{air}$ and fuel $\dot{m}_{fuel}$:

$$x_{EGR} = \frac{\dot{m}_{EGR}}{\dot{m}_{EGR} + \dot{m}_{fuel} + \dot{m}_{air}} \tag{2-24}$$

The EGR rate is mostly defined mass related, but also volumetric definitions are found in literature.

Stoichiometric operated Otto engines benefit from the lower O_2 fraction of the exhaust gas-air mixture that requires less throttling, thus reducing pumping losses in part load operation [76, 167]. While this is particularly true for naturally aspirated engines, EGR also aims at reducing process temperatures of super- or turbocharged configurations that operate at high IMEP. The motivation behind this is either to lower the knocking tendency [123] or to reduce the amount of extra fuel injected for cooling in high part or full load operation [171]. A once popular approach, still followed by Daimler [135], is to apply EGR to an Otto engine with stratified lean mixture to reduce NO_x emissions. For the same reason, EGR has become a standard measure for Diesel engines in automotive applications, in which increasing soot formation represents one of the limiting factors for its use beyond part load.

High injection pressures combined with a particulate trap can overcome this issue to some extent as realised in large engines for rail applications [174]. To comply with Euro VI standards, however, additional SCR systems are needed for passenger cars as it is also the case for on-highway heavy duty vehicles [155].

Table 2-3: Overview for the use of exhaust gas recirculation

Fuel	Application	Mixture	λ	Load	Prevalence	Motivation	Source
Petrol	Automotive	Homogenous	1	Part load	Series	Reduce PMEP	[167]
Petrol	Automotive	Homogenous	1	Part / full load	Series	Reduce knocking	[123]
Petrol	Automotive	Homogenous	1	Part / full load	Series	Reduce enriching	[171]
Petrol	Automotive	Stratified	> 1	Lower part load	Rare series	Reduce NO_x	[135]
Diesel	Automotive	Stratified	> 1	Part load	Series	Reduce NO_x	[1]
Diesel	Automotive	Stratified	> 1	High load with SCR	Series	Reduce NO_x	[155]
Diesel	Rail	Stratified	> 1	Full load	Series	Reduce NO_x	[174]
Gas	Stationary	Homogenous	> 1	Full load	Research	Reduce NO_x	[107]
Gas	Automotive, stationary	Homogenous	1	Full load	Series, research	Reduce knocking	[138]

Unlike Diesel engines, natural gas engines emit practically no soot due to its premixed homogenous lean air-fuel mixture [88, 107]. It is therefore a promising approach to lower NO_x emissions in full load operation of stationary gas engines, which, to date, has not yet left the experimental stage. EGR is also gaining importance to stoichiometric air-gas mixtures due to lower combustion temperatures that hinder knocking combustion.

2.5.1 Efficacy of EGR

Apart from reduced pumping losses during part load, EGR is primarily applied to lower combustion temperature by increasing the absolute heat capacity of the mixture given by the product of mass and specific heat capacity. From an isochoric combustion formulated in Eq. (2-25)

$$Q \quad m \cdot c_v \cdot \Delta T \qquad (2\text{-}25)$$

it follows that rising either the mass m or the specific heat capacity c_v reduces the temperature rise ΔT caused by the combustion for the same heat added to the cycle Q. In stoichiometric operation, this is primarily achieved thanks to a rising in-cylinder mass as exhaust gas (seen as inert) is recirculated. In the case of lean mixtures, Wimmer et al. suggest that the reduced combustion temperature arises from the so-called mass and/or caloric effect [172, 173]. The mass effect describes the increasing stoichiometric mass of the non-premixed mixture that preferably ignites at locally stoichiometric or even understoichiometric conditions of $\lambda = 0.5 - 1.0$ as for Diesel engines [118]. The caloric effect originates from the high H_2O and CO_2 fractions of the exhaust gas, exhibiting higher specific heat

capacities than the main components of air, N_2 and O_2, as shown in Figure 2-16 (left).
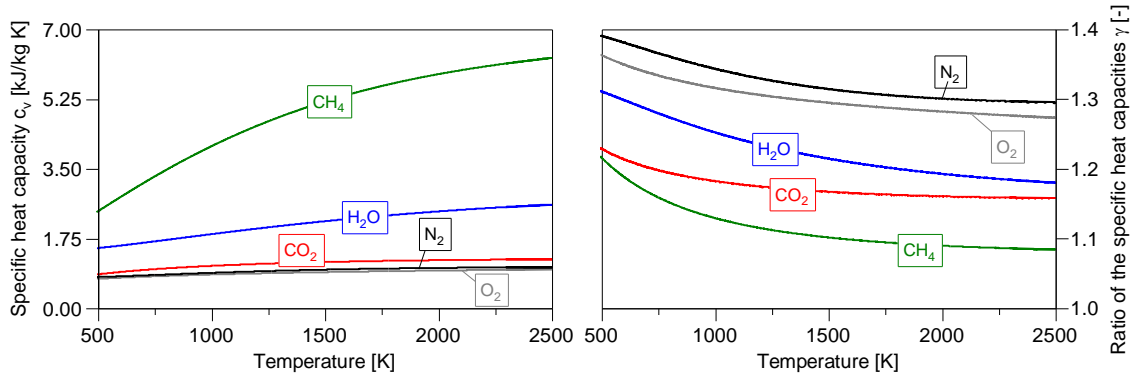

Figure 2-16: Specific heat capacity (left) and the ratio of the specific heat capacities (right) of methane (CH₄), nitrogen (N₂), oxygen (O₂), carbon dioxide (CO₂) and water (H₂O) as function of temperature (ideal gas, results from calculation using EES V10)

The specific heat capacity is calculated from the ratio of the molar heat capacity and the molar mass. The molar heat capacity increases with the number of atoms per molecule due to the additional degrees of freedom that accommodate thermal energy. Furthermore, the structure of the molecule plays an important role as the comparison between CO_2 and H_2O demonstrates. Both triatomic species reveal the same degrees of freedom (9), however, the linear molecular structure of CO_2 has contribution from two rotational and four vibrational degrees, while H_2O exhibits three rotational and three vibrational degrees. Since the vibrational mechanisms are predominant above room temperature, CO_2 reveals a higher molar specific heat capacity than H_2O [111]. Nevertheless, the specific heat capacity of H_2O is higher due to its smaller molar mass. Since the molar mass exerts no influence on the heat capacity ratio γ, CO_2 shows a lower value than H_2O over the temperature range depicted in Figure 2-16 (right). It is lower for both species compared to those of N_2 and O_2, thus posing challenges in maintaining the engine's efficiency when adding EGR to lean mixtures. If applied to stoichiometric mixtures, however, EGR even favours mixture composition in terms of ideal engine efficiency [54, 80, 149].

While the mass effect is predominant in Diesel combustion, gas engines only profit from the caloric effect due to the external mixture preparation that causes a homogenous charge composition (see Figure 2-17, left). Results from 0D calculations in Figure 2-17 (right) indicate that the Diesel engine's potential to reduce NO_x emissions is superior to the one of gas engines at same EGR rate, owing to the large mass effect. The gas engine exhibits a larger caloric effect due to the higher H/C ratio, producing exhaust gas with a higher fraction of H_2O and therefore higher specific heat capacity. The gas engine experiences smaller losses in ideal engine efficiency, presumably arising from a lower temperature level and lesser influence of altered mixture composition.
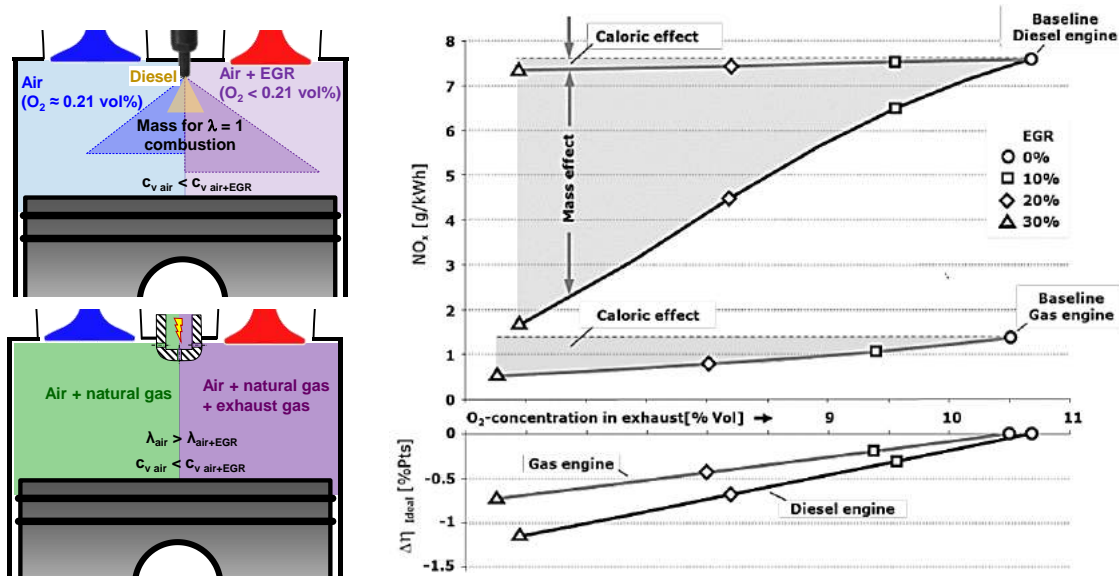
Figure 2-17: Caloric and mass effect of EGR schematically (left); NO_x emissions and ideal efficiency loss against O_2 concentration for Diesel and natural gas engine (0D calculation) (right) [173]

In actual engine operation, additional drawbacks regarding the inflammation and combustion duration emerge when applying EGR. The lower fraction of reactive O_2 prolongs the ignition delay and increases the activation energy to provoke inflammation [173]. Chemiluminescence imaging of a combustion inside a rapid compression expansion machine shows the influence of EGR on the formation of OH radicals [113]. The trials were conducted at same initial thermodynamic conditions, a constant mass of methane and same ignition timing. The exhaust gas was formed synthetically by assuming a concentration of 20 % CO_2 and 80 % N_2. Figure 2-18 (left) depicts the OH signal and the pressure trace for mixture compositions of $\lambda = 1.1$ with an EGR rate of 10 % and $\lambda = 1.0$ with an EGR rate of 20 %. The leaner mixture reaches 2 ms after ignition almost the same pressure level but a notably higher OH signal. Coupled with a wider and more intense combustion, as illustrated by the plots, this indicates a shorter ignition delay for the lower EGR rate. The OH signal of the $\lambda = 1.1/x_{EGR} = 10$ % mixture shows a pronounced combustion 4 ms after ignition (shortly before peaking). The richer mixture, on the contrary, appears to be extinguished at the same point of time as the low OH signal and the OH distribution indicate. The earlier end of combustion is presumably the reason for the advanced and lower peaking in the pressure signal of the $\lambda = 1.0/x_{EGR} = 20$ % mixture.

Next to an extended ignition delay, EGR affects the laminar burning velocity [34, 79, 173]. Figure 2-18 (right) shows the calculated laminar burning velocity over the relative air-fuel ratio for varying EGR rates. Increasing the EGR rate at same relative air-fuel ratio, reduces laminar burning velocity significantly, while it decreases rather moderately when substituting only a part of excess air with exhaust gas, indicated by the curve of constant mass. Since N_2 is the main component of both air and exhaust gas, its fraction remains similar and the species responsible for the altered laminar burning velocity are O_2, CO_2 and H_2O.

Studies that address the influence of each component on the combustion of premixed methane-air mixtures separately, reveal that increasing O_2 concentration leads to higher laminar burning velocity, while adding H_2O and CO_2 causes opposing behaviour. The authors uniformly ascribe these trends mainly to thermal effects rather than to kinetic or diffusion effects [25, 32, 33, 87]. From this, it can be concluded that the lowering effect of EGR on laminar burning velocity primarily arises from the increasing heat capacity.
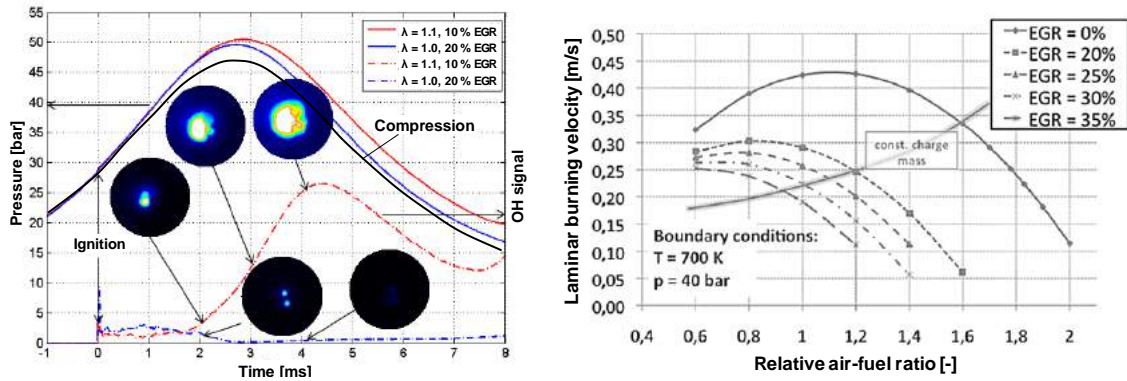

Figure 2-18: Pressure and OH signal over time for 10 and 20 % EGR and same mass of CH₄ (left) [113]; Effect of EGR and relative air-fuel ratio on laminar burning velocity for CH₄ (right) [173]

EGR decreases ideal engine efficiency, extends burn duration and retards combustion phasing unless ignition timing is adjusted. The occurring drawbacks can be counteracted or even overcompensated by advancing combustion phasing for both Diesel [88, 172] and NG engines [162, 163] while producing same NO_x emissions. Due to the reasons explained, this is only conducive upon a certain EGR rate. Diesel engines additionally face a challenge with soot as the EGR rate increases [1], while suffering combustion stability is the limiting factor in stoichiometric petrol operation [76].

At same thermodynamic conditions, exhaust gas reveals only a slightly lower density than air. Therefore, substituting a part of air with exhaust gas without changing the mixture's temperature, leads to in-cylinder charge of similar mass but higher heat capacity. A higher EGR rate and/or lower air-fuel ratio increases the fraction of CO_2 and H_2O. Stoichiometric calculations show that the exhaust gas of a CH₄-air combustion at $\lambda = 1.5$, for instance, has a mole fraction of 13.1 % H_2O. A mixture with the same mass of fuel but an EGR rate of 20 % increases the H_2O fraction up to 16.4 %, while simply reducing the air-fuel ratio down to $\lambda = 1.3$ results to 15.0 % of H_2O within the exhaust gas. These considerations assume that exhaust gas can be recirculated at the same temperature as the CH₄-air mixture. Practically, this can be challenging due to condensation of the exhaust gas, which for an exhaust gas of a $\lambda = 1.5$ combustion of methane would occur at approximately 50 °C and an absolute pressure of 1.1 bar. In the case of naturally aspirated engines, the increase of the mixture temperature should be avoided in order to guarantee similar mixture density and therefore same charging efficiency. Otherwise, the required EGR rate to lower combustion temperature increases and engine power suffers.

2.5.2 Exhaust Gas Recirculation in Natural Gas Operation

A number of comparisons between both mixture strategies lean-burn and stoichiometric with EGR can be found in literature [15, 34, 39]. Exhaust gas as additional diluent of a lean air-fuel mixture was merely subject of research projects [16, 78, 107, 113, 121, 150, 162, 163, 172, 173].

Wimmer et al. [172, 173] and Pizzirani et al. [121] studied the effect of EGR for large lean-burn gas engines numerically, concluding that NO_x emissions can be reduced significantly at slight expense of engine efficiency. Both see potential to increase engine efficiency through a higher compression ratio coupled with further measures to lower knocking tendency. Pizzirani et al. suggest using EGR itself, while Wimmer et al. recommend to implement Miller valve timing or to optimise combustion chamber geometry.

In [173], the authors conducted experiments on the effect of EGR using a single-cylinder research engine (6.2 litre) with scavenged prechamber in stoichiometric and lean-burn operation. Substituting a part of excess air with exhaust gas for a constant mass of charge, was found to reduce NO_x emissions by 35 % at an EGR rate of 10 %. This required advancing ignition timing so as to keep the combustion phasing CA50, which was only viable for EGR rates up to 10 %. Losses from imperfect combustion, non-ideal combustion or wall heat transfer remain practically the same, whereas the changed charge composition reduces efficiency of the ideal engine, thus leading to lower thermal efficiency.

Lee et al. [78] carried out a numerical study on a dedicated EGR system that recycles the entire exhaust gas of one cylinder to a separate intake manifold that feeds the rest of the cylinders of the natural gas engine (338 cm^3/cylinder). A separate air-fuel supply allows the dedicated cylinder to operate rich without EGR, resulting in an exhaust gas of high H_2 and CO fraction. The very high laminar burning velocities of both species lower the drawbacks in burn duration usually caused by EGR, while still ensuring low combustion temperature thanks to the CO_2 and H_2O fraction. The overall stoichiometric operated engine reaches a benefit in efficiency of 5.1 %-points caused by a higher degree of constant combustion and emits only the half of the NO_x emissions.

Tschalamoff and Kauert [162, 163] studied the effect of EGR for a single-cylinder 4.83 litre research engine with both scavenged and unscavenged prechamber spark plugs. EGR temperature was regulated to that of the air-fuel mixture of 30 °C, leading to a low water concentration in the exhaust gas. With increasing EGR rate, NO_x emissions and mean effective pressure were maintained constant by following two strategies, namely adjusting the fuel quantity (1) or the ignition timing (2), starting from a relative air-fuel ratio of $\lambda = 1.7$. EGR lengthens the combustion process for both strategies when it is initiated through an unscavenged prechamber spark plug and is therefore detrimental to the engine's efficiency, particularly for strategy 1 (see Figure 2-19). Enriching the mixture for an engine configuration using a scavenged prechamber, on the other hand, reduces burn duration

minorly for EGR rates up to 10 %. Shorter burn duration together with lower losses from incomplete combustion, indicated by reduced HC and CO emissions, improve engine efficiency by 0.5 %-points. Advancing ignition timing allows the engine to operate at significantly earlier CA50, leading to a benefit in efficiency of 1.5 %-points.
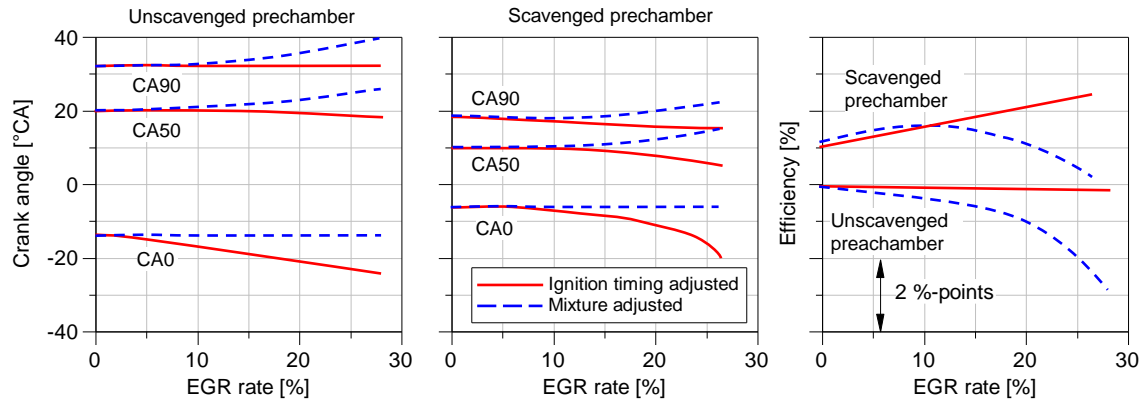

Figure 2-19: Mass fraction burnt and efficiency over EGR rate for open chamber spark ignition and scavenged prechamber (according to [163])

In [107], Nellen and Boulouchos compare air-diluted ($\lambda = 1.6$–1.77) engine operation to lean-burn with additional EGR ($\lambda = 1.2$–1.3, $x_{EGR} = 15$–25 %) for a 9.96 litre turbocharged stationary gas engine, running at 1500 rev/min. At BMEP = 12 bar, engine operation with EGR shows lower CO and HC emissions and a plus in engine efficiency of approximately 0.5 %-points at NO_x emissions of 250 mg/m$_N$. The authors do not discuss whether the improvement is solely caused by the lower imperfect combustion losses or also, for example, through an earlier combustion phasing.

With respect to possible stoichiometric concepts for small cogeneration gas engines, knocking combustion would become the limiting factor for rising the compression ratio. Because combustion temperature is also one of the driving parameters for knocking combustion, EGR provides a significant potential to reduce knocking tendency. Numerous studies prove that EGR extends the knock margin of natural gas engines in both lean [162, 163, 172] and stoichiometric operation [39, 58, 107, 108, 138, 173, 180, 181]. The falling combustion temperatures allow engines to operate at higher compression ratios and/or higher IMEP. Beside higher compression ratios and/or IMEP, wall heat losses decrease, particularly in stoichiometric operation [58, 138].

2.6 Summary and Conclusions

The literature review presented in this chapter explores the fundamentals and work of others on lean-burn combustion, Miller cycle and EGR. Slower combustion and poor combustion stability pose one of the challenges lean-burn gas engines are facing when complying with future emission regulations through further mixture dilution by means of excess

air. For naturally aspirated engines, the main issue is the decreasing IMEP that increases the FMEP/IMEP ratio at constant engine speed and eventually reduces engine brake efficiency. Miller cycle and EGR as alternative means could overcome this issue. Much research on each topic has been done and numerous series production engines already take advantage by applying at least one measure. A significant number of recently introduced passenger cars are equipped with naturally aspirated or turbocharged petrol engines that couple stoichiometric operation with Miller cycle and cooled EGR [64]. Similar approaches were taken for turbocharged gas engines discussed in [58, 180, 181] and a Diesel engine in [174]. The motivation behind the respective works to realise Miller cycle is uniformly to achieve high engine efficiency, while the purpose of cooled EGR is either to avoid knocking in the case of petrol and gas engines or to reduce NO_x emissions of the lean operated Diesel engine. However, to the author's knowledge, the combination of both Miller cycle and EGR for a naturally aspirated lean-burn gas engine has not been studied before. Based on the literature review, the following effects are substantial when realising the Lean-Miller-EGR working process:

- Miller cycle improves the efficiency of the ideal engine by increasing the expansion/compression ratio realised through an IVC before or after BDC and an adjusted geometrical compression ratio. Miller cycle increases the ratio between the expansion and compression work but overall cycle work suffers due to lower charging efficiency.

- Both early and late Miller approaches lead to the same outcome at same effective compression and expansion/compression ratio in the ideal engine cycle. Nonetheless, the effects of gas dynamics in actual engine operation make it much more complex to determine the effective compression ratio. A suitable method is essential for drawing a direct comparison between early and late Miller cycle in actual engine operation, which, to the authors knowledge, was not yet conducted by others.

- Beside the higher expansion/compression ratio, Miller valve timing favours engine efficiency by reducing the pumping losses due to a smaller mass flow. Since late Miller experiences a reverse flow in the beginning of the compression stroke, it holds a disadvantage in pumping work over early Miller valve timing.

- In addition to the differences in gas exchange, IVC also influences in-cylinder charge motion and tends to cause a higher turbulence level for late Miller cycle. Charge motion is decisive for combustion duration and stability, particularly for highly diluted mixtures, and regardless of the type of diluent.

- Adding exhaust gas as second diluent to the air-fuel mixture increases the specific heat capacity thanks to the rising H_2O and CO_2 fraction. To exploit the full potential of this approach, it is vital to cool the exhaust gas before recirculating it so to avoid losses in charging efficiency.

- In response to the increasing heat capacity of the mixture, combustion temperature falls and lowers NO_x emissions but entails losses in ideal engine efficiency. Furthermore, increasing burning delay and slower laminar burning velocity require advanced ignition timings to maintain CA50. In fact, to experience an advantage by introducing EGR, the engine needs to operate at even more advanced CA50, leading to either same efficiency but lower NO_x emissions or higher efficiency but same NO_x emissions.

3 Working Process Studied and Governing Parameters

Realising the Lean-Miller-EGR working process involves significant changes in mixture composition, valve timing and geometrical compression ratio. This chapter discusses the definition of mixture composition for air and EGR diluted mixtures, a basic study on Lean-Miller-EGR working process and a method for determining the effective compression ratio in due consideration of the effects of gas dynamics.

3.1 Definition of Mixture Dilution

The relative air-fuel ratio λ, defined in Section 2.1 by Eq. (2-2), is calculated from the ratio of moles of air-oxygen within the cylinder and those required for a stoichiometric combustion. With the addition of EGR, λ can no longer be used to quantify mixture dilution. For better understanding of the dependency between EGR rate and relative air-fuel ratio, the dilution ratio D is introduced

$$D = \frac{n_{air} + n_{EGR}}{n_{air\,stoich}} \tag{3-1}$$

where n_{air} and n_{EGR} are the number of moles of air and EGR added to the cylinder and $n_{air\,stoich}$ is the number of moles of air necessary for a stoichiometric combustion.

Figure 3 shows the influence of D and x_{EGR} (given by Eq. (2-24)) on λ quantitatively (left) and illustrates the composition of a mixture with a dilution ratio of D = 1.40 over an EGR rate from 0 to 20 % schematically (right). If mixture dilution is solely achieved by air, the relative air-fuel ratio matches with the dilution ratio $\lambda = D = 1.40$. With increasing EGR

43

fraction but constant dilution ratio D = 1.40 (1), excess air is replaced by exhaust gas. The decreasing amount of O_2 leads to lower relative air–fuel ratios of λ = 1.28 (2) and λ = 1.12 (3) for EGR rates of x_{EGR} = 10 and 20 %, respectively.
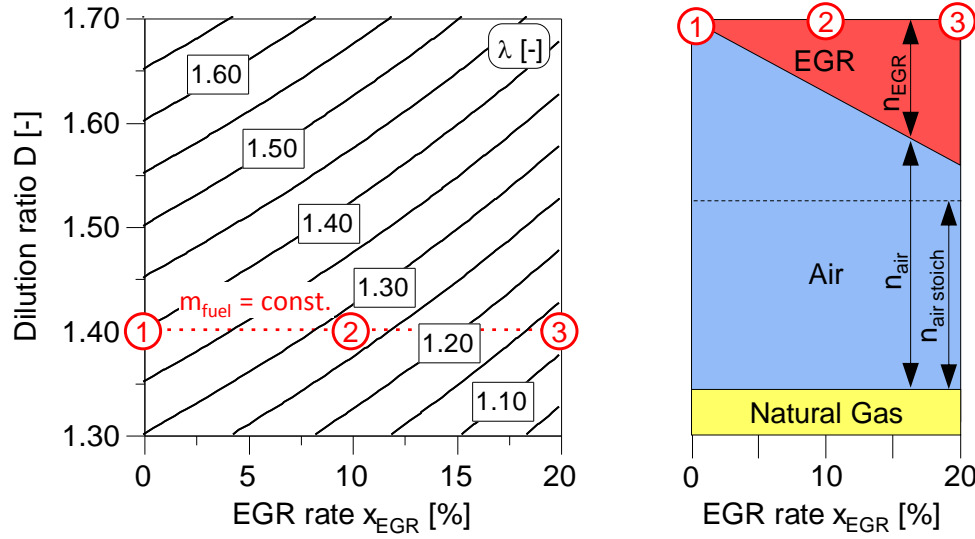

Figure 3-1: Relative air-fuel ratio of the combustion λ as function of the dilution ratio and EGR rate (left) and influence of the EGR rate on the mixture's mole fraction at constant dilution ratio schematically (right)

3.2 0D Study of Lean-Miller-EGR Working Process

The target of this section is to study the characteristics of lean-burn operation, Miller cycle and EGR as well as their combination from a theoretical standpoint using the engine process simulation software AVL BOOST [4]. Each configuration is analysed with respect to thermal engine efficiency η_{th}, produced cycle work W_i and peak combustion temperature T_{max} by first assuming isochoric combustion and adiabatic cylinder walls in 3.2.1. T_{max} is used as indicator for NO_x emissions due to their significant temperature dependency. To analyse how realistic heat release profiles and wall heat losses affect engine performance, a further study was conducted, in which Vibe parameters were varied and wall heat losses considered (see Section 3.2.2).

All calculations were conducted using methane as fuel and initiated at same temperature and pressure of T_0 = 293.15 K and p_0 = 1.0 bar. An engine setup characterised by a relative air-fuel ratio of λ = 1.5 and a compression ratio of r_{geo} = 13.0 is a commonly used setting for a series operating point of a naturally aspirated stationary gas engine and is thus serving as a reference for comparison.

3.2.1 Isochoric Combustion and Adiabatic Cylinder Walls

Contrary to the air-standard cycle, the 0D engine model accounts for the temperature-driven change of the mixture's thermochemical properties (c_p, $c_v = f(T)$). It is furthermore subject to assumptions that are similar but not necessarily identical to that of the ideal

engine [88, 175]:

- Isochoric combustion occurs at TDC (unless mentioned otherwise).
- Combustion takes place under consideration of dissociation until meeting the chemical equilibrium.
- Losses due to wall heat and friction are neglected, leading to an isentropic compression and expansion of the mixture.
- Isochoric gas exchange takes place with valve timings at BDC (unless mentioned otherwise).
- Perfect gas exchange occurs (i.e. no residual gas).

To evaluate the influence of the single means that form the Lean-Miller-EGR working process on the most important parameters η_{th}, W_i and T_{max}, relative air-fuel ratio λ (lean-burn), expansion/compression ratio ECR (Miller cycle) and EGR rate (exhaust gas recirculation) are varied. While the indicated work results from the product between fuel energy added and thermal efficiency, the parameters governing peak combustion temperature in this study are:

- Fuel energy added to the cycle (given by relative air-fuel ratio or dilution ratio)
- Temperature at the beginning of combustion (determined by compression ratio and combustion phasing)
- In-cylinder volume at which the heat is released (influenced over compression ratio and combustion phasing)
- Gas properties of the mixture (specified by dilution ratio and EGR rate)

The major factors that influence the ideal engine's thermal efficiency are:

- Gas properties of the mixture (affected by dilution ratio and EGR rate)
- Geometrical constraints (specified by compression ratio and expansion/compression ratio)
- Crank angle of heat release (varied over combustion phasing)

The effect of mixture dilution through air and geometrical constraints are discussed for lean-burn operation and Miller cycle assuming an isochoric combustion at TDC. Subsequently, a part of excess air is substituted with EGR for both combustion at TDC and for varying crank angle. Eventually, the most promising configurations are combined to compare Lean-Miller-EGR working process to the reference configuration in lean-burn operation.

Lean-burn operation for Otto Cycle

The purpose of this section is to show how leaning and adjusting the compression ratio affect η_{th}, W_i and T_{max} of the ideal engine rather than to evaluate their potential to improve the trade-off between the three respective parameters (see Figure 3-2). Since an air-diluted mixture is used for calculations, λ corresponds to the dilution ratio D. Engine efficiency

enhances by diluting the mixture due to a higher ratio of the specific heat capacities γ. Reducing fuel quantity, in turn, increases the excess mass and the absolute heat capacity available to absorb the heat during combustion, leading to lower peak combustion temperatures. The benefits achieved occur at the expense of indicated work as less fuel energy is added to the cycle. To compensate this through enhanced efficiency, the compression ratio can be augmented. As a result of a combustion that not only starts at a higher temperature level but also occurs in a smaller V_{TDC}, peak combustion temperature increases at same λ. The amount of heat added to the cycle remains nearly the same, while indicated work increases because of improved engine efficiency. The increase to the highest compression ratio investigated in this study of $r_{geo} = 18$ cannot compensate for the losses in work at $\lambda = 1.7$ but suffices for a mixture of $\lambda = 1.6$. Thermal engine efficiency increases by more than 4.5 %-points at a peak combustion temperature that remains 12 K below the reference. With respect to experimental engine operation, however, the chance of knocking would increase significantly due to its dependency on the pressure and temperature histories as well as on combustion speed. Besides, increasing wall heat losses as a result of an augmented A/V ratio, longer burn duration and higher COV would lower engine efficiency. Alternative ignition systems or increasing the degree of turbulence can counteract the drawbacks of leaning, however, such efforts are not considered herein as the focus is put on Miller cycle and EGR. Therefore, further considerations on leaning are not subject of this chapter and the dilution ratio is set constant to D = 1.5.
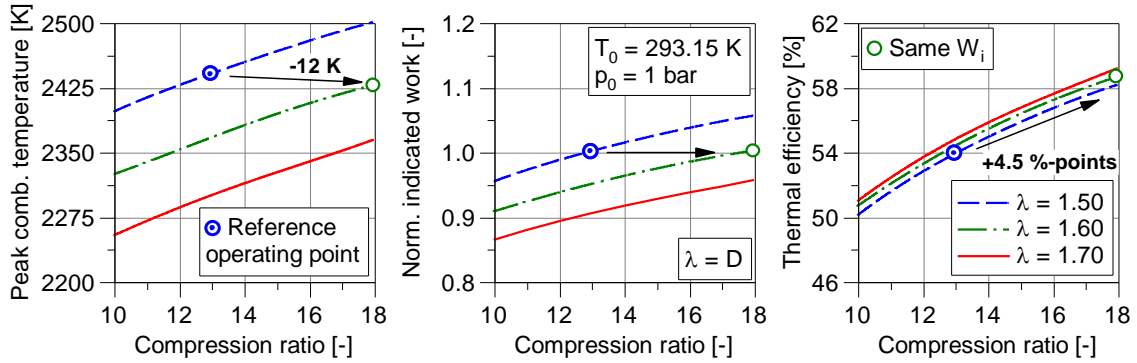

Figure 3-2: Peak combustion temperature, normalised indicated work and thermal efficiency over the geometrical compression ratio r_{geo} for varying relative air-fuel ratios λ

Miller Cycle in Lean-burn Operation

For introducing Miller cycle into the simulation environment, the inlet valve closes, as opposed to the Otto cycle, during the compression stroke after BDC. Meanwhile, the system loses mass, which occurs as isobaric change because of the assumption of an idealised gas exchange. This leads to same initial pressure and temperature conditions at IVC as at BDC. A comparison in Figure 3-3 exemplarily shows the p-V diagram of two cycles for an expansion/compression ratio (defined by Eq. (2-18)) of $ECR = 1.0$ (Otto) and $ECR = 1.2$ (Miller) at constant air-fuel ratio of $\lambda = 1.5$ and constant effective compression ratio of $r_{c,IVC} = 13.0$. The onset of the effective compression stroke is retarded as ECR increases.

In order to maintain the effective compression ratio $r_{c\,IVC}$, defined in Eq. (2-21), the geo-metrical compression ratio is adjusted by modifying V_{TDC} (cf. Figure 2-8, left). Consequently, the thermodynamic conditions at the end of the compression stroke and after the isochoric combustion are identical for a constant effective compression ratio. The lower fuel energy added and the increased expansion compression ratio ECR lead to a lower pressure level at the end of the expansion stroke.
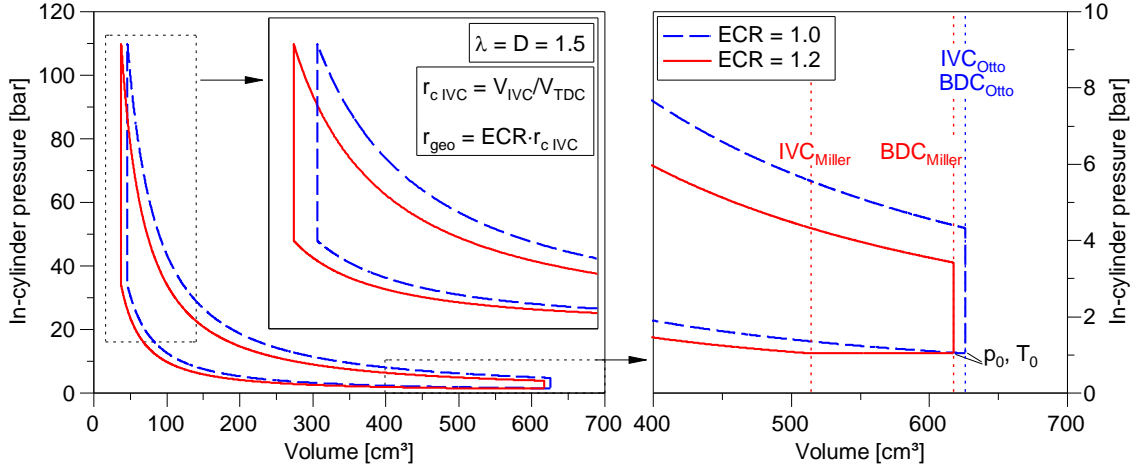

Figure 3-3: p-V diagram of Otto and Miller cycle at constant relative air-fuel ratio of $\lambda = 1.5$ and effective compression ratio $r_{c\,IVC} = 13.0$

Figure 3-4 displays T_{max}, W_i and η_{th} as a function of the effective compression ratio $r_{c\,IVC}$ for different expansion/compression ratios at $\lambda = D = 1.5$. Peak combustion temperature increases with rising effective compression ratio as observed in the prior section. Engine efficiency improves despite increased losses in charging efficiency that lower engine power. At the reference effective compression ratio of $r_{c\,IVC} = 13.0$, thermal efficiency increases from $\eta_{th} = 53.8\,\%$ to $55.3\,\%$ for $ECR = 1.1$ and to $56.5\,\%$ for $ECR = 1.2$.
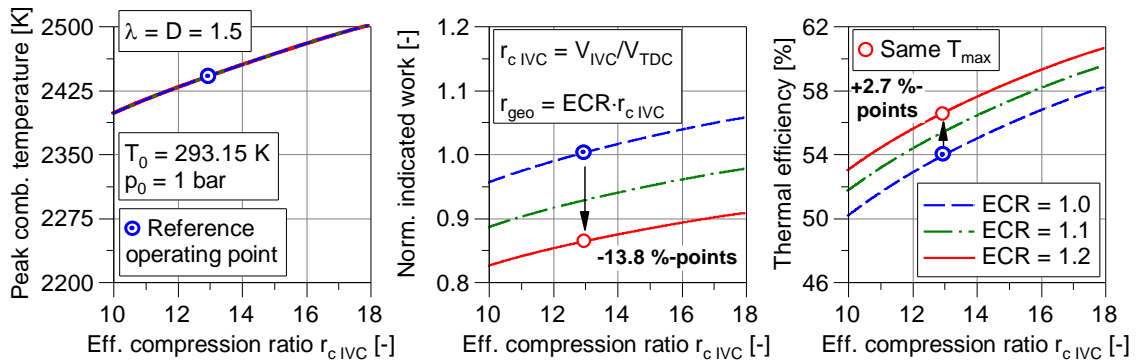

Figure 3-4: Peak combustion temperature, normalised indicated work and thermal efficiency over the effective compression ratio $r_{c\,IVC}$ for varying expansion/compression ratios ECR at constant relative air-fuel ratio $\lambda = 1.5$

The benefit in efficiency can be ascribed to the higher ratio between cycle volume work gained from the expansion stroke and that required for the compression stroke, increasing

from 3.66 to 3.78 and 3.88, respectively. However, the falling heat added to the cycle with increasing ECR at constant λ is detrimental to indicated work, as losses of 7.4 and 13.8 % quantify. It can be seen that the benefit in efficiency becomes smaller with both rising effective compression ratio and expansion/compression ratio since the cycle approaches its theoretical optimum.

<u>Exhaust Gas Recirculation for Otto Cycle</u>

Mixture composition is decisive for engine efficiency as the results from lean-burn operation clearly reveal. Adding EGR as a second diluent offers an additional degree of freedom to alter mixture composition. The impact caused by dilution either solely through excess air or in combination with exhaust gas is analysed in depth for an isochoric combustion. As the initial temperature of the cycle was defined with $T_0 = 293.15$ K, adding exhaust gas would lead to water condensation. The exhaust gas was therefore assumed to have a gaseous phase at cycle onset, being only a minor error due to the steep temperature rise of the mixture in the course of the compression stroke. Figure 3-5 shows the contour plot of thermal efficiency as function of dilution ratio and EGR rate for a geometrical compression ratio of $r_{geo} = 13.0$. The impact of mixture dilution on η_{th} clearly decreases for higher dilution ratios, regardless of whether only air or air combined with exhaust gas serves as diluent. When replacing air with exhaust gas of an air-diluted mixture at a dilution ratio of D = 1.5 (OP 1) to set an EGR rate of $x_{EGR} = 20$ % (OP 2), η_{th} decreases by 0.56 %-points, while for D = 1.3 (OP 3), the same EGR rate causes a drop of 1.24 %-points (OP 4). Beside the higher sensitivity of ideal engine efficiency to mixture composition at low dilution ratios, the larger effect for the lower dilution ratio can be ascribed to the increasing H_2O and CO_2 concentration. On the one hand, it lowers efficiency because of reduced γ, but on the other hand, it decreases combustion temperature as the ensuing analysis shows.

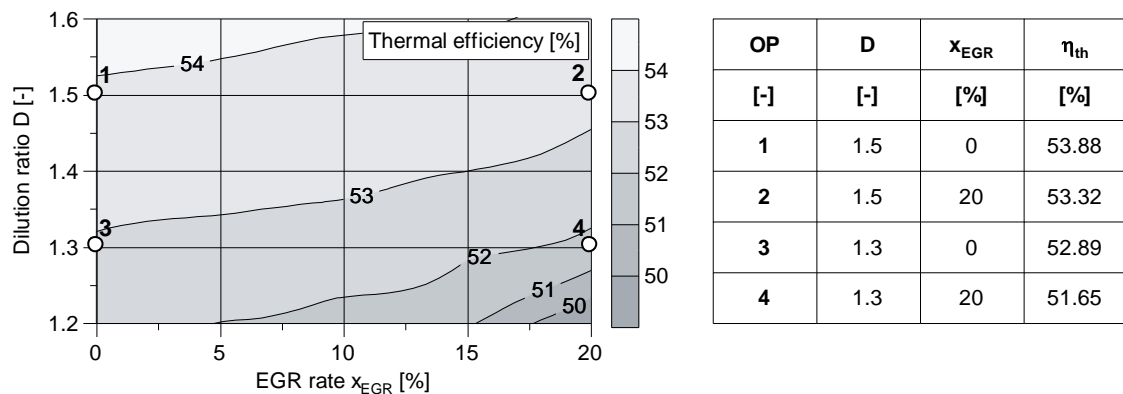| OP	D	x_{EGR}	η_{th}
[-]	[-]	[%]	[%]
1	1.5	0	53.88
2	1.5	20	53.32
3	1.3	0	52.89
4	1.3	20	51.65

Figure 3-5: Thermal efficiency as function of dilution ratio and EGR rate for isochoric combustion at TDC and a geometrical compression ratio of $r_{geo} = 13.0$

The findings in literature proved that substituting a part of excess air with exhaust gas is an effective means to advance CA50 without increasing NO_x emissions. Therefore, it is

reasonable to vary CA50 when analysing the influence of EGR on T_{max}, W_i and η_{th}. In actual engine operation, wall heat losses and non-isochoric combustion (addressed in Section 3.2.2) lead to a thermodynamic efficiency optimum of about CA50 = 8 to 10 °CA ATDC. While large gas engines meet the optimum combustion phasing regarding engine efficiency [45, 88, 172], the demand of low raw NO_x emissions require small lean-burn gas engines to retard CA50. Accordingly, the reference operating point is altered to a more realistic value of CA50 = 18 °CA ATDC. Releasing the same heat in a larger volume, reduces peak combustion temperature from T_{max} = 2439 K to 2389 K, while normalised indicated work drops by 8.5 % and thermal efficiency decreases from η_{th} = 53.8 % to 49.4 %.

Figure 3-6 depicts T_{max}, W_i and η_{th} over CA50 for different EGR rates at constant dilution ratio of D = 1.5 (i.e. constant mass of fuel). It can be seen that rising EGR rates reduce peak combustion temperature thanks to higher specific heat capacity. On the one hand, this is detrimental to engine efficiency and indicated work at same CA50, but on the other hand, the reduced temperature enables earlier combustion phasing. For CA50 of same thermal efficiency, peak combustion temperature remains below the reference operating point. Alternatively, the engine can operate at the peak combustion temperature of the reference operating point but higher efficiency and indicated power. EGR rates of x_{EGR} = 10 % / 20 %, for instance, allow the cycle to operate at combustion phasings of 14.5 °CA / 9.6 °CA ATDC, increasing both indicated work by 2.0 / 4.6 % and thermal efficiency by 1.2 / 2.5 %-points compared to the reference operating point.
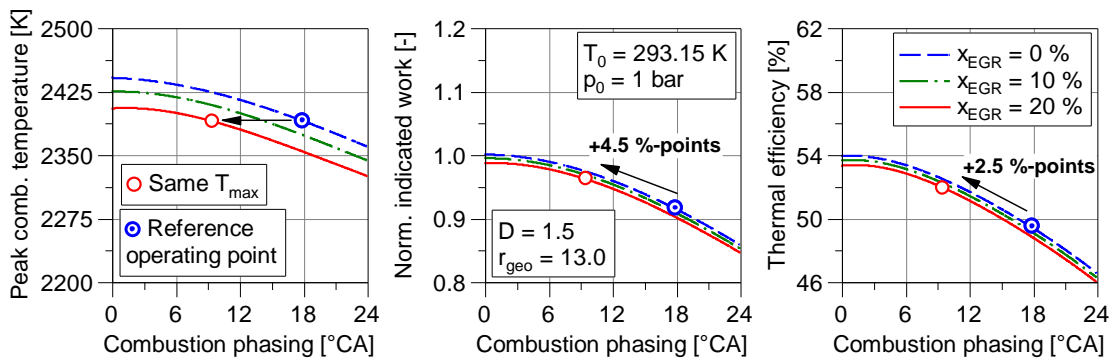

Figure 3-6: Peak combustion temperature, normalised indicated work and thermal efficiency over combustion phasing for varying EGR rates at constant dilution ratio D = 1.5 and geometrical compression ratio of r_{geo} = 13.0

Lean-Miller-EGR Working Process

After analysing the influences of the single means on ideal engine behaviour individually, all measures were combined to form the Lean-Miller-EGR working process. The dilution ratio and effective compression ratio are kept constant at D = 1.5 and $r_{c,eff}$ = 13.0. The expansion/compression ratio of the reference amounts to ECR = 1.0 and gives that the effective compression ratio equals the geometrical compression ratio ($r_{c,eff}$ = r_{geo} = 13.0).

Based on findings in literature [107, 162, 163], an EGR rate of $x_{EGR} = 20\%$ appears to cause the best compromise between advanced combustion phasing at same NO_x emissions (or vice versa), prolonged burn duration and losses in ideal engine efficiency. For this reason, a mixture setting of $D = 1.5$ / $x_{EGR} = 20\%$ was selected to analyse the influence of expansion/compression ratios of $ECR = 1.05$ and 1.1.

Figure 3-7 shows that both increasing EGR rate and ECR reduce indicated work at same combustion phasing. While $ECR = 1.05$ merely compensates the penalty in efficiency due to lower γ, increasing the expansion/compression ratio to $ECR = 1.10$ leads to a benefit of 0.6%-points compared to the reference operating point. The lower temperature level caused by EGR allows advancing combustion phasing. Engine efficiency and indicated work increase, however, only $ECR = 1.05$ reaches the indicated work of the reference operating point without exceeding its peak combustion temperature. In fact, for a combustion phasing of $CA50 = 11.2$ °CA, peak combustion temperature decreases by 9 K, while thermal efficiency increases from 49.4 to 52.8 %.
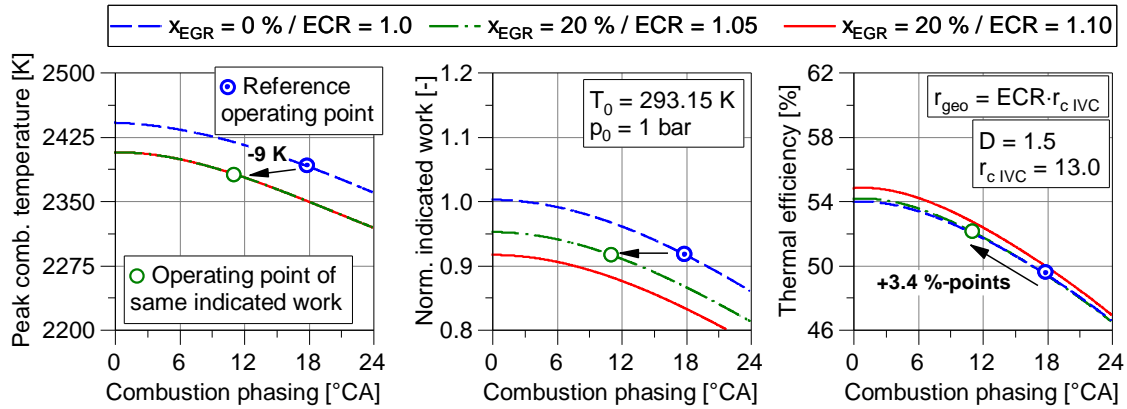

Figure 3-7: Peak combustion temperature, normalised indicated work and thermal efficiency over combustion phasing for varying expansion/compression ratios ECR and EGR rates at constant dilution ratio D = 1.5 and effective compression ratio $r_{c\,IVC}$ = 13.0

The study reveals a substantial potential to improve engine efficiency at lower combustion temperature and same cycle work. With respect to engine experiments, following assumptions will affect the working process considerably:

- Defining isochoric combustion assumes constant burn duration. This is clearly not the case with the addition of EGR since it prolongs ignition delay and reduces laminar burning velocity. Furthermore, modifying IVC is expected to alter charge motion and therefore influence the turbulence level.

- Indicated work was adjusted by advancing the combustion phasing. Nevertheless, it might be expedient to increase the amount of fuel instead or to combine both measures.

- The effects of gas dynamics lead to a non-linear behaviour between cylinder mass and IVC. As a result, higher expansion/compression ratios could be feasible.

- Wall heat losses will clearly affect engine efficiency, in particular for increasing geometrical compression ratios as it is the case for higher ECR.

3.2.2 Role of Combustion and Wall Heat Losses

Mixture composition and geometrical constraints are the key parameters that need to be changed in order to realise the Lean-Miller-EGR working process. After analysing both by assuming an isochoric combustion within an adiabatic system, the influence of combustion phasing, burn duration and wall heat losses on ISFC are subject of this section. For this reason, combustion is no longer assumed to be isochoric but defined through a more realistic heat release using a Vibe function. The cumulative normalised heat over crank angle $x(\alpha)$ can be written as

$$x(\alpha) = 1 - e^{-a\left(\frac{\alpha - \alpha_{SOC}}{\Delta\alpha_{BD}}\right)^{m+1}} \tag{3-2}$$

where a stands for a constant describing the amount of heat that is released, α_{SOC} the start of combustion, $\Delta\alpha_{BD}$ the burn duration and m the form parameter. The last governs the shape of the combustion and was set to $m = 1.5$ for this study. By assuming $a = 6.908$, 99.9 % of the fuel is burnt at the end of combustion.

The cycle analysis becomes more representative by also considering the wall heat losses. While heat transfer caused by radiation is usually neglected in Otto engines, convective wall heat losses are determined via Newton's approach. It considers mean charge temperature, cylinder wall temperature, wall area and wall heat transfer coefficient h. A prevailing model to calculate h was postulated by Woschni [177], defining Eq. (3-3) and (3-4), and extended by Huber [60], introducing Eq. (3-5).

$$h = 130 \cdot D_{cyl}^{-0.2} \cdot p_{cyl}^{0.8} \cdot T^{-0.53} \cdot (C_1 \cdot w)^{0.8} \tag{3-3}$$

$$w = v_{pm} + \frac{C_1}{C_2} \frac{V_d T_{IVC}}{p_{IVC} V_{IVC}} (p_{cyl} - p_m) \tag{3-4}$$

$$w = v_{pm} \cdot \left[1 + 2\left(\frac{V_{IVC}}{V}\right) IMEP^{-0.2}\right] \tag{3-5}$$

The parameters are:

D_{cyl}: Cylinder bore diameter

v_{pm}: Mean piston velocity

p_{cyl}: In-cylinder pressure (fired engine)

V_d: Displacement volume

p_m: In-cylinder pressure (motored engine)

V_{IVC}: Cylinder volume at IVC

T_{cyl}: Mean in-cylinder temperature

p_{IVC}: In-cylinder pressure at IVC

w: Characteristic velocity

T_{IVC}: In-cylinder temperature at IVC

C_1: Constant (depending on swirl and engine speed)

C_2: Constant (depending on engine type and combustion chamber)

The characteristic velocity w comprises the mean piston velocity and a combustion term that accounts for the increasing wall heat transfer during combustion based on the pressure difference between fired and motored engine operation. Under low load, the term in Eq. (3-4) tends to calculate values that are too low. To overcome this issue, Eq. (3-5) considers the cylinder volume as function of crank angle and IMEP. For calculation of the heat transfer coefficient, simply the higher value of both is used [88].

Differentiating Eq. (3-2) by the crank angle α, gives the normalised rate of heat release plotted in Figure 3-8 (left) at $CA50 = 8$ °CA ATDC for all burn durations investigated. The constant form parameter m leads to a stretched shape of a lower peak as combustion duration increases. Its influence on ISFC over combustion phasing at $\lambda = 1.5$ and a geometrical compression ratio of $r_{geo} = 13.0$ is shown Figure 3-8 (right) for two cases: In case 1, the combustion chamber is treated as adiabatic system, while case 2 considers wall heat losses assuming a constant wall temperatures of 180 °C.
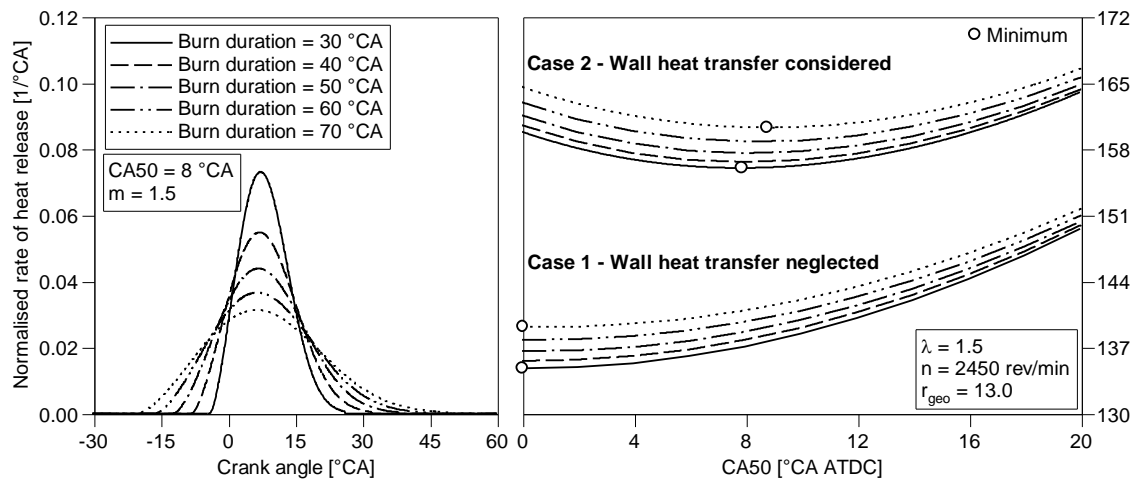

Figure 3-8: Normalised rate of heat release at CA50 = 8 °CA AlC (left) and indicated specific fuel consumption over combustion phasing for varying burn duration for neglected and considered wall heat losses (right) (0D calculation)

For case 1, lowest ISFC is found at a combustion phasing of CA50 at TDC combined with the shortest burn duration. It increases with lengthening burn duration that exerts the largest influence on ISFC at TDC due to the increasing proportion of heat released during the compression stroke. Evidently, this effect decreases as combustion phasing is retarded, leading to a smaller sensitivity of ISFC to combustion duration, while its dependency on CA50 becomes stronger. Overall, ISFC is more sensitive to CA50 than to burn duration, in particular for late combustion phasing for the investigated range. Altering CA50 from TDC to 20 °CA ATDC, increases ISFC from 134.8 to 149.5 g/kWh and from 139.1 to 151.6 g/kWh for burn durations of 30 °CA and 70 °CA, respectively. When considering wall heat losses in case 2, ISFC increases by more than 20 g/kWh and shifts the optimum to about 8/9 °CA ATDC for a combustion duration of 30 / 70 °CA, as illustrated in Figure 3-8 (right). The offset to TDC stems from increasing wall heat losses at very low A/V

ratios. For combustion phasings beyond the ISFC optimum, burn duration and combustion phasing show same trends as the calculations without wall heat transfer. The potential to improve engine efficiency through a more favourable combustion phasing is primarily given for late CA50, where combustion duration plays a smaller role. For example, reducing the burn duration from 70 to 30 °CA at CA50 = 20 °CA ATDC, decreases ISFC from 166.4 to 163.9 g/kWh. To achieve the same savings through a more favourable combustion phasing, it only needs to be advanced by 2.7 °CA to CA50 = 17.3 °CA.

After discussing the dependency of ISFC on both combustion phasing and duration, the influence of engine parameters relevant for realising Lean-Miller-Working process (i.e. piston surface area, expansion/compression ratio and EGR rate) are reviewed at constant fuel mass and same burn duration of 50 °CA. The purpose of this analysis is to assess the influence of the respective parameters on engine performance rather than to evaluate the potential of the working process to improve the ISFC-NO_x trade-off at constant IMEP.

Figure 3-9 shows peak combustion temperature T_{max}, IMEP, ISFC and wall heat losses Q_{wall} normalised to the fuel energy added of several configurations with a constant effective compression ratio of $r_{c\,IVC} = 13.0$.
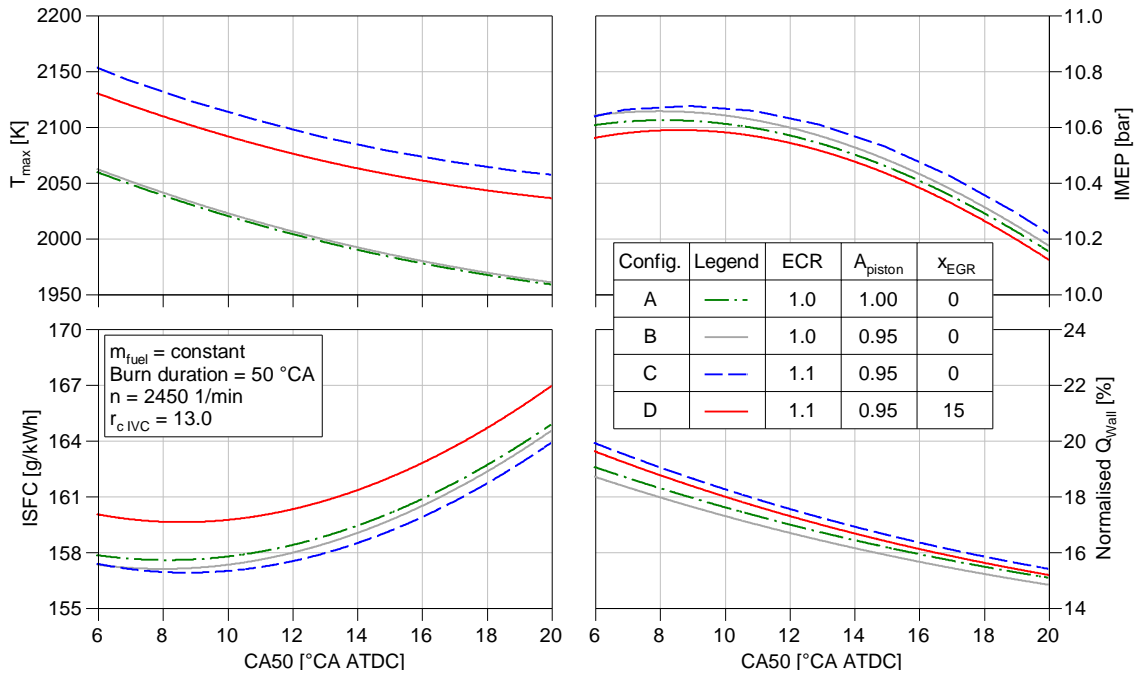

Figure 3-9: Peak combustion temperature, IMEP, ISFC and wall heat losses normalised to the heat added to the cycle over CA50 for a constant effective compression ratio $r_{c\,IVC} = 13.0$ and burn duration of 50 °CA

Starting from a conventional setup of an Otto engine (configuration A), the piston surface area is reduced by 5 % to form configuration B. The motivation behind this step is that realising Miller cycle at a later point of this work will include decreasing the piston bowl size. In the case given, the A/V ratio decreases by 1 % from configuration A to B, leading to slightly higher peak temperature by virtue of lower wall heat losses, which in turn,

increase IMEP and reduce ISFC. As combustion phasing is retarded, the differences in T_{max}, W_i and η_{th} and Q_{wall} between A and B diminish because of the decreasing difference of the A/V ratios. Increasing ECR from 1.0 to 1.1 (B to C), augments the A/V ratio by 3 % and reduces charging efficiency. Peak combustion temperature rises as a result of a lower dilution ratio that is required to keep the amount of fuel constant. T_{max} falls with retarding CA50 with a slightly lower slope for $ECR = 1.1$ compared to $ECR = 1.0$. The fact that a higher reduction of wall heat losses occurs for $ECR = 1.1$ can be ascribed to the more pronounced decrease of the A/V ratio with retarded CA50. For this reason, the benefit in ISFC increases from 0.6 g/kWh at CA50 = 8 °CA ATDC to 1.1 g/kWh at CA50 = 20 °CA ATDC. Finally, in configuration D excess air is partly replaced with exhaust gas to set an EGR rate of $x_{EGR} = 15$ %. Peak combustion temperature decreases by approximately 22 K, thus reducing the wall heat losses rather moderately. Suffering ideal engine efficiency from a lower ratio of the specific heat capacities leads to higher ISFC and lower IMEP.

The study performed indicates that wall heat losses are crucial for the later engine performance. However, its importance significantly decreases with late CA50, which is the expected operating range for the investigated working process to achieve low NO_x emissions. Due to the exponential rise of thermal NO with temperature, the diminishing effect on peak combustion temperature caused by EGR is expected to lower NO_x emissions. Nonetheless, the decrease is too small to reduce wall heat losses to an extent that would compensate the losses in ideal efficiency. It can therefore be concluded that mixture composition and combustion phasing are the key factors determining engine efficiency.

3.3 Determination of the Effective Compression Ratio in Actual Engine Operation

Unlike the 0D calculations conducted thus far, the gas exchange of an actual engine underlies effects of gas dynamics. This demands a reliable approach to determine the effective compression ratio for a representative comparison between early and late Miller cycle. The majority of methods found in literature (see Section 2.4.5) substitute the geometrical with an effective BDC volume. A backward calculation starting from IVC, as shown in [53], proved to give plausible results. As opposed to a constant polytropic exponent n, considering a variable value for n over crank angle is expected to yield to more accurate results.

It is crucial whether the effective compression ratio is determined in fired or motored operation as the higher temperature level caused by the combustion influences gas exchange significantly. This becomes even more relevant for very late IVC, owing to the reverse flow during the compression stroke that heats up the mixture in the intake port. The extent of this effect depends on the temperature of the outflowing mixture, which, in turn, is driven by the engine settings such as λ or ignition timing. From this it follows, that selected the

operating point influences the effective compression ratio. Therefore, it is expedient to
define a reference setting for which the effective compression ratio is to be determined when
comparing different engine configurations.

Figure 3-10 illustrates the method applied in this thesis to determine the effective com-
pression ratio for a naturally single-cylinder gas engine operating with nearly filling opti-
mised valve timing. A steep pressure rise can be observed around BDC as result of an
arriving pressure wave shortly prior to IVC. It leads to a mixture flow into the cylinder
even beyond BDC (known a ram effect), and subsequently followed by a reverse flow,
ending at IVC. Drawing a polytropic process starting from IVC towards BDC, helps to
visualise both gas dynamic effects, yet its actual purpose is to determine $V_{BDC\,eff}$ found at
ambient pressure p_{amb}. Using p_{amb} as target values is only valid for engine operation at
constant engine speed where neither throttling nor boosting occurs, as it is the case in this
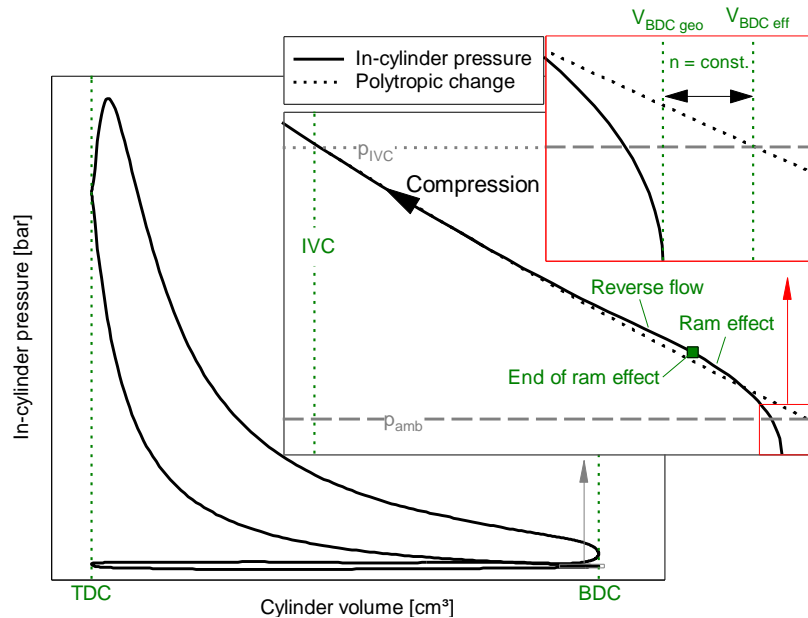work. Otherwise, the author suggests a calculation to the mean intake port pressure.

Figure 3-10: p-V diagram of the reference operating point (1D CFD calculation)

A pronounced ram effect leads to a high pressure level at IVC (p_{IVC}, V_{IVC}) that causes a
polytropic curve that exceeds the ambient pressure p_{amb} at BDC. For this reason, the pol-
ytropic curve is to be extrapolated to determine a fictive cylinder volume that is required
to achieve the same pressure level at IVC without the effects of gas dynamics. The volume
$V_{BDC\,eff}$, found at the so-called effective BDC, can be calculated as follows:

$$V_{BDC\,eff} = V_{IVC} \left(\frac{p_{IVC}}{p_{amb}} \right)^{\frac{1}{n}}$$

(3-6)

The change of the polytropic exponent n between IVC and BDC was taken into account,

while beyond BDC it was assumed to be constant. Since n varies marginally around BDC, only a minor error is expected. Eventually, the effective compression ratio considering the effects of gas dynamics $r_{e\,eff}$ can be calculated according to Eq. (3-7):

$$r_{e\,eff} = \frac{V_{IVC} \left(\frac{p_{IVC}}{p_{amb}}\right)^{\frac{1}{n}}}{V_{TDC}}$$

(3-7)

When it applies that $V_{BDC\,eff} > V_{BDC}$, it becomes evident that the effective compression ratio can be even higher than its geometrical definition. Note that only IVC after BDC requires the polytropic calculation to find $V_{BDC\,eff}$ as shown for an engine configuration with relatively late IVC in Figure 3-11 (left). The reverse flow annihilates the pressure rise caused by the ram effect, leading to a polytropic curve that meets ambient pressure at a cylinder volume lower than V_{BDC} so that no extrapolation is required. Closing the intake valve before BDC, on the other hand, avoids effects of gas dynamics to take place during the compression stroke and $V_{BDC\,eff}$ is found where the pressure trace intersects ambient pressure during the compression stroke (see Figure 3-11, right).
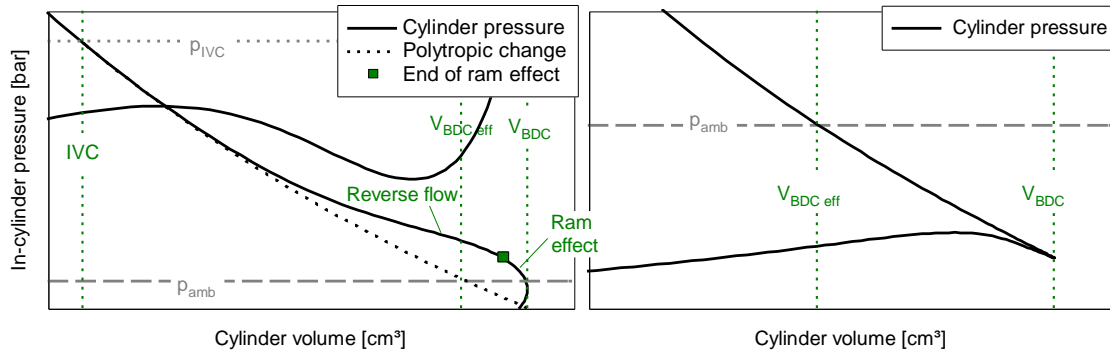

Figure 3-11: Determination of the effective compression ratio of an engine configuration with late (left) and early (right) intake valve closing

It becomes clear that a geometrical definition of the effective compression ratio is not expedient. The same applies to the expansion/compression ratio defined for the idealised engine cycle in Eq. (2-18). In order to account for the effects of gas dynamics, an effective expansion/compression ratio ECR_{eff} is introduced:

$$ECR_{eff} = \frac{r_{e,o}}{r_{e\,eff}}$$

(3-8)

Since the exhaust valve opening EVO is not altered in this work, the numerator from the former expression remains constant.

4 Experimental Setup and Numerical Tools Used

This chapter covers the experimental equipment and numerical models that were used in this work. For fundamentals of fluid dynamics and numerical solving please refer to pertinent literature, e.g. [28, 88].

4.1 Constant Volume Combustion Chamber

The laminar burning velocity is of high interest when analysing different mixture compositions since it strongly influences the rate of heat release during the cycle and therefore engine efficiency and its emissions. To determine the laminar burning velocity of various mixture compositions, experiments using a constant volume combustion chamber (CVCC) were carried out at the Universidad de Valladolid (UVa), Spain.

4.1.1 Specifications and Metrology

The CVCC is made of stainless steel and features a spherical shape with an inner diameter of 200 mm, corresponding to a 4.19 litre volume. It is connected to several gas bottles and an air compressor on the intake and a vacuum pump on the outlet side (see Figure 4-1). Four piezoresistive sensors of different pressure range and a thermocouple, with its tip located inside the centre of CVCC, are used, to measure the initial conditions of pressure and temperature. The CVCC is thoroughly insulated and equipped with an electrical heater on the bottom that facilitates setting initial mixture temperatures up to 650 K can be set.
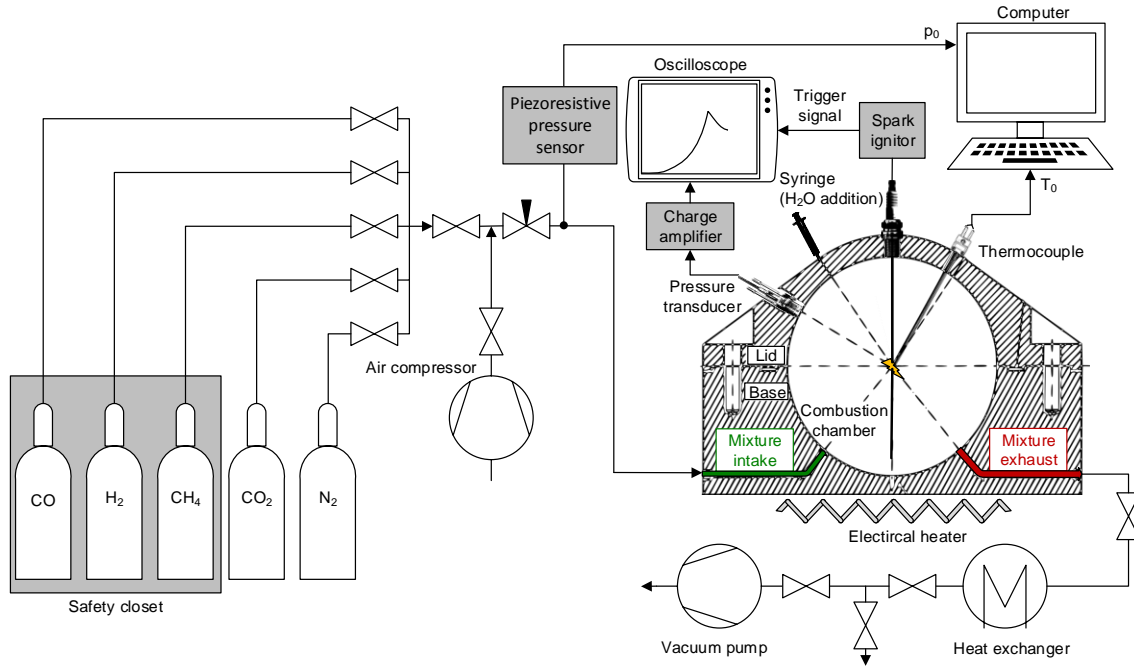
Figure 4-1: Schematic layout of the constant volume combustion chamber

Two prolonged electrodes form the spark gap in the centre of the CVCC, favouring a uniform flame propagation with a spherical shape. The pressure signal over time is measured by the means of a Kistler 7063A pressure transducer, connected to an oscilloscope for data recording.

4.1.2 Chamber Pressure Analysis Code

The data measured is evaluated using a proprietary two-zone combustion analysis model, developed in a former work [62] which divides the gas within the CVCC into burnt and unburnt fraction. It enables analysing the combustion of various fuels, including dual fuel mixtures, yet the possibility of adding exhaust gas to the fresh mixture needed to be integrated as a part of this work. The model considers exhaust gas of the initial mixture as products of perfect combustion CO_2, N_2, O_2, H_2O and Ar, while for combustion itself it solves 12 equilibrium equations of the major species. The thermochemical properties, taken from NIST-JANAF tables, account for the temperature dependency of the specific heat capacities. The calculation model assumes following behaviour:

- Combustion commences in the centre of the vessel, leading to a flame front that propagates spherically with negligible thickness.
- The pressure during combustion is uniform throughout the whole vessel.
- The CVCC is an adiabatic system, meaning that no heat is lost through the walls.
- Ideal gas behaviour is assumed.
- Gas in the unburnt zone is isentropically compressed as combustion proceeds.

The first law of thermodynamics for non-stationary open systems is applied to burnt and

unburnt zone to describe their change of internal energy. After adding mass conservation and volume equation, the laminar burning velocity s_l results to Eq. (4-1)

$$s_l = \frac{dm_b/dt}{A_l \cdot \rho_u} \tag{4-1}$$

where the mass burning rate dm_b/dt is calculated from pressure data, the flame area A_l of the laminar flame front is determined for the burnt volume by assuming spherical flame shape and ρ_u is the density of the unburnt zone. For the derivation of Eq. (4-1) and a more detailed description of the pressure analysis model and the experimental setup, the authors refer to the Annex A.2 and to former work conducted at UVa [62, 73, 125, 156, 157].

4.2 Test Bed Engine

The ICE used in this thesis, represents the core component of the cogeneration unit Dachs 5.5 G from SenerTec. Trials with two different engines of the same type and specifications were carried out: Engine I was installed at the project partner's and engine II at the Karlsruhe UAS facilities. Engine I was primary used at the beginning of the research work in order to build a 1D CFD model that allows designing new components to realise the Lean-Miller-EGR working process and to carry out first trials with modified valve timing and adjusted compression ratio (see Chapter 5 and Section 7.3.1). All other engine tests were performed using engine II that was put into operation in the course of the project.

4.2.1 Gas Path and Specifications of the Test Bed Engine

The naturally aspirated engine, illustrated in Figure 4-2 (left), runs without a throttle at a constant speed of n = 2450 rev/min, generating 5.5 kW of electric power in its reference operating point (ROP). Under warm engine operating conditions, this corresponds to an indicated mean effective pressure of about IMEP = 6.35 bar. Electric power is controlled by adjusting the fuel mass flow at constant ignition timing of 8 °CA BTDC. The air-NG mixture is prepared in a venturi mixer, located above the intake of the gas path shown in Figure 4-2 (right). The gas path design on the intake side is fairly complex, containing several plenums that damp the pressure pulsations in the venturi mixer caused by the single-cylinder engine. Another plenum, positioned between flame arrester and air-filter, has the purpose of reducing the pressure drop as mixture is inducted and increase charging efficiency. The cogeneration unit is encapsulated to ensure low noise emissions and thorough insulation, leading to relative high casing temperatures of approximately 85 °C. The mixture heats up as it flows through the gas path with an approximate length of 2000 mm, reaching temperatures shortly before the intake valve of about $T_{intol} = 75$ °C. Once the exhaust valve opens after combustion, the burnt mixture escapes the cylinder and flows through an oxidation catalyst, followed by a heat exchanger and a muffler. To investigate the impact of exhaust gas on the generally lean operating baseline engine, an EGR system,

mainly consisting of automotive components, was incorporated. The exhaust gas is fed back into the intake system just before the intake port and the EGR rate is regulated through an EGR valve.
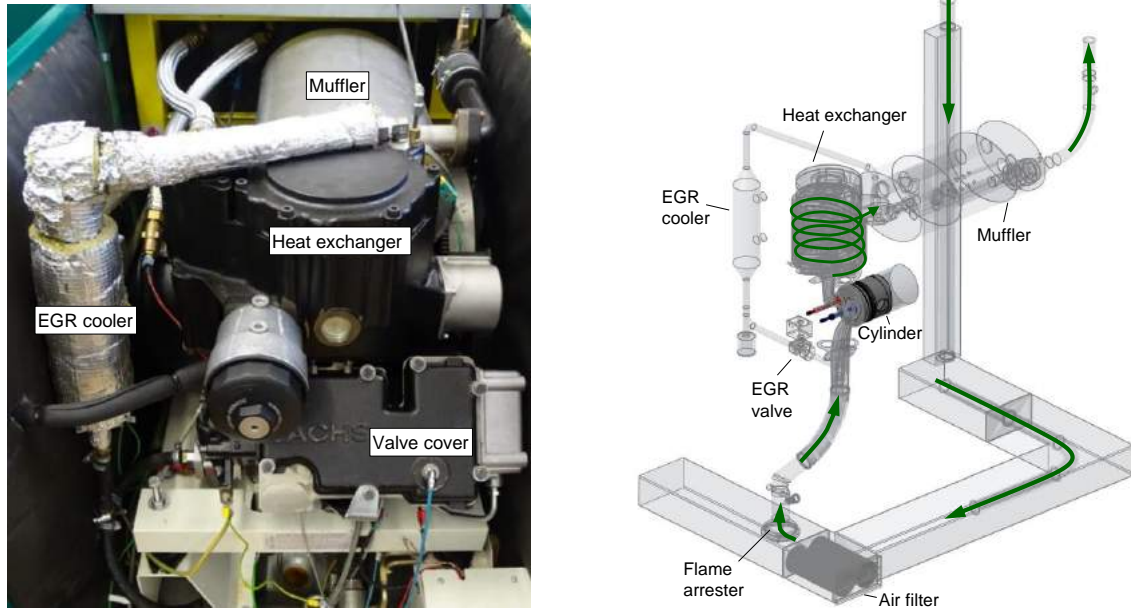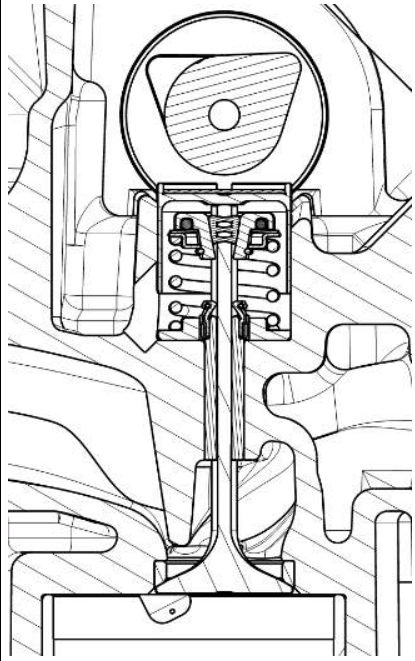

Figure 4-2: Test bed engine (left); CAD model of the gas path beginning after venturi mixer (right)

The engine comprises of a monobloc cylinder head with a heron combustion chamber and an overhead camshaft actuating two valves over a flat tapped as shown in the cutting view of the cylinder head in Table 4-1. The monobloc design forms both head and cylinder in one unit, thereby avoiding the use of prone cylinder head gaskets. The geometrical compression ratio amounts to $r_{geo} = 13.20$ and the displacement volume to 578 cm^3. The intake port is designed as swirl port, leading to a pronounced motion as mixture is aspirated. A squish ratio of $C_{sq} = 0.63$ combined with a clearance distance of 1.7 mm additionally intensify charge motion as the piston approaches TDC during the compression stroke. An unscavenged prechamber spark plug, arranged 27 ° to the longitudinal axis, ignites the lean air-NG mixture of an relative air-fuel ratio of $\lambda = 1.5 - 1.6$ and ensures stable and fast combustion. It is connected to the main combustion chamber via 5 orifices with a diameter of 1.2 mm. One is oriented in the centre and 4 tangentially to produce a highly turbulent flow as the mixture enters the prechamber. The ratio between the prechamber volume and V_{TDC} amounts to 1.39 %. Further engine data are listed in Table 4-1, where valve opening and closing events refer to valve clearance corresponding to delivery conditions at room temperature. For the given intake path design and engine speed, intake valve closing is set to achieve highest charging efficiency.

Table 4-1: Engine specifications and cutting view of the cylinder head (through the intake valve)

Engine	SenerTec Dachs G5.5 / swirl port	
Fuel	Natural Gas (NG)	
Mixture preparation	External (naturally aspirated)	
Cylinder	1	
Nominal speed	2450 rev/min	
Stroke	91 mm	
Bore	90 mm	
Displacement volume	578 cm³	
Number of valves	2	
Compression ratio (geometrical)	13.20:1	
C_{sq}	0.63	
IVO (room temperature)	20°CA BTDC	
IVC (room temperature)	50°CA ABDC	
EVO (room temperature)	35°CA BBDC	
EVC (room temperature)	16°CA ATDC	

4.2.2 Test Bed and Measurement Metrology

A conditioning unit that mainly comprises a roots blower and an intercooler enables controlling the temperature and pressure of the air entering the cogeneration unit by adjusting the coolant temperature and the blower speed through a frequency converter. The coolant temperature entering the cylinder block was controlled to 58 °C using a three-way valve from Siemens that mixes hot coolant that exits the cogeneration unit with cold water from the bottom of heat storage tank. Numerous absolute static pressure transducers and thermocouples were positioned along the gas path to monitor the thermodynamic conditions of the mixture. The same absolute pressure level across all sensors was ensured by calibrating them to the value of a high-precision barometer at the beginning of every measuring day. A piezoelectric pressure sensor of type 6125C11 and a 5018A charge amplifier both from Kistler were used to measure in-cylinder pressure. The sensor was mounted flush with the cylinder head in order to avoid pipe oscillations. The engine was equipped with low-pressure indication in the intake and exhaust port using Kistler piezoresistive pressure transducers of type 4007B and 4075A, positioned approximately 100 mm before the intake and 60 mm after the exhaust valve, respectively. This allows for an accurate validation of 1D CFD model and for a better analysis of the gas exchange process. Both low and high pressure signals were acquired in increments of 0.1 °CA using an AVL Indimodul 622 indicating system. Besides detecting direct indicating parameters such as peak pressure or pressure rise, it determines indirect parameters including IMEP or its coefficient of variation COV_{IMEP} over a predefined number of 200 consecutive cycles. Characteristic combustion

parameters such as burning delay IT-CA5 (crank angle from ignition timing (IT) to 5 % mass fraction burnt, combustion phasing CA50 (50 % mass fraction burnt) and burn duration CA5-CA90 (crank angle from 5 to 90 % mass fraction burnt) are calculated based on the net rate heat release dQ_n/da obtained from the first law of thermodynamics as described in Eq. (4-2):

$$\frac{dQ_n}{da} = \frac{\gamma}{\gamma\text{-}1} \cdot p \, \frac{dV}{da} + \frac{1}{\gamma\text{-}1} \cdot V \, \frac{dp}{da} \tag{4-2}$$

The ratio of the specific heat capacities was defined with $\gamma = 1.358$ for the compression and $\gamma = 1.30$ for the expansion stroke. For a detailed derivation of this method, the reader is referred to literature [57].

Knocking detection was conducted by analysing the in-cylinder pressure signal. The signal of every cycle was high-pass filtered with a cut-off frequency of 4 kHz and subsequently rectified to determine the peak value of the superimposed oscillations. If a cycle exceeded the predefined threshold, knocking combustion was detected. The threshold value used in literature varies depending on engine specification, application and allowed knocking intensity [109]. Schoeffler et al. [138] and Riztinger [128] analysed knocking in natural gas operation and applied values of 0.5 and 0.47 bar, respectively. Test bed trials with the engine used in this work proved that a conservative threshold of 0.25 bar suffices for defining the knock margin.

The air mass flow was monitored using a hot-film air-mass meter model HFM 5 from BOSCH, calibrated to measure mass flows of the expected range. A Bronkhorst F-103-lowΔp thermal mass flow meter for NG was used for monitoring fuel consumption. Engine-out emissions were measured using an exhaust gas analyser ABB AO2000, which determines the concentrations of CO_2, CO and O_2 under dry and of NO, NO_2 and C_3H_8 under wet conditions. The exhaust gas was drawn from the exhaust port and transferred to the analyser via a heated sample line. The oxidation catalyst that is located shortly after the exhaust port was replaced by a dummy component of same geometry but without catalytic coating to avoid erroneous raw engine-out emissions caused by possible back flow out of the catalyst. Knowing the single exhaust gas components, enables calculating the relative air-fuel ratio λ of the combustion quite accurately and determining the composition of the exhaust gas that is fed back into the intake section. Intake port temperature was measured using a type K thermocouple with a diameter of 1.5 mm, whose tip is located right above the intake valve. The Natural gas composition of engine II was monitored using an Inficon Micro GC Fusion Gas Analyser. During all trials carried out with engine II, only minor variations of the single species fractions were registered, as Table 4-2 reveals.

Table 4-2: Mean measured gas composition, lower heating value and density at standard conditions for temperature and pressure of all measuring days conducted at Karlsruhe UAS (engine II)

	Unit	Mean	Min	Max
Methane	Vol.-%	93.00	92.31	93.85
Ethane	Vol.-%	4.519	3.766	5.129
Nitrogen	Vol.-%	0.996	0.718	1.675
Carbon dioxide	Vol.-%	0.818	0.555	0.968
Propane	Vol.-%	0.491	0.013	0.614
iso-Butane	Vol.-%	0.083	0.000	0.129
n-Butane	Vol.-%	0.066	0.047	0.092
iso-Pentane	Vol.-%	0.016	0.000	0.059
n-Pentane	Vol.-%	0.011	0.000	0.021
n-Hexane	Vol.-%	0.003	0.000	0.007
LHV	MJ/kg	47.90	47.36	48.29
ρ_N	kg/m$_N^3$	0.771	0.762	0.777

Test bed engine I of the project partner SenerTec was operated only in lean-burn operation without EGR. It is equipped with highly precise thermal mass flow meter ABB Sensyflow FMT700-P. Together with the indicated pressure traces, the exact mass flows are of vital importance for validating the 1D CFD model. Further relevant differences between the two test beds used are given in Table 4-3.

Table 4-3: Major differences between test bed engine I and II

Measured variable	SenerTec - Engine I	Karlsruhe UAS - Engine II
Air mass flow	Thermal mass flowmeter ABB Sensyflow FMT700-P	Hot-film air-mass meter BOSCH model HFM 5
Fuel mass flow	Volumetric flowmeter ELSTER EXBGZ DE05	Thermal mass flowmeter Bronkhorst F-103
In-cylinder pressure	Kistler 6145A	Kistler 6125C11
Gas composition	Monthly obtained from municipal utilities	Hourly natural gas analysis

A detailed overview of the test bed setup of engine II (Karlsruhe UAS), including all measuring points, is found in the Annex A.3.

Differences in natural gas composition, overall engine operating hours and component dimension within the manufacturing tolerances lead to slight differences in the reference operating points. To set an IMEP of 6.35 bar at CA50 = 18.5 °CA ATDC (−/- 0.5), engine I operates at $\lambda = 1.57$ and generates NO_x emissions of 1.1 g/kWh. Engine II operates slightly richer at $\lambda = 1.50$, thus leading to higher NO_x emissions of 1.4 g/kWh.

4.2.3 Data Analysis

While the indicating system and the LabView graphic user interface of the test bench calculate numerous values online, data such as imperfect combustion losses, wall heat losses, effective compression ratio, residual gas concentration or in-cylinder temperature traces are determined in post-processing. The work flow in Figure 4-3 involves the use of three tools including a proprietary MATLAB routine and commercial software such as AVL BURN and AVL BOOST.

Experiment

- HC, CO …
- $\dot{m}_{air}$, $\dot{m}_{NG}$, $\dot{m}_{EGR}$
- Gas composition

Matlab – Gas exchange (EVO to IVC)

- Residual gas concentration
- Effective compression ratio
- Gas exchange losses
- Fuel conversion ratio
- LHV

AVL BURN – Combustion (IVC to EVO)

- Temperature trace of burnt and unburnt zone
- Wall heat losses
- $ROHR_g$

AVL BOOST – Ideal cycle

- $ISFC_{ideal}$
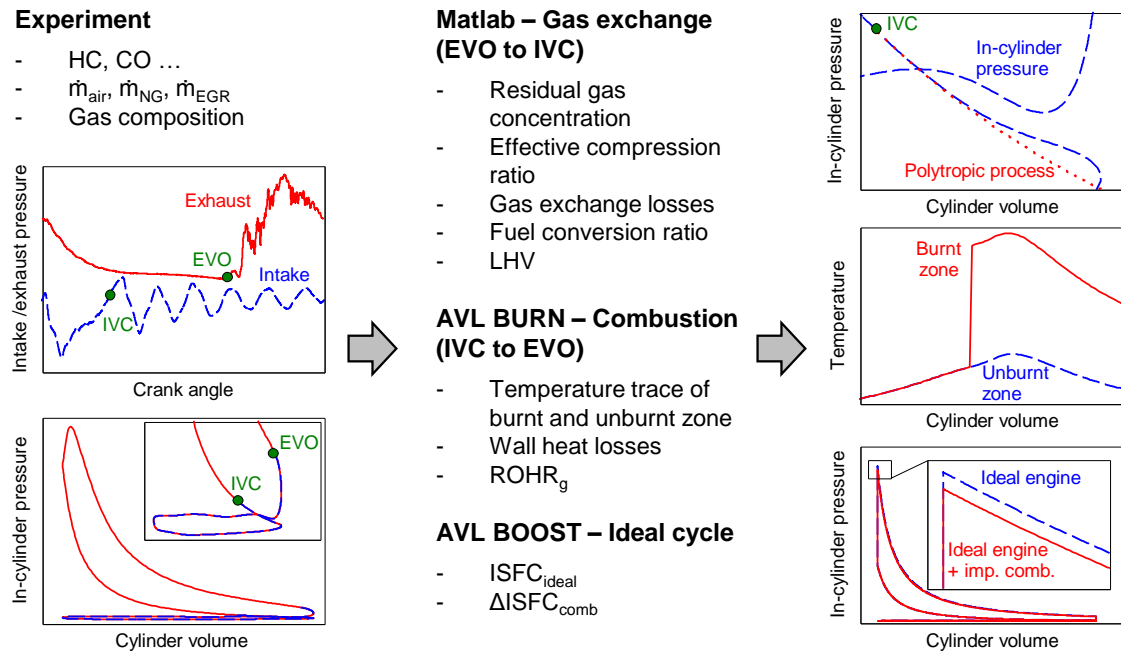- $\Delta ISFC_{comb}$

Figure 4-3: Post-processing workflow for analysing measured operating points

The proprietary MATLAB routine enables evaluating the gas exchange, i.e. between EVO and IVC, the effective compression ratio and the fuel conversion efficiency. Data needed as input are engine specifications such as displacement volume, geometrical compression ratio, valve lift curves and flow coefficients of the intake and exhaust in either flow direction. Furthermore, the routine requires measured engine data including in-cylinder, intake and exhaust pressure trace, air and NG mass flow and exhaust gas emissions. Fuel energy that does not get converted into heat during combustion together with the residual gas fraction need to be considered for obtaining the correct energy balance in combustion analysis [88]. Precise mixture composition and fuel energy added to the cycle are also needed for calculating the theoretical efficiency, given by the ideal engine, and losses from imperfect combustion.

Residual gas concentration

The MATLAB routine calculates the residual gas fraction from the pressure difference between intake and exhaust port during valve overlap assuming perfect mixing. The analysis is initialised at IVO, for which the residual gas mass is calculated using the product of

the respective cylinder volume and the density of the residual gas obtained from the thermodynamic conditions measured in the exhaust port. The further course of the analysis requires only accounting for the mass that exits via the exhaust port as the entire residual gas in the intake port is aspirated during the intake stroke. Residual gas enters the intake port due to either the high pressure difference to the cylinder at IVO or a reverse flow during the compression stroke. For the latter case, a homogenous mixture composition consisting of residual gas, air and fuel is assumed. A detailed explanation of this approach, postulated by Bargende and Spicher et al., is given in [7, 71].

Effective Compression Ratio

For determining the effective compression ratio, through the method presented in Section 3.3, the temperature-dependent gas properties and the wall heat losses during the polytropic backward calculation need to be considered. For this reason, the thermochemical properties of the single species were assigned to the model.

Fuel Conversion Ratio

The use of an oxidation catalyst allows the engine to operate at low tail-out CO and HC emissions in the field, yet analysing their raw emissions can help to gain a better understanding of the combustion process. More precisely, they enable determining the fuel conversion ratio FCR, also known as combustion efficiency [57], of the combustion process. It is defined in Eq. (4-3)

$$FCR = 1 - \frac{q_{unb}}{q_{max}} \qquad (4\text{-}3)$$

where q_{max} stands for the theoretical specific heat released and q_{unb} represents the specific heat that could not be converted due to incomplete and imperfect combustion. Starting from the simplest way to describe the combustion of a hydrocarbon, given by Eq. (2-1), q_{max} is obtained from the product of the number of moles of fuel n_{fuel} added to the cycle and the lower heating value LHV_{fuel}: $q_{max} = n_{fuel} \cdot LHV_{fuel}$. Under rich conditions, the lack of oxygen avoids the whole fuel to be burnt, reducing the fuel conversion ratio as shown in Figure 4-4 (left). Additional losses occur even when assuming the combustion reaches chemical equilibrium. The influence is well-pronounced under rich conditions, whereas it is negligibly small for lean combustion. Under actual engine operating conditions, imperfect combustion losses further decrease the fuel conversion ratio, arising from heterogeneous mixture composition and insufficient time to reach the chemical equilibrium. In order to account for the losses from incomplete and imperfect combustion, the mole fractions (x) of CO, HC, H_2 and soot (C) are multiplied with their LHV and divided by the molar mass of the exhaust gas M_{exh}:

$$q_{unb} = (x_{CO} \cdot LHV_{CO} + x_{H_2} \cdot LHV_{H_2} + x_{CH_4} \cdot LHV_{CH_4} + x_C \cdot LHV_C) \cdot \frac{1}{M_{exh}} \qquad (4\text{-}4)$$

Merker [88] assumes HC emissions to consist solely of C_3H_8, however, engine experiments

with natural gas showed that CH_4 poses with 85 to 90 % the main HC source and was therefore used instead. The H_2 concentration was calculated using the water shift reaction [144], while soot could be omitted.

Combustion Analysis

The wall heat losses of selected operating points were analysed by applying the approach of Woschni (explained in Section 3.2.2) using the AVL utility BURN that focuses on analysing the high-pressure phase of the in-cylinder pressure trace (i.e. from IVC to EVO) [4]. It allows for the calculation of the gross rate of heat release $ROHR_g$, which is not to be confused with net rate of heat release $ROHR_n$ obtained from Eq. (4-2). Further output traces are, amongst others, mean temperature of burnt and unburnt zone. Measurements of the cylinder head temperature conducted prior to this work served for setting the wall temperatures as function of combustion phasing and IMEP (see Figure 4-4, right). Linear interpolation was used when analysing operating points of IMEP's in-between.
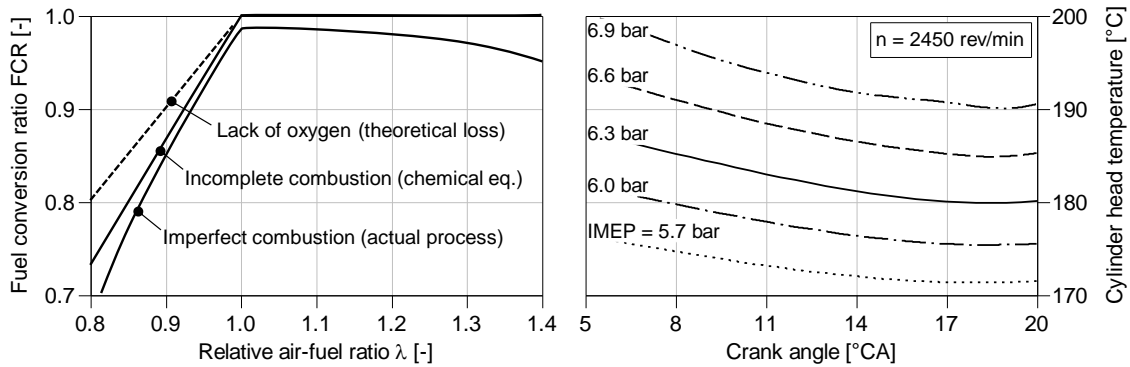

Figure 4-4: Conversion ratio over relative air-fuel ratio (left) according to [88] and measured cylinder head temperature over of test bed engine over CA50 for varying IMEP (right)

Ideal Engine Efficiency and Imperfect Combustion Losses

For analysing different engine setups from a theoretical stand of point, the efficiency of the ideal engine is calculated using an abstracted AVL BOOST model. Contrary to the definition of perfect in-cylinder filling stated in Section 3.2, the influence of real engine charge was taken into account. The following assumptions are made for the calculation:

- The relative air-fuel ratio equals that of the actual engine process.
- The calculated temperature and pressure at the beginning of the high pressure phase corresponds to the values of the actual engine cycle.
- Mass of in-cylinder charge corresponds to actual engine cycle.
- The residual gas fraction is the same as the one of the actual engine cycle.

After the indicated specific fuel consumption of the ideal engine $ISFC_{ideal}$ was calculated for the listed conditions, the calculation was repeated with a reduced LHV to consider the fuel conversion ratio of the actual cycle. Forming the difference between the ISFC obtained from reduced LHV and $ISFC_{ideal}$ yields the losses from imperfect combustion $\Delta ISFC_{comb}$.

4.2.4 EGR System and EGR Rate Model

Exhaust gas is extracted from the outlet of the heat exchanger, where its temperature amounts to around 160 °C and the pressure level is still high enough to enable EGR rates up to 25 %. The temperature of the exhaust gas recirculated depends on coolant temperature of the EGR cooler, designed as shell and tube heat exchanger. A process thermostat, type DC50-K40 from ThermoHAAKE, allows the coolant's temperature to be varied over a wide range. Its minimum temperature is limited to 58 °C to prevent that the exhaust gas condensates inside the EGR cooler, leading to temperatures of the recirculated exhaust gas of around $T_{EGR} = 75$ °C at EGR rates of $x_{EGR} = 20$ %. A PI controller that was integrated into the test bed user interface ensures constant EGR temperature with a deviation of +/- 0.5 °C. Possible condensation also motivated to feed the exhaust gas close to the intake port. The fact that the air-fuel-exhaust gas mixture can homogenise only over a short distance before it enters the combustion chamber, encouraged to conduct 3D CFD simulations. The results prove that a pronounced charge motion takes place as the mixture flows through the swirl port into the cylinder, leading to a sufficient mixture homogenisation.

While the mass flows of air and natural gas are fairly easy to monitor, measuring the EGR mass flow is far more complex for several reasons such as pressure pulsations, low mass flows, low acceptable pressure drops and the risk of corrosion caused by the aggressive condensate from the exhaust gas. Therefore, the EGR rate is often determined by the ratio of CO_2 concentration of the air-fuel-exhaust gas mixture and the exhaust gas [39, 55, 113]. To obtain a representative result, the mixture extracted from the intake section for measuring must be homogeneous. However, because of the short mixing length combined with small installation space of the engine used, this method is inapplicable. Instead, an EGR model was developed and implemented into the test bed interface. The measured values required for calculating the EGR rate are shown in Figure 4-5.
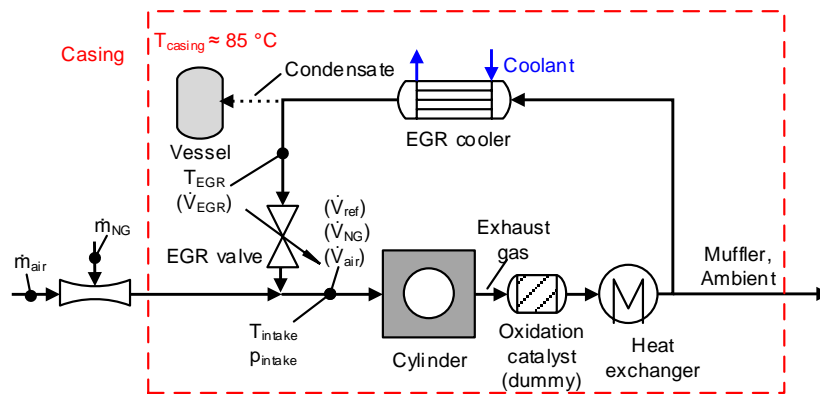

Figure 4-5: Abstracted gas path of the bed engine setup (values in brackets are calculated)

The approach taken to determine the EGR rate (defined by Eq. (2-24)) assumes a constant reference volume flow of the mixture $\dot{V}_{ref}$ in the intake port for a constant engine speed in

unthrottled engine operation. The reference volume flow is first calculated for engine operation under warm conditions without EGR by the sum of the volume flow of air $\dot{V}_{air}$ and NG $\dot{V}_{NG}$, where fuel is simplified to only contain methane. Both $\dot{V}_{air}$ and $\dot{V}_{NG}$ are calculated from the measured mass flows of air $\dot{m}_{air}$ and fuel $\dot{m}_{NG}$ as well as the temperature T_{intake} and static pressure p_{intake} in the intake port. Since $\dot{V}_{ref}$ is assumed to remain constant, the change in $\dot{V}_{air}$ and $\dot{V}_{NG}$ can be entirely ascribed to volume flow of EGR $\dot{V}_{EGR}$, following to Eq. (4-5):

$$\dot{V}_{EGR} = \dot{V}_{ref} - \dot{V}_{air} - \dot{V}_{NG} \tag{4-5}$$

The mass flow of the exhaust gas recirculated $\dot{m}_{EGR}$ follows form the product of its volume flow $\dot{V}_{EGR}$ and density ρ_{EGR}:

$$\dot{m}_{EGR} = \dot{V}_{EGR} \cdot \rho_{EGR} \tag{4-6}$$

The density of the exhaust gas is the sum of each component's partial density, which can be calculated from its temperature and partial pressure. According to Dalton's law, the pressure of an ideal gas mixture, here measured at the intake port p_{intake}, equals to the sum of its component's partial pressure p_i [13]:

$$p_{intake} = \sum_{i=1}^{n} p_i \tag{4-7}$$

The partial pressure of a species follows from the product of mole fraction x_i and the absolute pressure:

$$p_i = p_{intake} \cdot x_i \tag{4-8}$$

The mass flows of fuel and air and the concentrations from the exhaust gas analysis enable the calculation of the mole fraction of each component by applying stoichiometry. Since exhaust gas contains usually less than 1 % emissions, the model assumes that it consists only of H_2O, O_2, CO_2 and N_2. The density of the exhaust gas ρ_{EGR} results then to:

$$\rho_{EGR} = \rho_{O_2} + \rho_{H_2O} + \rho_{CO_2} + \rho_{N_2} \tag{4-9}$$

To calculate the respective partial densities as function of temperature (50 − 160 °C) and pressure (0.9 − 1.2 bar), high-order polynomial regressions were derived using Engineering Equation Solver (EES). The Temperature of the exhaust gas recycled short before it is added to the intake port T_{EGR} and the static pressure of the intake port p_{intake} were used as input data.

Engine trials proved that the sensitivity of the reference volume flow to CA50 and IMEP is small. Besides, 1D CFD calculations using a detailed engine model proved this a valid approach for unthrottled operation at constant engine speed, leading to a maximum error lower than 0.5 %-points for an EGR rate of $x_{EGR} = 25$ %.

4.3 1D CFD Engine Model

1D CFD (Computational Fluid Dynamics) engine simulation has become an established numerical tool in nowadays engine development. Given the capability of accurately calculating engine flow behaviour and performance, it was used in this work not only to analyse Lean-Miller-EGR working process but also to find engine configurations for later engine testing. To this end, a detailed 1D CFD engine model of the cogeneration engine was created using the '*Virtual Engine Simulation Tool*' AVL BOOST. It was adjusted to the reference operating point (IMEP = 6.35 bar, λ = 1.57, CA50 ≈ 19 °CA ATDC) and validated for several operating points of varying IMEP, CA50 and λ. The gas path of the test bed engine was modelled in detail according to CAD data. The swirl coefficients of the intake and the flow coefficients of the intake and exhaust ports were determined in either flow directions on a flow bench (see Annex A.4).

The build-up process of the 1D CFD model in Figure 4-6 shows a comparison between the measured and simulated p-V diagram of the reference operating point. It further reveals the deviation δ of characteristic engine operating parameters such as indicated mean effective pressure (IMEP), indicated specific fuel consumption (ISFC), NO_x emissions (in ppm) and mean mixture mass flow ($\dot{m}$). While the simulated and measured mass flows are in good agreement, the model tends to slightly overpredict IMEP, causing mildly lower ISFC and higher NO_x emissions.
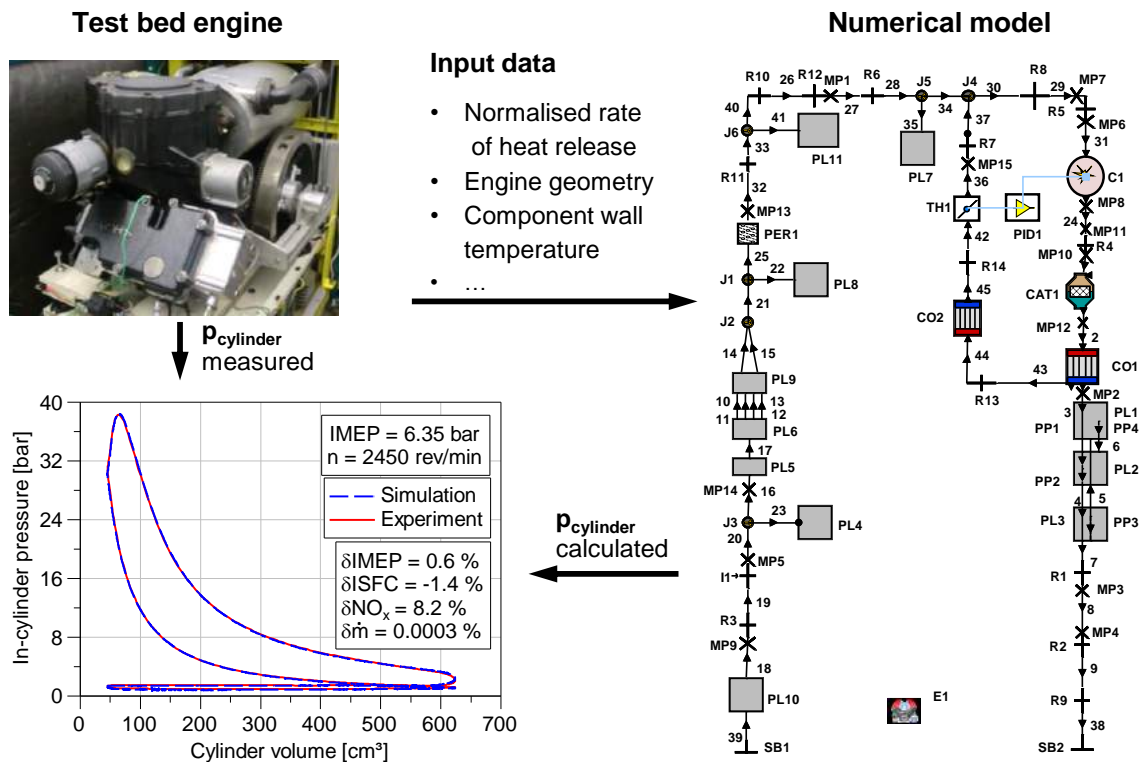

Figure 4-6: Build-up and validation process of the 1D CFD model

The combustion process was realised by employing a normalised two-zone gross rate of heat release ($ROHR_g$) deduced from the measured in-cylinder pressure trace of the reference operating point. It divides the cylinder volume into burnt and unburnt zone as the calculation of NO emissions based on the work of Pattas and Häfner [112] requires. The model utilises a super-extended Zeldovich mechanism that comprises six reactions. Reactions 1 to 3 stand for the thermal NO formation corresponding to Eq. (2-7) to (2-9), while reactions 4 to 6 account for NO caused by Nitrous Oxide mechanism (cf. 2.2.1). The model assumes that NO formation takes place in the gas volume behind the flame front. The final rate of NO production/decomposition is calculated by a differential equation (Eq. (4-10))

$$\frac{d(NO)}{dt} = 2 \cdot (1 - \beta^2) \cdot \left[\frac{r_1}{1 + \beta \cdot \dfrac{r_1}{r_2 + r_3}} + \frac{r_4}{1 + \beta \cdot \dfrac{r_4}{r_5 + r_6}} \right] \qquad (4\text{-}10)$$

where r_i ($i = 1...6$) are the reaction rates and β relates the actual NO concentration to the equilibrium concentration. A detailed description of the NO model is given in [112]. It is worth mentioning that the simulation neglects the reaction from NO to NO_2, particularly occurring at low temperatures. However, because of the fact that the entire NO eventually converts to NO_2 under ambient conditions, specific NO_x emissions in g/kWh are calculated using the molar mass of NO_2. The calculation of the NO_x requires modifying software-integrated adjustment parameters. These were adapted for operating points of varying IMEP, λ and CA50 shown in Figure 4-7 (left).
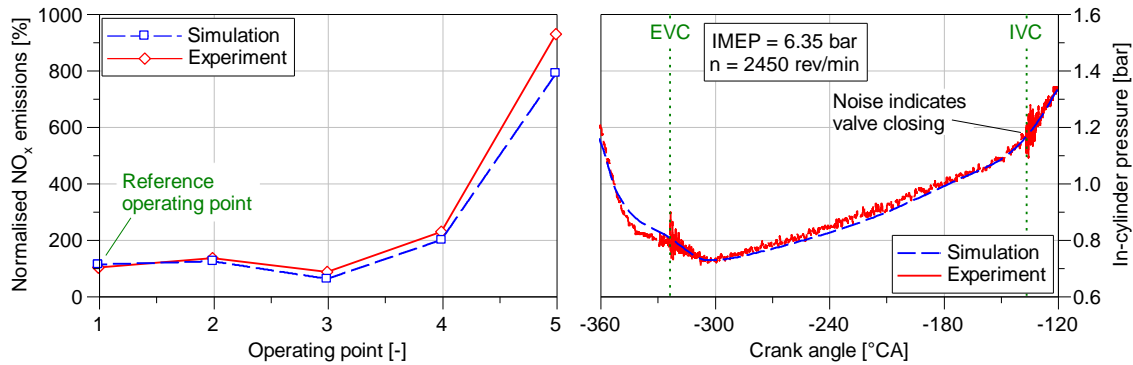

Figure 4-7: Measured and simulated NO_x emissions (normalised to reference operating point in ppm) (left) and in-cylinder pressure trace over crank angle between EVC and IVC (right)

Valve clearance not only changes over engine lifetime but also depends on engine operating conditions due to its sensitivity to temperature, particularly on the exhaust side. It notably influences the pressure trace in the intake and exhaust port and affects the gas exchange as results from 1D CFD calculations show. When comparing an engine configuration with a valve clearance in factory settings (exhaust/intake 0.6/0.3 mm) to one without valve clearance at same normalised $ROHR_g$ and constant λ, IMEP varies between 6.38 and 6.00 bar. A fairly realistic valve clearance during engine operation can be determined by analysing the in-cylinder pressure signal with respect to a sudden noise occurring as the

valves impinge upon the valve seat (see Figure 4-7, right). Given the exact valve closing timing while assuming that the valve train components do not deform as the engine is running, the valve clearance can be readily inferred from the static valve lift curve.

The measured and calculated intake (left) and exhaust (right) pressure trace of the reference operating point in Figure 4-8 shows that the model calculates both pressure traces very well in spite of a highly complex gas path (cf. Figure 4-2). On the intake side, only a slight shift of the amplitudes over the cycle occurs after the intake valve closes (IVC). The prediction of the exhaust pressure is also satisfying although the geometry of the heat exchanger, containing of 6 helix pipes of differing lengths, was challenging to approximate into the 1D CFD model.
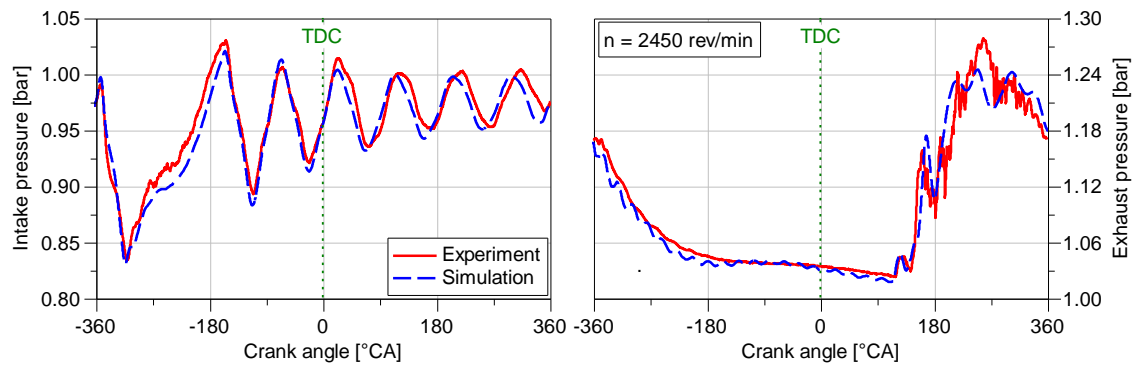

Figure 4-8: Measured and calculated intake (left) and exhaust (right) pressure trace over crank angle of the reference operating point (n — 2450 rev/min)

Engine settings of the 1D CFD model, such as compression ratio or valve timing, need to be modified when studying the Lean-Miller-EGR working process. This would evidently influence combustion process parameters as well as system wall temperatures in actual engine operation. Nevertheless, the created 1D model is expected to give sufficiently accurate predictions for conducting a preparatory study, despite being subject to the following key assumptions:

- A constant normalised ROHRg profile (const. CA50) is employed.
- Temperature levels of all components, including cylinder wall, piston and cylinder head, remain unchanged.
- Wall heat losses are calculated according to the approach of Woschni described in Section 3.2.2.
- Losses from imperfect combustion were accounted for as the ROHRg was derived. No additional losses are considered as mixture composition is varied.
- FMEP and valve clearance are constant.

4.4 3D CFD Model for Gas Exchange Calculation

In order to analyse the charge motion for the valve timings studied, 3D CFD calculations

are carried out using the commercial software AVL FIRE. The fluid domain, created from CAD data, consists of intake and exhaust port, combustion chamber and prechamber. It is discretised into a grid of finite volumes to form the original shape that allows solving the conservation equations in any cell and enables the analysis of the global flow conditions. The calculation begins towards the end of the exhaust stroke, namely at 40 °CA BTDC, and ends after compression at TDC, resulting in four calculation intervals shown, with their respective mesh, in Figure 4-9.

| Exhaust stroke | Valve overlap | Intake stroke | Comrpession stroke |
| -40 °CA to IVO | IVO to EVC | EVC to IVC | IVC to BDC |
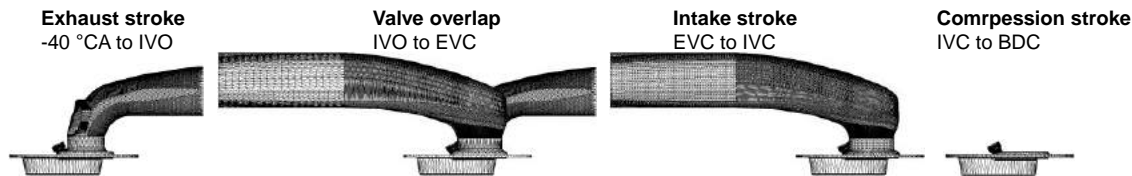
Figure 4-9: Meshes of the four calculation intervals

Valve lift curves and piston position over crank angle, calculated from geometrical relations, govern mesh movement. The created meshes, activated depending on the current time step, result to a minimum and maximum number of cells of 221.000 and 765.000, respectively, at a cell size of 2 mm. The mesh resolution was increased for sections of high flow velocities such as the area between intake valve and seat, the prechamber and its orifices. The initial and boundary conditions for the intake and exhaust port, mean temperature and pressure over crank angle, are taken from test bed measurements. Calculated cylinder temperature and pressure level from 1D CFD are assigned as initial cylinder conditions. Component wall temperatures were set equal to those in the 1D CFD model. Turbulence is calculated using the implemented k-ζ-f model, which was specifically developed for engine calculation, thus being more robust and more accurate than the prevailing k-ε model [88, 152]. More detailed information on the 3D CFD calculation model is given in [139].

5 1D-Study of Lean-Miller-EGR Working Process

The idealised gas exchange assumed in the studies in Section 3.2 leads to the fact that only the absolute offset to IVC respective to BDC affect cycle parameters. It is therefore not possible to differentiate between early and late Miller cycle. The detailed 1D-CFD model of test bed engine I, on the other hand, allows simulating a far more realistic engine behaviour, including the prediction gas dynamic effects. The model was therefore used to carry out a study that primarily aims at understanding the differences between both early and late Miller cycle and finding comparable configurations for engine testing. It also shows the potential and challenges of the Lean-Miller-EGR working process to improve the ISFC-NO_x trade-off at constant IMEP. To ensure comparability of the different Miller configurations to the baseline engine, the effective compression ratio was kept constant. All calculations were carried out at constant engine speed of n = 2450 rev/min and a constant normalised $ROHR_g$ profile, leading to a fixed combustion phasing of CA50 = 18.5 °CA ATDC. This avoids that influences of differing combustion characteristics distort the comparison of varying configurations and puts the focus on analysing the effects of gas dynamics. Motivated by different definitions of the effective compression ratio, the last section compares the method applied to those in literature (cf. Section 2.4.5).

5.1 Implementation of Miller Cycle into the Model

Ideal early and late Miller cycle is defined by IVC before or after BDC, respectively. The former leads to mixture expansion between IVC and BDC, while the latter causes a reverse flow of in-cylinder charge into the intake section after the piston passes BDC. Both effects are characteristic for each approach but only the ideal definition of early Miller IVC is still

73

applicable under actual engine operating conditions. Configurations for which in-cylinder charge neither expands during the intake stroke nor notably flows back into the intake section before the intake valve closes, correspond, to the author's definition, to the behaviour of the conventional Otto cycle and are therefore not investigated.

The Miller valve lift curves are designed by modifying IVC of the series valve lift curve, while maintaining its peak valve lift to achieve high charging efficiency. Taking over the opening and closing ramp of the baseline, ensures similar closing speed of the valves as well as same sensitivity of the opening and closing events to valve clearance. Intake valve opening (IVO) and exhaust valve closing (EVC) remain unchanged, to achieve same valve overlap and, hence, similar residual gas fraction of the in-cylinder charge that significantly influences charging efficiency, engine efficiency and emissions [57, 100]. Figure 5-1 (left) depicts the array of investigated intake valve lift curves, including that of the baseline engine. The modification of IVC under the defined constraints alters the shape of the valve lift, leading to higher/lower valve speeds and accelerations for early/late Miller valve timings. It affects the required valve spring force to avoid a lift-off between valve cam and tappet, which was the limiting factor for further advancing IVC. Static valve train calculations proved that the earliest IVC that still complies with the limit (given by the valve spring specifications) amounts to -10 °CA BBDC. To keep the effective compression ratio of the baseline engine, calculated to $r_{c,eff} = 13.27$, the geometrical compression ratio r_{geo} was adjusted for varying valve timing (see table in Figure 5-1, right) by reducing V_{TDC} at constant piston stroke. The maximum deviation of the effective compression ratio $\Delta r_{c,eff}$ across all investigated configurations amounts to +/- 0.025. Because of yet unknown piston design, the piston area remained constant as the geometrical compression ratio was increased, thus likely overpredicting wall heat losses.

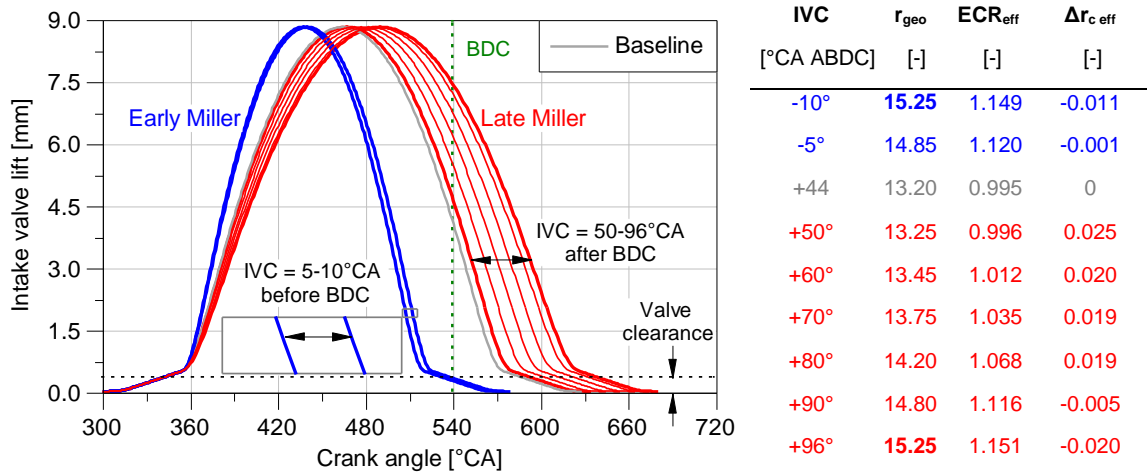| IVC	r_{geo}	ECR_{eff}	$\Delta r_{c\,eff}$
[°CA ABDC]	[-]	[-]	[-]
-10°	15.25	1.149	-0.011
-5°	14.85	1.120	-0.001
+44	13.20	0.995	0
+50°	13.25	0.996	0.025
+60°	13.45	1.012	0.020
+70°	13.75	1.035	0.019
+80°	14.20	1.068	0.019
+90°	14.80	1.116	-0.005
+96°	15.25	1.151	-0.020

Figure 5-1: Intake valve lift curve of the baseline and Miller configurations (left); IVC, geometrical compression ratio, expansion/compression ratio and the deviation of the effective compression ratio (right)

The highest geometrical compression ratio of all cases, determined for IVC = 96 and -10 °CA ABDC, amounts to $r_{geo} = 15.25$, leading to the highest expansion/compression

ratios of $ECR_{eff} = 1.15$ (−/- 0.001) analysed in this study. The small difference in expansion/compression ratio of $\Delta ECR_{eff} = 0.002$ between both extreme valve timings, stems from minor deviation in the effective compression ratios.

5.2 Miller Cycle in Lean-burn Operation

Engine configurations with the valve lift curves from Figure 5-1 (left) are first analysed at constant relative air-fuel ratio of $\lambda = 1.57$ without EGR. Along with a constant normalised $ROHR_g$ profile, this enables an isolated analysis of the influence of IVC at same $r_{c,eff}$. The residual gas fraction was found to be negligible across all configuration by virtue of taking over the valve overlap of the baseline engine.

Figure 5-2 displays selected simulation data as function of intake valve closing timing IVC. Charging efficiency decreases with advancing or retarding IVC either due to shorter intake valve opening duration (early Miller) or mixture that is forced to flow back into the intake section during the compression stroke (late Miller). IMEP decreases in response to the lower mass of in-cylinder charge at same λ, while ISFC improves owing to increased ECR_{eff}. For the earliest and latest Miller configuration ($ECR_{eff} = 1.15$), compression work $W_{compression}$ is reduced by about 13 % compared to the baseline engine. The augmented ECR_{eff} expands the mixture to a lower pressure and temperature level. Combined with a smaller mass flow, the enthalpy flow out of the engine decreases. A smaller in-cylinder charge additionally favours gas exchange as reflected in a lower pumping work. Miller cycle improves thermal efficiency, yet the engine cannot exploit the benefit due to the worsened IMEP/FMEP ratio that, in turn, increases brake specific fuel consumption BSFC. Despite a constant effective compression ratio, the peak combustion temperature T_{max} and pressure p_{max} decrease due to falling mass of fuel. As a result of a lower pressure and temperature history, both IMEP and NO_x emissions drop. However, the wall heat losses normalised to the added fuel energy Q_{wall} increase with ECR_{eff} due to the rising A/V ratio. A major difference between both valve timing strategies is observed for mixture temperature in the intake port T_{intake}. For the near-optimal intake valve closing regarding charging efficiency of the baseline, 0.6 % of the maximum in-cylinder charge flows back into the intake port during the compression stroke. Minor changes in IVC have a significant effect on T_{intake}: Retarding the baseline value from IVC = 44 to 50 °CA ABDC, for instance, leads to an increase of T_{intake} by 4.6 K. The mass affected by the reverse flow rises notably as IVC is further retarded, yet the gradient of T_{intake} diminishes beyond 70 °CA ABDC. This can be explained by a constant defined intake port wall temperature of 80 °C that cools mixtures with temperatures above. While early Miller cycle experiences no reverse flow, the proportion of mass that flows out of the cylinder into the intake port increases to more than 15 % for most retarded Miller valve timing, leading to a temperature difference in the intake port of almost 45 °C.
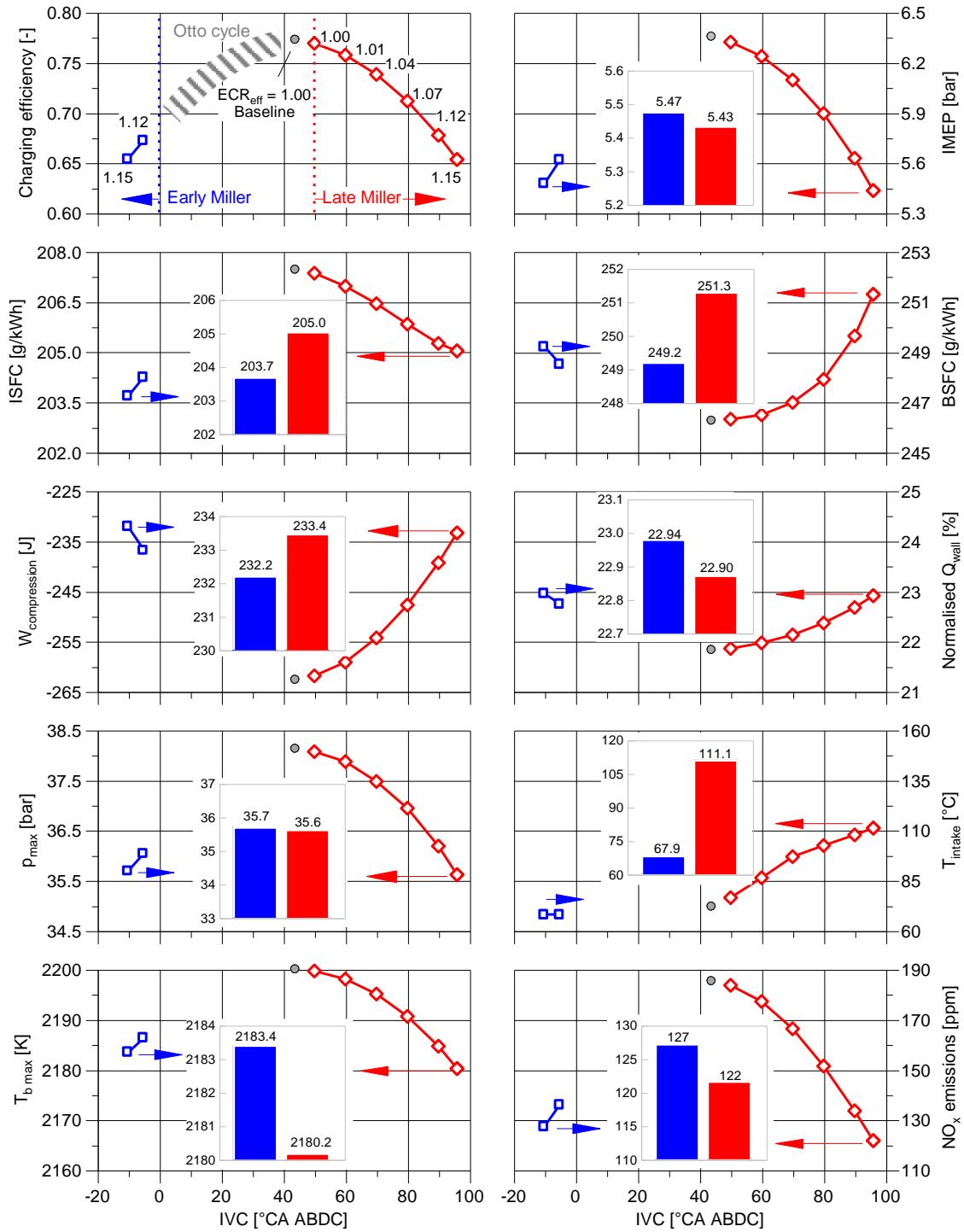
Figure 5-2: Charging efficiency, IMEP, ISFC, BSFC, $W_{compression}$, normalised Q_{wall}, p_{max}, T_{intake}, $T_{b\,max}$ and NO$_x$ emissions over IVC for baseline and Miller configurations ($\lambda = 1.57$, n = 2450 rev/min)

A direct comparison between early and late Miller cycle (IVC = -10°/96 °CA ABDC) of same expansion/compression ratio of $ECR_{eff} = 1.15$ highlights the key differences between both valve timing strategies that achieve the same mass of in-cylinder charge. The root cause of lower ISFC for early Miller cycle becomes obvious when analysing the p-V diagram of both Miller configurations (see Figure 5-3, left). Both cycles show an almost coherent

in-cylinder pressure while the valves are closed. This emphasises the applicability of the presented method to determine the effective compression ratio. The first differences between both p-V plots occur after the exhaust stroke, namely at IVO, where the higher slope of the early Miller valve lift curve causes a larger effective flow area at the beginning of the intake stroke. This reduces the frictional pressure losses between valve seat and disc when the mixture is inducted. An arriving pressure wave short before IVO further enhances the benefit (see Figure 5-3, right), which, however, it is not to be considered as characteristic of either cycles, since the pressure pulsations in unthrottled engine operation for a given IVC and engine speed primarily depend on intake path geometry.
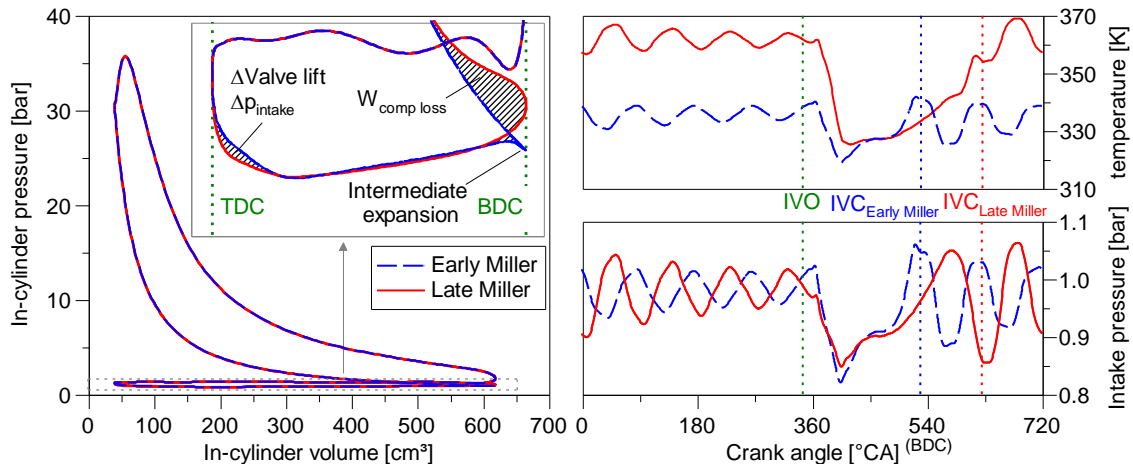
Figure 5-3: p-V diagram (left) and intake pressure and temperature over crank angle (right) for early and late Miller cycle of same compression expansion ratio (ECR_{eff} = 1.15, TDC at 0/360/720 °CA, λ = 1.57)

In fact, the main differences between both engine setups can be observed shortly before/after the compression stroke commences: While early Miller exhibits an intermediate expansion, a pronounced ram effect takes place for late Miller cycle. The ram effect is followed by a notable reverse flow that causes additional piston work without generating any benefit. The loss that occurs in this context is known as loss from imperfect compression $W_{comp loss}$. It is calculated, similar to $r_{c,eff}$ (see Section 3.3), by a polytropic calculation starting from IVC towards BDC, with the crucial distinction that the polytropic process ends at BDC and not at ambient pressure. The area enveloped by the pressure trace and the polytropic curve visualises the loss due to imperfect compression [133, 170, 175]. The aforementioned similarities between the method to determine $r_{c,eff}$ and the losses in compression lead to a polytropic curve that almost matches with the pressure trace of early Miller. Therefore, the polytropic change to determine $W_{comp loss}$ is not shown. The losses in compression $W_{comp loss}$ plays an important role when splitting IMEP into its components gross indicated mean effective pressure $IMEP_g$ and pumping mean effective pressure PMEP. These are calculated from the pressure-volume integral of the compression and expansion stroke as well as the exhaust and intake stroke, respectively, and eventually divided by the displacement volume V_d (see Table 5-1). As a result of balancing from BDC to BDC, PMEP

of both Miller cycles are almost identical. The losses in compression are entirely ascribed to IMEP$_g$, leading to a deficit of 0.04 bar compared to early Miller cycle. Since $W_{comploss}$ occurs during gas exchange, literature suggests to impute it to PMEP when analysing high and low pressure loop of configurations with IVC after BDC [80, 95]. In order to maintain the balance of work, the same amount must be added to IMEP$_g$, leading to gross results that are more representative. ISFC$_g$, for example, decreases with the corrected balancing method for the given late Miller configuration by 0.6 g/kWh. Note that only late Miller cycle requires this balancing method, since neither the early Miller nor the baseline setup experience a considerable reverse flow during the compression stroke.

Table 5-1: IMEP$_g$ and PMEP for different balancing methods (ECR_{eff} = 1.15, λ = 1.57) (combustion TDC at 0/720 °CA)

Parameter (all in bar)	Formula	Equation	Early Miller	Late Miller
IMEP	IMEP$_g$ + PMEP	(5-1)	5.47	5.43
IMEP$_g$ (BDC to BDC)	$\dfrac{1}{V_d}\left(\displaystyle\int_0^{180} p\ dV + \int_{540}^{720} p\ dV\right)$	(5-2)	5.91	5.87
PMEP (BDC to BDC)	$\dfrac{1}{V_d}\displaystyle\int_{180}^{540} p\ dV$	(5-3)	-0.44	-0.44
IMEP$_g$ ($- W_{comploss}$)	$\dfrac{1}{V_d}\left(\displaystyle\int_0^{180} p\ dV + \int_{540}^{720} p\ dV - W_{comploss}\right)$	(5-4)	5.91	5.91
PMEP ($- W_{comploss}$)	$\dfrac{1}{V_d}\left(\displaystyle\int_{180}^{540} p\ dV + W_{comploss}\right)$	(5-5)	-0.44	-0.48

To understand why $T_{b,\,m,n}$, p_{max} and NO_x emissions are similar for both configurations despite markedly lower T_{intake} for early Miller, in-cylinder temperature, pressure and mass flow into the cylinder over crank angle during the gas exchange are further analysed (see Figure 5-4). Starting from identical IVO, a small amount of exhaust gas enters the intake port as a result of the pressure difference to the cylinder shortly before the mixture is aspirated. The mass flow of both Miller designs peaks around the middle of the intake stroke and decreases right after. The intake valve of early Miller is already closing again, causing a sharp decrease of mass flow that ends at IVC. For late Miller cycle, on the other hand, the mass flow into the combustion chamber continues until the piston passes approximately 20 °CA ABDC. Subsequently, the reverse flow takes place, reducing the mass of in-cylinder charge by more than 15 % and resulting to the same mass of charge at IVC as early Miller cycle. Since the temperature of the mass that exits the cylinder during the compression stroke varies over the compression stroke from 390 to 450 K, T_{intake} of late Miller increases notably. Consequently, the in-cylinder charge aspirated reveals a consist-

ently higher temperature during the intake stroke. Both configurations show similar pressure as mixture is aspirated until the piston reaches about 500 °CA, at which the onset of the intermediate expansion becomes visible. It causes a temperature drop of 3 K, whereas the temperature of late Miller increases consistently. Temperature and pressure of both cycles approach each other during the compression stroke and meet at almost identical values at IVC of late Miller valve timing. This arises from the method applied to maintain the effective compression ratio constant as it becomes clear when adding the polytropic process for late Miller to Figure 5-4 (bottom right).
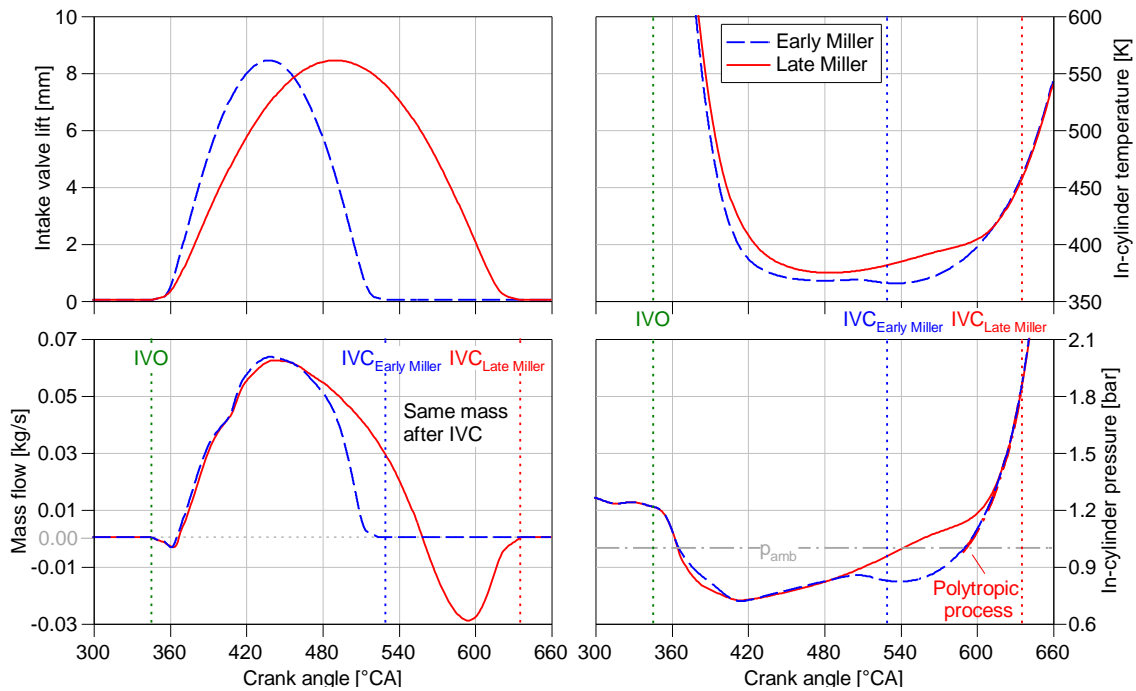
Figure 5-4: Intake valve lift curve (top left), mass flow (bottom left), in-cylinder temperature (top right) and pressure (bottom right) over crank angle for early and late Miller vale timings of $ECR_{eff} = 1.15$

5.3 Miller Cycle in Lean-burn Operation with EGR

In an attempt to take advantage of the lower ISFC achieved through Miller cycle effectively, losses in IMEP with respect to the reference operating point need to be compensated without increasing NO_x emissions. Therefore, EGR is added as second diluent to the air-fuel mixture, forming the Lean-Miller-EGR working process. Replacing a part of the excess air with exhaust gas in order to increase the heat capacity of the mixture is expected to enable engine operation at higher IMEP but same NO_x emissions. Literature suggests [162, 163, 173] that the effect on the rate of heat release of a lean-burn combustion is little for EGR rates up to $x_{EGR} = 10\%$ when adjusting the amount of fuel and/or advancing the ignition timing. Since only small EGR rates are expected to be necessary to lift IMEP to its baseline value, using a constant normalised $ROHR_g$ profile deemed to be an acceptable assumption. For this purpose, the mass of fuel and the added EGR rate were adjusted until

meeting both threshold values of IMEP = 6.35 bar and of 1.2 g/kWh in indicated specific NO_x emissions. The addition of EGR affect the thermodynamic properties of the in-cylinder charge and the pressure pulsations within the intake port but calculations showed that the influence on the effective compression ratio $r_{c,eff}$ is marginal.

It is clear from theoretical considerations that it is conducive to add the exhaust gas at the lowest temperature possible (in due consideration of condensation) for obtaining highest mixture density. However, increasing system costs and complexity when employing an EGR cooler, encouraged to assess engine operation if the exhaust gas is only cooled by the exhaust gas heat exchanger of the CHP unit as first approach (semi-cooled EGR). For the second approach, engine operation using an additional EGR cooler was analysed. With respect to the capabilities of the EGR cooler used in experiments, EGR temperature is controlled to $T_{EGR} = 80$ °C (cooled EGR). Figure 5-5 (left) depicts BSFC of all cycle configurations studied as function of ECR_{eff} at constant NO_x emissions and IMEP for semi-cooled and cooled EGR. Expansion/compression ratios higher 1.11 combined with low EGR rates improve BSFC, regardless of the IVC strategy employed and EGR temperature. As with the results in lean-burn operation at $\lambda = 1.57$, early Miller holds an advantage in BSFC over late Miller valve timing due to a more favourable gas exchange. Both valve timing strategies require similar EGR rates x_{EGR} to comply with the threshold NO_x emission level (see Figure 5-5, right). The higher density at lower EGR temperature of $T_{EGR} = 80$ °C evidently reduces the required EGR rate. As a results of more favourable mixture properties (i.e. higher γ), the penalty in ideal engine efficiency decreases, leading to a lower BSFC. The largest benefit of 2.7 g/kWh is predicted for engine operation with early Miller valve timing and cooled EGR. While cooled EGR improves engine efficiency over the entire ECR_{eff} range, the semi-cooled approach causes higher fuel consumption for ECR_{eff} lower than 1.07 (late Miller). In this case, the drawback in ideal engine efficiency caused by less favourable mixture properties outweighs the benefit from increasing ECR_{eff}.
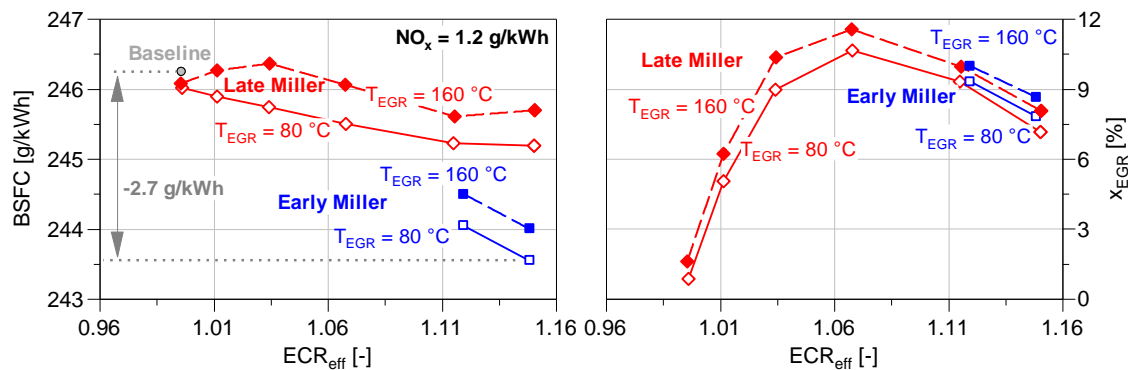

Figure 5-5: BSFC (left) and EGR rate (right) over ECR_{eff} for cooled and semi-cooled EGR at constant NO_x emissions (n = 2450 rev/min, IMEP = 6.35 bar, NO_x = 1.2 g/kWh)

One might expect that the EGR rate increase consistently with the expansion/compression ratio rather than decreasing again after the maximum of $x_{EGR} = 9.7$ % ($T_{EGR} = 80$ °C) and

10.5 % ($T_{EGR} = 160$ °C) at $ECR_{eff} = 1.07$. To sharpen the understanding of this trend, the interaction between dilution ratio D, mass of in-cylinder charge m_{charge}, EGR rate x_{EGR} and the specific heat capacity c_v of the exhaust gas for varying ECR_{eff} is reviewed. Figure 5-6 shows the respective parameters for late Miller valve timing at an EGR temperature of $T_{EGR} = 80$ °C. The falling mass of in-cylinder charge with increasing ECR_{eff} not only requires lower dilution ratios to keep IMEP constant, it also reduces the absolute heat capacity that absorbs the released heat during combustion. The dilution ratio D decreases with increasing ECR_{eff} leading to higher H_2O and CO_2 fractions in the exhaust gas that increase its c_v. However, since the influence of enhanced fuel energy outweighs the rising specific heat capacity regarding combustion temperature, another effect must cause the inflection point of the EGR rate. For that purpose, it is worthwhile to note that the determination of the specific NO_x emissions involves the measured NO_x fraction in ppm and the engine-out mass flow as well as the molar masses of NO_2 and the exhaust gas. Because the molar mass of the exhaust gas varies only slightly within the investigated operated range and that of NO_2 is constant, the NO_x fraction and engine-out mass flow mainly govern the indicated specific NO_x emissions. Both increasing ECR_{eff} and EGR rate, indeed, reduce the engine-out mass flow, thus enabling the engine to emit higher NO_x in ppm at constant NO_x in g/kWh. For $ECR_{eff} > 1.07$, the reduction of the exhaust gas mass flow outweighs the increase of NO_x fraction and, in turn, the EGR rate can be reduced again.
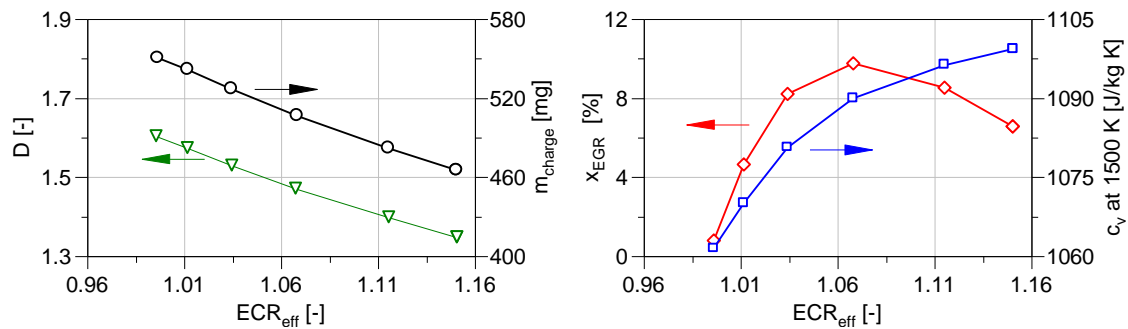

Figure 5-6: Dilution ratio D and mass of in-cylinder charge m_{charge} (left); EGR rate x_{EGR} and specific heat capacity c_v of the exhaust gas at 1500 K (right) over ECR_{eff} for late Miller valve timing at $T_{EGR} = 80$ °C (IMEP = 6.35 bar)

The interaction between volumetric NO_x emissions (ppm) and engine-out mass flow at constant specific NO_x emissions (g/kWh) becomes clear when comparing characteristic engine values of the baseline engine and the Lean-Miller-EGR working process of $ECR_{eff} = 1.15$ with cooled EGR at constant IMEP of 6.35 bar (see Figure 5-7, left). Both Miller setups reach higher peak combustion temperatures that increase NO_x emissions in ppm. The increasing NO_x fraction still leads to constant specific NO_x emissions in g/kWh owing to the reduced engine-out mass flow. As a result of the enhanced T_{max} and a higher A/V ratio, the Miller configurations experience higher wall heat losses Q_{wall}. Higher Q_{wall} combined with increasing losses in ideal engine efficiency caused by EGR, almost cancel

out the benefit in ISFC$_g$ through enhancing $ECR_{\textit{eff}}$. Nevertheless, Miller cycle combined with cooled EGR still improves ISFC at constant IMEP and FMEP, leading to lower BSFC compared to the baseline engine. The analysis of the 3 configurations at IMEP = 6.35 bar in the p-V diagram in Figure 5-7 (right) illustrates that both Miller valve timings favour gas exchange with reduced PMEP by 13.71 % for early and 5.1 % for late Miller IVC. For this reason, both valve timing strategies require lower IMEP$_g$ to achieve the same IMEP as the baseline. The potential is lower for late Miller valve timing due to the reverse flow that causes a $W_{comp,loss}$. Therefore, both fuel consumption and EGR rate increase for meeting the threshold values in NO$_x$ emissions and IMEP compared with early Miller.
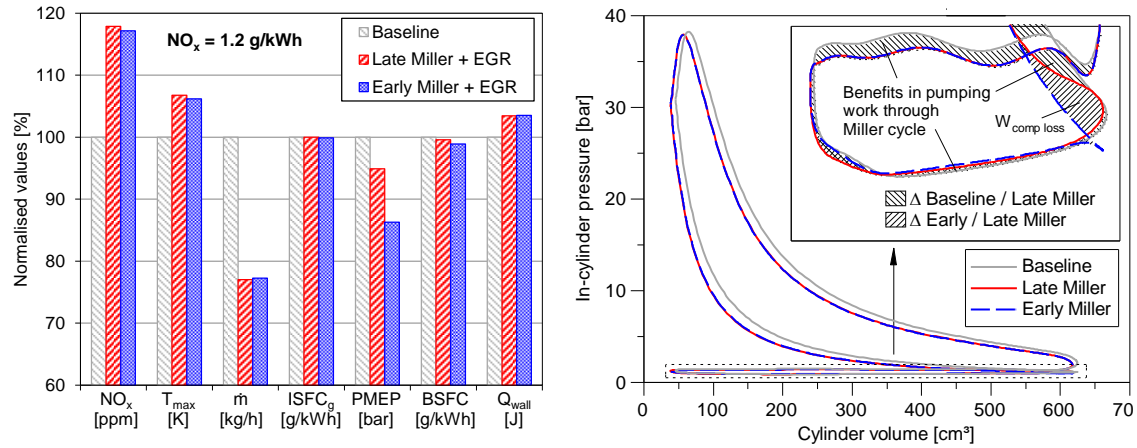
Figure 5-7: Normalised NO$_x$ emissions in ppm, T_{max}, engine-out mass flow, ISFC$_g$, PMEP, BSFC and Q_{wall} for baseline and both Miller configurations with cooled EGR (left); p-V diagram of baseline and early/late Miller cycle with cooled EGR at same IMEP and NO$_x$ emissions in g/kWh (right)

The findings indicate that $ECR_{\textit{eff}} = 1.15$, realised through intake valve closings of IVC = -10 °CA or 96 °CA ABDC and a compression ratio of $r_{geo} = 15.25$, lead to highest engine efficiency for both Miller strategies. The setups are selected for a direct comparison, which is one of the main objectives of this thesis. In the remainder of this work, the respective configurations are simply termed as early and late Miller cycle.

5.4 Comparison of Different Methods to Assess the Effective Compression Ratio

The applied method to hold $r_{c,eff}$ constant leads to early and late Miller configurations with almost identical pressure traces while the valves are closed. Figure 5-8 shows how the effective compression ratio of the baseline and both Miller configuration varies when applying different approaches from literature. It can be seen that the linearisation, presented by He et al. [53], starting from the start of combustion (SOC) to IVC, for the baseline and late Miller, and from SOC to BDC for the early Miller configuration, leads to similar values for all 3 configurations. As a result of considering data of the late compression phase, i.e.

at high temperature, the averaged polytropic exponent is rather low. Consequently, $V_{BDC,eff}$ and therefore $r_{c,eff}$ reach higher values compared to a polytropic backward calculation of variable n, in particular for configurations with late IVC. Applying the approach of Fuku-zawa [46], given by Eq. (2-23), leads to lower absolute values in $r_{c,eff}$. The deviation be-tween the selected Miller and baseline configurations increases but is reduced between the early and late Miller setup. The difference increases when $V_{BDC,eff}$ is defined at the inter-section of the pressure trace during exhaust and compression stroke, as suggested by Löb-bert [80] for part load operation. The method leads to acceptable values for engine setups with different valve timings of same geometrical compression ratio, yet configurations of unequal geometrical compression ratios show notable deviations of up to 0.8. The definition of the effective compression ratio of the ideal cycle, defined in Eq. (2-21), leads to insuffi-cient results between the selected engine setups, again emphasising the necessity of ac-counting for effects of gas dynamics when determining the effective compression ratio.
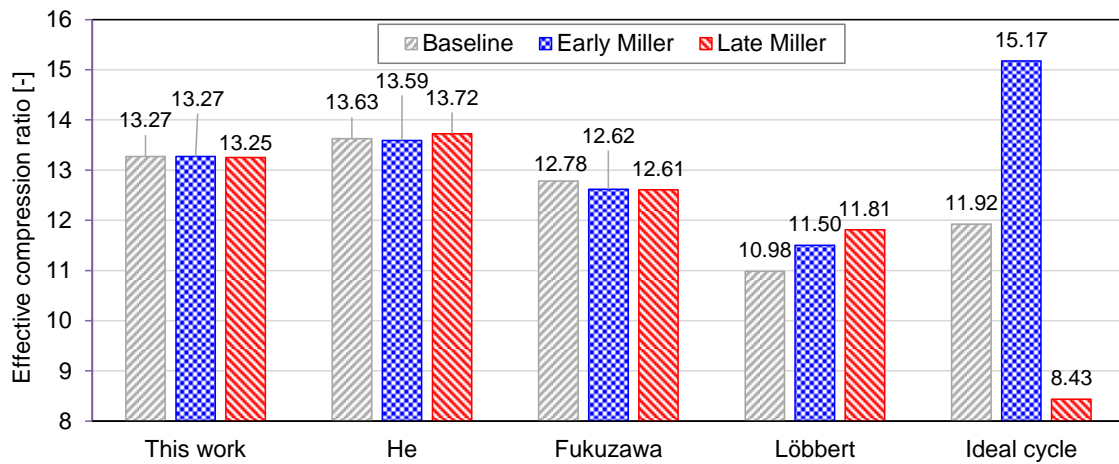

Figure 5-8: Effective compression ratio determined through different methods for Miller ($r_{geo} = 15.25$) and baseline configuration ($r_{geo} = 13.20$) at $\lambda = 1.57$

The impact of the applied method to determine $r_{c,eff}$ becomes even more significant when first calculating the value of the baseline as a threshold, and then the according geometrical compression ratios for the given Miller valve timings using different methods. The peak in-cylinder pressure and temperature in motored engine operation are one of the indicators that are used by Koehler et al. [70] to assess suitability of different methods for determining $r_{c,eff}$. Since in this work the different approaches are evaluated in fired engine operation, the level of pressure and temperature at the start of combustion p_{SOC} and T_{SOC}, occurring at 3 °CA BTDC, are used instead. Figure 5-9 depicts a table that lists p_{SOC} and the p-V diagrams of all configurations at $\lambda = 1.57$. The approach of this work reveals the strongest correlation between $r_{c,eff}$ and p_{SOC} across all engine setups. Both early and late Miller reach slightly lower p_{SOC} than the baseline configuration. Late Miller shows a higher difference to the baseline of -0.31 bar than early Miller, partly caused by a slightly lower $r_{c,eff}$ of 13.25

(cf. table in Figure 5-1, right). Contrary to the approach of this work, Fukuzawa's method [46] calculates r_{geo} that lead to a slightly higher p_{SOC} than the baseline and shows the smallest difference of 0.04 bar between both Miller configurations but larger deviation to the baseline. As the authors suggested, the geometrical compression ratio was adjusted in motored operation first by assuming a ratio of the specific heat capacities of $\gamma = 1.38$. Subsequently, the determined Miller setups were analysed in fired operation. The linearisation, shown by He et al. [53], also gives satisfying results, however, the difference between the calculated r_{geo} of both Miller valve timings increases. While baseline and early Miller exhibit very similar p_{SOC}, they both show a deviation of about 0.5 bar to late Miller. The error further increases when applying the approach of Loebbert [79] due to its sensitivity to pressure pulsations on the intake and exhaust side. The geometrical definition suggests even geometrical compression ratios of 12 and 21.95 that lead to differences in $p_{SOC} > 25$ bar.

Method	p_{SOC} [bar]		
	Early M.	Late M.	Basel.
This work	30.15	30.01	30.32
He	30.28	29.76	30.32
Fukuzawa	30.66	30.62	30.32
Loebbert	28.40	27.57	30.32
Ideal cycle	22.19	47.02	30.32
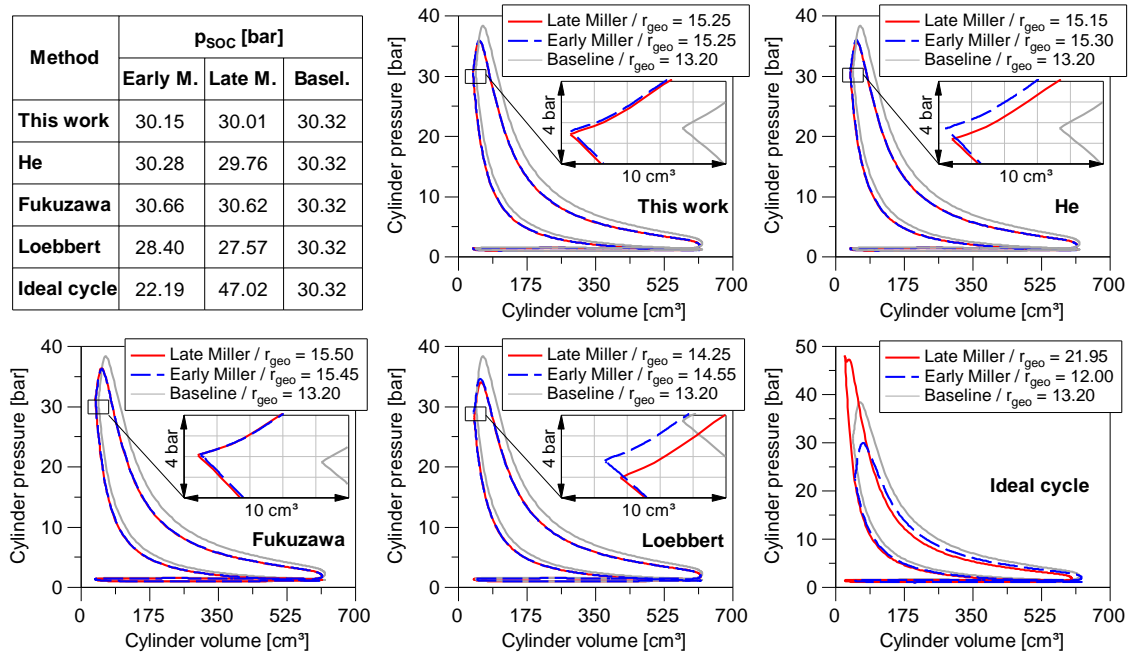
Figure 5-9: p-V diagram of the baseline and the Miller configurations selected at same effective compression ratio by applying different methods ($\lambda = 1.57$)

Next to p_{SOC}, T_{SOC} is an interesting parameter to investigate as it has significant influence on the laminar burning velocity. The deviation between both p_{SOC} and T_{SOC} of the investigated configurations relative to the baseline engine is illustrated in Figure 5-10. The temperature, given in K, is less affected by varying geometrical compression ratios than pressure. The deviation of both parameters correlates well with the exception of the geometrical compression ratios of $r_{geo} = 15.15$ and 15.25. In both cases, p_{SOC} is lower than the baseline, yet a higher T_{SOC} is reached due to reduced wall heat losses during the compression stroke. While the A/V ratio increases for both $r_{geo} = 15.15$ and 15.25, the pressure history from IVC to SOC is below that of the baseline, thus reducing the wall heat transfer coefficient

(cf. Eq. (3-4)). For all remaining cases, increasing or decreasing the geometrical compression ratio uniformly leads to higher or lower temperature and pressure at SOC.
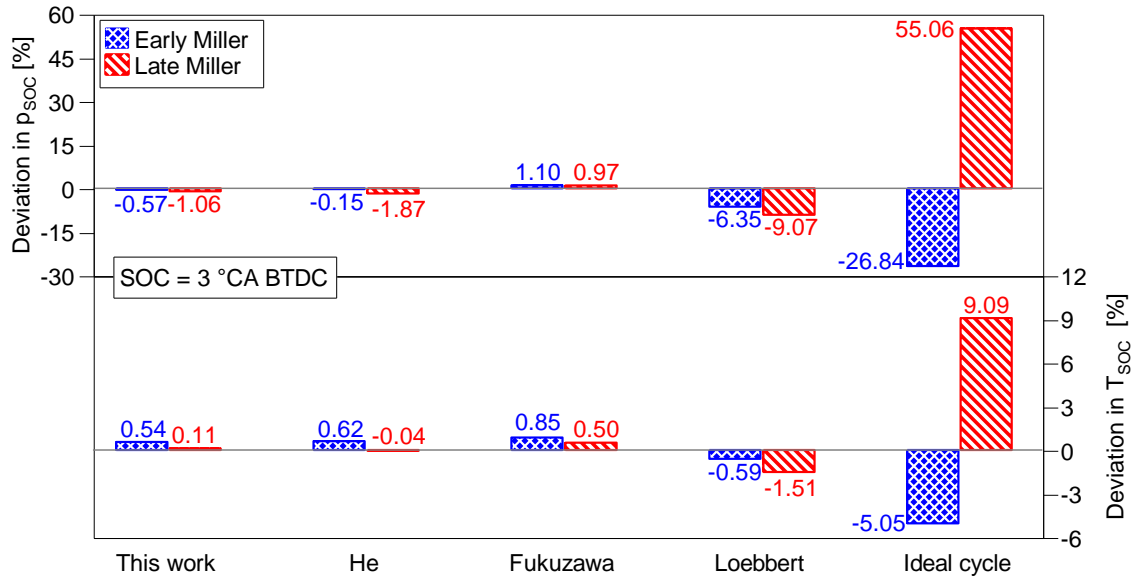

Figure 5-10: Deviation in pressure and temperature at SOC of the baseline and the Miller configurations at same effective compression ratio defined by different methods

The configurations determined by applying the method of this work (presented in Section 3.3) show the smallest deviations in p_{SOC} and T_{SOC} compared to the baseline engine. The approaches suggested by He and Fukuzawa also deliver acceptable results, whereas the one of Löbbert determines non-comparable configurations with respect to thermodynamic conditions at SOC. The definition given for the ideal engine cycle leads to the largest error and is clearly not applicable to actual engine operation.

5.5 Summary and Conclusions of the 1D Study

The aim of the 1D study described in this chapter was to assess the differences between early and late Miller valve timing, to evaluate the potential of the Lean-Miller-EGR working process to improve the ISFC-NO$_x$ trade-off at constant IMEP and to select two configurations for upcoming engine testing. Starting from the baseline configuration, the valve timings were varied while the effective compression ratio was kept constant by adjusting the geometrical compression ratio. The major assumption of this study was the constant normalised ROHR$_g$ profile, derived from the measured in-cylinder pressure trace of the cogeneration engine's reference operating point. The key findings can be summarised as follows:

- The developed method to determine the effective compression ratio, presented in Section 3.3, leads to early and late Miller valve timings that show very similar pressure traces during the span all valves of both cycles are closed. Compared

to other approaches, the presented method leads to thermodynamic conditions at SOC that are most similar to those of the baseline engine.

- The crucial difference between early and late Miller valve timing occurs shortly before BDC, where early Miller experiences an intermediate expansion. Late Miller cycle causes a reverse flow after BDC that also leads to losses in compression work, being the main reason why late Miller shows drawbacks in ISFC for all investigated configurations at same ECR_{eff}.

- Increasing the expansion/compression ratio at constant relative air-fuel ratio to $ECR_{eff} = 1.15$, reduces ISFC by 3.8 and 2.5 g/kWh for early and late Miller valve timing, respectively. The losses in lower charging efficiency decrease IMEP of both Miller configurations, causing a lower IMEP/FMEP ratio and, in turn, higher BSFC.

- The simultaneous addition of fuel and moderate EGR rates ($x_{EGR} < 10$ %) allows both Miller configurations to increase IMEP to 6.35 bar without exceeding the specific NO_x emissions of the baseline engine. A comparison of two EGR temperature levels, namely $T_{EGR} = 80$ °C and 160 °C, shows that the lower EGR temperature is less detrimental to ISFC. For engine operation at $T_{EGR} = 80$ °C, BSFC improves for early and late Miller valve timing by 2.7 and 1.1 g/kWh, respectively. The decreasing mass flow of both Miller cycles enables higher NO_x emission in ppm but constant specific NO_x emissions.

- Two comparable configurations of same effective compression ratio and expansion/compression ratio were found, which are to be manufactured for experimental engine trials.

6 Realisation of the Working Process

This chapter addresses the design of the components required to realise the Miller engine configurations determined in Chapter 5, including the modification of valve timing and piston design.

6.1 Valve Cam Design

The cast iron camshaft of the baseline configuration was replaced with an assembled camshaft prototype that ensures identical valve opening and closing events. In fact, the only difference between both is that the prototype camshaft allows for a simple replacement of the intake valve cam. The valve cam is made of heat-treated alloy steel 42CrMo4 and its running surface was plasma-nitrided with the aim to guarantee sufficient durability. For designing the cams that cause the selected valve timings, early Miller (IVC = -10 °CA ABDC) and late Miller (IVC = 96 °CA ABDC), the commercial software AVL EXCITE Timing Drive was used. It approximates the valve train as multibody model by dividing its components into a series of mass points and/or rigid bodies. These are connected by spring and damping elements (exhibiting stiffness and damping characteristics of each component) as well as joints and bearings. Rotational camshaft speed, specific geometries and the baseline cam profile were assigned to the model, whose build-up process is illustrated in Figure 6-1. The model calculates the dynamic system behaviour, including lift, velocity, acceleration and the force of the single valve train components over cam angle. Furthermore, the occurring Hertzian pressure between cam and tappet, one of the decisive parameters in cam design regarding durability, can be determined. Peaking occurs at the highest

cam lift due to the maximum valve spring force coupled with the smallest valve cam curvature.
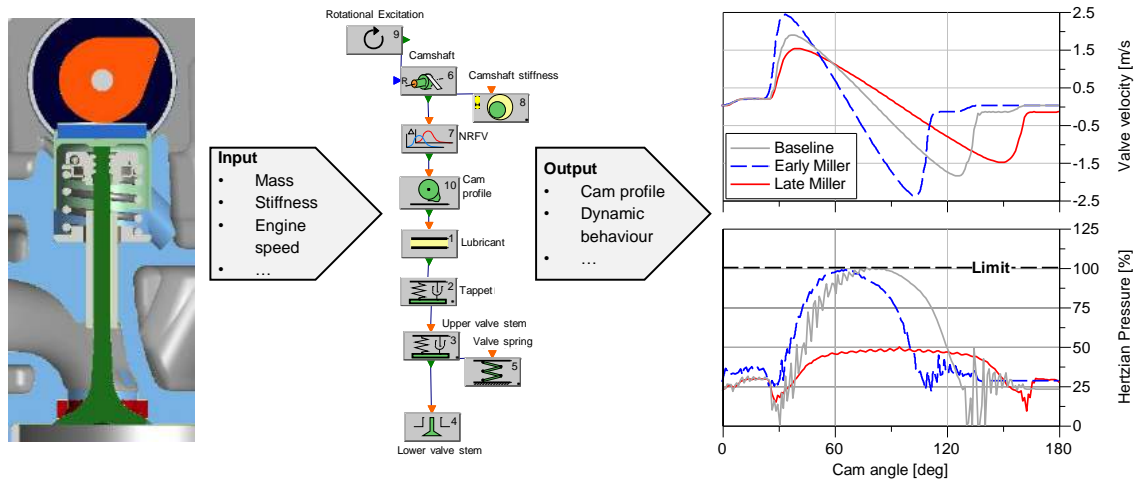

Figure 6-1: Simulation-assisted valve train design using multibody approach

Exceeding the limit in Hertzian pressure, given by the value of the baseline engine, would lead to pitting of the cam and the transmission components, thus increasing the risk of damaging the engine [147]. It is even of higher importance to keep the valve closing velocity constant due to its substantial impact on wear of the valve seat and the valve seat ring [82]. Besides, the minimum valve cam curvature, prescribed by the camshaft manufacturer, needed to be complied with in order to avoid a shear-off of the cam. Late Miller valve timing could be readily realised by adding material to the cam profile, leading to a smaller valve lift gradient, velocity, acceleration and component stress. For early Miller cycle, on the contrary, the increasing valve velocity required considerable modifications of the valve train and the cylinder head to achieve mechanical load that was acceptable for engine testing (see Figure 6-2).
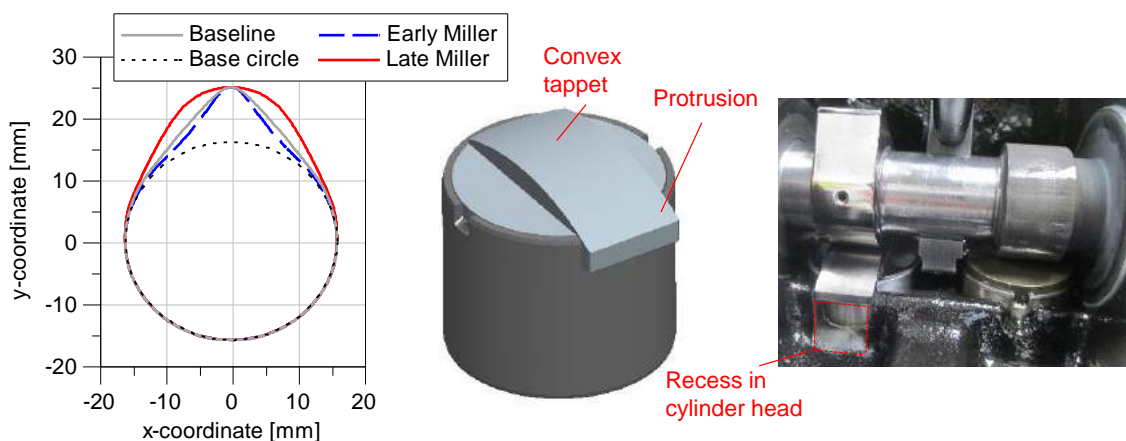
Figure 6-2: Cam profile of the baseline, early and late Mille valve timing (left); convex tapped to realise early Miller (centre); assembled valve train of early Miller configuration (right)
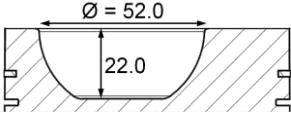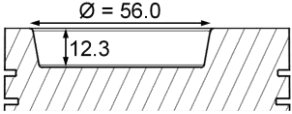
The calculated stress between cam and follower markedly decreases by designing a concave

cam profile that requires a convex tappet. It is of vital importance to prevent the tappet from rotating during engine operation, as it could cause severe damage to the engine otherwise. To this end, it was equipped with a protrusion that is guided through a recess, which was machined into the cylinder head.

6.2 Piston Design

To ensure same effective compression ratio for the selected valve timings, a new piston was designed with a geometrical compression ratio of $r_{geo} = 15.25$. Table 6-1 lists the characteristic parameters of the piston, which exhibits the same clearance volume to the cylinder head at TDC as the baseline piston. The A/V ratio, given at TDC, increases for the new piston design from 0.32 to 0.36, however, at a relatively late combustion phasing of $CA50 \approx 19$ °CA ATDC, at which the engine usually operates, both values decrease to 0.27 and 0.29, respectively (see Figure 6-3, left).

Table 6-1: Specifications of the baseline and Miller piston

Description	Unit	Baseline	Miller
Geo. comp. ratio r_{geo}	-	13.2	15.25
Piston bowl area	mm²	4287	4217
A/V ratio (TDC)	mm⁻¹	0.32	0.36
Piston clearance	mm	1.7	1.7
Squish ratio C_{sq}	-	0.63	0.58
Piston bowl shape	-	Ø = 52.0 / 22.0	Ø = 56.0 / 12.3
Piston design	-		

Internal investigations conducted by the cogeneration engine manufacturer showed that the piston bowl area is one of the driving parameters with respect to NO_x formation and was therefore kept constant. The report also suggests that reducing piston bowl depth at the expense of squish area is beneficial to burn duration at late combustion phasing due to shorter flame travel distance [143]. Based on these findings, a wider piston bowl of lower

depth but similar area was designed. Sharper bowl edges should provoke the charge motion to decay into turbulences and partly compensate for the smaller squish ratio. The steeper valve lift gradient for early Miller valve timing made it necessary to machine a valve pocket into the piston, in order to avoid collision of both components as the intake valve opens. The valve pocket may favour the macroscopic flow to break up, but literature reports valve pockets to only have a small effect on turbulence [182].

Squish occurs at the end of the compression stroke as the piston face approaches the cylinder roof. The volume in the squish region, depicted as shaded area in Figure 6-3 (right), is displaced into the piston bowl and thereby promoting the generation of turbulence [10, 166]. The velocity at which the mixture exits the squish region, termed as the squish velocity, quantifies the squish intensity. The theoretical squish velocity v_{sq} of a heron combustion chamber can be calculated according to Eq. (6-1)

$$v_{sq} = v_p \cdot \frac{D_B}{4 \cdot z} \cdot \left[\left(\frac{D_{cyl}}{D_B} \right)^2 - 1 \right] \cdot \frac{V_B}{\frac{\pi \cdot D_{cyl}^2}{4} \cdot z + V_B} \tag{6-1}$$

where v_p is the instantaneous piston velocity, D_B the piston bowl diameter, D_{cyl} the cylinder bore, V_B the piston bowl volume and z the distance between squish surface and cylinder roof. Despite neglecting the influence of gas inertia, friction, blow-by and heat transfer, the approach yields fairly accurate results compared to that obtained from measurements [57]. Figure 6-3 (centre) illustrates v_{sq} of the baseline piston to be higher than that of the Miller piston until meeting BDC, where both values decrease down to zero.
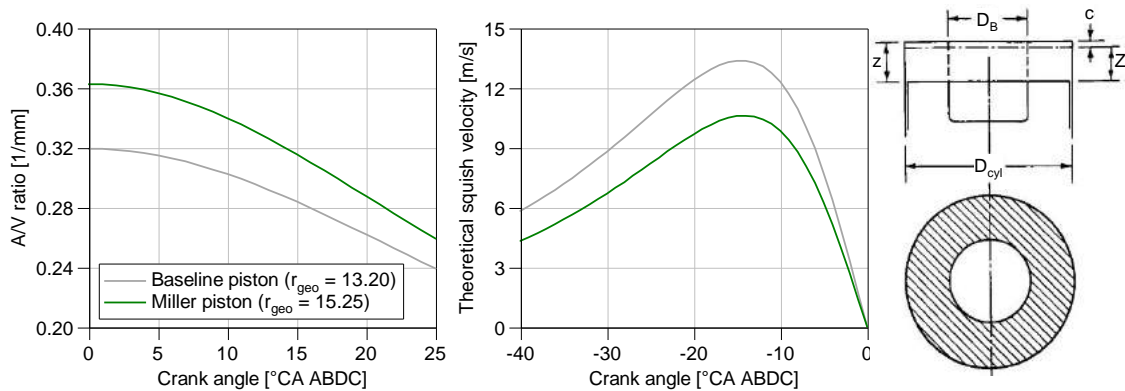

Figure 6-3: A/V ratio (left) and theoretical squish velocity (centre) over crank angle for the baseline and Miller piston; Geometrical relations for calculating the theoretical squish velocity (right) [57]

It is expected that the higher theoretical squish velocity of the baseline generates a higher turbulence level. Work of others confirm increasing squish to reduce combustion duration [10, 145]. However, their trials focused on optimal combustion phasing in terms of engine efficiency. For this reason, shorter combustion duration is expected at early combustion phasing, while the shortened flame travel distance could outweigh higher turbulence level with retarding combustion phasing as the findings in [143] indicate.

7 Experimental Results

This section discusses experimental data obtained from the constant volume combustion chamber (CVCC) and engine testing with different valve timings and compression ratios. Even minor changes to an engine may impact its performance markedly so that it would be difficult to fully understand single effects of the Lean-Miller-EGR working process by realising it within one step. For this purpose, an iterative testing procedure was followed, where EGR and Miller cycle were first studied separately for an isolated examination, and subsequently both combined, as depicted in Figure 7-1. Preliminary trials were performed to analyse the effect of substituting a part of excess air with exhaust gas on combustion, particularly on the laminar burning velocity, using the CVCC. After, engine trials on engine II were carried out for varying EGR rates to study its effects on the baseline engine's performance. At the same time, multiple Miller configurations, consisting of a modified intake valve closing and a higher geometrical compression ratio, were analysed in lean-burn operation on test bed engine I (for which the 1D-CFD model was validated). The target of the trials was to select an early and late Miller valve timing of same effective compression ratio and expansion/compression ratio and that enable a representative comparison of both strategies. Transferring the configurations found for engine I to engine II, required a reevaluation of the effective compression ratio due to tolerances in the manufacturing process of engine components. Subsequently, a detailed comparison between early and late Miller cycle was drawn for varying mixture settings. Results from 3D CFD calculations aided the interpretation of differing combustion characteristics. In the next step, the Lean-Miller-EGR working process was studied in depth and compared to the lean operated baseline configuration. The primary focus was placed on engine operation at constant IMEP = 6.35 bar (+/- 0.01 bar) corresponding to the reference operating point ROP. For

engine II, ROP is found at a relative air-fuel ratio of $\lambda = 1.50$ and a constant ignition timing IT = -8 °CA ATDC, leading to a combustion phasing of $CA50 \approx 19$ °CA ATDC and indicated specific NO_x emissions of approximately 1.4 g/kWh. Note that these settings will serve as a reference when comparing different engine configuration in the further course of this work. The deviation to the NO_x emissions calculated from the 1D model of nearly 20 % has two reasons: First, the 1D-CFD model was adapted to engine I that operates at slightly lower NO_x emissions; second, the NO_x model of the 1D CFD model in the ROP with an error of about 8 % (cf. Figure 4-7, left).
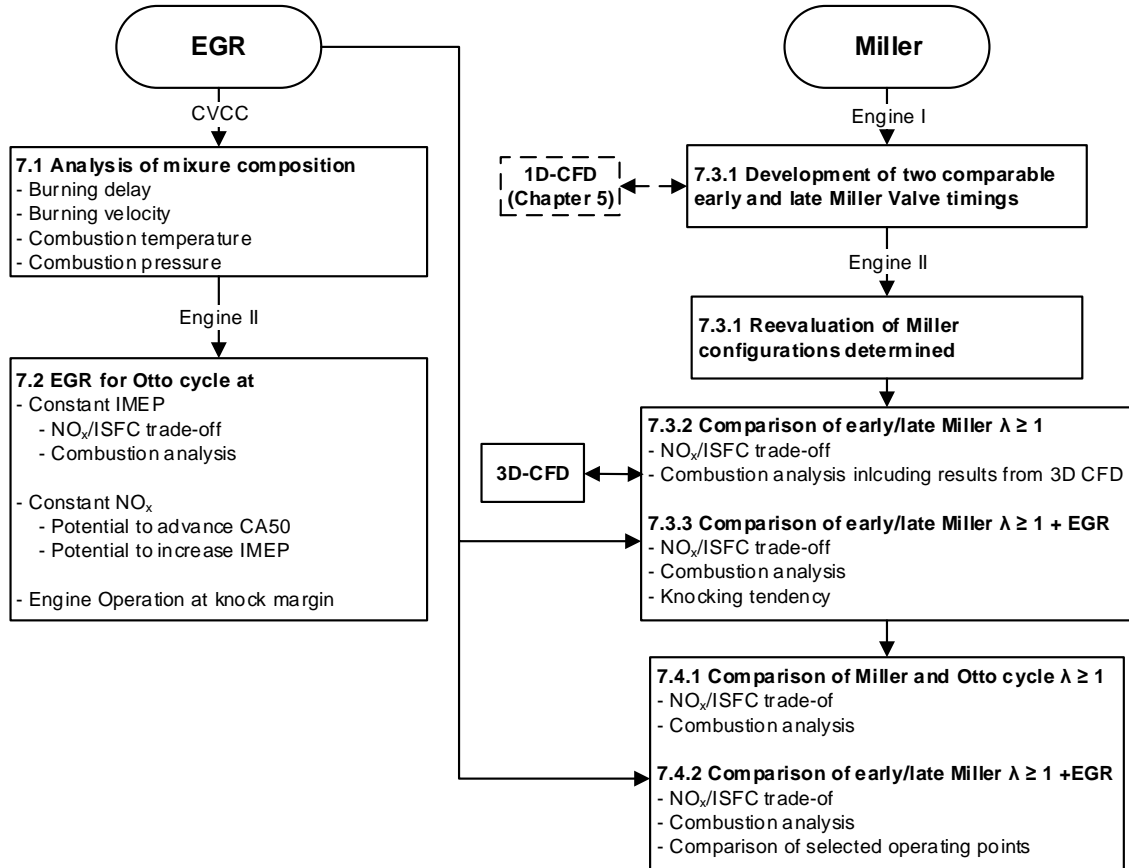
Figure 7-1: Work flow of experimental investigations

All engine trials were carried out in unthrottled operation at constant engine speed of 2450 rev/min. Pressure and temperature of the air entering the cogeneration unit were kept constant at $p_{air} = 995$ mbar and $T_{air} = 35$ °C to ensure reproducible inlet boundary conditions of the system. The outlet boundary conditions, given by the ambient conditions, varied only slightly over the course of all conducted trials. Every measurement was recorded three times. For direct comparisons of selected operating points, the average value is used. Thermodynamic zero-point correction to determine the absolute pressure level trace of the in-cylinder pressure was applied by assuming a constant polytropic exponent of n = 1.358 over a predefined crank angle range between 80 and 60 °CA BTDC.

7.1 Analysis of Combustion in a Constant Volume Combustion Chamber

Literature research shows that burning velocity is very susceptible to mixture composition. Most work centres on comparisons between either air-diluted mixtures or stoichiometric mixtures diluted with EGR. In experimental studies, exhaust gas is often simulated using synthetic gas, comprised of N_2 and CO_2 of different ratios such as N_2/CO_2 of 0.815/0.185 [122] and 0.83/0.17 [34] for stoichiometric or 0.88/0.12 [79] for both stoichiometric and lean mixtures. The motivation behind this procedure is to either prevent H_2O condensation thanks to initial conditions below the dew point [79] or the necessity of an additional combustion to form real exhaust gas [34]. Ponnusamy et al. [122] supported their definition by highlighting the averaged molar specific heat capacity over the temperature range investigated (300 to 400 K), being similar to the one of exhaust gas resulting from ideal combustion.

Figure 7-2 shows the molar (left) and specific (right) heat capacity of exhaust gas over temperature defined by different N_2/CO_2 ratios used in literature and under the assumption of an ideal combustion (5 species) for a stoichiometric and a lean mixture with an EGR rate of 20 %. Synthetic EGR defined by Ponnusamy et al. [122] or Doosje [34] exhibits a similar molar heat capacity as the one of exhaust gas from ideal stoichiometric combustion with x_{EGR} = 20 % EGR, leading to maximum errors for the range shown of 2.2 and 1.1 %, respectively. While CO_2 is the predominant component for the molar heat capacity, H_2O gains in importance for the mass related definition due to its lower molar mass compared with CO_2. The error to the multicomponent definition, considered in this work, then increases to 8.5 and 9.8 %, respectively.
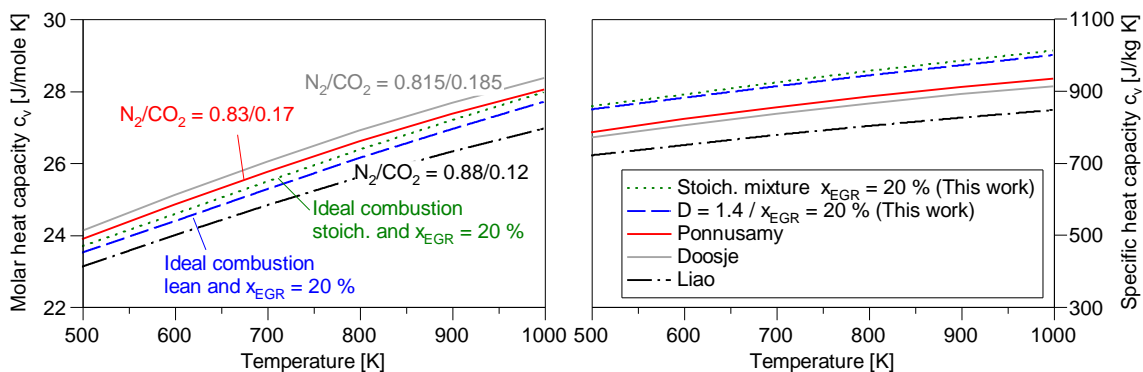

Figure 7-2: Molar (left) and specific (right) heat capacity of exhaust gas over temperature

Doosje [34] reportedly found the differences on laminar burning velocity caused by using synthetic instead of real exhaust gas to be small. The findings relate to stoichiometric combustion at x_{EGR} = 20 %; the agreement could differ when adding EGR to lean mixtures. From this it follows that using real exhaust gas is conducive as it accounts for the water vapour and thereby improves validity of the results.

7.1.1 Testing Procedure

The majority of trials was conducted (following the workflow in Figure 7-3) at the same number of moles by setting a constant initial temperature of $T_0 = 423.15$ K and initial pressure of $p_0 = 3.73$ bar. The initial conditions were determined by an isentropic change of state starting from 293.15 K and 1.0 bar. The dilution ratio was varied from $D = 1.3$ to $D = 1.8$ in increments of 0.1. Starting from an air-diluted mixture, a part of the excess air was substituted with exhaust gas for each dilution ratio up to $x_{EGR} = 20$ %. After every trial, the CCVC was scavenged with compressed air for a duration of 5 minutes to guarantee a residual gas free chamber. It was then evacuated down to an absolute pressure level of 20 mbar and refilled first with CH_4 and after with dry compressed air. The corresponding partial pressures of each mixture were calculated assuming ideal gas behaviour. After a delay time of 5 minutes that proved to be sufficient to achieve a well-homogenised mixture, allowing for reproducible results [73, 156], the mixture was ignited. Experiments including EGR required an additional working step. To provide exhaust gas components including H_2O and CO_2 within the vessel, first a stoichiometric combustion was conducted. After a waiting time of 3 minutes, the desired partial pressure to obtain the required CO_2 and H_2O fraction from the former combustion was adjusted using the vacuum pump. Subsequently, CH_4 and air were added, including the missing excess parts of N_2, O_2 and Ar of the exhaust gas after the stoichiometric combustion.
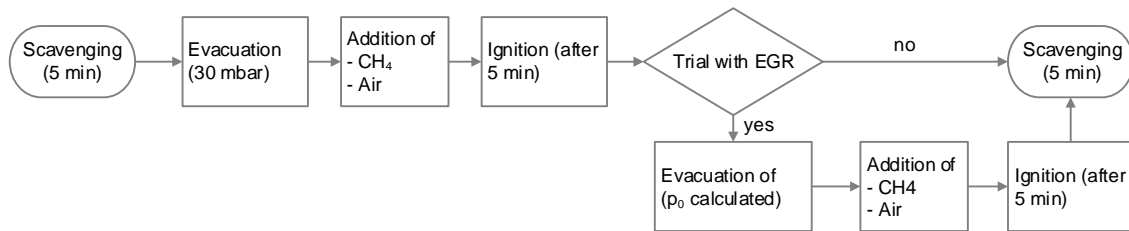

Figure 7-3: Procedure of experiments with different mixtures using the constant volume combustion chamber (CVCC)

In the case of EGR, the fuel of the stoichiometric combustion was assumed to be entirely burnt. An alternative method that does not require an additional combustion is to add the exhaust gas components individually. However, experiments showed that adding reproducible amounts of water was not possible without further modifications on the experimental installation.

7.1.2 Results of Varying Mixture Composition

Figure 7-4 shows pressure versus time for all dilution ratios investigated without exhaust gas ($D = \lambda$) and with varying EGR rates at constant ignition timing $t_{ig} = 0$ s. Under the premise of constant initial conditions, the mass of fuel falls for higher dilution ratios. Peak and slope of combustion pressure decrease and peaking is retarded. The similar effect is observed when exhaust gas is added for constant dilution ratios. Specific heat capacity

increases with the EGR rate, resulting in lower pressure rise with a lower pressure peak and retarded combustion. The sensitivity of the combustion to EGR decreases for higher dilution ratio as a result of lower specific heat capacity of the exhaust gas.
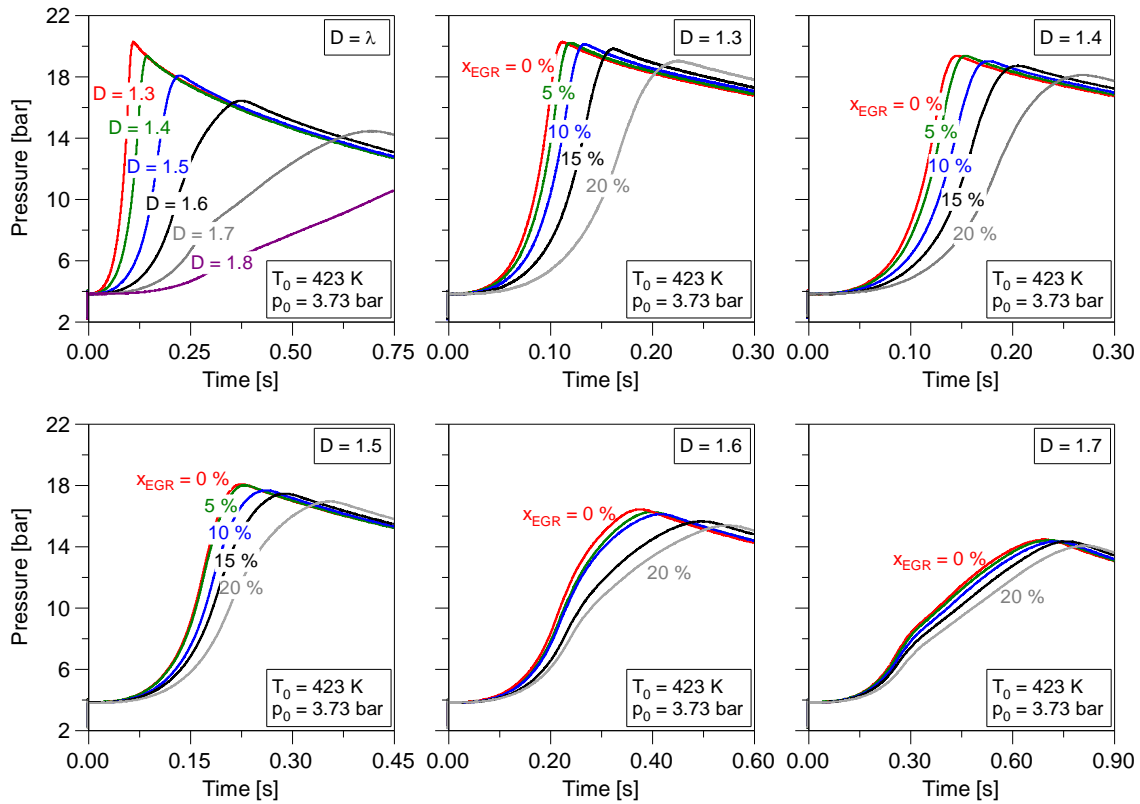

Figure 7-4: Pressure against time for different dilution ratios D without EGR (D = λ) and for different dilution ratios (D = 1.3–1.7) of varying EGR rates (right)

The measured pressure traces were evaluated using the MATLAB-based routine described in Section 4.1.2. Figure 7-5 shows the calculated burning velocity s_l against the temperature of the unburnt zone T_u for varying mixture compositions. The first part of the plotted traces between the initial temperature and approximately 475 K is futile for analysing burning velocity due to instability of the values. Burning velocity decreases with both increasing dilution ratio and EGR rate. The lower peak in combustion pressure, as a result of leaning or adding EGR, correlates with the maximum temperature of the unburnt zone, thus narrowing the evaluation window of the laminar burning velocity. For this reason, only dilution ratios of D = 1.3 to 1.5 with EGR and D = 1.6 without EGR are plotted in Figure 7-5. Once burning velocity reaches its maximum, it declines rapidly until the combustion is completed. The gradient of this range decreases with both higher dilution ratio and EGR rate, enhancing the time that the flame front dwells in the vicinity of the wall, thus promoting the chance of flame quenching.
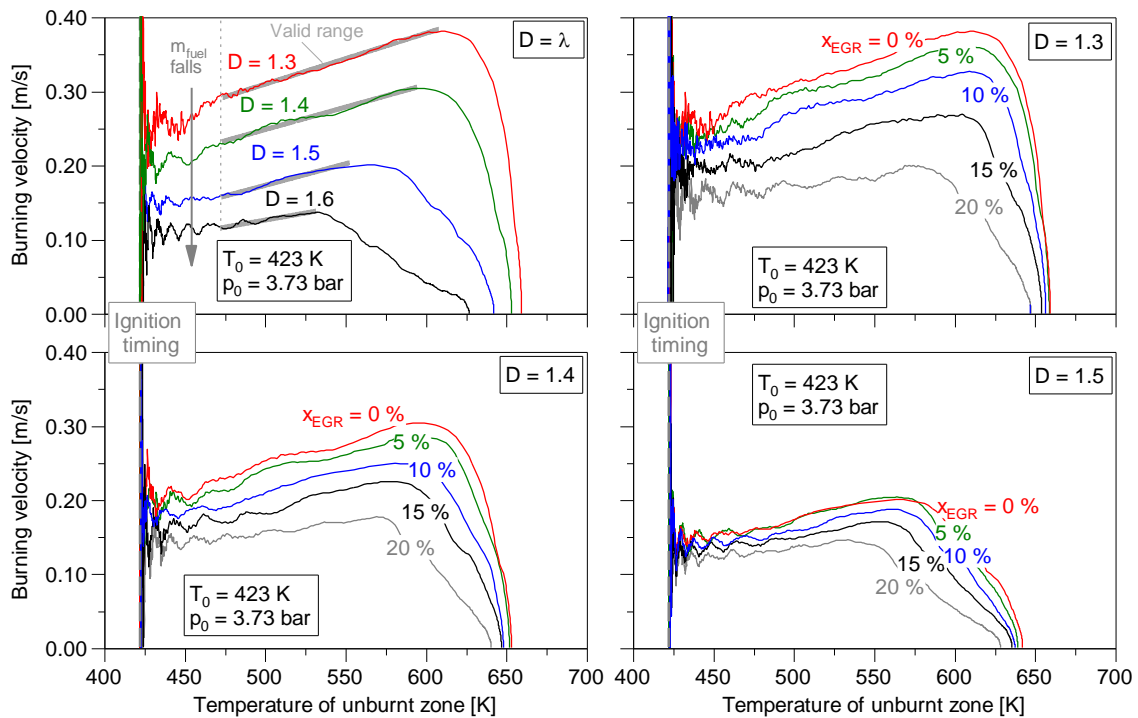
Figure 7-5: Burning velocity over temperature of unburnt zone for different dilution ratios and for constant dilution ratios of D = 1.3-1.6 of varying EGR rates

Figure 7-6 (left) depicts the mixture's initial specific heat capacity c_v (before ignition) against the EGR rate for various dilution ratios D. For a constant D, i.e. constant mass of fuel, the specific heat capacity enhances with increasing EGR rates. The effect is more marked for lower dilution ratios and higher EGR rates due to the increased CO_2 and H_2O fraction of the exhaust gas.
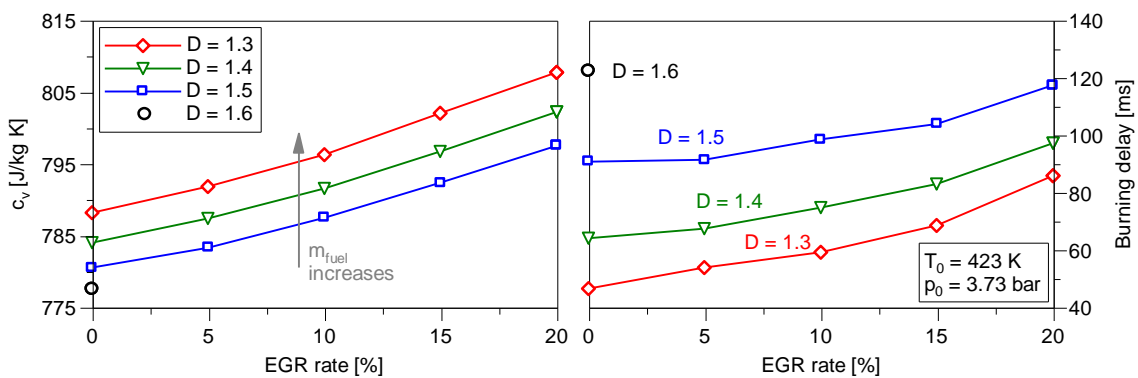

Figure 7-6: Specific heat capacity c_v of the mixture before start of combustion (left) and burning delay (right) as function of EGR rate for different dilution ratios

When dilution ratio increases at same EGR rate, c_v of the mixture becomes smaller caused by lower CH_4 fraction (cf. Figure 2-16). This, in turn, leads to a larger excess fraction that absorbs the heat during combustion and extends the burning delay, here defined as the time required until 5 % of the mass fraction is burnt (see Figure 7-6, right). The difference

between dilution ratios of same EGR rate decreases for higher exhaust gas fraction, since exhaust gas of richer mixture exhibits higher specific heat capacity.

Decreasing burning velocity is one of the major drawbacks when reducing combustion temperature through mixture dilution. Figure 7-7 (left) depicts burning velocity as function of the EGR rate and the temperature of the burnt zone T_b for various dilution ratios at constant temperature of the unburnt zone of $T_u = 525$ K and therefore at very similar pressure ranging from 8.53 and 8.70 bar. Burning velocity and combustion temperature decrease with rising EGR rate at constant dilution ratio. This can be explained by the decreasing O_2 and increasing H_2O and CO_2 concentration as literature reports [25, 32, 33, 87]. As expected, the lowest dilution ratio D = 1.3 reaches the highest values in temperature of the burnt zone ($T_b = 2250$ K) and laminar burning velocity ($s_l = 0.325$ m/s). For a mixture composition of D = 1.6 and no EGR, for instance, both values drop down to $T_b = 2044$ K and $s_l = 0.132$ m/s. Replacing air with exhaust gas, reduces combustion temperature while burning velocity falls markedly. The EGR rate required for same temperature of the burnt zone, increases for lower dilution ratios. At a dilution ratio of D = 1.4, the laminar burning velocity peaks at $s_l = 0.255$ m/s for a burnt zone temperature of $T_b = 2175$ K and an EGR rate of approximately $x_{EGR} = 3$ %. When further lowering the dilution ratio down to D = 1.3, the EGR rate required to achieve the same temperature rises to nearly $x_{EGR} = 19$ %, yet with a considerable drop in burning velocity to $s_l = 0.191$ m/s.
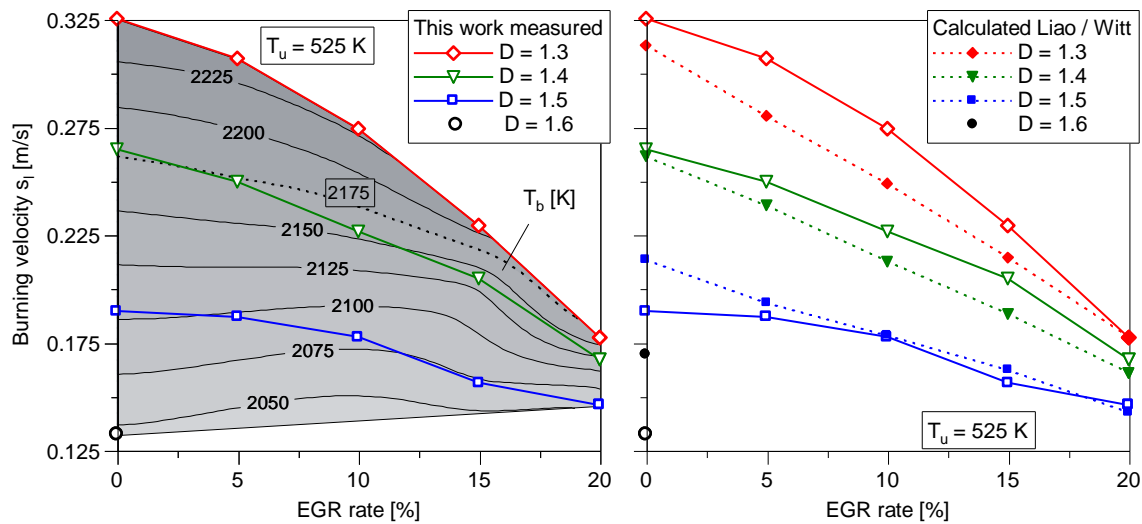

Figure 7-7: Laminar burning velocity and burnt zone temperature as function of EGR rate and dilution ratio at constant unburnt zone temperature (left); Comparison between laminar burning velocity determined in this work from experiments and calculated values using the correlation of Liao/Witt [79, 176] (right)

Comparing the results from the experiments to literature [79, 176], calculated from Eq. (2-4), shows a strong correlation expressed by a coefficient of determination of $R^2 = 0.93$ (see Figure 7-7, right). The experimental values of s_l for dilution ratios of D = 1.3 and D = 1.4 without EGR lie above the calculated ones. The laminar burning

velocity decreases for higher EGR rates at constant dilution ratio reciprocally to the change of specific heat capacity (cf. Figure 7-6, left). A steeper gradient of s_l can be observed with decreasing dilution ratios due to higher specific heat capacities auf the exhaust gas. The drop of calculated laminar burning velocity over EGR rate is also stronger for lower dilution ratios. Nonetheless, the gradient for a constant dilution ratio is almost linear. This likely arises from the fixed concentration of the single exhaust gas components, regardless of the fresh mixture's composition.

It can be seen that the highest dilution ratio of D = 1.6 exhibits the largest deviation. A possible explanation is the suffering accuracy when defining mixtures of low dilution ratios that require very low partial pressures to be set. The reason why the experiments of lower dilution ratios, such as D = 1.3 and 1.4, lead to higher laminar burning velocities, need a deeper explanation: It is possible that the shape of the flame front changes in the course of the combustion due to instabilities caused by hydrodynamic effects [50, 66]. These lead to flame cracking, being a precursor to a cellular flame structure. The latter exhibits a larger surface than the purely laminar and spherical flame shape, thus accelerating the combustion. In that case, the code overpredicts the burning velocity as it still assumes a laminar flame front (cf. Eq. (4-1)).

While flame structures can be assessed using optical metrology, an alternative method is to analyse the slope of the burning velocity as applied by Lafuente [73]. Multiple combustions at same relative air-fuel ratio are carried out at different initial thermodynamic conditions obtained from an isentropic change of state. By superimposing the laminar burning velocity as function of the burnt zone temperature, a sudden rise of the laminar burning velocity hints a transition from laminar into cellular flame regime. The trials described in [73] were carried out for a stoichiometric CH_4-air mixture, showing the transition regime from laminar to cellular flame front ranges between 5 to 6 bar corresponding to a temperature of the unburnt zone from of 460 and 505 K, respectively. It was also shown that the sensitivity to cellularity diminishes with leaning, allowing for a laminar flame front at higher pressures. In order to evaluate the possibility of laminar flame structure within this work, the aforementioned procedure was applied to dilution ratios of D = 1.3, 1.4 and 1.5 at differing initial conditions (see Figure 7-8). It can be seen that within the transition range of a stoichiometric mixture (5 to 6 bar / 460 to 505 K), a very modest rise of the burning velocity occurs, whose magnitude decreases with higher dilution ratio. This portends a change of flame structure, however, its effect appears to be rather small and would decrease by adding EGR. Similar experiments with mixtures containing EGR could not be conducted due to condensation of water at the lower initial temperatures required.

The experiments point out that the burnt zone temperature of lean mixtures can be achieved also for mixtures of larger fuel fraction by replacing a part of excess air with EGR. As a result, burning velocity decreases, which might be compensated by advancing ignition

timing in engine operation. In that case, one of the crucial differences are higher temperature and pressure levels and the motion of in-cylinder charge that leads to a combustion with a turbulent flame front.
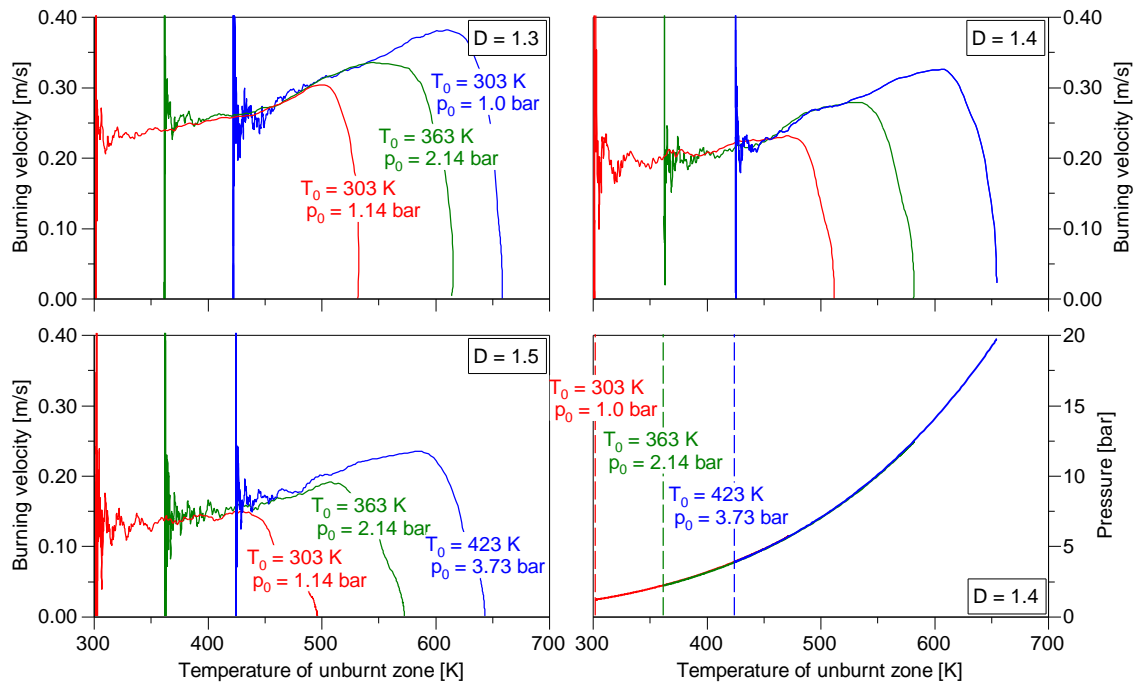

Figure 7-8: Burning velocity against temperature of unburnt zone for different dilution ratios of D = 1.3 / 1.4 / 1.5 of varying initial conditions and pressure over temperature of unburnt zone for D = 1.4

7.2 Lean-burn Engine Operation and EGR for Otto Cycle

First engine trials with EGR were carried out for the baseline configuration to evaluate its effect on efficiency, emissions and combustion at constant IMEP. Depending on the outcome, it could possibly represent an alternative to both the currently followed lean-burn strategy and the Lean-Miller-EGR working process. In light of a combination with Miller valve timing, which are expected to require notably lower dilution ratios for constant IMEP, the primary purpose of EGR is to reduce NO_x emissions. Alternatively, this can be seen as mean to increase IMEP at constant NO_x emissions, which was another focus of the trials described in this section.

The EGR rate was increased stepwise from 0 to 25 % in increments of $\Delta x_{EGR} = 5$ %. In order to avoid a significant influence of EGR on intake port temperature T_{intake} and thereby to isolate the effect on engine characteristics to altered mixture composition, the exhaust gas was recirculated at constant temperature of $T_{EGR} = 75$ °C. Only in the case of EGR rates above $x_{EGR} = 20$ %, the required coolant temperature would fall below its lower limit of 58 °C, causing condensation of the exhaust gas. To this end, the highest investigated EGR rate of $x_{EGR} = 25$ % affected with $T_{EGR} = 78$ °C the intake port temperature only slightly.

7.2.1 Investigations at Constant IMEP

CA50 sweeps were conducted for each EGR rate while IMEP was kept constant at IMEP = 6.35 bar by adjusting ignition timing and dilution ratio (variable mass of fuel). CA50 ranging from 6 to 10 °CA ATDC represents the high efficiency regime, where the engine operates at its highest NO_x emissions. The low NO_x regime, on the other hand, is found at retarded CA50 between 16 and 20 °CA ATDC, which are detrimental to engine efficiency. With both low NO_x and high efficiency regime being of high interest in this work, they were recorded in steps of ΔCA50 = 1 °CA, whereas in-between only CA50 = 13 °CA ATDC was taken into account.

7.2.1.1 Engine Efficiency and NO_x Emissions

Figure 7-9 depicts ISFC (top left) and CA50 (bottom left) over NO_x emissions of different EGR rates at constant IMEP for the entire CA50 sweep. With increasing EGR rate, the Pareto front gradually shifts towards lower NO_x emissions and higher ISFC. Analogous to experiments in the CVCC, EGR increasingly unfolds its effect for higher rates. Lower NO_x emissions at same CA50 are observed but at the expense of ISFC. While the losses in ISFC can be compensated through advanced CA50 in the low NO_x regime, EGR is detrimental to ISFC in the high efficiency regime, where the impact of CA50 on ISFC is rather small. Regardless of the EGR rate, CA50 = 8 °CA ATDC represents the efficiency optimum of the engine. The influence of CA50 on ISFC is rather small whether CA50 is 2 °CA advanced to or retarded from the efficiency optimum. NO_x emissions, on the other hand, increase notably due to their high sensitivity to temperature and in turn to combustion phasing.
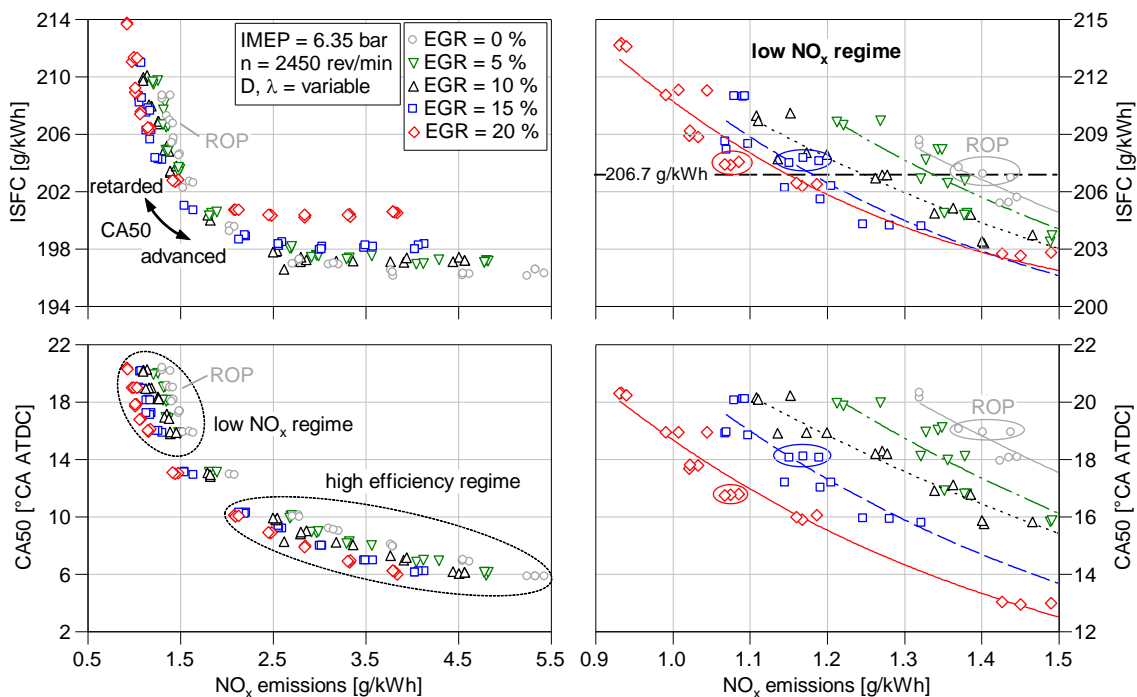

Figure 7-9: Indicated specific fuel consumption ISFC (top) and CA50 over NO_x emissions (bottom) at IMEP = 6.35 bar and n = 2450 rev/min (enlarged illustration on the right hand side)

A zoomed illustration that centres on the low NO_x regime, where the influence of CA50 on ISFC is much higher, is given in Figure 7-9 (right). In order to retain the ISFC of the ROP, CA50 needs to be advanced while NO_x emissions still remain lower. The largest improvement in NO_x at same efficiency is found for EGR rates of $x_{EGR} = 15$ and 20 %, requiring a combustion phasing of 16 °CA and 17 °CA ATDC, respectively. Compared with the ROP ($NO_x = 1.40$ g/kWh, ISFC = 206.7 g/kWh), ISFC and NO_x emissions amount to 207.4 g/kWh and 1.17 g/kWh for $x_{EGR} = 15$ % and to 207.2 g/kWh and 1.08 g/kWh for $x_{EGR} = 20$ %. For even further advanced combustion phasing with NO_x emissions similar to those of the ROP, fuel consumption diminishes notably, as it will be detailed in 7.2.1.3.

During engine testing, a falling pressure difference between intake and exhaust port with increasing EGR rate could be detected. The pressure compensation that takes place when the EGR valve opens indicates a dethrottling effect. To ensure that the improved ISFC through EGR majorly result from advanced CA50 rather than from reduced pumping losses, the gas exchange was analysed. The largest reduction in pumping work at same CA50 amounts to approximately 0.1 g/kW in ISFC and is caused for the highest EGR rate. This weak impact arises from the relatively low pressure difference between the exhaust gas extraction (i.e. after cogeneration unit heat exchanger) and discharge point (short before intake port).

For the interpretation of the results that follow in this section, mixture composition is analysed. Figure 7-10 (left) depicts the contour plot of dilution ratio D, relative air-fuel ratio λ and NO_x emissions for different EGR rate. The consideration of the residual gas fraction for the determination of λ and the use of different measurands when calculating D and λ, lead to differences between both parameters for lean mixtures without EGR. With increasing EGR rate at constant dilution ratio, excess air is replaced by exhaust gas, reducing the fraction of O_2 and therefore λ. For a constant EGR rate, both λ and D remain nearly the same within the high efficiency regime due to the small effect of CA50 on ISFC. Across all EGR rates investigated for constant IMEP, λ and D need to be decreased as CA50 is retarded, owing to the falling engine efficiency. Since the engine operates with EGR at lower ISFC, it exhibits a slightly higher dilution ratio at same NO_x emissions.

Literature [110, 140] shows that exhaust gas of lean natural gas engines tends to exhibit high NO_2/NO_x ratios due to low temperature combustion at high O_2 concentrations. As a result, the engine reaches the highest NO_2/NO_x ratio in air-diluted combustion at low NO_x emissions (see Figure 7-10, right). The NO_2/NO_x ratio of operating points of same NO_x emissions decreases with rising EGR rate, likely due to lower O_2 concentration that avoids reaction (2-12) to take place. The NO_2/NO_x ratio is of minor importance if the only after-treatment is an oxidation catalyst, yet far more relevant for the conversion efficiency of elaborate systems that aim at reducing NO_x tailpipe emissions of lean-burn combustion such as NSC (NO_x storage catalyst) or SCR [31]. While the complexity to integrate either of these is not justifiable for a small cogeneration engine, SCR systems are expected to

play the instrumental role in meeting future emission limits of large gas engines [5].
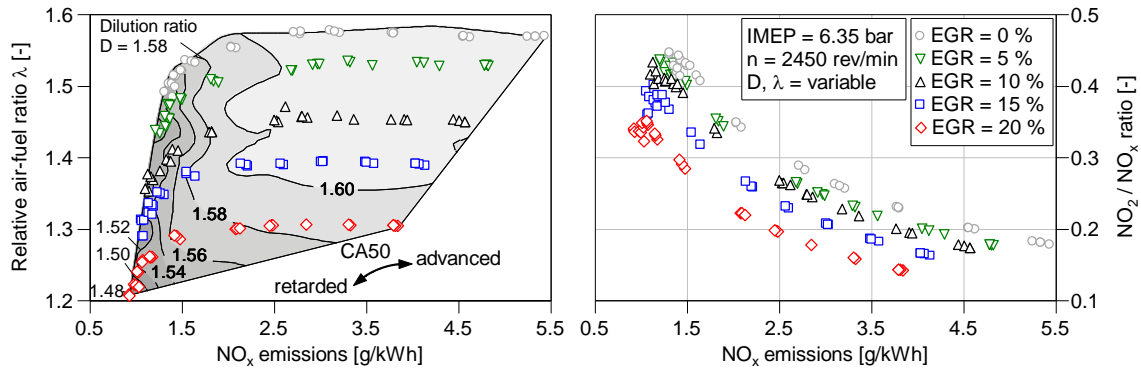

Figure 7-10: Relative air-fuel ratio and dilution ratio (left) and NO₂/NOₓ ratio (right) over NOₓ emissions

The results in Chapter 3 and 5 show that replacing excess air with exhaust gas reduces the ratio of the specific heat capacities, thus deteriorating mixture properties in terms of the theoretical achievable ISFC defined by the ideal engine ($ISFC_{ideal}$). Figure 7-11 (left) depicts the calculated $ISFC_{ideal}$, presented in 4.2.3, as function of the measured NO_x emissions. Note that all calculations were carried out assuming isochoric combustion at TDC (as shown in Figure 4-3). Recorded data show that initial thermodynamic conditions of the cycle and the residual gas fraction across the operating points vary marginally. As a result, external mixture composition, only defined by the dilution ratio and EGR rate, primarily determines $ISFC_{ideal}$. For a given EGR rate, $ISFC_{ideal}$ is, in line with the mixture composition, almost constant in the high efficiency regime. In the low NO_x regime, on the other hand, the more pronounced changes in mixture composition exert a stronger influence on $ISFC_{ideal}$. Owing to its higher sensitivity to lower λ, $ISFC_{ideal}$ varies particularly for higher EGR rates as the plot of over the measured CA50 in Figure 7-11 (right) shows.
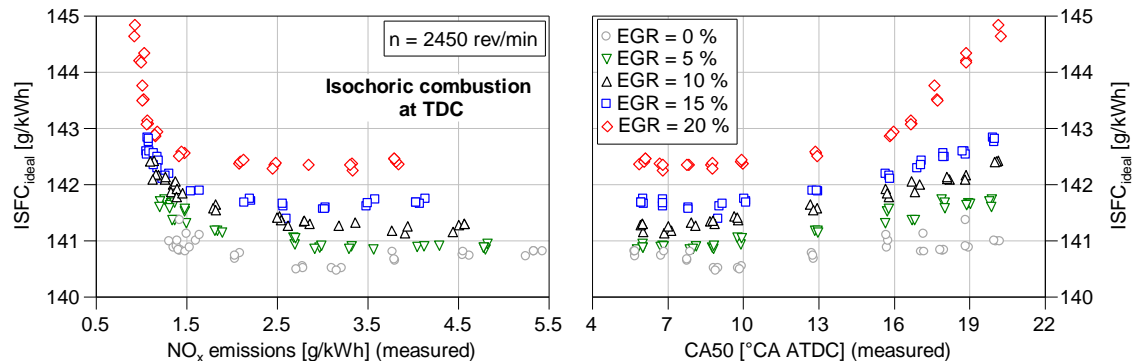

Figure 7-11: Indicated specific fuel consumption of the ideal engine over NOₓ emissions (left) and CA50 (right) (simulation results, isochoric combustion at TDC assumed)

The following example in Table 7-1 shall clarify that $ISFC_{ideal}$ allows inferring the disadvantages solely caused by unfavourable mixture composition through EGR: Starting from engine operation at CA50 = 8 °CA ATDC without EGR, an EGR rate of $x_{EGR} = 20\%$ decreases $ISFC_{ideal}$ from 140.7 to 142.3 g/kWh. Comparing the deficit of 1.7 g/kWh to the

one the actual engine experiences in ISFC of 3.7 g/kWh, the altered mixture composition is responsible for 43 % of the losses. Due to the richer mixture for late CA50, the penalty increases to 73 % at a combustion phasing of CA50 = 20 °CA ATDC.

Table 7-1: Comparison of ISFC and ISFC$_{ideal}$ for operating points at CA50 = 8 and 20 °CA ATDC and EGR rates of x$_{EGR}$ = 0 and 20 %

CA50	X$_{EGR}$	ISFC (actual cycle)	Losses in actual cycle	ISFC$_{ideal}$ (ideal cycle)	Losses in ideal cycle	Proportion of ideal losses
[°CA ATDC]	[%]	[g/kWh]	[g/kWh]	[g/kWh]	[g/kWh]	[%]
8	0	196.4	-3.9	140.7	-1.7	43
8	20	200.3	-3.9	142.3	-1.7	43
20	0	208.6	-5.1	141.0	-3.7	73
20	20	213.7	-5.1	144.7	-3.7	73

Next to the losses in ideal engine efficiency, drawbacks are likely caused by altered burn duration and fuel conversion ratio. Furthermore, slightly lower wall heat losses are expected due to the lower temperature level as reduced NO$_x$ emissions indicate.

7.2.1.2 Combustion Behaviour

The results from the CVCC show that EGR notably slows down the combustion process under quiescent conditions. A distinct difference in engine operation are turbulent flow conditions. Since EGR affects the gas exchange of the test bed engine only marginally without perceptible impact on charging efficiency, it can be assumed that the turbulence level remains similar, independent of EGR rate. The influence of EGR on ignition timing IT, burning delay IT-CA5 (left) and burn duration CA5-CA90 (right) as function of CA50 is illustrated in Figure 7-12. Laminar burning velocity falls and ignition delay increases with rising EGR rates, leading to advanced IT to keep CA50 constant. For the analysis of the burning delay, it is important to consider that the conditions inside the prechamber change as the compression stroke progresses. With delaying IT, the residual gas concentration within the prechamber decreases, whereas the mixture temperature inside both pre- and main combustion chamber increases. Furthermore, ignition conditions improve in both chambers, owing to lower dilution ratios required for engine operation at constant IMEP and late CA50. These three factors combined, namely lower residual gas fraction, higher mixture temperature and lower dilution ratio, are expected to intensify the flame jets that penetrate from the prechamber into the main combustion chamber, thus reducing burning delay as CA50 is retarded. For the CA50 sweep without EGR, burning delay increases only slightly, while the slope is steeper in engine operation with higher EGR rates. The decelerating effect of EGR on the combustion process leads to longer burn duration. Starting from CA50 = 6 °CA ATDC, burn duration decreases up to a combustion phasing of CA50 = 10 °CA ATDC due to nearly constant mixture dilution but improving ignition conditions. As combustion phasing is further retarded, burn duration increases in spite of

slightly richer mixtures, presumably due to long flame travel distance given by the relatively deep piston bowl.

The effect of EGR on the combustion process in engine operation is akin to that in the CVCC, yet far more complex to analyse due to varying thermodynamic conditions, turbulence level and mixture inhomogeneity. These factors directly influence the combustion inside the prechamber and therefore the strength of the flame jets. The changing combustion chamber geometry over crank angle becomes a key role for late combustion phasings as it influences flame travel distance.
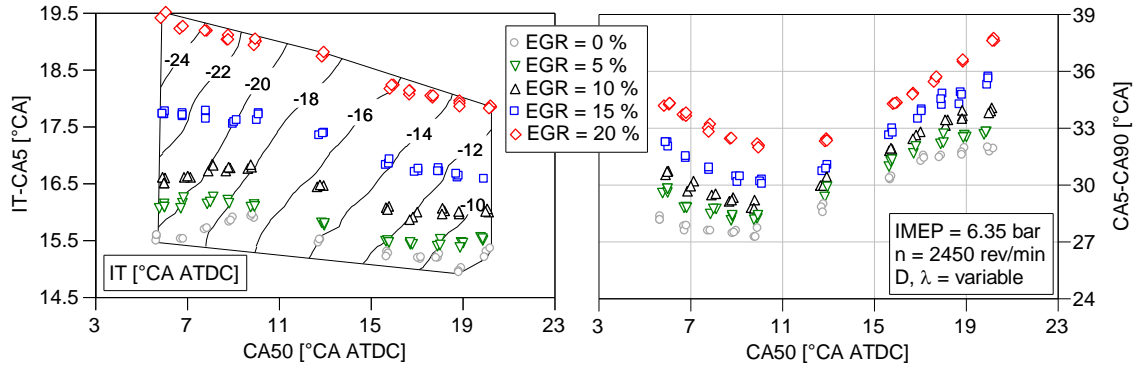

Figure 7-12: Burning delay IT–CA5 and ignition timing IT (left) as well as burn duration CA5–CA90 (right) as function of CA50 for the investigated EGR rates at IMEP = 6.35 bar and n = 2450 rev/min

The extended burn duration for higher EGR rates correlates with exhaust gas temperature T_{ub}, shown as function of NO_x emissions in Figure 7-13 (left). Regardless of EGR rate, T_{rk} reveals its maximum for the lowest NO_x emissions (i.e. most retarded combustion phasing). The prolonged combustion coupled with lower mixture dilution ratios for engine operation with EGR, increases exhaust gas temperature at constant CA50. However, when taking advantage of EGR by advancing CA50, exhaust gas temperature decreases. An EGR rate of $x_{EGR} = 20$ % allows the engine to operate at CA50 = 13 °CA ATDC while achieving NO_x levels similar to those of the ROP. Despite the longer burn duration, exhaust gas temperature falls by 30 K relative to the ROP, thus increasing the demand on the oxidation catalyst with respect to its light-off temperature. While CO converts readily to CO_2 even for low exhaust gas temperatures, the reduction of HC emissions could be challenging due to higher temperatures required for their conversion [88]. Higher exhaust gas temperatures at same CA50 for engine operation with EGR promote the conversion of HC and CO in the late part of the expansion stroke. As a result of a more complete combustion, losses in ISFC from imperfect combustion $\Delta ISFC_{comb}$ decrease (see Figure 7-13, right). In fact, $\Delta ISFC_{comb}$ diminishes within the high efficiency regime by more than 1 g/kWh, when adding an EGR rate of $x_{EGR} = 20$ %. The benefit decreases significantly in the low NO_x regime, where EGR enables the engine to emit less NO_x for $\Delta ISFC_{comb}$ similar to those of the ROP.
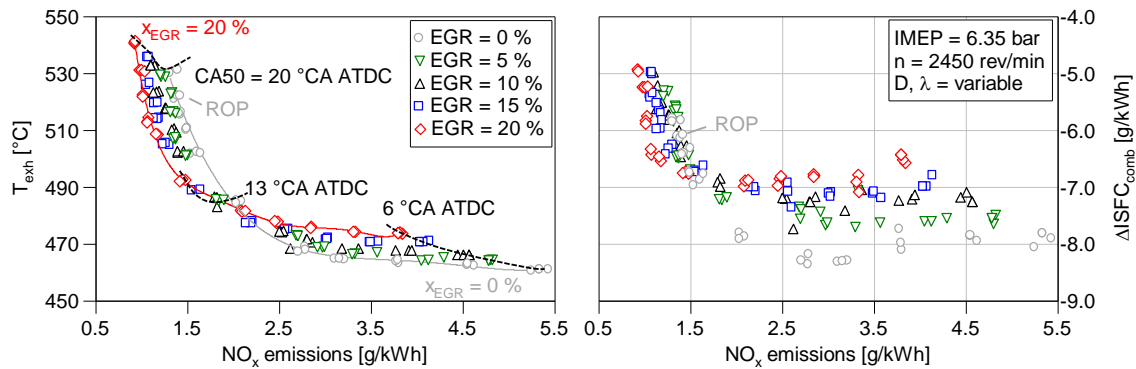
Figure 7-13. Exhaust gas temperature T_{exh} (left) and losses from imperfect combustion $\Delta ISFC_{comb}$ (right) at IMEP = 6.35 bar and n = 2450 rev/min

Combustion stability, often applied to define the lean-burn limit [68], plays a major role in lean-burn operation. High cycle-by-cycle variations are detrimental to engine efficiency and can lead to numerous cycles of early CA50 that increase NO_x emissions. To assess combustion stability, the coefficient of variation in indicated mean effective pressure COV_{IMEP} and the standard deviation of CA50 σ_{CA50} of 200 consecutive cycles are analysed (see Figure 7-14). Lowest COV_{IMEP} and σ_{CA50} occur in the high efficiency regime, where the most favourable conditions for combustion due to high temperature and short flame travel distances are found. Both COV_{IMEP} and σ_{CA50} increase and become much more sensitive to EGR for retarded CA50, i.e. at low NO_x emissions. Possible operation at earlier CA50 but same NO_x emissions with EGR reduce COV_{IMEP} and σ_{CA50} again to some extent.
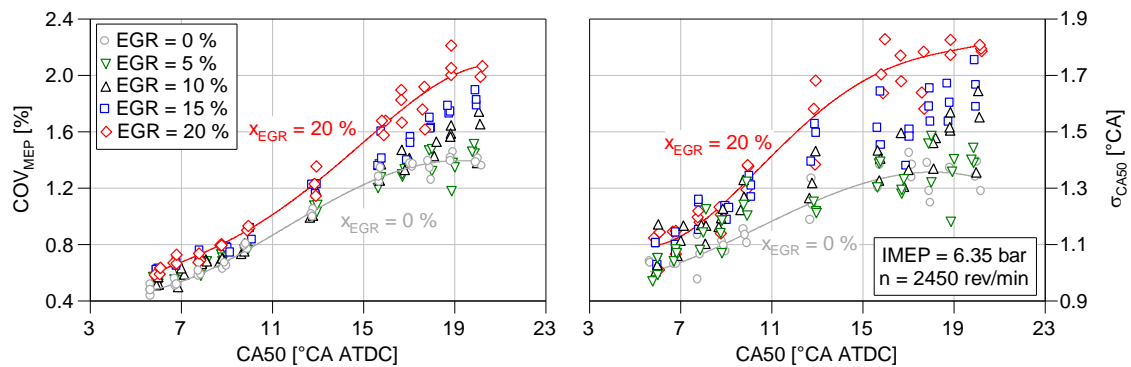

Figure 7-14: COV_{IMEP} (left) and σ_{CA50} (right) over CA50 for different EGR rates at IMEP = 6.35 bar and n = 2450 rev/min

Compared to the ROP, the largest difference in both COV_{IMEP} and σ_{CA50} at same CA50 is found for an EGR rate of x_{EGR} = 20 %. Analysing the ensemble pressure trace of 200 cycles of the respective operating points shows that the variation is rather small (see Figure 7-15, left). This can be explained by the lower dilution ratio (i.e. higher fuel fraction) for engine operation with EGR at same CA50, reducing the sensitivity to both σ_{CA50} and COV_{IMEP}.

The earlier combustion phasing required to keep engine efficiency with the addition of EGR increases peak combustion pressure p_{max}, as shown against NO_x emissions in Figure 7-15

(right). At constant NO_x emissions, p_{max} increases by more than 7 bar when operating the engine with an EGR rate of $x_{EGR} = 20$ % in the low NO_x regime. The effect becomes smaller in the high efficiency regime due to the exponential increase of NO_x emissions with advancing combustion phasing, leading to a maximum difference of merely 2 bar. While these comparisons apply to operating points of differing CA50, peak combustion pressure is very similar at same combustion phasing independent of mixture composition.
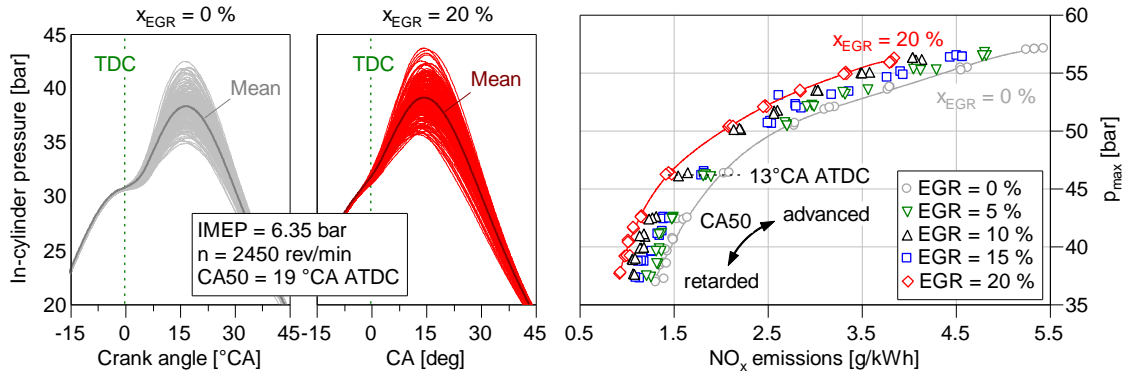

Figure 7-15: The ensemble of 200 pressure traces of operating points at CA50 = 19 °CA ATDC for engine operation without EGR and at $x_{EGR} = 20$ % (left) and peak combustion pressure p_{max} against NO_x emissions (right)

7.2.1.3 Comparison of Selected Operating Points

A more detailed analysis of selected operating points, including the traces of mean mixture temperature, temperature of the burnt zone, in-cylinder pressure and the cumulated normalised heat release at constant IMEP, gives a deeper insight into the effect of EGR on engine operation (see Figure 7-16). Advancing combustion phasing of the reference operating point from CA50 = 18.9 (ROP) to 12.8 °CA ATDC (OP1), allows the engine to reduce ISFC by 7.4 g/kWh but also increases mean in-cylinder temperature. Consequently, wall heat losses Q_{wall} normalised to the released energy during the cycle increase by 2.1 %-points. In spite of a relatively small rise in peak temperature of the burnt zone of about 17 K, NO_x emissions increase by 0.63 g/kWh, thereby giving proof to the strong exponential dependence on temperature as reported in literature [57]. Next to earlier combustion phasing, a reduction in burn duration of 3 °CA is responsible for the lower fuel consumption. Adding an EGR rate of $x_{EGR} = 20$ % (OP2), prolongs combustion, which, in turn, requires advanced ignition timing for same CA50. The peak in burnt zone temperature decreases down to that of the ROP, leading to comparable NO_x emissions. EGR reduces mean in-cylinder temperature at same CA50, however, the wall heat losses of 16.5 %-points are still relatively high compared to the ROP. This originates from the earlier heat release with comparable temperatures but at lower A/V ratios. Since burn duration of OP2 is slightly longer (0.8 °CA) than the one of the ROP, the benefit in ISFC of 4.6 g/kWh almost entirely arises from the thermodynamic more favourable combustion phasing.

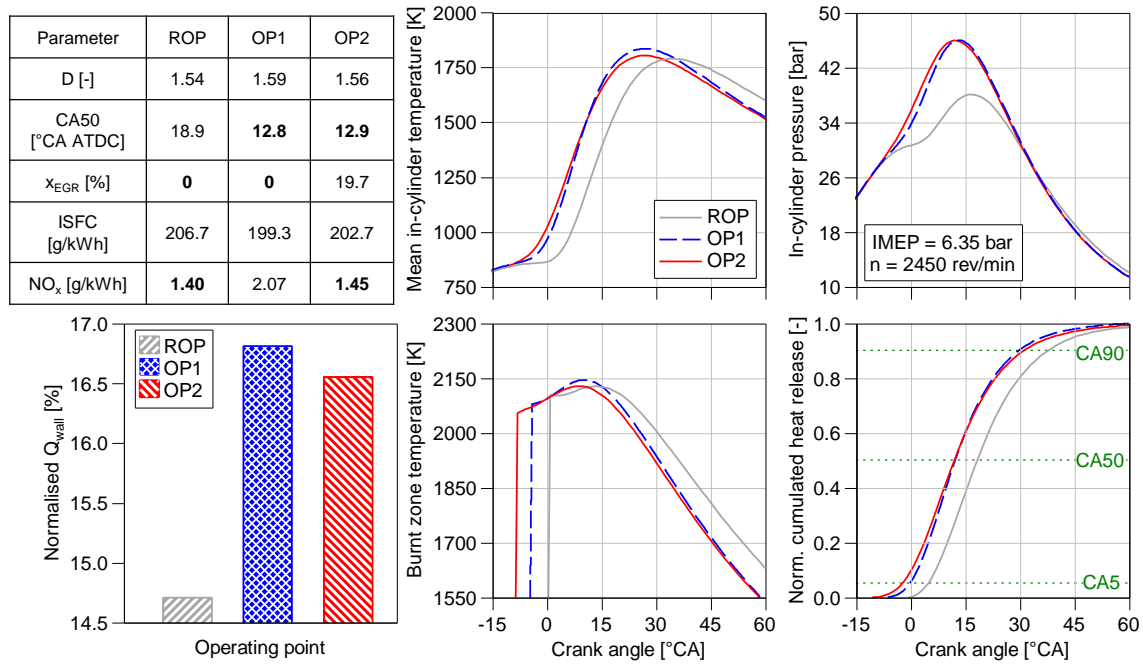| Parameter	ROP	OP1	OP2
D [-]	1.54	1.59	1.56
CA50 [°CA ATDC]	18.9	**12.8**	**12.9**
x_{EGR} [%]	**0**	**0**	19.7
ISFC [g/kWh]	206.7	199.3	202.7
NO_x [g/kWh]	**1.40**	2.07	**1.45**

Figure 7-16: Characteristic parameters, normalised wall heat losses and mean in-cylinder temperature, in-cylinder pressure, burnt zone temperature and normalised cumulated gross heat release over crank angle for selceted operating points at IMEP = 6.35 bar

The pressure traces of same CA50 are very similar, regardless of mixture composition, while comparing OP2 to ROP shows that a much higher pressure level at comparable combustion temperature becomes possible with the addition of EGR. This holds out the prospect of operating the engine at higher IMEP but same NO_x emissions.

7.2.2 Investigations at Constant NO_x Emissions

After studying the effect of EGR at constant IMEP, its potential to increase IMEP without altering NO_x emissions of the ROP of 1.4 g/kWh and the half of it (0.7 g/kWh) was evaluated. Starting from the ROP with $x_{EGR} = 0$ %, a part of air was substituted with exhaust gas and ignition timing advanced until meeting the predefined value in NO_x at an accuracy of −/- 5%. Subsequently, ignition timing was retarded and the amount of fuel increased in steps of 0.025 kg/h, leading to lower dilution ratios. This procedure was conducted for all EGR rates until CA50 exceeded 24 °CA ATDC.

Figure 7-17 shows IMEP (top) and ISFC (bottom) against CA50 for all EGR rates investigated at NO_x emissions of 1.4 g/kWh (left) and 0.7 g/kWh (right). EGR allows the engine to operate with the same amount of fuel at earlier CA50 but constant NO_x emissions. It can be seen that for both investigated NO_x values and all EGR rates, except $x_{EGR} = 25$ %, ISFC follows a practically linear trend. The enhanced intake port temperature that deteriorates charging efficiency is the reason why ISFC of $x_{EGR} = 25$ % has a distinct offset to the other operating points. For $NO_x = 1.4$ g/kWh, the highest advantage in engine efficiency is found at $x_{EGR} = 20$ % as CA50 can be advanced by 4.5 °CA, improving ISFC by

4.8 g/kWh and increasing IMEP by 0.15 bar compared to the ROP. With rising amount of fuel (i.e. lower dilution ratio D), ignition timing needs to be retarded to obtain CA50 that still complies with the predefined threshold NO_x emissions. IMEP further increases over the whole range. To reduce NO_x emissions to half of the reference value at same CA50, the engine needs to operate at higher λ, leading to an IMEP of 5.91 bar. The decreasing specific heat capacity of the exhaust gas diminishes the potential of EGR to hinder NO formation and therefore to increase IMEP and/or reduce ISFC. Again, $x_{EGR} = 20\%$ leads to the highest benefit in ISFC of -2.5 g/kWh (compared with $x_{EGR} = 0\%$) by advancing CA50 by 3.3 °CA. For similar ISFC, the highest IMEP amounts to 6.04 bar. For an EGR rate of $x_{EGR} = 25\%$ and NO_x emissions of 1.4 g/kWh, an inflection point occurs at about CA50 = 16 CA ATDC. The relative air-fuel ratio amounts to $\lambda = 1.06$, which is close to the peak in NO_x formation given in literature at about $\lambda \approx 1.1$ [57]. Hence, combustion phasing could be advanced beyond this value until nearly stoichiometric combustion was reached. It leads to the highest IMEP of this approach, however, at the expense of 3.1 g/kWh in ISFC.
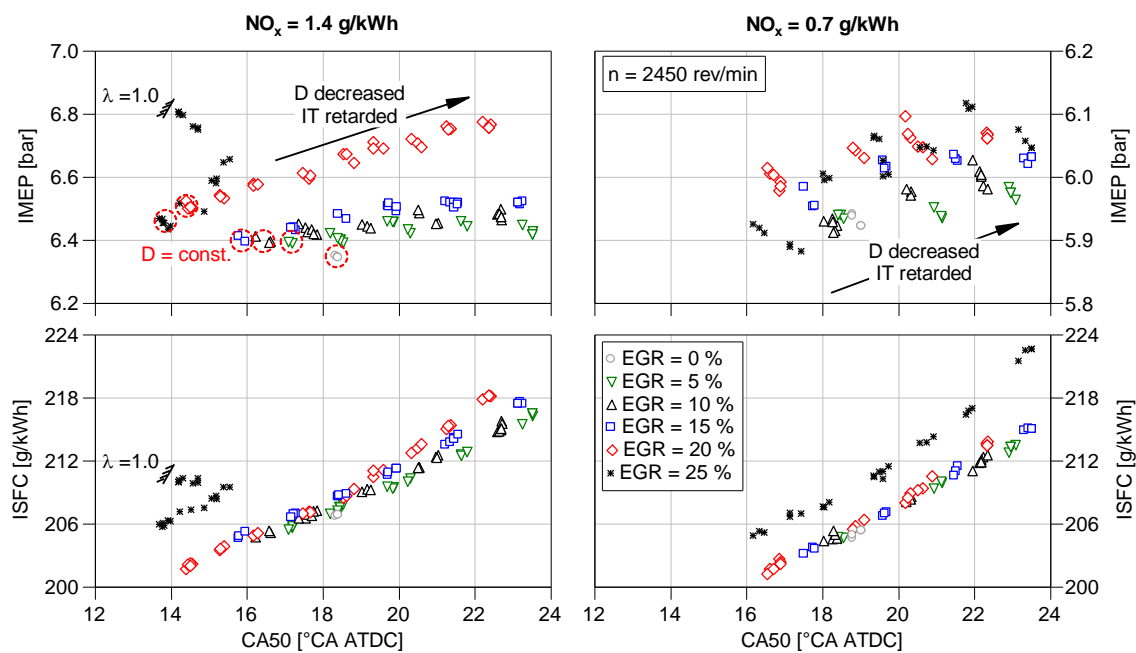

Figure 7-17. IMEP (top) and ISFC (bottom) over combustion phasing CA50 for different EGR rates and constant NO_x emissions of 1.40 g/kWh (left) and 0.70 g/kWh (right) at n = 2450 rev/min

Further analysis shall prove the reason of the aforementioned inflection point. In this context, it is important to highlight that combustion temperature and the concentrations of O_2 and N_2 are the decisive parameters for thermal NO production. Figure 7-18 plots the relative air-fuel ratio (top left), as indicator for O_2 fraction, and the fuel conversion ratio (bottom left) against CA50 for EGR rates of $x_{EGR} = 20\%$ and 25%. λ decreases practically linearly over CA50 for EGR rates up to $x_{EGR} = 20\%$, a trend that is representative for all lower EGR rates. This is also observed for $x_{EGR} = 25\%$ until the mixture exhibits $\lambda = 1.06$,

from which on CA50 advances again until meeting almost stoichiometric conditions. Operating points of same EGR rate, CA50 and NO$_x$ emissions but differing IMEP (OP1 and OP2) become possible. The temperature of the burnt zone of OP1, OP2 and the ROP in Figure 7-18 (top right) shows similar peaks for OP1 and ROP, while both differ to OP2 by approximately 40 K. Since the N$_2$ fraction of the mixture of OP1 and OP2 remains practically the same, the inflection point can be ascribed to the lack of O$_2$. The insufficient O$_2$ fraction also influences the fuel conversion ratio that usually increases as λ of a lean mixture is reduced, as exemplarily shown for x$_{EGR}$ = 20 %. However, the insufficient O$_2$ fraction for x$_{EGR}$ = 25 % hinders the whole fuel to be converted completely. As a result of a poor fuel conversion ratio, combustion duration of OP2 evidently increases, albeit it operates with lower λ and higher combustion temperature than those of OP1 (see Figure 7-18, bottom right). Compared to the ROP, the EGR rate of OP1 and OP2 increases burn duration significantly, while it diminishes the peak heat release rather moderately.
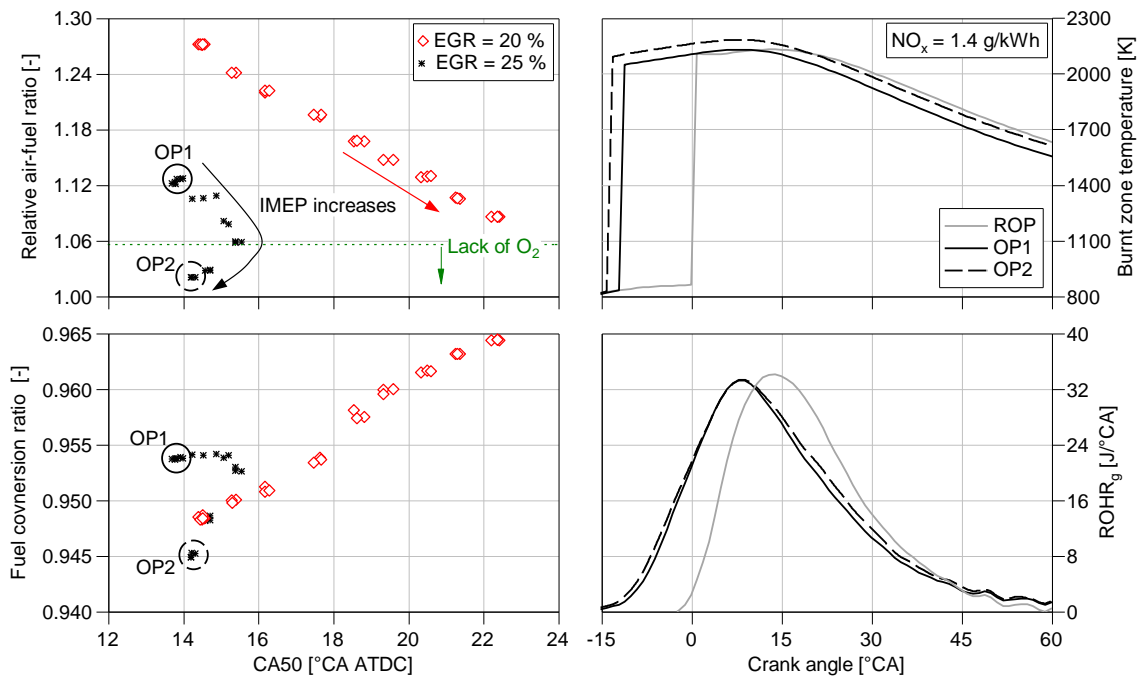

Figure 7-18: Relative air-fuel ratio λ (top left) and fuel conversion ratio (bottom left) against combustion phasing CA50 for x$_{EGR}$ = 20 and 25 %; Burnt zone temperature (top tight) and gross rate of heat release ROHR$_g$ (bottom tight) over crank angle for selected operating points (NO$_x$ emissions = 1.4 g/kWh)

The results suggest that the influence of EGR enhances with rising EGR rates and decreasing dilution ratios D. Both increase the mixture's specific heat capacity, as it becomes clear when analysing the molar mixture composition in the bar diagram in Figure 7-19. In this analysis, air is divided into a stoichiometric and an excess part, while the recirculated exhaust gas consists only of O$_2$, N$_2$, CO$_2$ and H$_2$O, meaning that emissions such as NO$_x$, CO and HC are neglected. Despite the use of precise actuators on the test bench, NG fraction of the analysed operating points varied slightly. Since the stoichiometric part of air is 10.6 times that of the NG used in the experiments, even minor differences might give

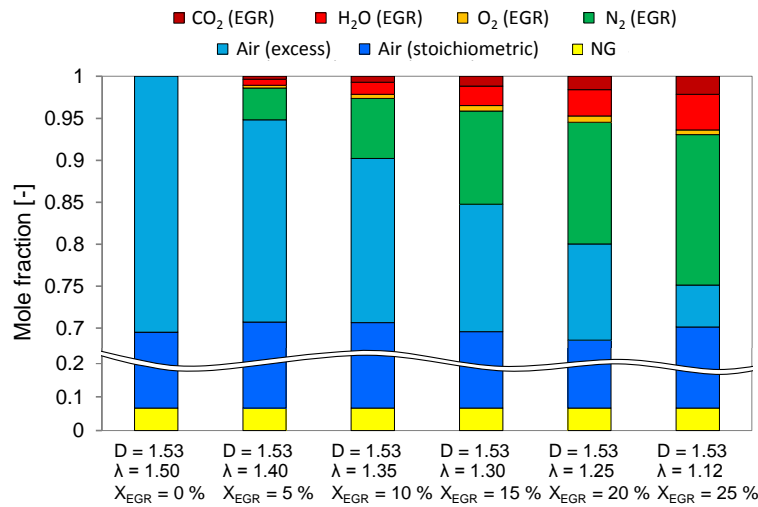the impression of a large deviation that is emphasised by an enlarged ordinate of the diagram from 0.7 to 1.0.

Figure 7-19: Mole fraction of the aspirated mixture for same dilution ratio and varying EGR rate at $NO_x = 1.40$ g/kWh and n = 2450 rev/min (residual gas neglected)

With augmenting EGR rate, the fraction of excess air and therefore that of O_2 falls. The O_2 concentration of the exhaust gas increases for EGR rates up to $x_{EGR} = 20$ %, whereas it becomes lower again for $x_{EGR} = 25$ % due to small fraction of excess air of the yet unburnt air-NG-exhaust gas mixture. All other components of the exhaust gas increase, while merely CO_2 and H_2O contribute to a higher mixture heat capacity.

7.2.3 Influence of EGR on Knocking Tendency

As literature reports (cf. Section 2.5.2), the temperature-reducing effect of EGR is also an effective means to avoid knocking, as it is particularly applied to stoichiometric running engines. $\lambda = 1.0$ combined with a TWC could also become a possible concept for small cogeneration engines if a tightening of the NO_x emission limits beyond those that enter into force in 2018 takes place. This encouraged to analyse the potential of EGR to reduce the knocking tendency of the test engine. Since the compression ratio of the baseline engine is quite resistant to knocking, it was increased by replacing the piston with the one designed for the Miller configurations. The engine was then operated at maximum brake torque (MBT, CA50 = 8 °CA), while IMEP was increased until the knock margin was met at IMEP of 6.6 bar. Knocking combustion was detected when the operating point fulfilled the threshold criteria, defined in Section 4.2.2, for at least 1 of 200 cycles of multiple consecutive measurements. Subsequently, the EGR rate was increased stepwise and ignition timing as well as dilution ratio adjusted to increase IMEP gradually, as shown in Figure 7-20 (left). The feasible IMEP increases up to 7.5 bar where an EGR rate of $x_{EGR} = 21$ % is required. The peak combustion pressure p_{max}, an interesting indicator for engine stress in terms of a possible series introduction, increases from 62 to 66 bar (see Figure 7-20, right).

Both IMEP and p_{max} rise with increasing EGR rate and decreasing dilution ratio (i.e. higher amount of fuel). Owing to an increase of burn duration and IMEP, exhaust gas temperatures enhance. For the highest achievable IMEP of 7.5 bar, the engine operates at ISFC = 198.2 g/kWh with a stoichiometric mixture. Coupled with an exhaust gas temperature of about $T_{exh} = 530$ °C, engine operation at $\lambda = 1.0$ would allow for converting all emissions using a TWC.
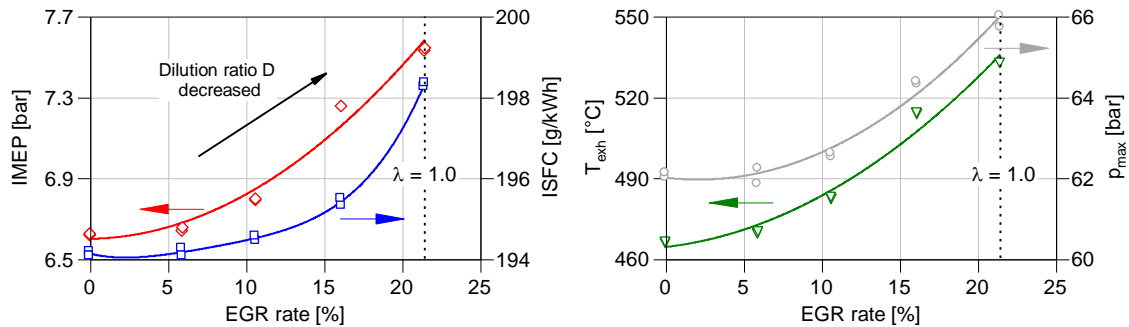

Figure 7-20: ISFC and IMEP (left) as well as exhaust gas temperature and maximum pressure p_{max} (right) over EGR rate for operating points at the knock margin (n = 2450 rev/min, r_{geo} = 15.25)

7.3 Comparison Between Early and Late Miller Cycle

The first goal of this section is to find early and late Miller configurations of same effective compression ratio that enable a direct comparison of both valve timing strategies. Based on the results in Chapter 5, the baseline piston was replaced with the Miller piston, increasing the geometrical compression ratio from 13.20 to 15.25. With respect to possible deviations between simulation and experiment, various Miller cam profiles were manufactured and tested using test bed engine I. Subsequently, the determined configurations were transferred to engine II, where trials with air- and air-EGR-diluted mixtures were carried out.

7.3.1 Determination of Comparable Early and Late Miller Configurations

Manufacturing tolerances can lead to erroneous valve timings and therefore require a reliable method to determine the accurate intake valve closing. In this work, it was determined by analysing the in-cylinder pressure signal with respect to noise caused by the impinging intake valve upon the valve seat of the cylinder head. The valve clearance was kept constant throughout all experiments to ensure comparability across the different configurations.

The approach to determine the effective compressions ratio described in Section 3.3, needs the precise absolute in-cylinder pressure for obtaining accurate results. To this end, the thermodynamic zero-line corrected pressure signal was used to iteratively adjust the integrated $ROHR_g$ to zero during the compression stroke in post-processing. The considered range varies in literature [6, 47, 72] and was set to $80 - 40$ °CA BTDC in this work. The

lower limit of this method is given by late Miller IVC, while the chance of erroneous results due to rising wall heat losses restricts values beyond 40 °CA BTDC.

First engine trials with modified valve timing and adjusted piston design were carried out using test bed engine I. The 1D study in Chapter 5 showed that taking over the valve overlap of the baseline for the Miller valve timings leads to fairly constant residual gas fractions. To validate this finding and to ensure that the direct comparison of early and late Miller valve timing is not affected by differing mixture composition, experimental data was analysed by applying the residual gas model addressed in Section 4.2.3. Figure 7-21 shows the residual gas fraction of engine experiments for all configurations at same λ and CA50. The value of the baseline engine of 4.85 % could be achieved for all Miller valve timings within a deviation of −/- 0.1 %-points except for IVC = 80 °CA, which is likely caused by errors in the manufacturing process of the valve cam.
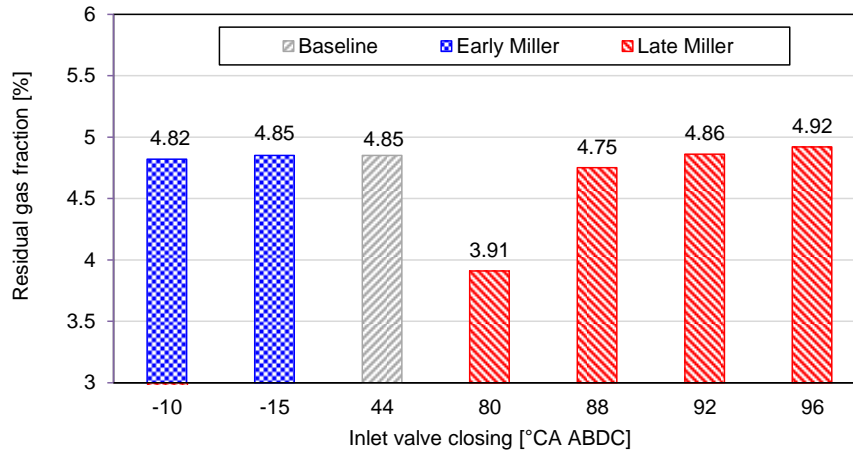

Figure 7-21: Residual gas fraction over intake valve closing determined for test bed engine I at $\lambda = 1.57$ and CA50 $\approx$ 19 °CA ATDC (baseline $r_{geo} = 13.20$; Miller $r_{geo} = 15.25$)

Knowing the exact mixture composition, the effective compression ratio was determined for all configurations. To achieve the same effective compression ratio as the baseline engine $r_{\epsilon,eff} = 13.53$, the valve timings needed to be advanced by -5 for early and -4 °CA for late Miller cycle relative to the IVC determined in the 1D study. Figure 7-22 shows the p-V diagram of the according configurations and the baseline engine. Owing to the sensitivity to mixture composition, temperature and pressure, it was important to evaluate $r_{\epsilon,eff}$ for the operating conditions of the reference operating point ($\lambda = 1.57$, CA50 $\approx$ 19 °CA ATDC). The inlet pressure of the air mass flow into the cogeneration unit, controlled by a conditioning unit, serves as ambient pressure $p_{air} = p_{amb} = 995$ mbar. Due to the strong dependency between $r_{\epsilon,eff}$ and pressure close to TDC, as shown in Chapter 5, the pressure level at the crank angle of the configuration with the earliest SOC (3 °CA BTDC) is analysed. All three valve timings show same pressure level at 3 °CA BTDC, whereas the peak combustion pressure p_{max} varies slightly due to differing heat release and wall heat losses.

The highest value in p_{max} reached by the baseline engine, stems from the larger in-cylinder charge, while the differences between both Miller valve timings likely occur due to dissimilar charge motion. The high-pressure loops match well while the valves of both Miller configurations are closed. The polytropic change of state for late Miller cycle reaches ambient pressure p_{amb} marginally earlier than the pressure trace of early Miller valve timing, leading to very similar volumes at the effective BDC $V_{BDC \ eff}$. Consequently, the effective compression ratio amounts to $r_{c \ eff} = 13.56$ for late and $r_{c \ eff} = 13.58$ for early Miller cycle.
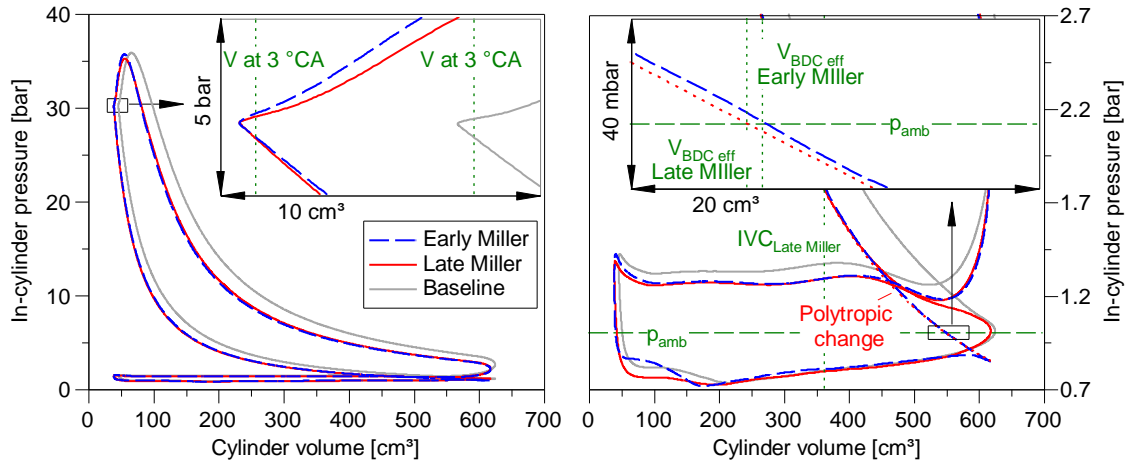

Figure 7-22: Measured p-V diagram of the baseline engine using engine test bed I at $\lambda = 1.57$ and CA50 $\approx$ 19 °CA ATDC

Figure 7-23 (left) shows all investigated configurations for engine I and engine II. The trials prove that $r_{c \ eff}$ is very sensitive to IVC at constant geometrical compression ratio of $r_{geo} = 15.25$. Advancing IVC from 96 to 92 °CA ABDC, for instance, increases $r_{c \ eff}$ by 0.42 units for engine I. After identifying two comparable Miller configurations using test bed engine I, engine testing carried out with test bed engine II showed a higher effective compression ratio for baseline valve timing of $r_{c \ eff} = 13.71$.

Based on the aforementioned findings, minor deviations in $r_{c \ eff}$ between the three different configurations were expected when they were transferred from one test bed to the other. However, neither of the valve timings experiences the same change in $r_{c \ eff}$ as the baseline engine. In fact, relative to the baseline, the effective compression ratio of early Miller (IVC = -15 °CA ATDC) increases to $r_{c \ eff} = 13.88$ and decreases to $r_{c \ eff} = 13.64$ for late Miller cycle. In order to still ensure a fair comparison between both Miller cycles, IVC needed to be advanced from 92 to 88 °CA ABDC to lift the effective compression ratio to $r_{c \ eff} = 13.98$. The effective expansion/compression ratio results to $ECR_{eff} = 0.968$ for the baseline, $ECR_{eff} = 1.091$ for the early and $ECR_{eff} = 1.099$ for the late Miller configuration.
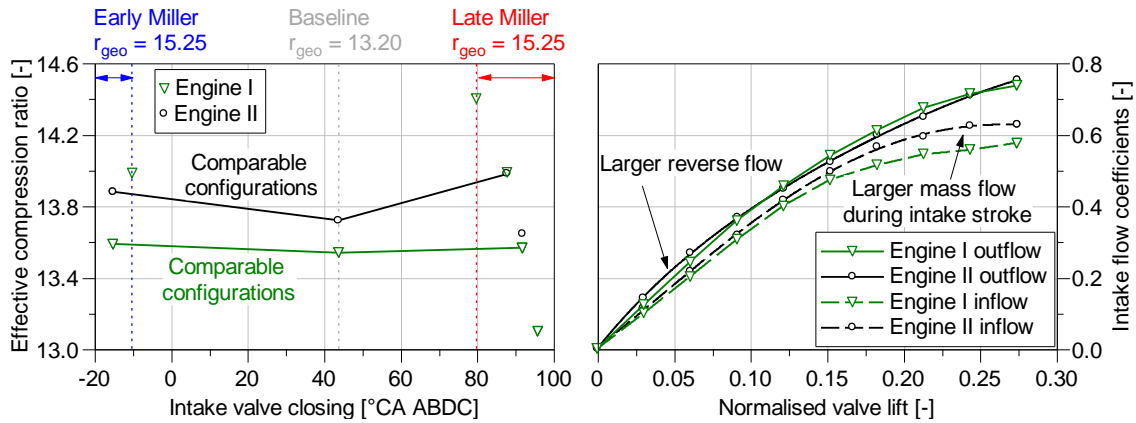
Figure 7-23: Effective compression ratio over intake valve closing at CA50 ≈ 19 °CA ATDC (Miller $r_{geo} = 15.25$, baseline $r_{geo} - 13.20$) (left) and flow coefficients of the intake port over normalised valve lift for cylinder head I and II (right)

The deviations in $r_{e,ff}$ are likely attributable to engine component tolerances, including the manufacturing process of the iron casted cylinder head. It leads to differing flow coefficients, determined through flow bench testing, as shown against the valve lift normalised to the inner valve seat diameter in Figure 7-23 (right). The higher values for both in- and outflowing direction observed for engine II, indicate, on the one hand, that the mass flow of the mixture that is aspirated during the intake stroke increases. On the other hand, it favours the mixture to exit the cylinder via the intake port during the compression stroke for intake valve closing markedly after BDC. When operating with late Miller cycle, the changes on the outflowing direction appear to be predominant, leading to lower charging efficiency, followed by a reduced pressure rise during the compression stroke. On the contrary, configurations for which no or only a marginal reverse flow takes place such as the baseline and early Miller valve timing benefit from the differing flow coefficient in terms of charging efficiency.

The modified valve timings alter intake port temperature. Starting from baseline engine of $T_{intake} = 75$ °C, it decreases to 73 °C for early Miller as it avoids the minor reverse flow that takes place for the baseline engine. Late Miller cycle, on the contrary, experiences a pronounced reverse flow during the compression stroke that increase intake port temperature to $T_{intake} = 108$ °C. Nevertheless, as 1D CFD calculations already suggested, configurations of the same effective compression ratio $r_{e,ff}$ lead to similar thermodynamic condition in the late part of the compression stroke, regardless of IVC. To evaluate how the small differences in the effective compression ratio between the selected Miller valve timings influence the thermodynamic conditions of the mixture, in-cylinder pressure (left) and temperature (right) are plotted at same relative air-fuel ratio versus crank angle in Figure 7-24. As a result of the higher effective compression ratio, pressure and temperature of the late Miller configuration lie slightly above the ones of early Miller. For the same reason, both Miller configurations exceed pressure and temperature of the baseline engine at the end of

the compression stroke. The deviations in the effective compression ratio between baseline and late Miller configurations lead to a modest difference of 0.68 bar and 6.7 K at SOC (3 °CA BTDC). Calculating the laminar burning velocity using the correlation of Liao/Witt [79, 176], for example, results to a deviation of only 1.5 %.
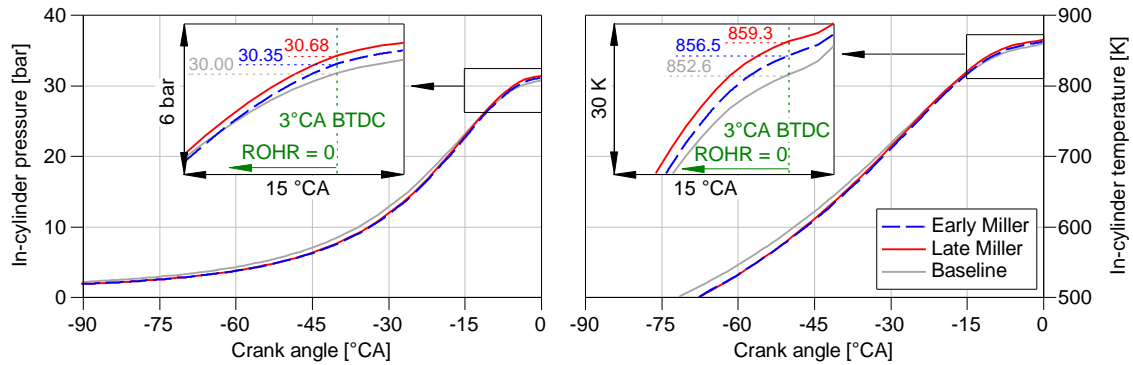

Figure 7-24: In-cylinder pressure (left) and mean temperature (right) versus crank angle of the baseline and selected Miller configurations using test bed engine II at constant λ

Table 7-2 summarises the parameters of the configurations selected for further engine trials using test bed engine II. From this, it can be derived that the deviations caused by slightly differing effective compression ratios are thoroughly acceptable for drawing a representative comparison between the three valve timing strategies, in terms of efficiency, emissions, combustion and gas exchange, in the remaining part of this thesis.

Table 7-2: Comparison of the baseline, early and late Miller configuration for test bed engine II

Parameter	Unit	Baseline	Early Miller	Late Miller
IVC	[°CA ABDC]	44	-15	88
r_{geo}	[-]	13.20	15.25	15.25
$r_{c\,eff}$	[-]	13.71	13.88	13.98
ECR_{eff}	[-]	0.968	1.091	1.099
T_{intake}	[°C]	75	73	108
T_{cyl} (3 °CA BTDC)	[K]	852.6	856.5	859.3
p_{cyl} (3 °CA BTDC)	[bar]	30.00	30.35	30.68

7.3.2 Miller Cycle in Lean-burn Operation

To evaluate fundamental differences between both Miller approaches in engine performance, CA50 sweeps in lean-burn operation were carried out at constant IMEP of 6.35 bar. The larger mass aspirated for late Miller cycle requires a leaner mixture to achieve same IMEP of 6.35 bar. In light of the significant influence of λ on combustion, an additional run was conducted, in which λ was adjusted for each CA50 to the same value of early Miller cycle. IMEP then increases from 6.35 to about 6.43 bar.

7.3.2.1 Engine Efficiency and NO$_x$ Emissions

ISFC (left) and CA50 (right) of the three respective configurations are plotted against NO$_x$ emissions in Figure 7-25. Late Miller cycle operated at IMEP = 6.35 bar shows the lowest NO$_x$ emissions due to the higher relative air-fuel ratio. In fact, a larger mass of excess air is available to absorb the released heat during combustion. It is possible to operate the engine within the low NO$_x$ regime at more advanced CA50 than with early Miller at same NO$_x$ emissions, thus leading to lower fuel consumption. The decreasing sensitivity of ISFC to CA50 in the high efficiency regime diminishes this advantage. Here, early Miller cycle shows a benefit in ISFC that can be observed at same CA50 over the whole range investigated. ISFC remains fairly unaffected as the relative air-fuel ratio is reduced by about $\Delta\lambda \approx 0.02$ for late Miller cycle. NO$_x$ emissions increase up to 20 %, deteriorating the trade-off compared to early Miller valve timing.
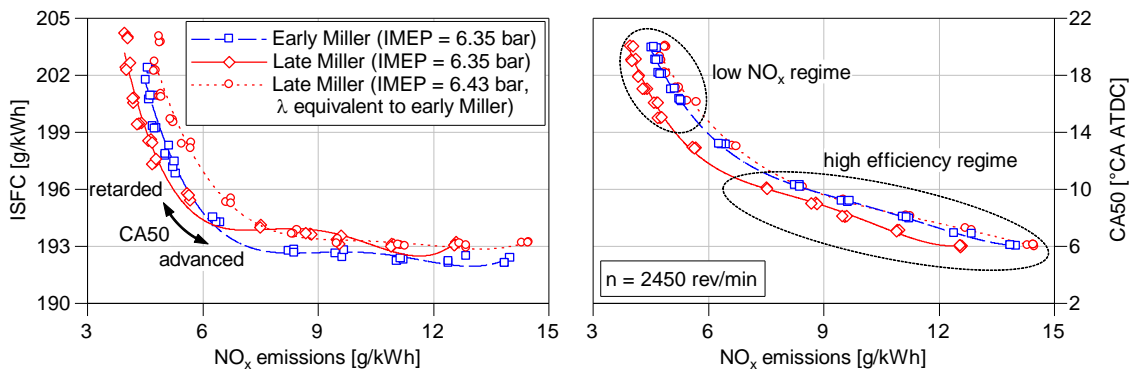

Figure 7-25: Indicated specific fuel consumption ISFC (left) and combustion phasing CA50 (right) over NO$_x$ emissions at n = 2450 rev/min

Splitting ISFC into its gross value (ISFC$_g$) (left) and the share that accounts for pumping work (ISFC$_p$) (right) is useful for identifying the sources that cause the differences between both valve timing strategies, as shown in Figure 7-26.
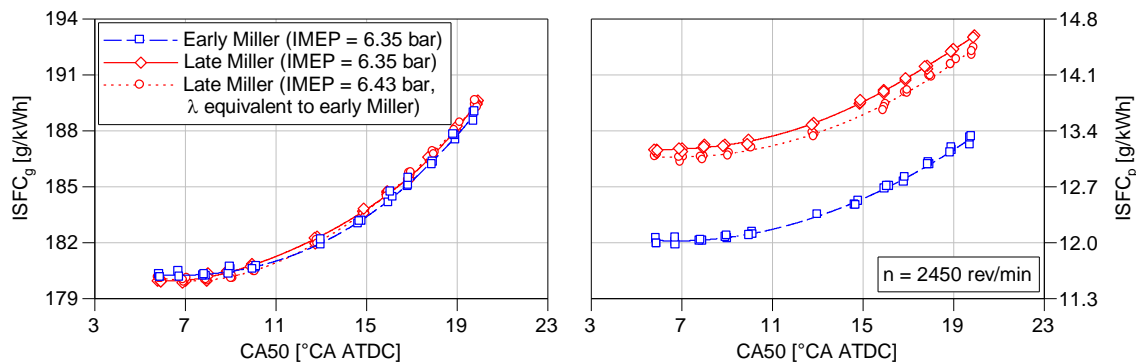

Figure 7-26: Gross indicated fuel consumption ISFC$_g$ (left) and pumping indicated fuel consumption ISFC$_p$ (right) over combustion phasing CA50 at n = 2450 rev/min

ISFC$_g$ is similar at same CA50 for all three series of measurements with minor advantages

for early Miller for combustion phasings after CA50 = 10 °CA ATDC. The major differences occur during gas exchange as the lower ISFC$_p$ for early Miller shows. The gap to late Miller valve timing remains practically the same across the CA50 sweep. The increasing ISFC$_p$ as combustion phasing is retarded can be explained by rising charging efficiency and pumping work in response to falling cylinder head temperature. For late Miller valve timing, a lower mixture dilution leads to a higher pressure level at EVO of same CA50, thus reducing pumping work for operating points of constant IMEP of 6.43 bar.

The comparison of both valve timing strategies at CA50 = 8 °CA ATDC and IMEP = 6.35 bar in the p-V diagram in Figure 7-27 (left) shows no discernible difference while the valves are closed. The first notable deviation between both cycles occurs during gas exchange around TDC. For early Miller valve timing, the steeper valve lift gradient combined with an arriving intake pressure wave shortly before IVO (see Figure 7-27, right), favours pumping work at the beginning of the intake stroke. While this attenuates pumping losses slightly, the key difference is found, again, in the losses in compression of late Miller, which, converted to mean effective pressure, amount to -0.03 bar. To cancel out the higher losses during gas exchange for achieving same IMEP, late Miller requires an IMEP$_g$ that is 0.04 bar higher than early Miller cycle.
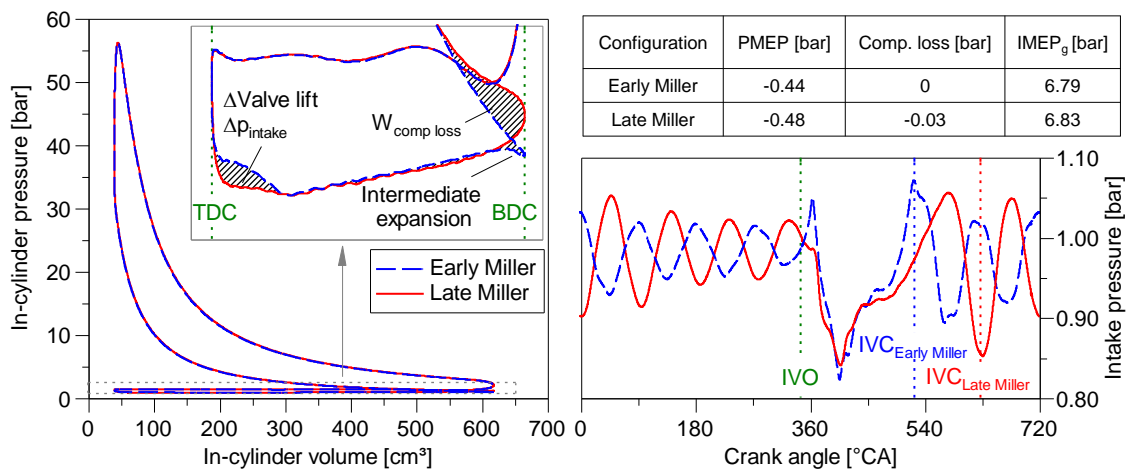

Configuration	PMEP [bar]	Comp. loss [bar]	IMEP$_g$ [bar]
Early Miller	-0.44	0	6.79
Late Miller	-0.48	-0.03	6.83

Figure 7-27: p-V diagram (left) and intake pressure (right) of early and late Miller cycle at CA50 = 8 °CA ATDC (IMEP = 6.35 bar)

7.3.2.2 3D CFD Assisted Combustion Analysis

Both Miller engine setups exhibit very similar ISFC$_g$, regardless of whether IMEP or the relative air-fuel ratio is held constant for a given CA50. The minor differences could be linked to varying burning behaviour caused by dissimilar charge motion. In order to obtain a deeper insight into the gas exchange, the degree of turbulence and the mixture homogeneity, 3D CFD simulations for both Miller valve timings were carried out.

Figure 7-28 (left) shows the mean turbulent kinetic energy TKE within pre- and main combustion chamber over crank angle for both valve timings. While inside the prechamber

only a small advantage is found for early Miller cycle, particularly at the end of the compression stroke, the differing turbulence history in the main combustion chamber requires deeper explanation: At the beginning of the intake stroke, the aperture between valve seat and lip is relatively small. This provokes shear layers with large velocity gradients, leading to a peak in TKE within the relatively small in-cylinder volume shortly after TDC (0 °CA). The smaller gap between valve disc and valve seat caused by the flatter gradient of the late Miller valve lift leads to a higher peak turbulence level. It occurs a little later than for early Miller cycle, which shows a second peak after reaching its maximum short before the intake valve closes as result of mixture flowing into the combustion chamber at high velocities. TKE decreases gradually for both valve timings until the compression stroke is halfway through. Late Miller IVC provokes the dissipation of TKE into heat as mixture exits the cylinder during the compression stroke, thus lowering the turbulence level inside the cylinder. For both valve timings, TKE increases in the second half of the compression stroke when macroscopic flow decomposes into turbulence. After reaching its final peak before TDC, it continues dissipating into internal energy. Since this occurs with a steeper gradient for early Miller thanks to a higher dissipation rate, turbulence is expected to fall below that of late Miller after TDC. Representative results beyond TDC, however, would require combustion modelling that accounts for the impact of the flame-jets that propagate from the prechamber into the main combustion chamber and thereby influencing its turbulence level.
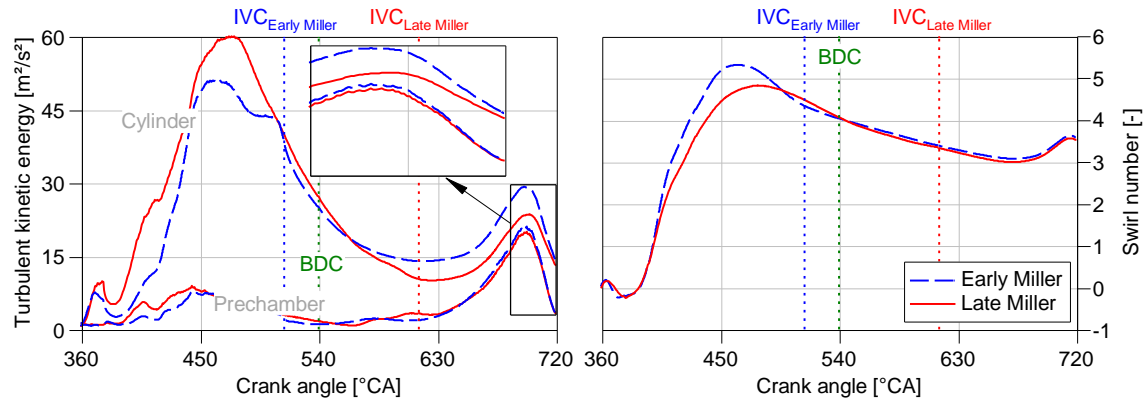

Figure 7-28: Mean turbulent kinetic energy (left) and swirl number (right) over crank angle for early and late Miller cycle

As with the 1D study in Chapter 5, both valve timings show very similar intake mass flows (cf. Figure 5-4) for about the first half of the intake stroke. It can be inferred that within that span, the same kinetic energy enters the main combustion chamber that consists either of large scale vortex motion, swirl and tumble, or microscale turbulence, i.e. TKE [3]. As a direct consequence, early Miller must exhibit either a more pronounced tumble or swirl motion. Figure 7-28 (right) proves that the swirl number of the early Miller configuration is higher in the respective range and falls shortly after the peak valve lift, owing to a

reduced mass flow into the combustion chamber. It remains at a similar level for both valve timings as the cycle progresses. As known from Diesel engines, a pronounced swirl promotes mixture homogenisation. Since the engine is equipped with only one intake port, designed as swirl port, practically no tumble could be observed.

Figure 7-29 displays ignition timing IT, burning delay IT-CA5 and burn duration CA5-CA90 over CA50 for both Miller valve timings. Note that λ was set constant for operating points of same CA50. The higher temperature level inside the pre- and main combustion chamber for late Miller cycle favour the laminar burning velocity, yet ignition timing and burning delay for engine operation at same CA50 are almost identical for both valve timings. Burning delay decreases as combustion phasing is advanced, despite increasing λ in the main combustion chamber as well as rising residual gas fraction and falling temperature within the prechamber. This likely stems from the higher TKE within the prechamber, peaking at about 25 °CA BTDC and decreasing right after (cf. Figure 7-28, left). Early Miller exhibits a shorter burn duration for CA50 before 16 °CA ATDC. It decreases with a steeper gradient until CA50 = 13 °CA and becomes then quite insensitive to combustion phasing. Late Miller, on the other hand, reveals a consistently decreasing trend for burn duration over CA50.
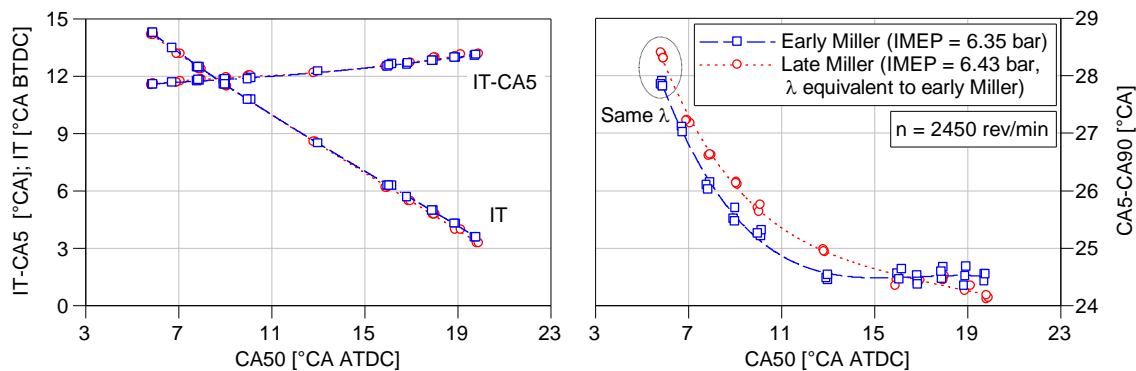

Figure 7-29: Burning delay IT-CA5 and ignition timing IT (left) as well as burn duration CA5-CA90 (right) over combustion phasing for both Miller valve timings

The higher mean TKE calculated for early Miller cycle explains the faster burn duration at early CA50. Its gradient becomes stronger as piston approaches TDC compared to late Miller cycle, correlating with the prolonging burn duration for late CA50. Because of the higher mean TKE and swirl number, one could expect early Miller to also show a shorter IT-CA5 and to require retarded IT for achieving same CA50. However, when analysing the TKE distribution within the prechamber and its close vicinity in the piston bowl, as exemplary shown at 12 °CA BTDC in Figure 7-30, similar values for both valve timings are observed. The high level of turbulence extends over a larger volume for early Miller, thus leading to a shorter overall burn duration.
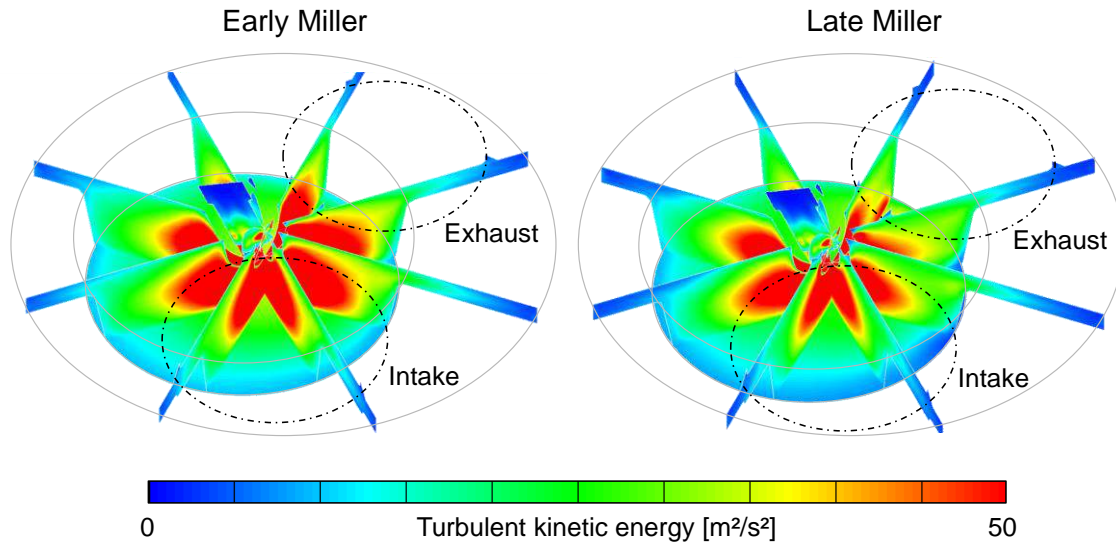
Figure 7-30: Distribution of turbulent kinetic energy for early (left) and late (right) Miller valve timing at 12 °CA BTDC

In addition to the turbulence level, also charge composition across the cylinder is decisive for combustion. The higher swirl during intake stroke for early Miller promotes the homogeneity of the air-fuel-residual gas mixture. The mass related residual gas fraction at 60 and 12 °CA BTDC, depicted for both valve timings in Figure 7-31, varies between approximately 3 and 8 %.
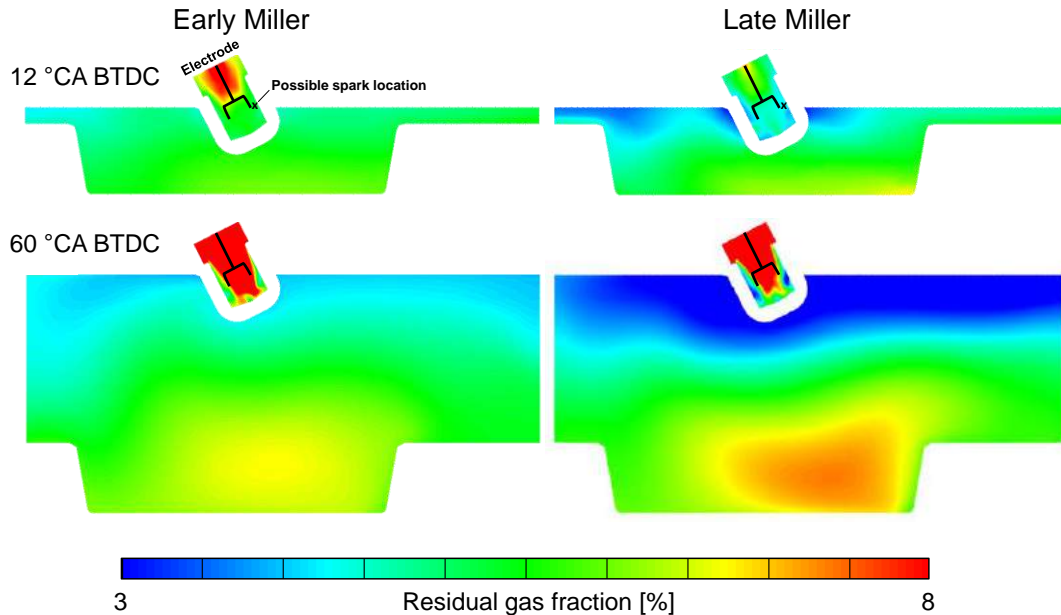

Figure 7-31: Residual gas fraction of early and late Miller valve timing at 60 and 12 °CA BTDC

For both crank angles, early Miller cycle exhibits a smaller gradient inside the main combustion chamber, whereas the residual gas content within the prechamber is significantly higher than for late Miller valve timing. At 60 °CA BTDC, just before a significant amount

of mixture flows from the main combustion chamber into the prechamber, late Miller cycle reveals a mixture that is more stratified, including a residual gas cluster in the piston bowl and a very pure air-fuel mixture near the roof of the combustion chamber. Consequently, less residual gas enters the prechamber during the compression stroke, thus improving combustion conditions.

The findings obtained from experiments and 3D CFD can be summarised as follows:

- Late Miller cycle compensates for lower turbulence in the main combustion chamber and prechamber through higher temperature and better homogeneity inside the prechamber, thus leading to same burning delay.

- Higher mean turbulence level is responsible for shorter combustion before 16 °CA ATDC in the case of early Miller valve timing. For later CA50, TKE is likely to decrease and the higher temperature level of late Miller to become predominant for burn duration.

For the sake of comparability, the burning behaviour of both valve timings was analysed at same λ for a given CA50, leading to higher IMEP for late Miller valve timing. It is worthwhile to mention that comparing both valve timing strategies at same IMEP would show similar trends of larger difference caused by the leaner mixture required for late Miller cycle.

The higher TKE observed for early Miller valve timing stands in contrast to the majority of findings from literature [40, 127, 136]. Nevertheless, as opposed to work of others, where early Miller valve timing was usually realised by reducing the valve lift curve proportionally, the crucial difference in this thesis was holding the maximum valve lift constant. To the author's knowledge, a similar procedure was only followed by Schutting et al. [142], however, the results are hardly comparable since supercharging was applied, thus affecting charge motion significantly.

7.3.3 Miller Cycle in Lean-burn Operation and EGR

The reduced charging efficiency requires both Miller configurations to operate at lower relative air-fuel ratios to meet the threshold IMEP of 6.35 bar. In an attempt to counteract the increasing NO_x emissions, caused by rising peak combustion pressure and temperature, EGR is added to the mixture. Analogously to the experiments using the baseline configuration in Section 7.2, the EGR rates were varied in increments of $\Delta x_{EGR} = 5\%$ at constant EGR temperature of $T_{EGR} = 75$ °C.

7.3.3.1 Engine Efficiency and NO_x emissions

Figure 7-32 shows ISFC and CA50 over NO_x emissions for the early (left) and late (right) Miller configuration of varying EGR rates at IMEP = 6.35 bar. The effect of EGR is similar to that for engine operation with baseline valve timing: On the one hand, lower combustion temperatures curtail NO_x emissions at same combustion phasing, but on the other

hand, EGR is detrimental to ISFC due to lower $ISFC_{ideal}$ and longer combustion duration. Therefore, EGR only improves the trade-off in the low NO_x regime, where a thermodynamically more favourable combustion phasing can be set that overcompensates losses from longer burn duration and unfavourable mixture properties.

Early Miller seems to be more affected by EGR than late Miller over the entire CA50 sweep. At an early combustion phasing of CA50 = 6 °CA ATDC, for example, an EGR rate of x_{EGR} = 15 % reduces NO_x emissions from about 14 to 8.8 g/kWh (-37 %) for early and from 12.6 to 8.3 g/kWh (-34 %) for late Miller cycle. The relative reduction is enhanced to 40 and 35 % for early and late Miller when shifting combustion phasing to CA50 = 20 °CA ATDC. A possible explanation is the higher specific heat capacity as a result of a lower dilution ratios for late CA50. While an EGR rate of x_{EGR} = 20 % leads to an expected increase of the typical EGR effect, the influence is intensified markedly when operating with early Miller valve timing. A notable drawback in ISFC becomes evident as combustion phasing is retarded from 14 to 16.5 °CA. The engine could not operate beyond this value without suffering IMEP or reducing the EGR rate again. The reason is found in engine operation close to stoichiometric conditions, i.e. at low O_2 concentration, thus reducing the fuel conversion ratio and lowering the rise of NO_x emissions with earlier CA50.
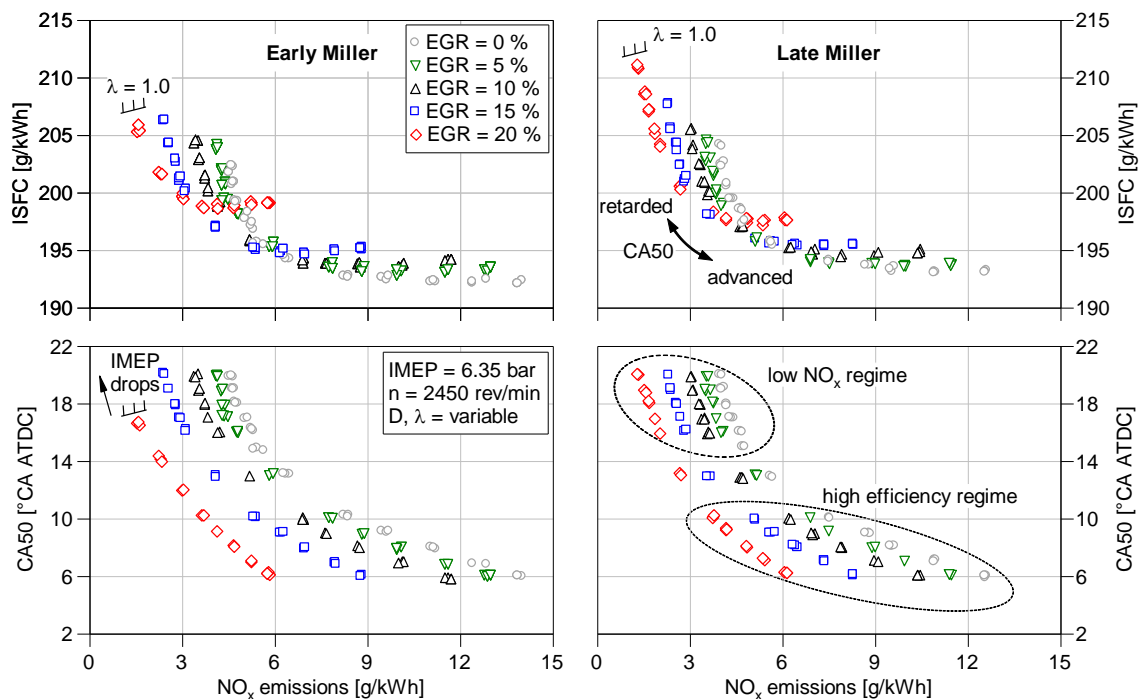
Figure 7-32: ISFC and CA50 over NO_x emissions for both Miller valve timings at varying EGR rates (IMEP = 6.35 bar, n = 2450 rev/min)

Figure 7-33 depicts the relative air-fuel ratio as function of NO_x emissions and the dilution ratio for all operating points investigated at IMEP = 6.35 bar. The dilution ratio becomes almost unaffected when operating the engine in the high efficiency regime and a constant EGR rate, arising from the small dependency of engine efficiency on early CA50. Since the

exhaust of a leaner mixture exhibits a higher O_2 concentration, the relative air-fuel and dilution ratio decrease with a lower gradient for late Miller valve timing. This is further enhanced by the fact that fuel consumption increases more for early than for late Miller cycle. At $x_{EGR} = 20\,\%$, early Miller mostly operates at $\lambda \approx 1.06$ and below. For the baseline engine, the respective relative air-fuel ratio was proven to be the edge to the lack of oxygen region, where NO_x emissions and fuel conversion ratio start to differ from their convenient dependency on O_2 known from lean-burn operation (cf. Section 7.2.2).
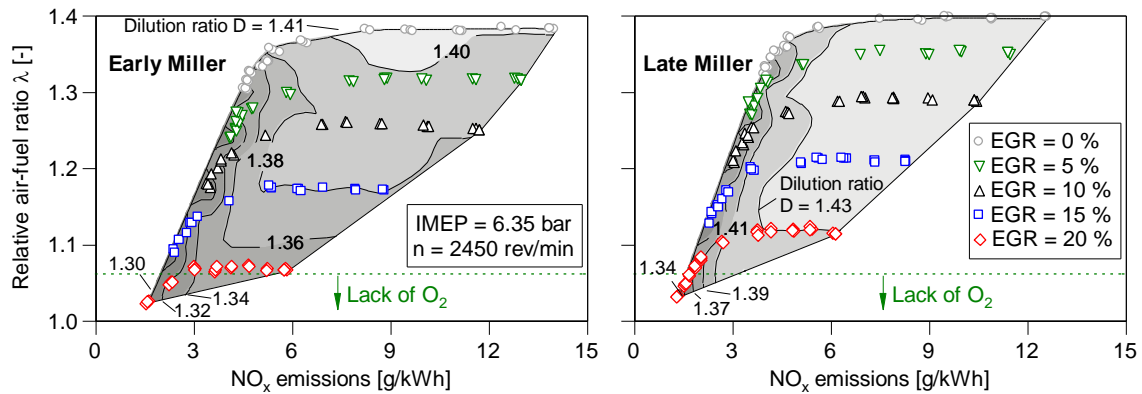

Figure 7-33: Relative air-fuel as function of NO_x emissions and dilution ratio for early and late Miller cycle of varying EGR rate at IMEP = 6.35 bar and n = 2450 rev/min

The lower dilution ratio required for early Miller leads to a higher fraction of CO_2 and H_2O and thereby increases the specific heat capacity of the exhaust gas. On the downside, and far more importantly, the amount of excess mass decreases with falling dilution ratio. The product of both mass and specific heat capacity yields its absolute heat capacity, which governs the heat absorbed during combustion. It is therefore decisive for combustion temperature and the formation of thermal NO. Figure 7-34 shows the diluent's absolute heat capacity of both valve timings as function of NO_x emissions for different EGR rates at a representative temperature for the start of combustion of 800 K.
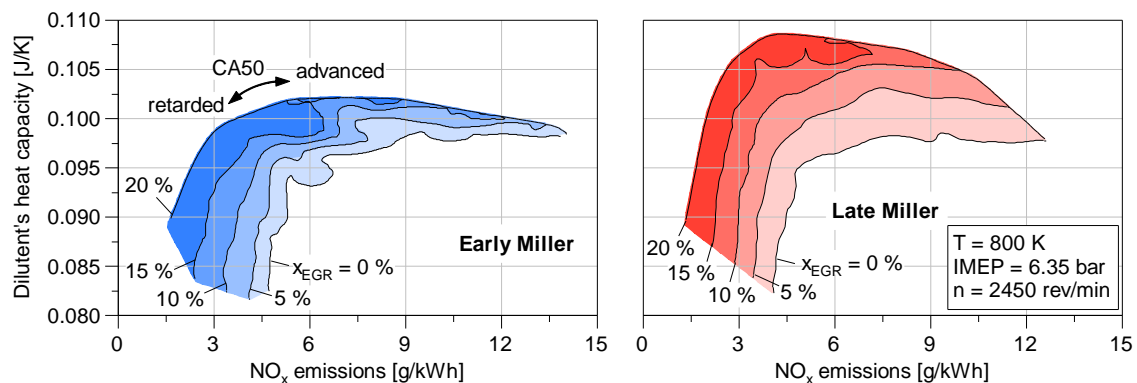

Figure 7-34: Absolute heat capacity of the diluent as function of the EGR rate and NO_x emissions for both Miller valve timings at a mixture temperature of T = 800 K

The reduced charging efficiency for early Miller leads to lower values, particularly for an

EGR rate of $x_{EGR} = 20\%$. Here, the significant increase in fuel consumption due to the lack of O_2 additionally decreases the amount of diluent, thus limiting the potential to increase the diluent's absolute heat capacity through EGR. From this it follows that lower charging efficiency is the reason why early Miller experiences higher NO_x emissions at same IMEP.

7.3.3.2 Combustion Behaviour

Owing to the small effect of EGR on the gas exchange (as described in Section 7.2.1.1) the main differences occur in the high-pressure loop, namely during combustion process. The lower dilution ratio and mostly more favourable flow conditions, discussed in Section 7.3.2.2, lead to slightly shorter burning delay and burn duration in engine operation with air-diluted mixtures at IMEP = 6.35 bar for early Miller cycle (see Figure 7-35).
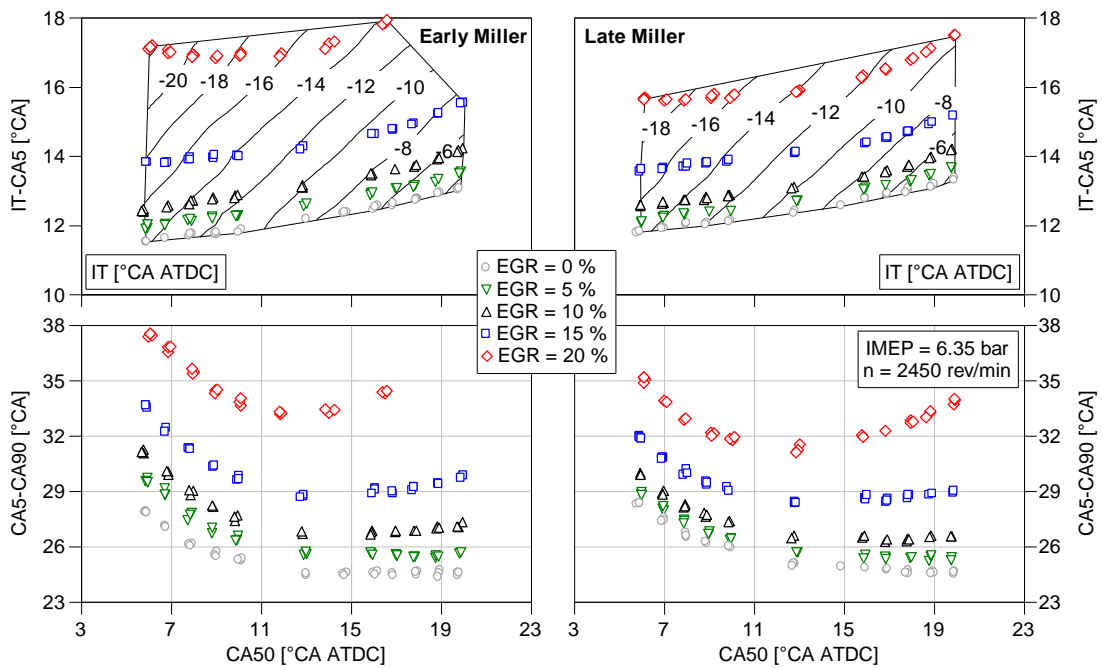

Figure 7-35: Burning delay IT–CA5 as function of ignition timing IT (top) as well as burn duration CA5-CA90 (bottom) as function of CA50 for the investigated EGR rates for early Miller (left) and late Miller (right) cycles at IMEP = 6.35 bar and n = 2450 rev/min

In line with prior outcome using the baseline engine configuration, EGR prolongs burning delay and burn duration with an increasing gradient for higher EGR rates, regardless of intake valve closing. As can be seen, the combustion process of early Miller is more affected by EGR than that of late Miller, particularly for EGR rates of $x_{EGR} \geq 10\%$. This can be explained by the different level of turbulence and mixture distribution inside the prechamber and main combustion chamber for both valve timings:

- IT: The increased concentration and rather uneven distribution of residual gas within the prechamber for early Miller intensifies the need of advancing the ignition timing with increasing EGR rates.

- IT-CA5: As a result of the detrimental ignition conditions inside the prechamber, the strength of the prechamber flame jets decreases, as the longer burning delay for early Miller suggests.

- CA5-CA90: Beside the lower efficacy of the prechamber spark plug, the dependency of TKE on crank angle is likely another casual agent for different sensitivities of the combustion process to EGR for both valve timings. Since TKE of early Miller is expected to decrease with a steeper slope for crank angles after TDC, the reduction of the laminar burning velocity through EGR exerts a larger effect on burn duration.

The increased proportion of heat that is released late in the cycle leads to lower NO_x emissions and higher fuel consumption for early Miller. For this reason, not only the diluent's heat capacity governs the EGR effectiveness but also motion and distribution of the in-cylinder charge as it strongly influences the heat release rate.

The influence of mixture distribution and turbulence can be emphasised by forming the difference in burn duration $\Delta CA5$-$CA90$ of both valve timings at $x_{EGR} = 0$ and 15 % shown in Figure 7-36 (left). Negative values correspond to a shorter burn duration for early Miller cycle as consistently found for engine operation without EGR. For engine operation without EGR, early Miller reveals a shorter burn duration throughout the entire range due to richer mixture and higher TKE crank angles before and shortly after TDC (cf. Figure 7-28, left). The opposite trend can be observed for an EGR rate of $x_{EGR} = 15$ %, where late Miller valve timing exhibits a shorter burn duration. From this it can be derived that the better conditions inside the prechamber and the presumably higher TKE at late crank angle for late Miller outweigh the higher TKE around TDC for early Miller valve timing.
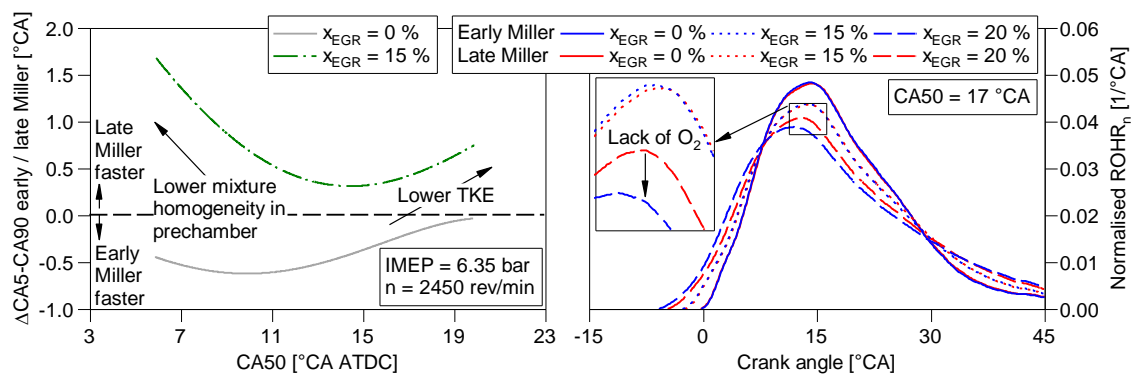
Figure 7-36: Difference in burn duration between early and late Miller cycles over CA50 for engine operation at $x_{EGR} = 0$ and 15 % (left); Normalised net rate of heat release over crank angle for both valve timings for engine operation with varying EGR rates at CA50 = 17 °CA ATDC (right)

As it was shown in Figure 7-35, burning delay and duration of early Miller cycle particularly increase for an EGR rate of $x_{EGR} = 20$ %. It is not expected that this solely originates from different charge motion and distribution but also from the aforementioned lack of oxygen. Its influence on the combustion shows the normalised $ROHR_n$ in Figure 7-36 (right)

for both valve timings at CA50 = 17 °CA ATDC and EGR rates of x_{EGR} = 0, 15 and 20 %. While an EGR rate of x_{EGR} = 15 % leads to a comparable drop of the peak $ROHR_n$ between both valve timings, the influence of x_{EGR} = 20 % increases notably for early Miller. It also requires a significantly earlier ignition timing due to a fairly extended combustion.

The engine tests proved that an EGR rate of 20 % is the highest possible for both valve timings. The difference to the baseline engine, which achieves EGR rates up to 25 %, can be attributed to a decreased exhaust gas pressure level caused by a lower mass flow for Miller cycle.

7.3.3.3 Knocking Tendency

The enhanced combustion temperature caused by a lower dilution ratio not only favours the formation of NO_x but also increases sensitivity to knocking. Figure 7-37 (left) shows the combustion phasing CA50 at which the engine exceeds the knock margin over the EGR rate for both valve timings at IMEP = 6.35 bar. This means that the majority of the operating points discussed in 7.3.2.1 and 7.3.2.2 operate at the knock margin or beyond. Nevertheless, the measured peak value of 0.31 bar surpasses the conservative threshold of 0.25 bar only slightly. For an EGR rate of about 10 %, the possible CA50 without meeting the knocking margin shifts from about 11 to 6 °CA. Both valve timings show similar trends with a slight advantage for early Miller cycle.
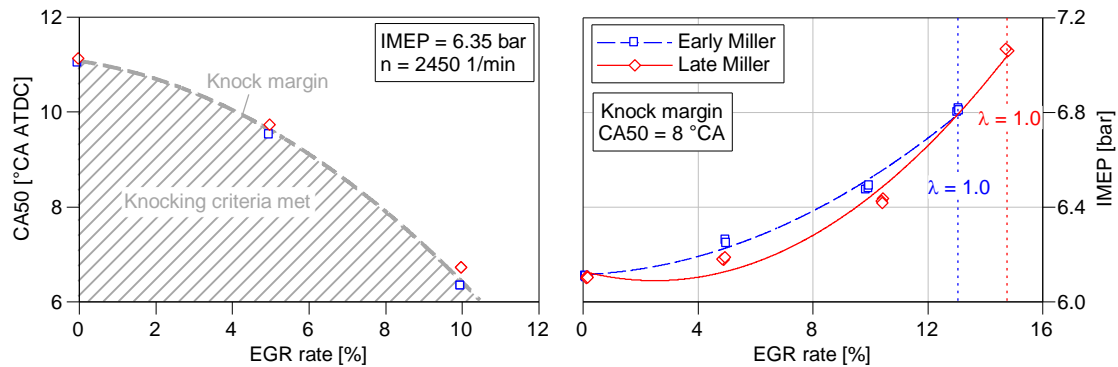
Figure 7-37: CA50 required to meet the knock margin as function of the EGR rate (left); IMEP over the EGR rate at MB1 for early and late Miller valve timing at the knock margin (right)

To further evaluate the knocking tendency of both valve timings, a procedure analogous to Section 7.2.3 was followed, where the effect of EGR to lift the possible IMEP at MBT combustion phasing of CA50 = 8 °CA ATDC was reviewed (see Figure 7-37, right). For a given EGR rate, the amount of fuel was increased and ignition timing adjusted until meeting the threshold. Late Miller tendentially shows a higher tendency to knocking and requires higher EGR rates to achieve the same IMEP because of a higher temperature level. This is caused by a higher effective compression ratio and the fact that late Miller valve timing requires a higher $IMEP_g$ to compensate for losses in compression. To operate under stoichiometric conditions, the early / late Miller configuration requires an EGR rate of x_{EGR} = 13 / 15 % and generates an IMEP of about 6.90 / 7.15 bar.

7.4 Comparison between Miller and Otto Cycle

So far, the comparison between Miller and Otto cycle in an experimental environment chiefly addressed the influence on the effective compression ratio (cf. 7.3.1). The analysis, carried out in an operating point of same CA50 and λ, proved that all three configurations reach similar thermodynamic conditions around ignition timing and same residual gas fraction. To further explore the cycles in depth, this section discusses CA50 sweeps conducted at IMEP = 6.35 bar.

7.4.1 Miller and Otto Cycle in Lean-burn Operation

Following a systematic analysis process, the essential differences between the baseline and both Miller configurations are elaborated first in air-diluted engine operation.

7.4.1.1 Engine Efficiency and NO_x Emissions

Before analysing the trade-off between engine efficiency and NO_x emissions, the influence of Miller valve timing on NO_x emissions is discussed. Figure 7-38 shows volumetric NO_x emissions (left), temperature of the burnt zone (centre) and normalised cumulative heat release (right) for operating points of same indicated specific NO_x emissions at constant IMEP. With reducing cylinder mass, and therefore a smaller engine-out mass flow, the engine can operate at higher NO_x in ppm, while still achieving constant indicated specific NO_x emissions (as discussed in Section 5.3). At NO_x emissions of 4.62 g/kWh, for instance, the baseline value of 516 ppm rise to 603 ppm for early and 560 ppm for late Miller cycle, while peak combustion temperature increases from 2164 K to 2263 and 2267 K, respectively. Distinct combustion characteristics, mixture composition and gas exchange across the configurations require the engine to operate at varying CA50 for drawing this comparison at same IMEP.

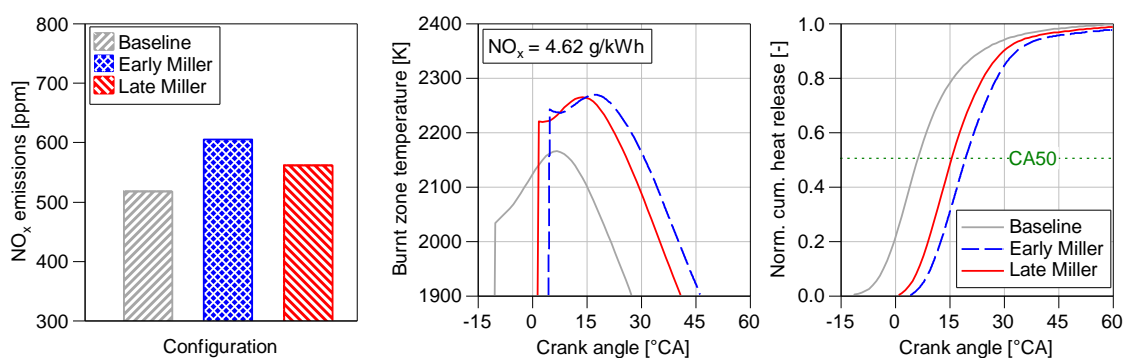Figure 7-38: Volumetric NO_x emissions (left), temperature of the burnt zone (centre) and normalised cumulated gross heat release (right) at constant indicated specific NO_x emissions (IMEP 6.35 bar, n = 2450 rev/min)

The significantly later combustion phasing of the Miller configurations to achieve NO_x emissions similar to those of the baseline engine already hints that the trade-off between

engine efficiency and NO_x emissions in Figure 7-39 (left) deteriorates. The lower relative air-fuel ratio required to achieve threshold IMEP, reduces the available heat capacity for absorbing heat during combustion, thus being the major reason for higher NO_x emissions. Compared to the baseline engine, the lower λ causes less favourable mixture properties in terms of theoretical achievable indicated fuel consumption $ISFC_{ideal}$. However, both Miller configurations overcompensate this through an enhanced geometrical compression ratio. The potential of improving ISFC of the actual engine cycle becomes visible, when plotting it over combustion phasing (Figure 7-39, right). The largest benefit compared to the baseline, found at CA50 = 18 °CA ATDC, amounts to 6.2 g/kWh and 4.6 g/kWh for early and late Miller cycle, respectively. The benefit diminishes by about 2 g/kWh when analysing $ISFC_g$, pointing out that the main advantages come from reduced losses during gas exchange. The differences in $ISFC_g$ between the configurations indicate dissimilar combustion characteristics and wall heat losses over CA50, which will be addressed in Sections 7.4.1.3 and 7.4.1.4.
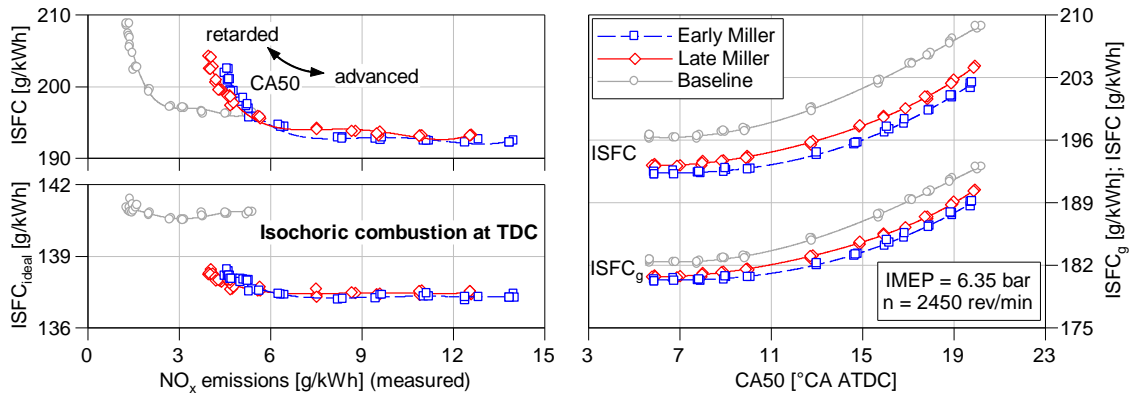

Figure 7-39: ISFC and $ISFC_{ideal}$ over NO_x emissions (left); ISFC and $ISFC_g$ over CA50 (right) for engine operation without EGR

7.4.1.2 Gas Exchange Analysis

Figure 7-40 (left) reveals the expected benefits in gas exchange in the p-V diagram of all three configurations exemplarily at CA50 = 17 °CA ATDC. In spite of the smaller amount of fuel added to the cycle, both Miller cycles reach higher peak combustion pressure than the baseline due to combustion within a smaller volume. The higher expansion ratio of Miller cycle reduces expansion pressure compared to the baseline engine. Due to the lower charging efficiency, the main difference in the pumping loop is found during the exhaust stroke, where the piston requires less work to expel the burnt mixture (cf. Chapter 5). Furthermore, late Miller cycle exhibits losses in compression of -0.03 bar, whereas intake valve timing and intake gas path of the baseline production engine are designed for highest charging efficiency, thus leading to negligibly small losses in compression. As a result of reduced losses during gas exchange, $IMEP_g$ of both Miller valve timings can be lowered by 0.08 and 0.04 bar, respectively, to still achieve same IMEP.
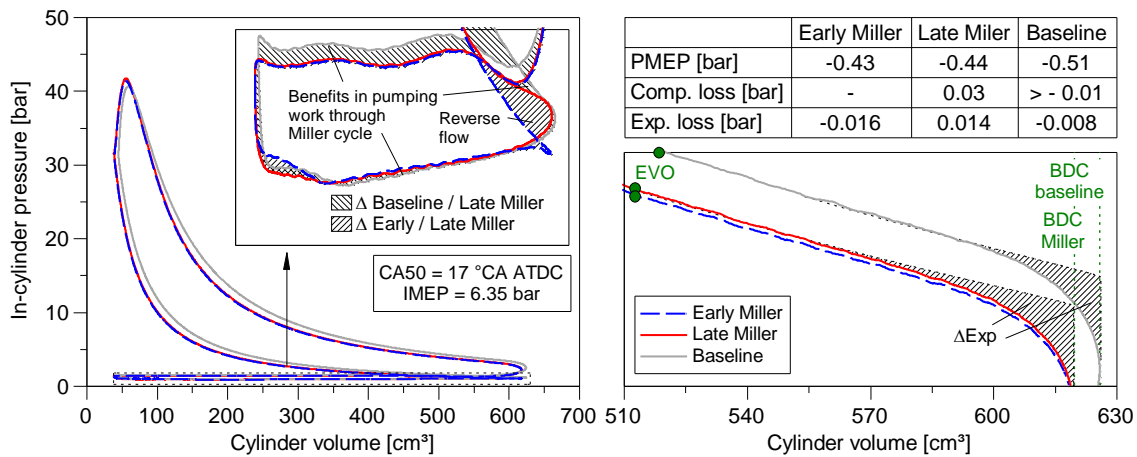
Figure 7-40: p-V diagram (left) and losses from imperfect gas exchange (right) of the baseline engine and both Miller configurations at CA50 = 17 °CA ATDC (IMEP = 6.35 bar)

Up to this point, only the work required during pumping loop and the beginning of the compression stroke were considered as losses in gas exchange. In fact, an additional loss compared to an ideal gas exchange occurs when the exhaust valve opens before BDC. This so-called expansion loss can be determined by adding a polytropic process starting from EVO towards BDC, as shown in Figure 7-40 (right) for the baseline and the late Miller configuration. The baseline engine exhibits EVO closer to BDC due to the lower geometrical compression ratio, which further leads to a flatter polytropic change, thus leading to a smaller theoretical potential that is easier to meet. It is worthwhile to mention that, contrary to the losses in compression, the expansion loss is not additionally considered when balancing net and gross ISFC.

Summarising the mentioned losses occurring between EVO and IVC, yield a benefit of -0.072 bar for early and -0.034 bar for late Miller cycle compared with the baseline engine. Since the losses elaborated show fairly small sensitivity to CA50 in unthrottled engine operation at constant engine speed, discussion of further operating points is not required.

7.4.1.3 Combustion Behaviour

The realisation of the Miller cycle involves an increase of the geometrical compression ratio from $r_{geo} = 13.20$ to 15.25. In order to analyse the influence of the altered combustion chamber design on combustion behaviour, engine trials with Miller piston design and baseline valve timing were conducted. On the one hand, the use of baseline valve timing instead of Miller valve timing increases temperature and pressure during the high-pressure loop, making it challenging to assess the changes on combustion solely caused by an altered piston geometry. On the other hand, it avoids the turbulence level to change as a result of altered valve timing. Hence, despite lacking comparability regarding the thermodynamic conditions at ignition timing, analysing the burning behaviour using the baseline valve timing allows for a comparison at similar λ and same IMEP. It can therefore contribute to a deeper understanding of the influences on the combustion process solely caused by the

Miller piston design. The higher compression ratio increases mean temperature of the charge by about 30 K at an SOC of 10 °CA BTDC compared to the baseline compression ratio.

Influence of altered piston design

Figure 7-41 shows burning delay (IT-CA5), relative air fuel ratio and burn duration (CA5-CA90) over CA50 for both the baseline ($r_{geo} = 13.20$) and the Miller ($r_{geo} = 15.25$) piston at IMEP = 6.35 bar. The augmented geometrical compression ratio enables IMEP = 6.35 bar at higher relative air-fuel ratios over the whole CA50 range investigated due to higher engine efficiency. The Miller piston leads to a shorter burning delay than that of the baseline configuration at any given CA50. This presumably arises from improved ignition conditions, including higher temperatures and lower residual gas fractions inside the prechamber. Furthermore, the higher pressure difference between prechamber and main combustion chamber increases the mass flow and therefore the TKE. Findings in literature of a very similar comparison support this explanation [100]. While burning delay tends to decrease with retarding CA50 for the baseline piston, the Miller piston shows the opposing trend. However, their changes over CA50 are relatively small, particularly compared to burn duration. Furthermore, there appears to be no correlation between burning delay and burn duration.
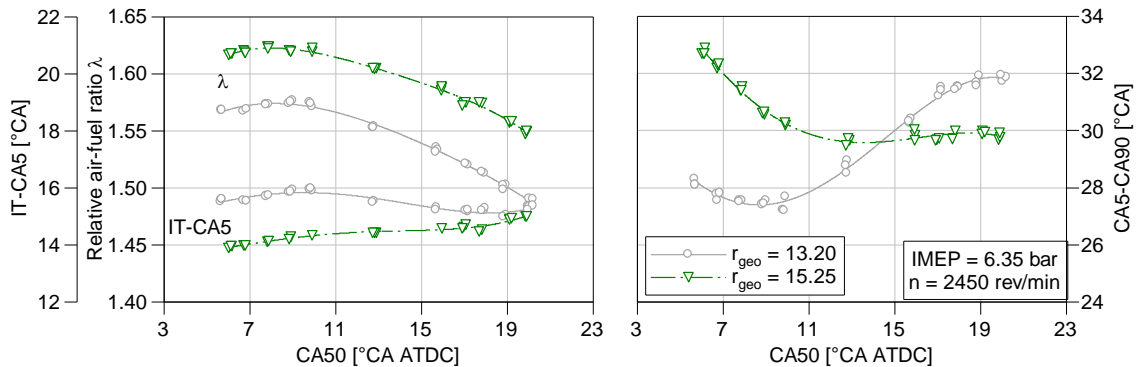
Figure 7-41: Relative air-fuel ratio, burning delay (left) and burn duration (right) over CA50 for compression ratios $r_{geo} = 13.20$ and $r_{geo} = 15.25$ with baseline valve timing at constant IMEP = 6.35 bar

The baseline piston holds an advantage in burn duration over the Miller piston for late CA50. In fact, burn duration of the baseline follows an s-shape trace with mostly rising values from early to late CA50. The Miller piston shows an opposing trend for which burn duration diminishes with retarding CA50 until it stagnates at about CA50 = 13 °CA ATDC. Burn duration of the baseline compression ratio continues to increase and becomes even longer for CA50 = 16 °CA ATDC and beyond. The advantage in burn duration at earlier CA50 when using the baseline piston can likely be ascribed to the higher squish intensity, whereas at retarded CA50, the Miller piston benefits from shorter flame travel distance thanks to a lower piston bowl depth. The positive effects of increasing squish [10,

130, 145 and shorter flame travel distance to reduce burn duration [166] are also reported by others.

To further analyse the influence of the altered piston design in the expected operating range of the Lean-Miller-EGR working process, operating points of same CA50 = 19 °CA ATDC and varying λ are selected. Figure 7-42 shows $ROHR_n$ (left) and characteristic parameters (right) of the operating points, including the reference operating point (ROP) of the baseline configuration. The higher compression ratio (OP2) allows the engine to operate leaner to achieve CA50 and IMEP equivalent to the ROP. Lower NO_x emissions indicate lower combustion temperatures in spite of a higher pressure and temperature level at the end of the compression stroke. Similar burning behaviour in the beginning of the combustion leads to nearly identical burning delay. The baseline reaches its maximum earlier with a smaller curvature than the higher compression ratio that shows a higher value after passing CA50 and a burn duration that is shortened by 1.8 °CA. The baseline can achieve similar burn duration to OP2 by reducing the relative air-fuel ratio to $\lambda = 1.40$ (OP1). This evidently increases NO_x emissions and combustion stability, however, the modified piston still exhibits lowest COV_{IMEP} of 0.93 % (OP2).

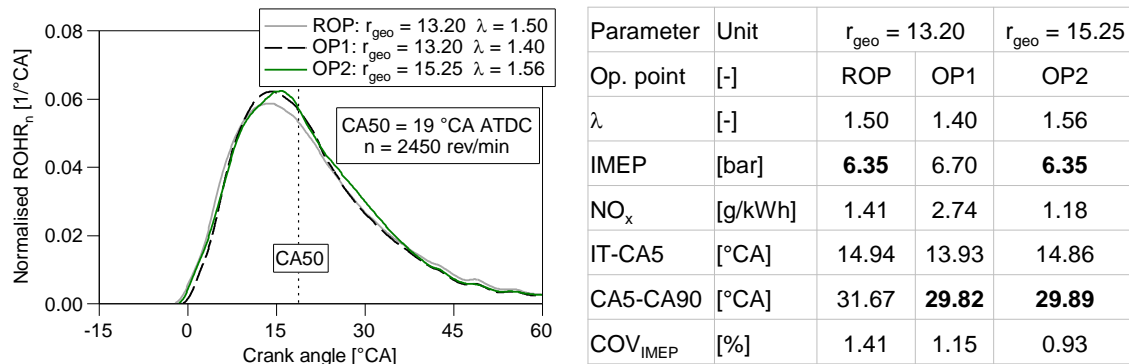| Parameter	Unit	r_{geo} = 13.20		r_{geo} = 15.25
Op. point	[-]	ROP	OP1	OP2
λ	[-]	1.50	1.40	1.56
IMEP	[bar]	**6.35**	6.70	**6.35**
NO_x	[g/kWh]	1.41	2.74	1.18
IT-CA5	[°CA]	14.94	13.93	14.86
CA5-CA90	[°CA]	31.67	**29.82**	**29.89**
COV_{IMEP}	[%]	1.41	1.15	0.93

Figure 7-42: Normalised net rate of heat release over crank angle for engine operation with baseline valve timing and a geometrical compression ratio of r_{geo} = 13.20 and 15.25 (CA50 = 19 °CA ATDC)

For a more detailed description of engine tests with high compression ratio and baseline valve timing, the author refers to [106].

Influence of Miller valve timing at $\lambda = 1.5$

Further analysis of the combustion behaviour centres on engine operation in baseline configuration ($r_{geo} = 13.20$), and both Miller valve timing with a geometrical compression ratio of $r_{geo} = 15.25$. In addition to engine operation at IMEP = 6.35 bar, the difference between baseline and Miller valve timing on combustion is assessed at constant relative air-fuel ratio and combustion phasing of $\lambda = 1.50$ and CA50 = 19 °CA ATDC (see Figure 7-43). Lower charging efficiency reduces IMEP by 0.65 for late and by 0.67 bar for early Miller cycle. NO_x emissions decrease compared to the baseline configuration, suggesting lower

combustion temperature. The trace of the normalised $ROHR_n$ is similar for all three configurations until approximately 8 °CA ATDC. The gradient of the baseline engine decreases from there, while both Miller cycles further increase to a peak that occurs a little later. Both traces fall below the baseline configuration at around 35 °CA ATDC and show a shortened burn duration by about 3.6 °CA (−/- 0.5). The accelerated combustion also improves combustion stability as lower COV_{IMEP} reveal.
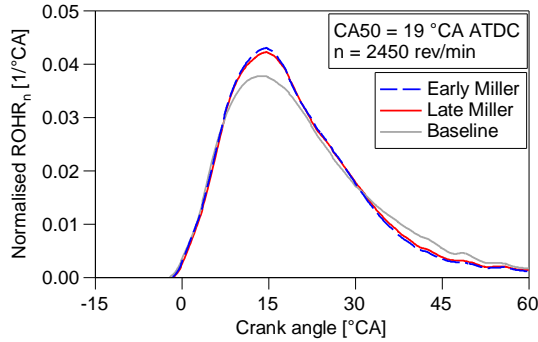
Parameter	Unit	Baseline	Early Miller	Late Miller
λ	[-]	1.50	1.50	1.50
IMEP	[bar]	6.35	5.68	5.70
NO_x	[g/kWh]	1.41	1.27	1.21
IT-CA5	[°CA]	14.94	14.79	15.02
CA5-CA90	[°CA]	31.67	27.54	28.39
COV_{IMEP}	[%]	1.41	0.79	0.83

Figure 7-43: Normalised net rate of heat release over crank angle for engine operation with baseline and both Miller valve timings at constant relative air-fuel ratio λ = 1.50

The engine trials with different piston and valve timings prove that intake valve closing indeed influences combustion behaviour. However, the altered piston design that leads to shortened burn duration for late combustion phasing appears to have the major impact, which could become a crucial advantage for engine operation with EGR.

Influence of Miller valve timing at IMEP = 6.35 bar

With respect to engine operation at the threshold of IMEP = 6.35 bar, combustion is further analysed for operating points with relative air-fuel ratios that are approximately 0.17 to 0.19 lower than that of the baseline configuration at same CA50. Laminar burning velocity increases and initial conditions for combustion improve, thus favouring combustion stability given by σ_{CA50} (see Figure 7-44, left).

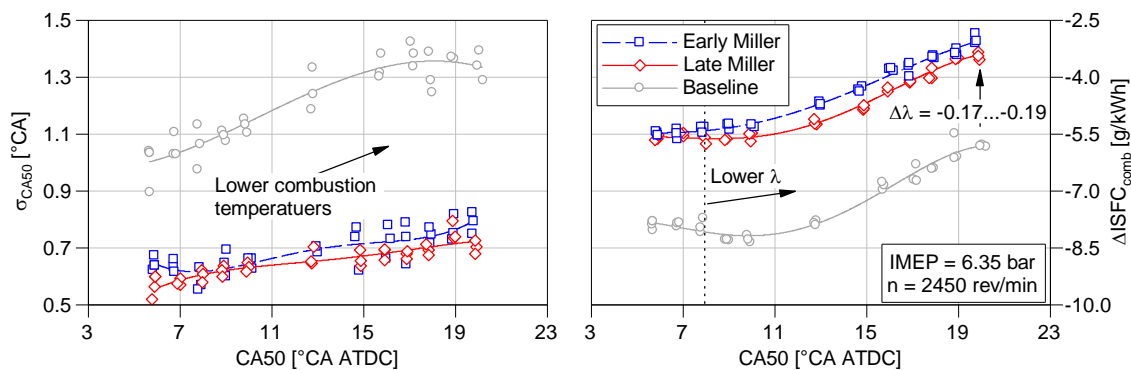Figure 7-44: σ_{CA50} (left) and $\Delta ISFC_{comb}$ (right) over CA50 for baseline and Miller valve timing at IMEP = 6.35 bar

Across all configurations, σ_{CA50} increases as CA50 is retarded due to falling combustion

temperatures. The stronger gradient of the baseline engine stems from the higher sensitivity of leaner mixtures to combustion conditions. Mixture composition also strongly influences the losses from imperfect combustion, expressed by $\Delta ISFC_{comb}$. Figure 7-44 (right) shows the known behaviour of lean mixtures, where $\Delta ISFC_{comb}$ decreases with reducing relative air-fuel ratio.

The lower mixture dilution required for both Miller setups to keep IMEP = 6.35 bar, additionally reduces burning delay and burn duration for the most part of the span investigated (see Figure 7-45). Burning delay shows a strong dependency on CA50 for both Miller configurations, whereas it remains nearly constant for the baseline configuration. As with the results obtained using the Miller piston with baseline valve timing, burn duration increases with advancing CA50, owing to altered in-cylinder charge motion and flame travel distance. The baseline engine reveals opposing behaviour with very similar burn duration at CA50 = 6 °CA ATDC.

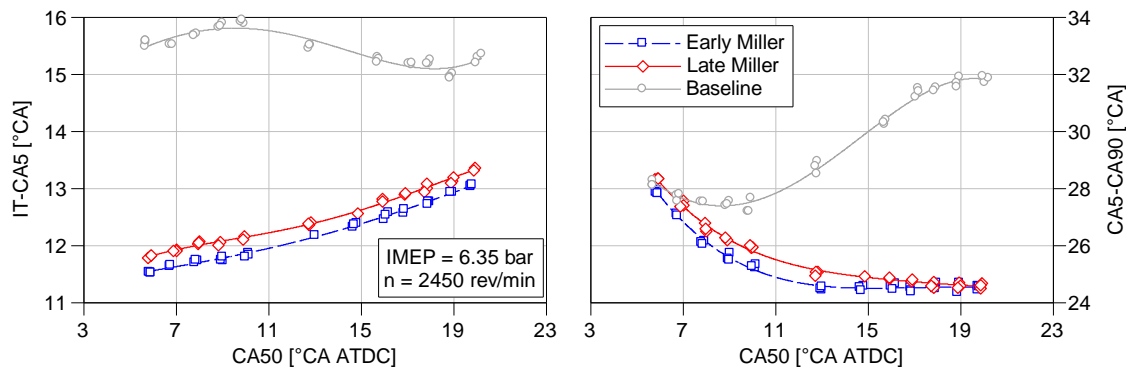

Figure 7-45: Burning delay (left) and burn duration (right) over combustion phasing at engine operation without EGR at constant IMEP = 6.35 bar

Selecting operating points of similar CA5-CA90 = 28 °CA ATDC (−/- 0.2 °CA) at constant IMEP (6.35 bar) and same CA50 (6 °CA ATDC), enables the subsequent comparison regarding wall heat losses and cycle work under relatively similar combustion characteristics.

7.4.1.4 Wall Heat Losses and Cycle Work

Figure 7-46 illustrates in-cylinder pressure and mean in-cylinder temperature over crank angle as well as the normalised wall heat losses during the cycle for all three valve timings at CA50 = 6 °CA ATDC and IMEP = 6.35 bar. Engine operation at lower dilution ratios for both Miller valve timings (necessary to reach IMEP = 6.35 bar) increase peak combustion pressure and mean in-cylinder temperature compared to the baseline engine. Together with an enhanced A/V ratio, the normalised wall heat losses increase from $Q_{wall} = 19.0$ % for the baseline to $Q_{wall} = 19.6$ % for early and 19.7 % for late Miller cycle. The difference between both Miller setups originates from the dependency of the heat transfer coefficient not only on temperature but also on pressure. In the given case, the higher pressure of late Miller cycle outweighs the lower temperature, thus resulting in slightly higher computed
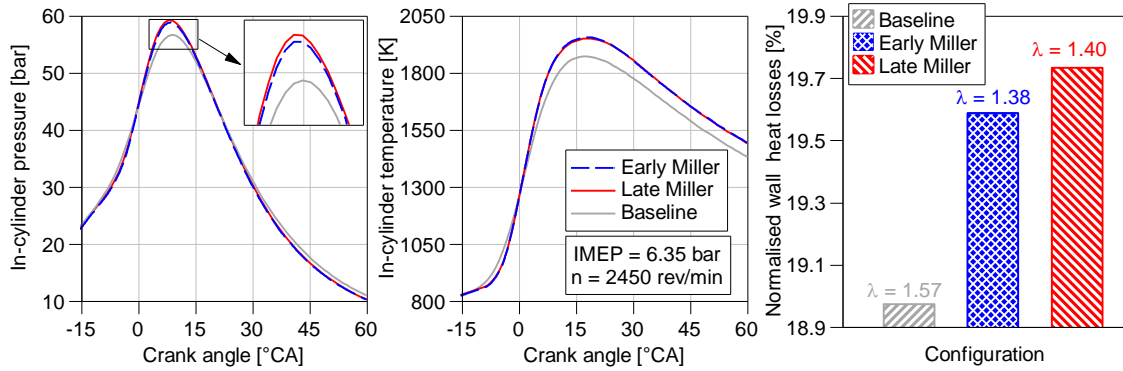
wall heat losses.

Figure 7-46: In-cylinder pressure (left) and mean temperature (centre) and wall heat losses related to re-leased energy (right) at CA50 = 6 °CA ATDC and IMEP = 6.35 bar

Wall heat losses decrease as combustion phasing is retarded due to lower combustion temperatures at lower A/V ratio. A shift from CA50 = 6 °CA to 19 °CA ATDC diminishes Q_{wall} from 19.0 to 14.7 % for the baseline engine and decreases from 19.6 to 15.1 % and 19.7 to 15.2 % for early and late Miller configuration, respectively (see Figure 7-47, left). The larger reduction in the case of both Miller valve timings can be attributed to the steeper decrease of the A/V ratio over crank angle for higher geometrical compression ratios. Figure 7-47 (right) shows the wall heat flow over crank angle for all three configurations at CA50 = 6 and 19 °CA ATDC. In correspondence with the total wall heat losses, the peak heat flow decreases stronger for both Miller than for the baseline configuration as combustion phasing is shifted.
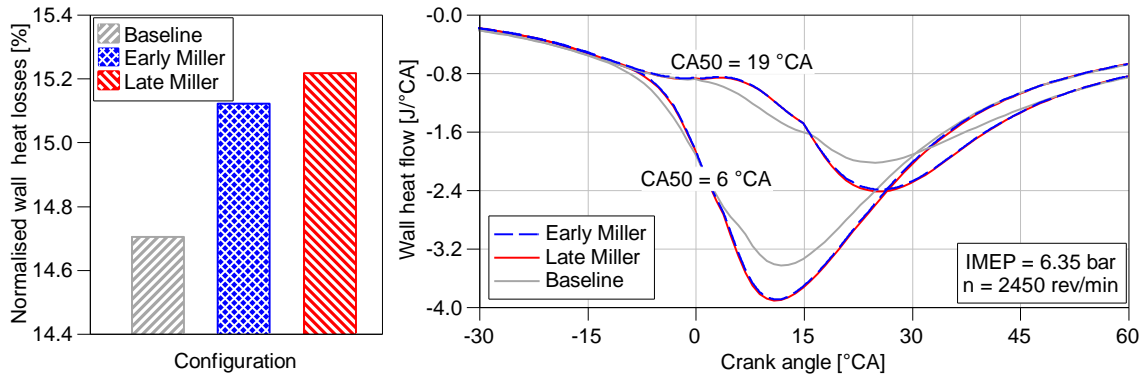
Figure 7-47: Normalised wall heat losses at CA50 = 19 °CA ATDC (left) and wall heat flow over crank angle at CA50 = 6 and 19 °CA ATDC (right)

For the most part of the compression stroke, both Miller configurations reveal a smaller wall heat flow before TDC, owing to lower in-cylinder temperature. The lower dilution ratio required for Miller valve timing allows the engine to operate with retarded ignition timing, leading to a larger amount of heat that is released later in the cycle. Since this occurs at higher temperature, heat flow during combustion exceeds the value of the baseline engine significantly, regardless of combustion phasing.

The more advanced ignition timing of the baseline of about 5 °CA increases the amount of heat released before TDC, where the A/V ratio is relatively small (see Figure 7-48, left). The cumulative heat released before passing TDC amounts to about 207 J for the baseline engine and about 179 J for both Miller valve timings. The rising in-cylinder pressure and temperature as the piston still ascends not only augments the wall heat losses during the compression stroke but also the compression work. Figure 7-48 (right) shows the cumulated work caused by volume change during the compression and expansion stroke. The work calculated at TDC is the one required for the compression stroke ($W_{compression}$) and the amount from TDC to BDC accounts for the expansion work obtained from the cycle ($W_{expansion}$). Both Miller configurations reduce the compression work significantly compared to the baseline engine due to the higher ECR_{eff} at similar $r_{e,eff}$. Early Miller shows a slightly smaller compression work than late Miller cycle, arising from the minor differences in effective compression ratio and the fact that no reverse flow occurs. Both Miller configurations output less expansion work than the baseline engine and an overall deficit in cycle work of about 25 and 28 J for late and early Miller cycle, respectively. However, both still achieve same IMEP, since a lower IMEPg due to the reduces pumping losses.
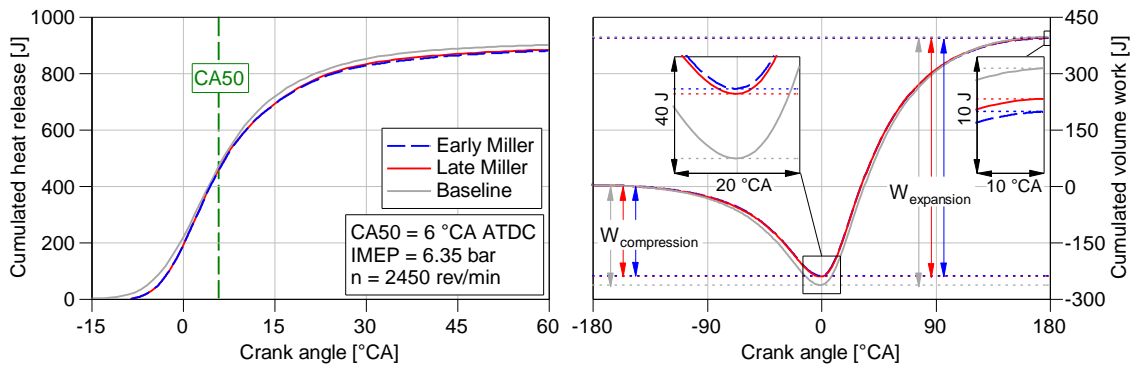
Figure 7-48: Cumulated heat released (left) and cumulated volume work (right) for the baseline engine and both Miller configurations at CA50 = 6 °CA AITDC and IMEP = 6.35 bar

The varying heat release profile during the compression stroke make it difficult to infer to what extent the lower compression work is caused by Miller cycle. Analysing operating points of same IMEP but differing CA50, allows for assessing the influence of the heat release on compression work as exemplarily shown in Figure 7-49 (left) for the baseline engine. It can be seen that retarding combustion phasing from CA50 = 6 °CA to 13 and 19 °CA ATDC, reduces the heat released before TDC by 170 and 216 J while compression work decreases by only 1.2 and 3.8 J, respectively (Figure 7-49, right). This, in turn, supports the conclusion that the savings of Miller cycle in compression work of more than 24 J at CA50 = 6 °CA ATDC primarily originate from the higher ECR_{eff} at constant $r_{e,eff}$ rather than from the lower amount of heat released before BDC. The increase of the ratio between expansion and compression work from 1.48 for the baseline engine to 1.62 for early and 1.61 for late Miller cycle explains the lower ISFCg at same CA50.
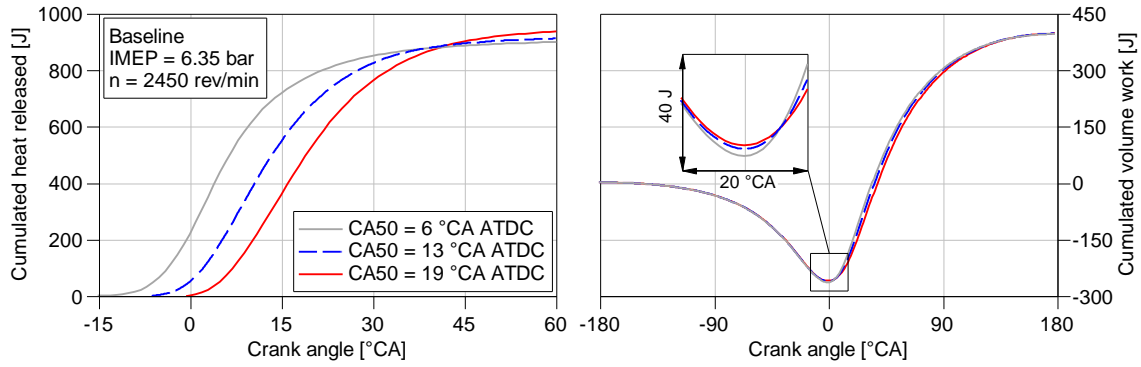
Figure 7-49: Cumulated heat released (left) and cumulated volume work (right) for the baseline engine with varying CA50 at IMEP = 6.35 bar

The results discussed show that in air-diluted engine operation both Miller cycles improve ISFC mainly due to lower pumping work and reduced ideal engine fuel consumption. Analogous to the ideal engine, the actual cycle experiences a benefit thanks to a higher ratio of expansion to compression work. The reduced mixture dilution improves combustion in terms of duration, stability and losses on the one hand, but increases NO_x emissions and wall heat losses significantly on the other.

7.4.2 Miller and Otto Cycle in Lean-burn Operation with EGR

To overcome the drawback of increasing NO_x emissions promoted by the lower dilution ratio for the early and late Miller configuration, EGR is added to the cycle, eventually forming the Lean-Miller-EGR working process. As shown in Section 7.3.3.1, EGR rates of $x_{EGR} = 15\%$ and 20% show the largest effect to reduce NO_x emissions and are therefore compared to the baseline engine.

7.4.2.1 Engine Efficiency and NO$_x$ Emissions

Figure 7-50 illustrates ISFC (left) and $ISFC_g$ (right) over NO_x emissions at constant IMEP for the baseline engine operating without EGR and for both Miller valve timings at $x_{EGR} = 15\%$ and 20%. Compared to the baseline engine, the Lean-Miller-EGR working process deteriorates the ISFC-NO_x trade-off at IMEP = 6.35 bar. For an EGR rate of 20% and most retarded combustion phasings (OP1 and OP2), both Miller configurations achieve NO_x emissions and ISFC that are the closest to the ROP of the baseline configuration ($NO_x = 1.4$ g/kWh, ISFC = 206.7 g/kWh). While early Miller (OP1) improves ISFC to 205.8 g/kWh at NO_x emissions of 1.6 g/kWh, late Miller (OP2) reduces NO_x to 1.35 g/kWh at the expense of ISFC that amounts to 210.8 /kWh. Analysing $ISFC_g$ of the three configurations shows even larger differences, leading to the conclusion that the small benefits accomplished in the high efficiency regime can be entirely ascribed to lower pumping work.
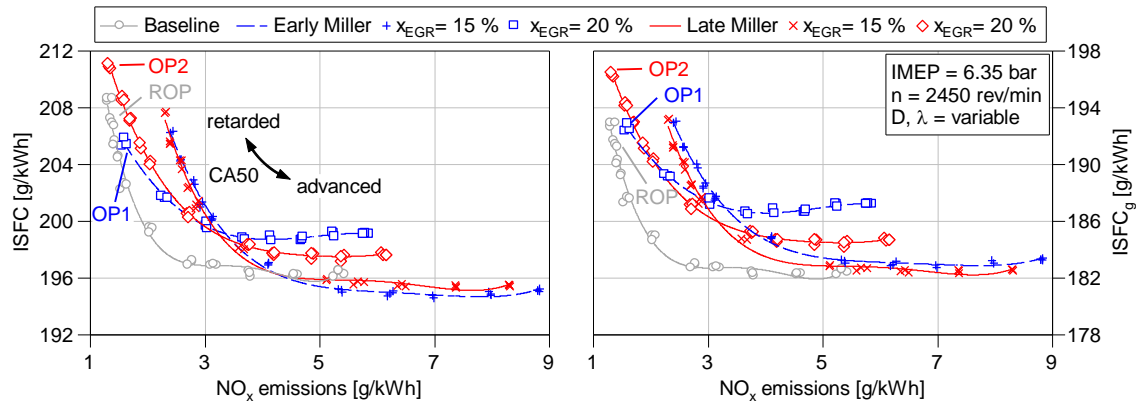
Figure 7-50: ISFC (left) and ISFC$_g$ (right) over NO$_x$ emissions for the baseline configuration without EGR and both Miller cycle at x$_{EGR}$ = 15 % and 20 % (IMEP = 6.35 bar)

7.4.2.2 Influence of Mixture Composition

Mixture composition markedly influences NO$_x$ emissions and mainly governs the efficiency of the ideal engine. Splitting the aspirated mixture into its mole fractions clarifies the influence of the dilution ratio and EGR rate on mixture composition, as shown for the baseline without EGR and both Miller configurations with EGR rates of x$_{EGR}$ = 20 % in Figure 7-51. Analogously to 7.2.2, air, divided into a part required for stoichiometric combustion and for mixture dilution, consists of N$_2$ and O$_2$, while the four-component exhaust gas also includes H$_2$O and CO$_2$.
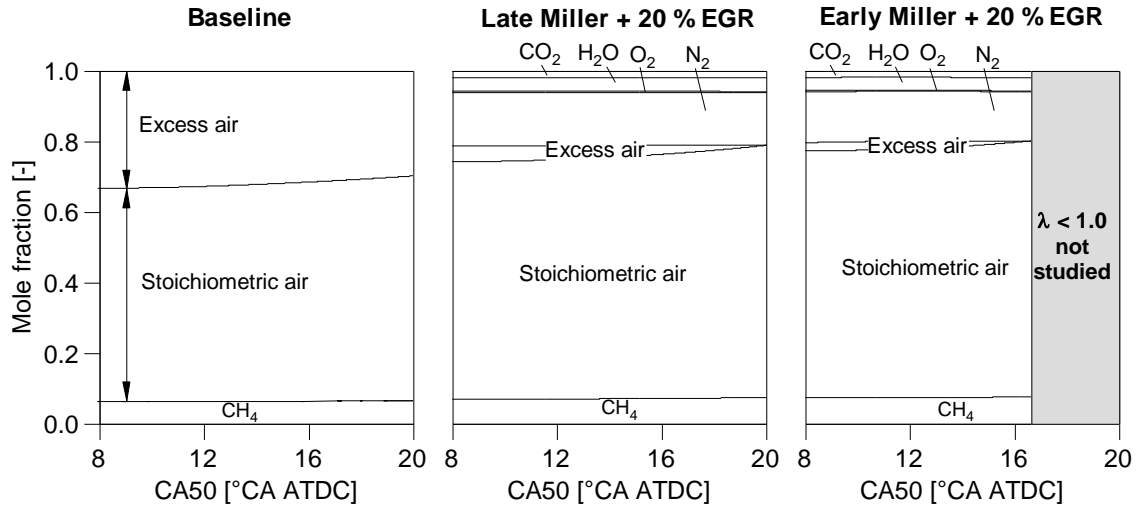
Figure 7-51: Mole fraction of the baseline configuration without EGR (left) as well as late Miller (centre) and early Miller (right) cycle with x$_{EGR}$ = 20 % (IMEP = 6.35 bar, n = 2450 rev/min)

The increasing fuel consumption for engine operation at late combustion phasings is reflected in a smaller fraction of diluent, regardless of mixture strategy. While the composition of the dilution remains constant using excess air, it varies for mixtures that include EGR. Starting from lean combustion at CA50 = 8 °CA ATDC, the fraction of excess air decreases as CA50 retarded. Owing to a lower charging efficiency, early Miller reaches

almost stoichiometric conditions at about CA50 = 17 °CA ATDC. It was therefore not possible to investigate further retarded operating points without either reducing the EGR rate or experiencing losses in IMEP. Since not the entire oxygen takes part in combustion due to mixture inhomogeneity, the exhaust gas of a stoichiometric mixture still contains minute traces of O_2. Due to the lower charging efficiency and higher fuel consumption of both Miller configurations, the mole fraction of air from a stoichiometric combustion is much higher. This, in turn leads to a smaller fraction that is available for dilution, thus producing higher NO_x emissions.

As temperature-driven species, NO_x emissions clearly depend on the amount of fuel and the absolute heat capacity of the diluent. Both parameters are shown for the baseline and Miller configuration of all EGR rates investigated in Figure 7-52 at a mixture temperature relevant for ignition timing of 800 K. As expected, the diluent of the baseline configuration exhibits the highest absolute heat capacity for the same mass of fuel. For a fuel mass flow of $\dot{m}_{fuel} = 1.50$ kg/h and engine operation without EGR, the absolute heat capacity of the baseline engine is 81 % and 75 % higher than that of early or late Miller cycle, respectively. By virtue of the high H_2O and CO_2 fraction of the exhaust gas, an EGR rate of $x_{EGR} = 20$ % reduces this deficit to 59 % for late and 47% early Miller. From this it can be derived that the higher charging efficiency for late Miller outweighs the higher CO_2 and H_2O fraction of the exhaust gas for early Miller cycle in terms of the absolute heat capacity of the diluent.
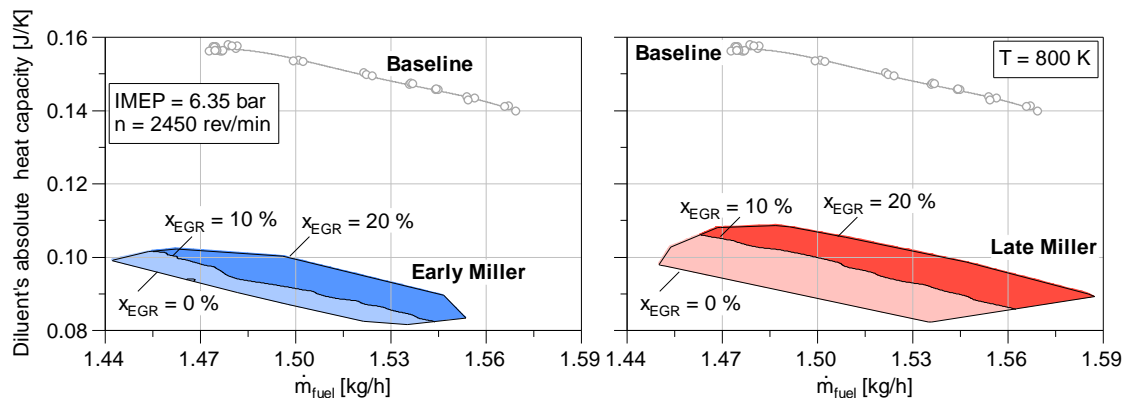
Figure 7-52: Heat capacity of the diluent over fuel mass flow for the baseline engine without EGR and both Miller cycles at varying EGR rates (IMEP = 6.35 bar, n = 2450 rev/min, l = 800 K)

Despite a markedly lower heat capacity of the dilution, both Miller configurations reach same or even slightly lower specific NO_x emissions when operating at late combustion phasing. Multiple points explain this:

- Lower charging efficiency allows for higher NO_x emissions in ppm, i.e. higher temperature, to maintain emissions in g/kWh constant.
- The specific heat capacity increases in the course of the combustion for CO_2 and particularly for H_2O with a higher gradient than N_2 and O_2.
- The lack of O_2 at EGR rates of $x_{EGR} = 20$ % reduces NO_x formation.

- Reduced losses in gas exchange require lower IMEP$_g$ to achieve the threshold IMEP of 6.35 bar.
- Higher combustion stability is expected to bring forth a reduced number of cycles with advanced heat release and therefore higher temperature, with which the NO$_x$ emissions increase exponentially.

Using the mixture composition of the recorded operating points enables calculating the ISFC$_{ideal}$ as shown in Figure 7-53 for both Miller valve timings of varying EGR rate in comparison to the baseline engine. Since the ideal engine excludes pumping work, this analysis only relates to the high-pressure loop. Although relatively low dilution ratios are required to achieve IMEP = 6.35 bar, both Miller configurations hold an advantage in ISFC$_{ideal}$ over the baseline engine for EGR rates of 10 % and below. This can be attributed to the higher compression ratio of $r_{geo} = 15.25$. At $x_{EGR} = 15$ % and low NO$_x$ emissions as well as the entire CA50 sweep at $x_{EGR} = 20$ %, the drawback caused by lower dilution outweighs the higher compression ratio, leading to losses in ISFC$_{ideal}$. For lowest NO$_x$ emissions, the disadvantage of each Miller configuration is about 3 g/kWh in ISFC compared to the baseline engine.
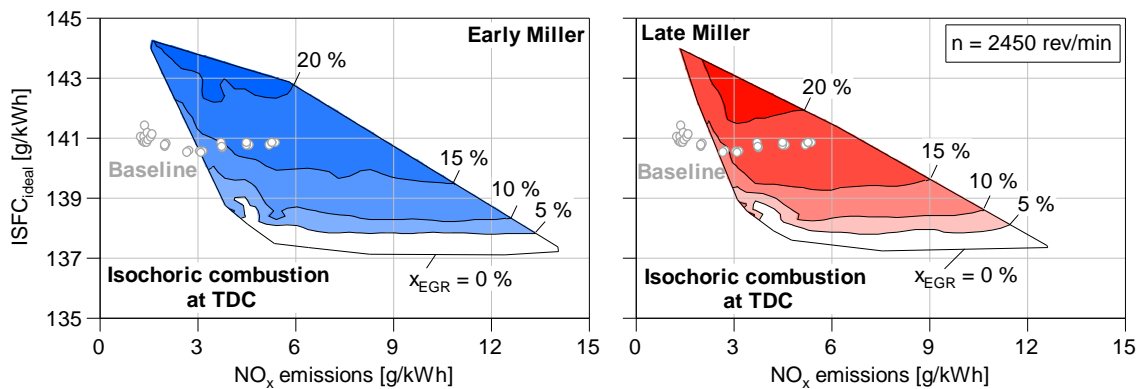
Figure 7-53: Ideal engine ISFC over NO$_x$ emissions for early (left) and late Miller valve timing (right) over NO$_x$ emissions (mixture composition of operating points at IMEP = 6.35 bar used for calculation)

While EGR clearly leads to losses in ideal engine for both Miller cycles, further drawbacks could arise from an altered combustion process, which is subject of the next analysis.

7.4.2.3 Combustion Behaviour

The following analysis addresses comparison of selected parameters that describe the burning behaviour. For a detail explanation of the differing combustion characteristics, the author refers to Section 7.2.1.2 and 7.3.3.2.

Both Miller valve timings show the best trade-off in the high efficiency regime for $x_{EGR} = 15$ % and in the low NO$_x$ regime for of $x_{EGR} = 20$ %. The comparison of combustion characteristics (see Figure 7-54) of these four configurations with the baseline engine without EGR provides deeper understanding of deficits in efficiency. Burning delay at $x_{EGR} = 15$ % is almost consistently shorter, whereas for burn duration this is only the

case for CA50 after 13 °CA ATDC. Increasing the EGR rate to $x_{EGR} = 20$ %, leads to comparable IT-CA5 between the baseline and late Miller configurations at early CA50, whereas early Miller reveals a drawback over the entire investigated range. The advantage in burn duration observed for the baseline engine decreases from 9 and 7 °CA to 2.6 and 1 °CA with retarding combustion. however, CA5-CA90 remains shorter at any given CA50. The marked difference of early Miller at $x_{EGR} = 20$ % stems from the lack of oxygen.
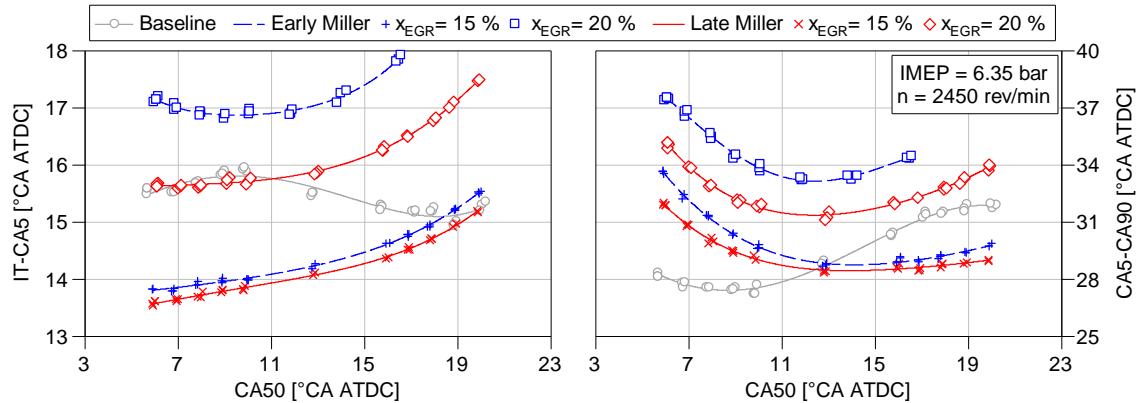
Figure 7-54: Burning delay (left) and burn duration (right) for the baseline configuration without EGR and Miller valve timing at $x_{EGR} = 15$ % and 20 % (IMEP = 6.35 bar)

Modified valve timing combined with EGR also affect combustion stability, which can be a source for rising NO_x emissions, particularly in lean-burn operation. Figure 7-55 (left) shows that combustion stability across all configurations decreases as CA50 is retarded on account of lower combustion temperatures. The baseline configurations holds an advantage in σ_{CA50} over the Miller setups for early CA50, yet combustion stability decreases to a larger extent as its phasing is retarded. As a result of shorter flame travel distance caused by the altered piston design, the Miller setups experience better combustion stability for late CA50. Therefore, combustion stability poses only a source to higher NO_x emissions for advanced combustion phasings.

The dilution ratio decreases with delaying CA50, thus attenuating losses from imperfect combustion. This behaviour is well pronounced for the baseline and both Miller configuration at $x_{EGR} = 15$ %. As the EGR rate increases to $x_{EGR} = 20$ %, $\Delta ISFC_{icomb}$ falls significantly, likely due to the increasing influence of mixture inhomogeneity on incomplete combustion for mixtures close to $\lambda = 1.0$. The larger drawback occurs for early Miller, although 3D CFD showed better homogeneity of in-cylinder charge compared to late Miller cycle. This can be ascribed again to the lower dilution ratio, causing a larger lack of oxygen (see Figure 7-55, right).
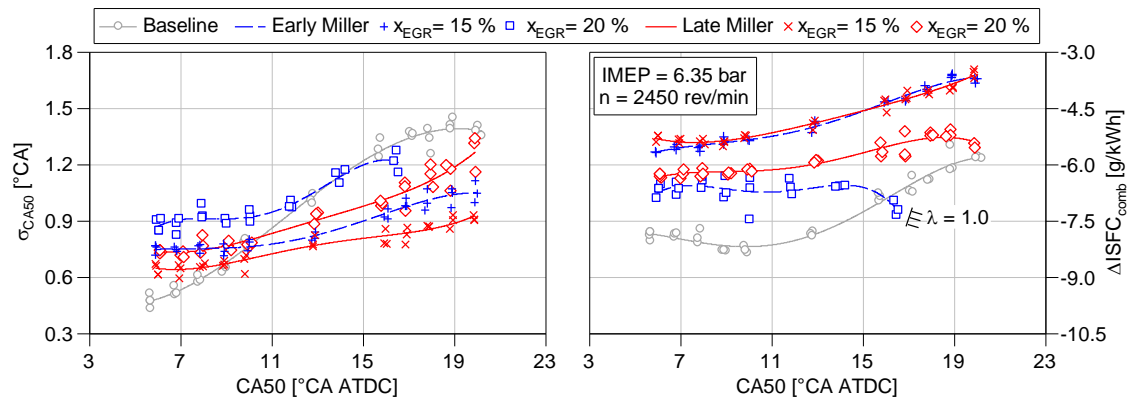
Figure 7-55: Standard deviation of CA50 σ_{CA50} (left) and combustion losses $\Delta ISFC_{comb}$ (right) over CA50 for the baseline configuration without EGR and Miller valve timing at x_{EGR} = 15 % and 20 % (IMEP = 6.35 bar)

7.4.2.4 Comparison of Selected Operating Points

The conducted series of measurements show a disadvantage for the Lean-Miller-EGR working process in terms of the ISFC-NO_x trade-off at constant IMEP. Combustion phasing strongly influences engine behaviour, regardless of configuration. Perceptible differences could be observed between the respective engines setups as CA50 was varied. To detail the reasons that deteriorate the trade-off, selected operating points at early and late CA50 of the baseline are compared to the Miller configurations. Figure 7-56 shows characteristic parameters of the baseline engine without EGR and both Miller valve configurations at x_{EGR} = 20 % and CA50 = 8 °CA ATDC.

Figure 7-56: ISFC, $ISFC_g$, $ISFC_{ideal}$, $\Delta ISFC_{comb}$, CA5-CA90, Q_{wall} and specific NO_x emissions for the baseline engine without EGR and Miller cycle with an EGR rate of x_{EGR} = 20 % at CA50 = 8 °CA ATDC (IMEP 6.35 bar, n = 2450 rev/min)

Both Miller setups reduce ISFC at the expense of increasing specific NO_x emissions. Miller valve timing causes the benefit through lower pumping losses. This becomes clear by analysing $ISFC_g$ as it shows that the high-pressure loop of the baseline engine is more efficient than that of the Miller configurations. The fact, that the same trend is seen in $ISFC_{ideal}$,

despite a higher compression ratio, emphasises the penalty in fuel consumption due to unfavourable mixture composition. This entails higher combustion temperatures, thus reducing the losses from imperfect combustion since fuel conversion improves. This is also favoured by longer burn duration which, however, is detrimental to engine efficiency. As one would expect, increasing combustion temperatures result in higher wall heat losses.

Retarding combustion phasing to 17 °CA ATDC further increases $ISFC_g$ so that the losses during the high-pressure loop outweigh the advantage in pumping work of both Miller valve timings (see Figure 7-57). The decreasing dilution ratio markedly deteriorates $ISFC_{ideal}$, yet it reduces the gap in burn duration. While the imperfect combustion losses of late Miller cycle are still lower than that of the baseline engine, the early Miller configuration shows a notable drawback mainly caused by the lack of oxygen. It is also responsible for lower NO_x emissions compared to late Miller, albeit combustion reaches higher temperatures. As a direct consequence of increasing temperature levels for Miller valve timings, wall heat losses increase.
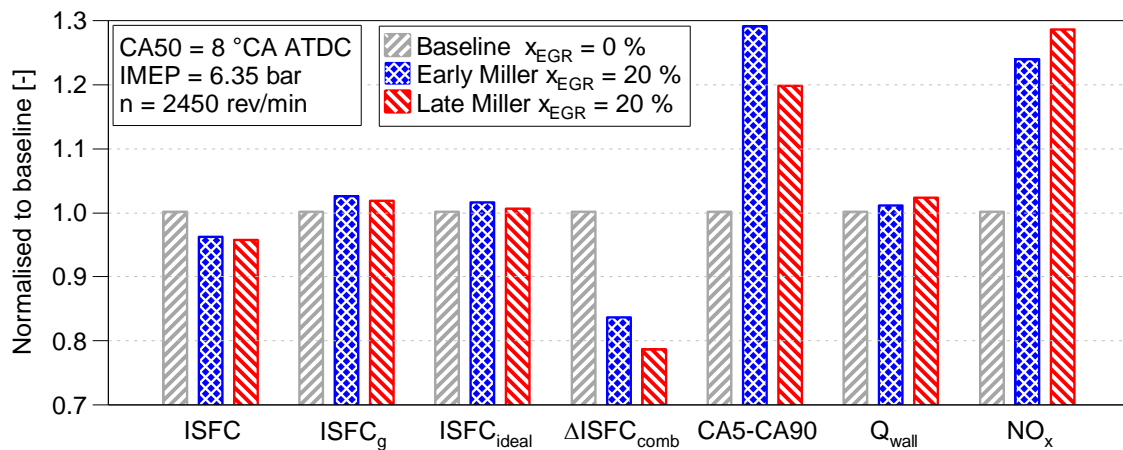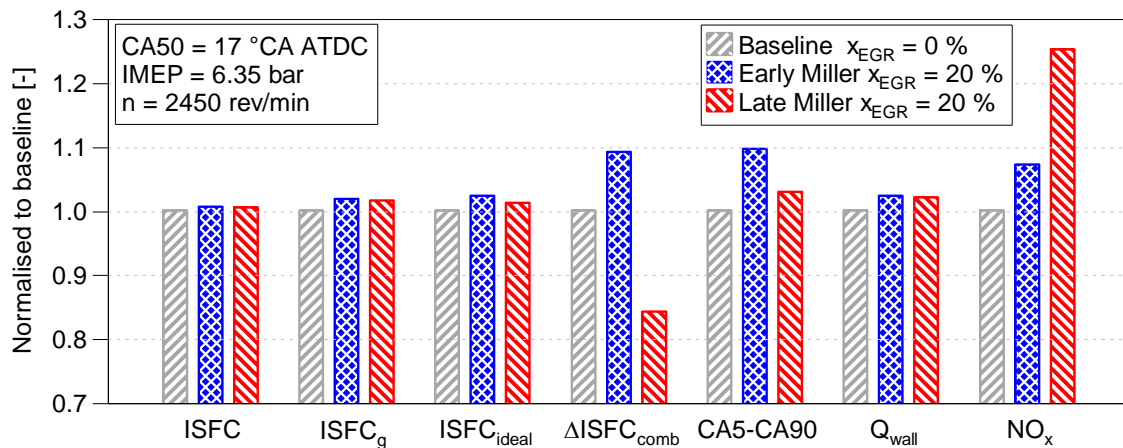

Figure 7-57: ISFC, $ISFC_g$, $ISFC_{ideal}$, $\Delta ISFC_{comb}$, CA5-CA90, Q_{wall} and specific NO_x emissions for the baseline engine without EGR and Miller cycle with an EGR rate of $x_{EGR} = 20\ \%$ at CA50 = 17 °CA ATDC (IMEP 6.35 bar, n = 2450 rev/min)

The main disadvantages occur for Miller cycle due to lower charging efficiency. It requires high EGR rates to achieve large heat capacity of the mixture. However, even when nearly the entire excess air is substituted with exhaust gas and the engine operates close to stoichiometric conditions, the heat capacity is too small to achieve combustion temperatures that lead to low NO_x emissions. Due to the rather low ratio of the specific heat capacities, the efficiency of the ideal engine suffers, thus annihilating the benefit caused by the high expansion/compression ratio.

7.5 Summary and Conclusions of the Experiments

The subject of this chapter was to investigate the Lean-Miller-EGR working process in

terms of engine efficiency, emissions, combustion process and gas exchange. After first analysing the influence of exhaust gas on lean air-methane combustion inside a CVCC, its impact in engine experiments was evaluated. Subsequently, engine operation with early and late Miller configurations was studied under lean operating conditions. In an attempt to counteract rising NO_x emissions, EGR was added to both Miller configurations and a thorough comparison to the air-diluted baseline engine could be drawn. The key findings are:

- Under quiescent flow conditions and at a constant dilution ratio, i.e. same amount of fuel, the temperature of the burnt zone and the laminar burning velocity diminish when a part of excess air is substituted with exhaust gas. The effect of EGR increases gradually with rising EGR rates and falling dilution ratios thanks to higher H_2O and CO_2 fraction that increase the specific heat capacity of the exhaust gas. The values determined for dilution ratios of $D = 1.3 - 1.6$ and EGR rates of $x_{EGR} = 0 - 20$ % match well with literature.

- The effect of EGR during engine trials with baseline valve timing agrees well with the findings from the CVCC as EGR reduces combustion temperature at the expense of increasing burn duration and burning delay. A further similarity is that the effect of exhaust gas increases with decreasing dilution ratio and rising EGR rate. As a direct consequence of the reduced laminar burning velocity, ignition timing needs to be advanced to keep combustion phasing constant. Operating points of same IMEP and CA50 achieve lower NO_x emissions but higher ISFC in engine operation with EGR, primarily due to losses in ideal engine efficiency and a prolonged combustion. In the low NO_x regime (i.e. late CA50), the drawbacks can be either compensated by advancing the combustion phasing to operate at same ISFC but lower NO_x emissions or overcompensated to achieve same NO_x emissions but lower ISFC. Due to the strong correlation between combustion phasing and efficiency, this strategy is only applicable to the low NO_x regime. In the high efficiency regime, on the other hand, the influence of combustion phasing on ISFC becomes smaller, thus avoiding that advanced CA50 balance the losses caused by EGR. Engine trials at constant NO_x emissions show that starting from CA50 = 19 °CA ATDC, EGR allows the engine to increase IMEP through either advanced CA50 and/or increased amount of fuel. The maximum increase can be achieved for the highest studied EGR rate of $x_{EGR} = 25$ %. However, the mixture is then close to stoichiometric conditions that lead to notable losses from imperfect combustion caused by a lack of O_2.

- Engine trials at the knock margin proved that the reduction of combustion temperature through EGR lowers the knocking tendency. For a compression ratio of $r_{geo} = 15.25$ combined with baseline valve timing, the possible IMEP at MBT increases gradually from 6.6 to 7.5 bar with rising EGR rates up to $x_{EGR} = 20$ %.

The engine operates then with a stoichiometric mixture and reaches exhaust gas temperatures that would allow for the use of a TWC and therefore low engine-out emissions.

- Comparable early and late Miller configurations with effective compression ratios $r_{c,eff}$ similar to the baseline engine were found. Together with same residual gas fractions, all three setups reach similar thermodynamic in-cylinder conditions at crank angles relevant for ignition timing. The increase of the geometrical compression ratio of the baseline from $r_{g,0} = 13.20$ to 15.25 augments the effective expansion/compression ratio of the baseline from $ECR_{eff} = 0.968$ to 1.091 for the early and to 1.099 for the late Miller configuration. The maximum pressure and temperature difference shortly before TDC amount to 0.68 bar and 6.7 K.

- In line with the 1D CFD study, the pressure traces of the selected Miller configurations match each other while the valves are closed. The main differences between both Miller configurations are found during gas exchange, where a reverse flow during the compression stroke causes losses in compression $W_{comp,loss}$ for late Miller cycle. Further deviations can be observed during the combustion process: Albeit early Miller experiences a slightly smaller mass flow, 3D CFD calculations reveal a higher turbulence level and better mixture homogeneity inside the main combustion chamber. Late Miller, on the other hand, holds the advantage of a lower residual gas fraction inside the prechamber. The flow conditions and mixture distribution lead to shorter combustion duration for early Miller when operating with air-diluted mixtures and early combustion phasings. Since TKE decreases for early Miller with a steeper slope as the piston approaches TDC, burn duration falls below that of late Miller cycle for late CA50. With increasing EGR rate, the mixture distribution inside the prechamber becomes more significant than TKE, leading to shorter burn duration for late Miller cycle, regardless of combustion phasing.

- In comparison to the baseline engine, both Miller configurations show different burning behaviour that primarily originates from the altered piston design. The lower charging efficiency of both Miller strategies requires a lower relative air-fuel ratio to achieve an IMEP of 6.35 bar. In response to an enhanced combustion temperature and A/V ratio, wall heat losses of both Miller configurations increase. However, ISFC improves in lean-burn operation compared to the baseline configuration at same combustion phasing and burn duration found at CA50 = 6 °CA ATDC. The advantage can be explained through reduced pumping losses and higher effective expansion/compression ratio ECR_{eff}. It augments the ratio between expansion and compression work, thus improving ideal engine efficiency despite a mixture of less favourable thermodynamic properties. The benefit increases as CA50 is retarded due to a more pronounced decrease of wall heat losses

for higher geometrical compression ratios and reduced burn duration from the lower dilution ratio and the altered piston design. The lower charging efficiency enables both Miller configurations to operate at higher volumetric NO_x emissions (ppm) to achieve same specific NO_x emissions (g/kWh). Nevertheless, it cannot compensate for the markedly higher NO_x emissions caused by low dilution ratios.

- As with the baseline engine, EGR improves the ISFC-NO_x trade-off at constant IMEP of Miller configurations to some extent, yet NO_x emissions comparable to those of the baseline engine are only achieved for nearly stoichiometric mixtures, for which a lack of O_2 counteracts the NO_x formation. For early Miller cycle, the lowest NO_x emissions of 1.6 g/kWh are coupled with an ISFC of 205.8 g/kWh, while late Miller reduces NO_x emissions to 1.35 g/kWh but reaches a higher ISFC of 210.8 g/kWh. Compared to the reference operating point (NO_x = 1.40 g/kWh, ISFC = 206.7 g/kWh), both Miller valve timings lead to a worsened trade-off. The causal agent for the limited potential to achieve low NO_x emissions is found in the small absolute heat capacity of the in-cylinder charge as a result of reduced charging efficiency when implementing Miller cycle.

8 Conclusions and Future Work

Tightening emission standards push developers of cogeneration gas engines to find alternative engine setups for the prevailing lean-burn concepts. In this context, the working process studied in this thesis combines Miller cycle and EGR for a naturally aspirated lean-burn cogeneration engine operating with natural gas. While EGR is an established means in Diesel and petrol engines, Miller cycle has recently gained wide popularity. The motivation behind following these approaches depends on the specific application. Miller cycle can improve the thermal efficiency of naturally aspirated ICE by increasing its expansion/compression ratio. Nevertheless, falling engine power because of suffering charging efficiency poses a challenge to maintain brake efficiency. Lean-burn engines can readily compensate this by enriching the mixture, however, NO_x emissions increase in response to higher combustion temperature. Substituting a part of excess air with exhaust gas allows the engine to operate at lower combustion temperatures owing to the larger CO_2 and H_2O fraction of the mixture. Based on a comprehensive literature survey and 0D calculations, an improvement of the trade-off between ISFC and NO_x emissions at same IMEP was expected.

8.1 Conclusions

The study of the Lean-Miller-EGR working process was thoroughly studied using different numerical tools and experimental test rigs that either needed to be adjusted or built up from scratch. The cogeneration unit at Karlsruhe UAS was equipped with comprehensive metrology and modified to form a fully controllable research engine. A cooled EGR system was incorporated that allows regulating the temperature of the exhaust gas recirculated. In the meantime, experimental data of the same engine type from the cogeneration unit manufacturer were used to build up and validate a detailed 1D CFD model that predicts

147

realistic engine behaviour. One of its purposes was to find comparable early and late Miller configurations, i.e. of same effective compression ratio and expansion/compression ratio, for engine testing. A spring mass model was created for designing the cam profiles, which additionally required the development of a multi-part camshaft and machining the cylinder head.

Preliminary experiments contributed to the understanding of how mixture dilution affects the combustion in a constant volume combustion chamber. The already existing analysis code needed to be extended for adding exhaust gas as second diluent. Subsequently, numerous and extensive series of measurements were carried out on the test bed engine to compare configurations of different geometrical compression ratios and valve timings for varying mixture composition. The analysis of experimental data in terms of gas exchange, combustion process and ideal engine efficiency was conducted using a proprietary MATLAB routine and commercial software. To gain deeper insight into charge motion of the valve timings investigated, a 3D CFD gas exchange model was built. The conclusions of this work are the following:

- Experiments in a CVCC prove that increasing the heat capacity of the diluent by substituting a part of excess air with exhaust gas reduces combustion temperature but also laminar burning velocity. The effect is the highest for low dilution ratios and high EGR rates due to the high H_2O and CO_2 fraction in the exhaust gas.

- The effect of EGR is similar in engine operation, where the reduced combustion temperature lowers NO_x emissions and the reduced laminar burning velocity prolongs combustion duration. Another crucial disadvantage occurs due to losses in ideal efficiency. The drawbacks can be overcompensated through advanced combustion phasing, leading to same ISFC but lower NO_x or vice versa. Alternatively, the engine can operate at higher IMEP without increasing NO_x emissions. However, the applicability of this approach is limited to the low NO_x regime (i.e. late CA50) due to the high sensitivity of engine efficiency to combustion phasing.

- A method was presented that determines the effective compression ratio in due consideration of the effects of gas dynamics, including ram effect and reverse flow. Compared to other approaches in literature, it leads to most similar thermodynamic conditions at the end of the compression stroke for engine configurations of same effective compression ratio but differing valve timings and geometrical compression ratios.

- The direct comparison between early and late Miller cycle, given for constant effective compression ratio and expansion/compression ratio, shows that the pressure traces are coherent when the valves are closed. Late Miller holds a clear disadvantage in engine efficiency mainly caused by the reverse flow that occurs during the compression stroke, thus leading to losses in compression. Further differences are found in combustion characteristics due to the influence of inlet valve

timing on motion and homogeneity of the in-cylinder charge.

- In comparison to the baseline engine, both Miller configurations require a lower dilution ratio to achieve the threshold IMEP of 6.35 bar, leading to high combustion temperatures. The increasing NO_x emissions can be reduced by adding EGR, however, losses in ideal engine efficiency, higher wall heat losses and extended combustion duration outweigh the benefit caused by Miller cycle, thus hindering an improvement of the ISFC-NO_x trade-off at constant IMEP.

8.2 Future Work

Both engine efficiency and NO_x emissions could benefit from further configurations of advanced or retarded valve timing that increase charging efficiency. Yet, the expected improvements are relatively low unless additional but vast modifications in the intake path design are made, as reported in [103, 105]. With respect to even stricter long-term emission standards (as stipulated in [20]) than the one put in force in 2018, however, the potential of lean-burn is limited. For this reason, stoichiometric operation coupled with a TWC could gain popularity as long-term solution for small cogeneration engines. The significantly decreasing tailpipe emissions allow the engine to operate at thermodynamically optimal combustion phasing. Engine trials with Miller valve timing prove that knocking-free operation is possible with EGR rates of $x_{EGR} = 20\ \%$, in spite of much higher combustion temperatures and still longer burn durations (see Figure 8-1). In comparison to the reference operating point of the baseline configuration, wall heat losses increase significantly but ISFC decreases, primarily from advanced MBT combustion phasing of CA50 = 8 °CA ATDC. Both Miller configurations reveal similar IMEP while raw NO_x emissions rise drastically. However, assuming a conversion ratio of 95 % for the TWC, tailpipe emissions could be reduced to a level that is 20 % below the current ROP.
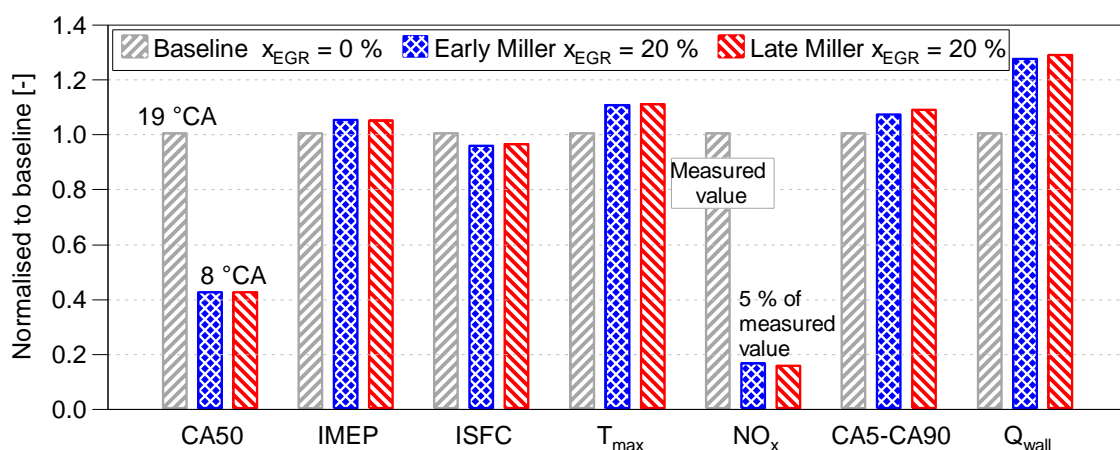
Figure 8-1: Combustion phasing, IMEP, ISFC, T_{max}, measured/estimated tailpipe NO_x emissions, CA5-CA90 and Q_{wall} of the ROP of the baseline engine and both Miller configurations in stoichiometric operation at $x_{EGR} = 20\ \%$

Based on the promising results achieved by operating Miller cycle with a stoichiometric mixture and EGR, further development work is suggested:

- The valve timings analysed require an EGR rate of 20 % to achieve the threshold IMEP in stoichiometric operation. However, a combination of lower EGR rates and more advanced or retarded Miller valve timing might lead to lower fuel consumption caused by reduced burn duration and higher expansion/compression ratio. To reduce development time and costs, another 1D CFD study needs to be carried out for different valve timings and EGR rates. To this end, the 1D CFD model created in this work requires adjustments to predict engine performance in stoichiometric operation and at optimal combustion phasing regarding engine efficiency.

- The piston design to adjust the effective compression ratio for both Miller configurations was initially designed for engine operation with high dilution ratios and relatively late combustion phasing to meet NO_x emission limits without additional aftertreatment to the oxidation catalyst. It is likely that an altered piston design would be more favourable for reducing combustion duration at early CA50. The rising temperature level coupled with higher compression ratios bring forth challenges regarding wall heat losses.

- The increasing thermal load necessitates endurance runs with particular focus on exhaust valve seat wear.

Engine testing will show whether early or late Miller valve timing is expedient from a thermodynamically perspective. In light of field operation, however, engine start, fluctuations in mixture composition and increasing thermal load become major subjects during the overall development process.

References

[1]   Alberti, P.: "Von der Gemischbildung zu den Schadstoffemissionen im Dieselmotor auf direktem Weg", Ph.D. Thesis, Otto-von-Guericke-Universität Magdeburg, 2010.

[2]   Atkinson, J., "Gas Engine", US367496 A, 1887.

[3]   Auer, M.: "Erstellung phänomenologischer Modelle zur Vorausberechnung des Brennverlaufes von Magerkonzept-Gasmotoren", Ph.D. Thesis, Universität München, 2010.

[4]   AVL List GmbH: "BOOST Users Guide v2013.2", Handbook, 2013.

[5]   Baas, H.: "TA Luft 2017, Messungen von Abgasemissionen an stationären Gasmotoren, Betriebserfahrungen mit SCR-Katalysatoren", MWM-Planertage, Mannheim, June 29, 2017.

[6]   Barba, C.: "Erarbeitung von Verbrennungskennwerten aus Indizierdaten zur verbesserten Prognose und rechnerischen Simulation des Verbrennungsablaufes bei Pkw-DE-Dieselmotoren mit Common-Rail- Einspritzung", Ph.D. Thesis, ETH Zürich, 2001.

[7]   Bargende, M., Spicher, U., Köhler, U. and Schwarz, F.: "Entwicklung eines allgemeingültigen Restgasmodells für Verbrennungsmotoren", FVV-Informationstagung Motoren, 2002.

[8]   Bauer, M. and Wachtmeister, G.: "Entstehung von Formaldehyd in Mager-Gasmotoren", MTZ Motortechnische Zeitschrift, vol. 70(07-08): pp. 580–587, 2009.

151

[9]   Behrens, R., Henn, R. and Stellwagen, K.: "TBG 632 - Ein neuer Großgasmotor
        mit hohem Wirkungsgrad", MTZ Motortechnische Zeitschrift, vol. 62(2): pp. 136–
        144, 2001.

[10]   Birgel, A., Köberl, S., Böwing, R. and Trapp, C.: "GE's J920 FleXtra Gas Engine
        – 60 Hz Application and further Improvements for low NO_x Emissions",
        Proceedings of the 9th Dessau Gas Engine Conference: pp. 25–38, 2015.

[11]   Blair, G.P.: "Design and Simulation of Four-Stroke Engines", Society of
        Automotive Engineers Inc, ISBN 978-0768004403, 1999.

[12]   Böckhoff, N., Mondrzyk, D. and Terbeck, S.: "Kontinuierliche Weiterentwicklung
        des 51/60G zum 51/60G TS der MAN Diesel & Turbo SE", Proceedings of the
        10th Dessau Gas Engine Conference: pp. 61–71, 2017.

[13]   Borgnakke, C. and R. E. Sonntag: "Fundamentals of Thermodynamics", 7th ed.,
        John Wiley & Sons, Hoboken, ISBN 978-0-470-04192-5, 2009.

[14]   Bougrine, S., Richard, S., Nicolle, A. and Veynate, D.: "Numerical study of
        laminar flame properties of diluted methane-hydrogen-air flames at high pressure
        and temperature using detailed chemistry", International Journal of Hydrogen
        Energy, vol. 36(18): pp. 12035–12047, 2011.

[15]   Boulouchos, K., Zbiorcyk, A. and Inhelder, J.: "Optimale Auslegung
        umweltfreundlicher Gasmotoren mit Hilfe von Simulationswerkzeugen", MTZ
        Motortechnische Zeitschrift, vol. 58(9): pp. 486–499, 1997.

[16]   Bowen, Y., Mingfa, Y., Bin, M., Yongzhi, L. et al.: "A Comparative Study on the
        Fuel Economy Improvement of a Natural Gas SI Engine at the Lean Burn and
        the Stoichiometric Operation both with EGR under the Premise of Meeting EU6
        Emission Legislation", SAE Technical Paper 2015-01-1958, 2015.

[17]   Brünglinghaus, C.: "Neuer 1.5-l-TSI-Motor von Volkswagen kommt Ende 2016",
        https://www.springerprofessional.de/ottomotor/neuer-1-5-l-tsi-motor-von-
        volkswagen-kommt-ende-2016/10059428?searchBackButton=true, October 21,
        2016.

[18]   Budack, R., Wurms, R., Mendl, G. and Heiduk, T.: "Der neue 2,0-l-R4-TFSI-
        Motor von Audi", MTZ Motortechnische Zeitschrift, vol. 77(5): pp. 16–25, 2016.

[19]   Bundesministerium für Umwelt, Naturschutz und Reaktorsicherheit: "Technische
        Anleitung zur Reinhaltung der Luft", 2002.

[20]   Bundesministerium für Umwelt, Naturschutz, Bau und Reaktorsicherheit:
        "Entwurf zur Anpassung der Ersten Allgemeinen Verwaltungsvorschrift zum
        Bundes– Immissionsschutzgesetz (Technische Anleitung zur Reinhaltung der Luft
        – TA Luft)", 2016.

References | 153

[21] Bundestag: "Gesetz zur Neuregelung des Kraft-Wärme-Kopplungsgesetzes", Bundesgestzblatt Jahrgang 2015 Teil I Nr. 55: pp. 2498–2516, 2015.

[22] Burger, B.: "Stromerzeugung in Deutschland im Jahr 2016", Fraunhofer-Insittut für solare Energiesysteme ISE, Freiburg, 2016.

[23] Butcher, D.: "Influence of asymmetric valve timing strategy on in-cylinder ow of the internal combustion engine", Ph.D. Thesis, Loughborough University, 2016.

[24] Byun, J.J.: "Laminar Burning Velocities and Laminar Flame Speeds of Multi-Component Fuel Blends at Elevated Temperatures and Pressures", Ph.D. Thesis, University of Texas at Austin, 2011.

[25] Cai, X., WANG, J., Zhang, W., Xie, Y. et al.: "Effects of oxygen enrichment on laminar burning velocities and Markstein lengths of $CH_4/O_2/N_2$ flames at elevated pressures", Fuel, (184): pp. 466–473, 2016.

[26] Changup, K. and Choongsik, B.: "Hydrocarbon Emissions from a Gas Fueled SI Engine under Lean Burn Conditions", SAE Technical Paper 1999-01-3512, 1999.

[27] Cheng, W., Hamnin, D., Heywood, J. and Hochgreb, S.: "An Overview of Hydrocarbon Emissions Mechanisms in Spark-Ignition Engines", SAE Technical Paper 932708, 1993.

[28] Chiodi, M.: "An Innovative 3D-CFD-Approach towards Virtual Development of Internal Combustion Engines", Ph.D. Thesis, University of Stuttgart, 2011.

[29] Colin R. Ferguson, A. T. Kirkpatrick: "Internal Combustion Engines: Applied Thermosciences", 3rd ed., Wiley, Chichester, ISBN 978-1118533314, 2015.

[30] Damköhler, G.: "Der Einfluss der Turbulenz auf die Flammengeschwindigkeit in Gasgemischen", Zeitschrift f. Elektrochem. u. angew. Chemie, vol. 46(11): pp. 601–626, 1940.

[31] Devadas, M., Köcher, O., Elsener, M., Wokaun, A. et al.: "Influence of NO_2 on the selective catalytic reduction of NO with ammonia over Fe-ZSM5", Applied Catalysis B: Environmental, vol. 67(3-4): pp. 187–196, 2006.

[32] Di Benedetto, A., Di Sarli, V., Salzano, E., Cammarota, F. et al.: "Explosion behavior of $CH_4/O_2/N_2/CO_2$ and $H_2/O_2/N_2/CO_2$ mixtures", Hydrogen Energy, vol. 34(16): pp. 6970–6978, 2009.

[33] Dlugogorski, B., Hichens, R., Kennedy, E., Bozzelli et al. (eds.), "Water Vapour as an Inerting Agent", Halon Options Technical Working Conference, 1997.

[34] Doosje, E.: "Limits of mixture dilution in gas engines", Ph.D. Thesis, Eindhoven University, 2010.

[35] Ehleskog, M., Gjirja, S. and Denbratt, I.: "Effects of Variable Inlet Valve Timing

and Swirl Ratio on Combustion and Emissions in a Heavy Duty Diesel Engine", SAE Technical Paper 2012-01-1719, 2012.

[36] Eifler, W., Schlücker, E., Spicher, U., and Will. G.: "Küttner Kolbenmaschinen", 7th ed., Vieweg+Teubner Verlag. ISBN 978-3-8351-0062-6, 2009.

[37] Eilts, P.: "Das Miller- und Atkinsonverfahren an Verbrennungsmotoren", 7. MTZ-Fachtagung Ladungswechsel im Verbrennungsmotor, Stuttgart, 2014.

[38] Eilts, P. and Broda. A.: "Potentiale des variablen Ventiltriebs am Dieselmotor", 2. MTZ-Fachtagung Ladungswechsel im Verbrennungsmotor, Stuttgart, 2008.

[39] Einewall, P., Tunestål, P. and Johansson, B.: "Lean Burn Natural Gas Operation vs. Stoichiometric Operation with EGR and a Three Way Catalyst", SAE Technical Paper 2005-01-0250, 2005.

[40] Elsner, N., Günther, M., Spannaus, T., Scheidt. M. et al.: "Brennverfahrensaspekte bei Realisierung einer Miller-/Atkinson-Strategie am Downsizing-Konzept", 7. MTZ-Fachtagung Ladungswechsel im Verbrennungsmotor, Stuttgart, 2014.

[41] Endo, H., Tanaka, K. and Kakuhama. Y.: "Development of the Lean Burn Miller Cycle Gas Engine", The Fifth International Symposium on Diagnostics and Modeling of Combustion in Internal Combustion: pp. 374–381, Nagoya, 2001.

[42] European Union: "Energy Roadmap 2050", Communication from the Comission to the European Parliament, the Council, the European Economic and Social Committee and the Comittee of the Regions, Brussels, 2011.

[43] European Union: "Commission Regulation (EU) No 813/2013 of 2 August 2013 implementing Directive 2009/125/EC of the European Parliament and of the Council with regard to ecodesign requirements for space heaters and combination heaters", Official Journal of the European Union, 2013.

[44] Flierl, R., Gollasch, D., Knecht, A., Pohl, D. et al.: "Perspektiven des vollvariablen Ventiltriebs Univalve auf Basis eines 2,0-l-Ottomotors", MTZ Motortechnische Zeitschrift, vol. 67(07-08): pp. 560–567, 2006.

[45] Fuchs, J., Leitner, A., Tinschmann, G. and Trapp. C.: "Konzept für direkt gezündete Gross-Gasmotoren", MTZ Motortechnische Zeitschrift, vol. 74(5): pp. 386–391, 2013.

[46] Fukuzawa, Y., Shimoda, H., Kakuhama, Y., Endo, H. et al.: "Development of High Efficiency Miller Cycle Gas Engine", Mitsubishi Heavy Industries, vol. 38(3): pp. 146–150, 2001.

[47] Gorenflo, E.: "Einfluß der Luftverhältnissteuerung auf die zyklischen

Schwankungen beim Ottomotor", Ph.D. Thesis, Universität Karlsruhe, 1997.

[48] Goto, T., Isobe, R., Yamakawa, M. and Nishida, M.: "Der Neue Ottomotor SKYACTIV-G von Mazda", MTZ Motortechnische Zeitschrift, vol. 72(6): pp. 476–483, 2011.

[49] Graf, J. and Lauer, T.: "Innovative Zündung", FVV Abschlussbericht Vorhaben Nr. 1008, 2011.

[50] Gu, X.J., Haq, M.Z., Lawes, M. and Woolley, R.: "Laminar Burning Velocity and Markstein Lengths of Methane–Air Mixtures", Combustion and Flame, vol. 121(1–2): pp. 41–58, 2000.

[51] Haas, S.-F.: "Experimentelle und theoretische Untersuchung homogener und teilhomogener Dieselbrennverfahren", Ph.D. Thesis, Universität Stuttgart, 2007.

[52] Hannibal, W. and Schütte, S.: "Aktuelle Variable Ventilsteuerungskonzepte und deren historischer Background", 7. MTZ-Fachtagung Ladungswechsel im Verbrennungsmotor, Stuttgart, 2014.

[53] He, X., Durrett, R. and Sun, Z.: "Late Intake Valve Closing as an Emissions Control Strategy at Tier 2 Bin 5 Engine-Out NO_x Level", SAE Int. J. Engines, vol. 1(1): pp. 427–443, 2008.

[54] Heikes, H.: "System- und Komponentenanalyse fuer hohen thermodynamischen Wirkungsgrad beim Ottomotor", Ph.D. Thesis, Universität Stuttgart, 2014.

[55] Helmantel, A., Gustavsson, J. and Denbratt, I.: "Operation of a DI Diesel Engine With Variable Effective Compression Ratio in HCCI and Conventional Diesel Mode", SAE Technical Paper 2005-01-0177, 2005.

[56] Herdin, G.: "Gasmotoren Potenziale und Zukunft", DVV Kolloquium, Wien, 2004.

[57] Heywood, J.: "Internal Combustion Engine Fundamentals", McGraw-Hill, ISBN 0-07-028637-X, 1988.

[58] Hoffmann, K., Benz, M., Weirich, M. and Herrmann, H.-O.: "Der neue Erdgasmotor für mittelschwere Nfz von Mercedes-Benz", MTZ Motortechnische Zeitschrift, vol. 75(11): pp. 12–19, 2014.

[59] Hofmann, P.: "Hybdridfahrzeuge", 2nd ed., Springer, Wien, ISBN 978-3-7091-1779-8, 2014.

[60] Huber, K.: "Der Wärmeübergang schnelllaufender, direkt einspritzender Dieslmotoren", Ph.D. Thesis, Technische Universität München, 1990.

[61] Huneke, B., Kleesattel, J., Löser, S. and Zundel, M.: "Der neue Sechszylinder-Marinemotor von MAN für Yachten und Arbeitsboote", MTZ Motortechnische Zeitschrift, vol. 77(5): pp. 50–55, 2016.

[62] Iglesias, D.: 'Metodología para el estudio de propiedades de combustión de sustancias líquidas a partir de ensayos en bomba de combustión a volumen constante'. Final thesis, Universidad de Valladolid, 2008.

[63] Intergovernmental Panel on Climate Change: "Climate Change 2014: Mitigation of Climate Change", Cambridge University Press, ISBN 978-1-107-05821-7, 2014.

[64] JSAE: "Yearbook", Journal of Society of Automotive Engineers of Japan, (8), 2015.

[65] Kammerstätter, S.: "Verbrennungsablauf und Schadstoffbildung in Erdgas-Großmotoren mit Vorkammerzündung", Ph.D. Thesis, Technische Universität München, 2012.

[66] Keppeler, R.: "Entwicklung und Evaluierung von Verbrennungsmodellen für die Large Eddy Simulation der Hochdruck-Vormischverbrennung", Ph.D. Thesis, Universität der Bundeswehr München, 2013.

[67] Kerr, T.: "Combined Heat and Power: Evaluating the Benefits of Greater Global Investment", International Energy Agency, 2008.

[68] Kettner, M.: "Experimentelle und numerische Untersuchungen zur Optimierung der Entflammung von mageren Gemischen bei Ottomotoren mit Direkteinspritzung", Ph.D. Thesis, Universität Karlsruhe, 2006.

[69] Kocher, L., Koeberlein, E., van Alstine, D., Stricker, K. et al.: "Physically based volumetric efficiency model for diesel engines utilizing variable intake valve actuation", International Journal of Engine Research, vol. 13(2): pp. 169–184, 2011.

[70] Koehler, L., Blei, L., Broda, A. and Eilts, P.: "Theoretische Betrachtung und Bewertung von Ladungswechselkenngrößen aktueller und zukünftiger Variabilitäten", 4. MTZ-Fachtagung Ladungswechsel im Verbrennungsmotor, Stuttgart, 2011.

[71] Köhler, U. and Bargende, M.: "A Model for a Fast Prediction of the In-Cylinder Residual Gas Mass", SAE Technical Paper 2004-01-3053, 2004.

[72] Kozuch, P.: "Ein phänomenologisches Modell zur kombinierten Stickoxid- und Rußberechnung bei direkteinspritzenden Dieselmotoren", Ph.D. Thesis, Universität Stuttgart, 2004.

[73] Lafuente, Á.: 'Metodología para el diagnóstico de la velocidad de combustión laminar de mezclas de gases combustibles a partir de la medida de la presión instantánea en una bomba de combustión a volumen constante", Ph.D. Thesis, Universidad de Valladolid, 2008.

[74] Lämmle, C.: "Numerical and Experimental Study of Flame Propagation and Knock in a Compressed Natural Gas Engine". Ph.D. Thesis, ETH Zürich, 2005.

[75] Lancefield, T., Methley, I., Räse, U. and Kuhn, T.: "The Application of Variable Event Valve Timing to a Modern Diesel Engine". SAE Technical Paper 2000-01-1229, 2000.

[76] Lauer, T. and Geringer, B.: "Bewertung der Restgastoleranz bei homogenen Brennverfahren für hohe Abgasrückführraten". MTZ Motortechnische Zeitschrift, vol. 69(2): pp. 154–161, 2008.

[77] Law, C.K., Makino, A. and Lu, T.F.: "On the off-stoichiometric peaking of adiabatic flame temperature". Journal of Combution and Flame, vol. 145(4): pp. 808–819, 2006.

[78] Lee, S., Ozaki, K., Iida, N. and Sako, T.: "A Potentiality of Dedicated EGR in SI Engines Fueled by Natural Gas for Improving Thermal Efficiency and Reducing NO_x Emission". SAE Int. J. Engines, vol. 8(1): pp. 238–249, 2015.

[79] Liao, S., Jianf, D. and Cheng, Q.: "Determination of laminar burning velocities for natural gas". Fuel, vol. 83: pp. 1247–1250, 2004.

[80] Löbbert, P.: "Möglichkeiten und Grenzen der Teillaststeuerung von Ottomotoren mit vollvariablem Ventilhub". Ph.D. Thesis, TU Dresden, 2006.

[81] Luria, D., Taitel, Y. and Stotter, A.: "The Otto-Atkinson Engine - A New Concept in Automotive Economy". SAE Technical Paper 820352, 1982.

[82] MAHLE: "Ventiltrieb". Springer, Wiesbaden, ISBN 978-3-8348-2490-5, 2012.

[83] Marshall, S., Stone, R., Heghes, C., Davies, T. et al.: "High pressure laminar burning velocity measurements and modelling of methane and n-butane". Combustion Theory and Modelling, vol. 14(4): pp. 519–540, 2010.

[84] Martins, J., Uzuneanu, K., Ribeiro, B.S. and Jasansky, O.: "Thermodynamic Analysis of an over-expanded Engine". SAE Technical Paper 2004-01-0617, 2004.

[85] Mayer, K.P.: "Swirl Measurement on the Stationary Flow Test Bench by Means of a Momentum Meter". Internal report AVL, 1982.

[86] Mayer, K.P. and Thien, G.E.: "Derivation of the Formulas for the Evaluation of Stationary Flow Measurements of Intake and Exhaust Ports". FA-Report No. 463 / Gen. / 072, 1978.

[87] Mazas, A., Lacoste, D., Fiorina, B., and Schuller, T. (eds.). "Effects of water vapor addition on the laminar burning velocity of methane oxygen-enhanced flames at atmospheric pressure". European Combustion Meeting, 2009.

[88] Merker, G.P. and Teichmann, R. (eds.). "Grundlagen Verbrennungsmotoren", 7th

ed., Springer Vieweg, Wiesbaden, ISBN 978-3-658-03194-7, 2014.

[89]   Mikalsen, R., Wang, Y. and Roskilly, A.: "A comparison of Miller and Otto cycle natural gas engines for small scal CHP applications", Applied Energy, vol. 86(6), 2009.

[90]   Miller, J. and Bowman, C.: "Mechanism and modeling of nitrogen chemistry in combustion", Progress in Energy and Combustion Science, vol. 15(4): pp. 287–338, 1989.

[91]   Miller, R.: "Supercharging and internal cooling cycle for high output", Transactions of ASME, vol. 69: pp. 453–457, 1947.

[92]   Miller, R.: "High-pressure supercharging system", US2670595 A, 1954.

[93]   Miller, R.: "High expansion, spark ignited, gas burning, internal combustion engines", US2773490 A, 1956.

[94]   Miller, R. and Liebherr, H.U.: "The Miller supercharging system for diesel and gas engines operating characteristics", Poceedings of CIMAC: pp. 787–803, 1957.

[95]   Mincione, G.: "Ventiltriebkonzepte zur Verbrauchsreduzierung bei Motorradmotoren", Ph.D. Thesis, Universität Stuttgart, 2013.

[96]   Mitchell, C.E. and Olsen, D.B.: "Formaldehyde Formation in Large Bore Natural as Engines Part 1: Formation Mechanisms", J. Eng. Gas Turbines Power, vol. 122(4): pp. 603–610, 1999.

[97]   Modiyani, R., Kocher, L., van Alstine, D., Koeberlein, E. et al.: "Effect of intake valve closure modulation on effective compression ratio and gas exchange in turbocharged multi-cylinder engines utilizing EGR", International Journal of Engine Research, vol. 12(6): pp. 617–631, 2011.

[98]   Murata, Y., Kusaka, J., Odaka, M., Daisho, Y. et al.: "Emissions suppression mechanism of premixed diesel combustion with variable valve timing", International Journal of Engine Research, vol. 8(5): pp. 415–428, 2007.

[99]   Nakazono, T., "Miller cycle", E-Mail (Yanmar R&D center), November 15, 2016.

[100] Neher, D., Fieg, S., Rieß, W., Bauer, J. et al.: "Simulationsgestützte Entwicklung eines hochverdichteten gemischansaugenden magerbetriebenen Erdgasmotors zur Erfüllung zukünftiger Emissionsgrenzwerte", Proceedings of the 10th Dessau Gas Engine Conference: pp. 179–194, 2017.

[101] Neher, D., Kettner, M., Scholl, F., Klaissle, M. et al.: "Numerical Investigations of Overexpanded Cycle and Exhaust Gas Recirculation for a Naturally Aspirated Lean Burn Engine", SAE Technical Paper 2013-32-9081, 2013.

[102] Neher, D., Kettner, M., Scholl, F., Klaissle, M. et al.: "Numerische

Untersuchungen eines alternativen Brennverfahrens für gemischansaugende stationär betriebene Erdgasmotoren", Proceedings IAV Engine Processes: pp. 205–228, Berlin, 2013.

[103] Neher, D., Kettner, M., Scholl, F., Klaissle, M. et al.: "Numerical Investigations of a Naturally Aspirated Cogeneration Engine Operating with Overexpanded Cycle and Optimised Intake System", SAE Technical Paper 2014-32-0109, 2014.

[104] Neher, D., Scholl, F., Bauer, J., Kettner, M. et al.: "Numerische und experimentelle Untersuchungen zu Miller- und Atkinson Steuerzeiten bei konstantem effektivem Verdichtungsverhältnis am Beispiel eines stationär betriebenen gemischansaugenden Gasmotors", 7. MTZ-Fachtagung Ladungswechsel im Verbrennungsmotor, Stuttgart, 2014.

[105] Neher, D., Scholl, F., Deinert, M., Kettner, M. et al.: "Miller/Atkinson Valve Timing as Full Load Concept for a Naturally Aspirated Cogeneration Engine", SAE Technical Paper 2015-32-0713, 2015.

[106] Neher, D., Scholl, F., Kettner, M., Schwarz, D. et al.: "The Effect of Cooled Exhaust Gas Recirculation for a Naturally Aspirated Stationary Gas Engine", SAE Int. J. Engines, vol. 4(9): pp. 2477–2492, 2016.

[107] Nellen, C. and Boulouchos, K.: 'Aufgeladene Gasmotoren mit AGR und Dreiwege-Katalysator - der Weg zu niedrigsten Emissionen bei hohem Wirkungsgrad und großer Leistungsdichte", MTZ Motortechnische Zeitschrift, vol. 61(1): pp. 54–62, 2000.

[108] Nellen, C. and Boulouchos, K.: 'Natural Gas Engines for Cogeneration: Highest Efficiency and Near-Zero-Emissions through Turbocharging, EGR and 3-Way Catalytic Converter", SAE Technical Paper 2000-01-2825, 2000.

[109] Ohler, S.: "Entwicklung und Vergleich von Kriterien zur Erkennung der klopfenden Verbrennung in Ottomotoren", Ph.D. Thesis, Helmut-Schmidt-Universität / Universität der Bundeswehr Hamburg, 2014.

[110] Olsen, D.B., Kohls, M. and Arney, G.: "Impact of Oxidation Catalysts on Exhaust NO_2/NO_x Ratio from Lean-Burn Natural Gas Engines", Journal of the Air & Waste Management Association, vol. 60(7): pp. 867–874, 2010.

[111] Oxtoby, D.W., Gillis, H. P., and Campion, A.: "Principles of Modern Chemistry", 7th ed., Brooks/Cole, Belmont, ISBN 978-0-8400-4931-5, 2010.

[112] Pattas, K.: "Stickoxidbildung bei der Ottomotorischen Verbrennung", MTZ Motortechnische Zeitschrift, vol. 34(12): pp. 397–404, 1973.

[113] Peer, J., Wachtmeister, G., and Boulouchos, K. (eds.). "Einfluss der Abgasrückführung bei Magerkonzept-Gasmotoren mit extremen Steuerzeiten auf

Brennverlauf und Schadstoffemissionen unter Berücksichtigung der Gasqualität", FVV Informationstagung, Leipzig, Germany, 2013.

[114] Pertl, P.: "Engine Development of an Extended Expansion Engine - Expansion to Higher Efficiency", Ph.D. Thesis, TU Graz, 2016.

[115] Peters, N.: "The turbulent burning velocity for large-scale and small-scale turbulence", Journal of Fluid mechanics, vol. 384: pp. 107–132, 1999.

[116] Peters, N.: "Technische Verbrennung", Lecture notes, RWTH Aachen, 2006.

[117] Petersen, E.L., Hall, J.M., Smith, S.D., Vries, J. de et al.: "Ignition of Lean Methane-Based Fuel Blends at Gas Turbine Pressures", Journal of Engineering for Gas Turbines and Power Vol. 129, (4): pp. 937–944, 2007.

[118] Pischinger, F.: "Sonderforschungsbereich 224 'Motorische Verbrennung" Abschlussbericht", Final Report RWTH Aachen, 2001.

[119] Pischinger, R., Klell, M., and Sams, T.: "Thermodynamik der Verbrennungskraftmaschine", 3rd ed., Springer, Wien, NewYork, ISBN 978-3-211-99277-7, 2009.

[120] Pischinger, S., Geiger, J., Neff, W., Böwing, R. et al.: "Einfluss von Zuendung und Strömung auf die Magerverbrennung", MTZ Motortechnische Zeitschrift, vol. 63(5): pp. 388–399, 2002.

[121] Pizzirani, N., Lauer, T., Geringer, B. and Murakami, S.: "A Numerical Method for Efficiency Optimization on Gas Engines", MTZ industrial, vol. 1(2): pp. 60–67, 2012.

[122] Ponnusamy, S., Checkel and M. Fleck: "Maintaining Burning Velocity of Exhaust-Diluted Methane/Air Flames by Partial Fuel Reformation", IFRF Combustion Journal, (200506), 2005.

[123] Potteau, S., Lutz, P., Leroux, S., Moroz, S. et al.: "Cooled EGR for a Turbo SI Engine to Reduce Knocking and Fuel Consumption", SAE Technical Paper 2007-01-3978, 2007.

[124] Ratzke, A.: "Modellierung der Flammenausbreitung und des Flammenlöschens im Gasmotor", Ph.D. Thesis, Leibniz Universität Hannover, 2013.

[125] Reyes Serrano, M.: "Caracterización de la combustión y el autoencendido de combustibles líquidos en mezclas homogéneas para su uso en motores térmicos en modo HCCI", Ph.D. Thesis, Universidad de Valladolid, 2008.

[126] Ribeiro, B. and Martins, J.: "Direct Comparison of an Engine Working under Otto, Miller and Diesel cycles: Thermodynamic Analysis and Real Engine Performance", SAE Technical Paper 2007-01-0261, 2007.

[127] Riess, M., Benz, A., Wöbke, M. and Sens, M.: "Einlassseitige Ventilhubstrategien zur Turbulenzgenerierung", MTZ Motortechnische Zeitschrift, vol. 74(07-08): pp. 580–585, 2013.

[128] Ritzinger, J.: "Einfluss der Kraftstoffe ROX95, Methan und Ethanol auf Flammenausbreitung und Klopfverhalten in Ottomotoren mit Abgasrückführung", Ph.D. Thesis, ETH Zürich, 2013.

[129] Roethlisberger, R. and Favrat, D.: "Investigation of the prechamber geometrical configuration of a natural gas spark ignition engine for cogeneration: part I. Numerical simulation", International Journal of Thermal Sciences, vol. 42(3): pp. 223–237, 2003.

[130] Röthlisberger, R.: "An Experimental Investigation of a Lean Burn Natural Gas Prechamber Spark Ignition Engine for Cogeneration", Ph.D. Thesis, Swiss Federal Institute of Technology of Lausanne, 2001.

[131] Saito, H., Morimoto, S., Okamoto, K., Ozaki, M. et al. (eds.), "Development of High-Efficiency Co-Generation System", 22nd World Gas Conference, Tokyo, 2003.

[132] Saito, H., Shirasuna, T. and Nomura, T.: "Extension of Lean Burn Range by Intake Valve Offset", SAE Int. J. Engines, vol. 4(6): pp. 2072–2084, 2013.

[133] Sauer, C., Kulzer, A., Rauscher, M. and Hettinger, A.: "Analysis of Different Gasoline Combustion Concepts with Focus on Gas Exchange", SAE Int. J. Engines, vol. 1(1): pp. 336–345, 2008.

[134] Saunders, R.J. and Abdul-Wahab, E.A.: "Variable Valve Closure Timing for Load Control and the Otto Atkinson Cycle Engine", SAE Technical Paper 890677, 1989.

[135] Schaupp, U., Altenschmidt, F., Laudenbach, N., Bertsch, D. et al.: "Benzin-Direkteinspritzung der 2. Generation: Neue Wege der Brennverfahrensentwicklung", 7. Internationales Stuttgarter Symposium, Stuttgart, 2007.

[136] Scheidt, M., Brands, C., Kratzsch, M. and Günther, M.: "Kombinierte Miller-Atkinson-Strategie für Downsizing-Konzepte", MTZ Motortechnische Zeitschrift, vol. 75(5): pp. 14–20, 2014.

[137] Schneider, S., Genieser, P., Birke, S. and Bücker, C.: "Potenziale eines variablen Ventiltriebs beim PKW-Dieselmotor", MTZ Motortechnische Zeitschrift, vol. 73(3): pp. 198–205, 2012.

[138] Schöffler, T., Hoffmann, K. and Koch, T.: "Stoichiometric Natural Gas Combustion in a Single Cylinder SI Engine and Impact of Charge Dilution by

Means of EGR", SAE Technical Paper 2013-24-0113, 2013.

[139] Scholl, F.: "Study of Premixed Combustion Induced by Controlled Hot Surface Ignition in Stationary Gas Engines", Ph.D. Thesis, University of Valladolid & Hochschule Karlsruhe, 2017.

[140] Scholl, F., Gerisch, P., Neher, D., Kettner, M. et al.: "Development of a NOx Storage-Reduction Catalyst Based Min-NOx Strategy for Small-Scale NG-Fueled Gas Engines", SAE Int. J. Fuels Lubr., vol. 9(3), 2016.

[141] Schutting, E., Dumböck, O., Kraxner, T., and Eichlseder, H. (eds.), "Thermodynamic consideration of the Miller cycle on the basis of simulation and measurements", Internationaler Motorenkongress 2016, 2016.

[142] Schutting, E., Neureiter, A., Fuchs, C., Schatzberger, T. et al.: "Miller- und Atkinson-Zyklus am aufgeladenen Dieselmotor", MTZ Motortechnische Zeitschrift, vol. 68(6): pp. 480–485, 2007.

[143] SenerTec Kraft-Wärme-Energiesysteme GmbH: "VB-244 2014 Abschlussbericht Projekt 117.2 Emissionsreduzierung Gas Mager", Internal report, 2016.

[144] Silvis, W.M.: "An Algorithm for Calculating the Air/Fuel Ratio from Exhaust Emissions", SAE Technical Paper 970514, 1997.

[145] Sita Rama Raju, A., Ramesh, A. and Nagalingam, B.: "Effect of Intensified Swirl and Squish on the Performance of a Lean Burn Engine Operated on LPG", SAE Technical Paper 2000-01-1951, 2000.

[146] statista: "Nettostromerzeugung in erdgasbefeuerten BHKW in Deutschland in den Jahren 2003 bis 2014 (in Terawattstunden)", https://de.statista.com/statistik/daten/studie/472806/umfrage/nettostromerzeugung-in-erdgasbefeuerten-bhkw-in-deutschland/, April 14, 2017.

[147] Stoffregen, J.: "Motorradtechnik", 8th ed., Springer Vieweg, Wiesbaden, ISBN 978-3-8348-1716-7, 2012.

[148] Stricker, K., Kocher, L., Koeberlein, E., van Alstine, D. et al.: "Estimation of effective compression ratio for engines utilizing flexible intake valve actuation", Proceedings of the Institution of Mechanical Engineers, Part D: Journal of Automobile Engineering, vol. 226(8): pp. 1001–1015, 2012.

[149] Südhaus, N.: "Möglichkeiten und Grenzen der Inertgassteuerung für Ottomotoren mit variablen Ventilsteuerzeiten", Ph.D. Thesis, RWTH Aachen, 1988.

[150] Sumit, B., Clark, N. and Hildebrand, W.: "Exhaust Gas Recirculation in a Lean-Burn Natural Gas Engine", SAE Technical Paper 981395, 1998.

[151] Takashima, Y., Tanaka, H., Sako, T. and Furutrani, M.: "Evaluation of Engine

Performance and Combustion in Natural Gas Engine with Pre-Chamber Plug under Lean Burn Conditions'. SAE Int. J. Engines, vol. 8(1): pp. 221–229, 2014.

[152]   Tatschl, R., Basara, B., Schneider, J., Hanjalic, K. et al.: "Advanced Turbulent Heat Transfer Modeling for IC-Engine Applications Using AVL FIRE", International Multidimensional Engine Modeling User's Group Meeting, Detroit, 2006.

[153]   Theißl, H., Kraxner, T., Seitz, H.F. and Kislinger, P.: "Miller-Steuerzeiten für zukünftige Nutzfahrzeug-Dieselmotoren", MTZ Motortechnische Zeitschrift, vol. 76(11): pp. 18–25, 2015.

[154]   Thewes, M., Hoppe, F., Baumgarten, H. and Selbel, J.: "Wassereinspritzung für ottomotorische Brennverfahren", MTZ Motortechnische Zeitschrift, vol. 76(2): pp. 26–31, 2015.

[155]   Tilch, B., Rezaei, R., Bertram, C., Horrick, P. et al.: "EURO VI Motoren- und Abgasnachbehandlungsentwicklung mittels modellbasierter Kalibrierung", 2. Internationaler Motorenkongress, Baden-Baden, 2015.

[156]   Tinaut, Fluixá, F. V., Giménez, Olavarría, B., Iglesias, Hoyos, D. and Lawes, M.: "Experimental Determination of the Burning Velocity of Mixtures of n-Heptane and Toluene in Engine-like Conditions", Flow, Turbulence and Combustion, vol. 89(2): pp. 183–213, 2012.

[157]   Tinaut, Fluixá, F. V., Melgar, A., Giménez, Olavarría, B. and Reyes, M.: "Characterization of the combustion of biomass producer gas in a constant volume combustion bomb", Fuel, vol. 89(3): pp. 724–731, 2010.

[158]   Tinschmann, G., Holand, P., Benetschik, H. and Eilts, P.: "Potenziale der zweistufigen Aufladung am Großdieselmotor 6L 32/44 CR von MAN", MTZ Motortechnische Zeitschrift, vol. 69(10): pp. 818–828, 2008.

[159]   Tippelmann, G.: "A New Method of Investigation of Swirl Ports", SAE Technical Paper 770404, 1978.

[160]   Toulson, E., Schock, J. and Attard, W.: "A Review of Pre-Chamber Initiated Jet Ignition Combustion Systems", SAE Technical Paper 2010-01-2263, 2010.

[161]   Trapp, C., Böwing, R., Birgel, A., Kopecek et al.: "GE's J920 Gasmotor – 10.3 MW Leistung bei bis zu 50 % elektrischem Wirkungsgrad", Proceedings of the 10th Dessau Gas Engine Conference: pp. 75–89, 2017.

[162]   Tschalamoff, T.: 'Abgasrückführung im mittelschnell laufenden Gasmotor", MTZ Motortechnische Zeitschrift, vol. 65(11): pp. 932–939, 2004.

[163]   Tschalamoff, T. and Kauert, L.: "Potenziale der Abgasrückführung im

mittelschnelllaufenden Gasmotor mit offenem Brennraum und Vorkammer", Proceedings of the 3rd Dessau Gas Engine Conference: pp. 66–75, 2003.

[164] United Nations Framework Convention on Climate Change: "Paris Agreement", 2015.

[165] van Basshuysen, R.: "Erdgas und erneuerbares Methan für den Fahrzeugantrieb", Springer Vieweg, Wiesbaden, ISBN 978-3-658-07158-5, 2015.

[166] van Basshuysen, R.: "Handbuch Verbrennungsmotor", 8th ed., Springer Vieweg, Wiesbaden, ISBN 978-3-658-04678-1, 2017.

[167] Wagner, C.: "Untersuchung der Abgasrückführung an Otto- und Dieselmotor", Ph.D. Thesis, TU Darmstadt, 1999.

[168] Wan, Y. and Du, A.: "Reducing Part Load Pumping Loss and Improving Thermal Efficiency through High Compression Ratio Over-Expanded Cycle", SAE Technical Paper 2013-01-1744, 2013.

[169] Warnatz, J., Maas, U., and Dibble, R.W.: "Combustion", 4th ed., Springer Berlin New York, ISBN 3-540-25992-9, 2006.

[170] Weberbauer, F., Rauscher, M., Kulzer, A., Knopf, M. et al.: "Allgemein gültige Verlustteilung für neue Brennverfahren", MTZ Motortechnische Zeitschrift, vol. 66(2): pp. 120–124, 2005.

[171] Wieske, P., Lüddecke, B., Ewert, S., Elsäßer, A. et al.: "Optimierung von Dynamik und Verbrauch beim Ottomotor durch Technikkombinationen", MTZ Motortechnische Zeitschrift, vol. 70(11): pp. 850–857, 2009.

[172] Wimmer, A.: "Gas Engine versus Diesel Engine", MTZ industrial, vol. 1(1): pp. 22–27, 2011.

[173] Wimmer, A., Pirker, G., Zelenka, J. and Chmela, F.: "The Potential of Exhaust Gas Recirculation in Large Gas Engines", Proceedings of the CIMAC Congress, Shanghai, 2013.

[174] Wintruff, I., Bücheler, O., Rall, H. et al.: "Die neuen Bahnmotoren der MTU-BaUreihe 4000 für die Emissionsstufe EU IIIB", MTZ, vol. 72(5): pp. 374–378, 2011.

[175] Witt, A.: "Analyse der thermodynamischen Verluste eines Ottomotors unter den Randbedingungen variabler Steuerzeiten", Ph.D. Thesis, Technische Universität Graz, Institut für Verbrennungskraftmaschinen und Thermodynamik, 1999.

[176] Witt, M. and Griebel, P.: "Numerische Untersuchung von laminaren Methan/Luft-Vormischflammen", Internal report, Paul Scherrer Institute, 2000.

[177] Woschni, G.: "Beitrag zum Problem des Wandwärmeübergangs im

Verbrennungsmotor". MTZ, vol. 26, 1965.

[178] Wülfert, K.: "Einfluss von Ladungswechselcharakteristiken auf den Verbrennungsablauf eines Gasmotors", Ph.D. Thesis, Technische Universität München, 2014.

[179] Wülfert, K., Wachtmeister, G. and Boulouchos, K.: "Erstellung eines phänomenologischen Modells zur Vorausberechnung des Brennverlaufes von Gasmotoren bei extremen Miller/Atkinson-Betrieb". Abschlussbericht über das Vorhaben Nr. 1017 (BMWi/AiF-Nr. 16232 N), 2012.

[180] Zhang, F.-R., Okamoto, K., Morimoto, S. and Shoji, F.: "Methods of Increasing the BMEP (Power Output) for Natural Gas Spark Ignition Engines", SAE Technical Paper 981385, 1998.

[181] Zhang, F.-R., Okamoto, K., Morimoto, S. and Shoji, F.: "Improving Performance and Reliability of Natural Gas Engines for Power Generation - A Concept of Realizing Lower Temperature and Higher Pressure Combustion", SAE Technical Paper 1999-01-3511, 1999.

[182] Zirngibl, S., Prager, M. and Wachtmeister, G.: "Entwicklung eines Dual-Fuel Zündstrahl- Brennverfahrens für den Einsatz in einem mit Biogas betriebenen Mini-BHKW". Proceedings of the 10th Dessau Gas Engine Conference; pp. 95–108, 2017.

Annex

A.1 Polynomials for Calculating Laminar Burning Velocity

The coefficients c and d for calculating the laminar burning velocity defined in Eq. (2-4), are given for $1 < p < 7$ bar as follows:

$$c = (-1.03 \cdot 10^{-2} \cdot T_u + 3.645)\left(\frac{1}{\lambda}\right)^2$$

$$+ (-4.12 \cdot 10^{-6} \cdot T_u{}^2 + 2.512 \cdot 10^{-2} \cdot T_u - 7.68) \cdot \frac{1}{\lambda} \tag{A-1}$$

$$+ (8.78 \cdot 10^{-6} \cdot T_u{}^2 - 1.547 \cdot 10^{-2} \cdot T_u - 4.19)$$

$$d = 7.5 \cdot 10^{-1} \cdot \left(\frac{1}{\lambda}\right)^2 - 1.6 \cdot \frac{1}{\lambda} + 1.337 - 2 \cdot 10^{-4} \cdot T_u \tag{A-2}$$

For $p > 7$ bar, c and d result to:

$$c = (-6.906 \cdot 10^{-5} \cdot T_u{}^2 + 6.875 \cdot 10^{-2} \cdot T_u - 25.13) \cdot \left(\frac{1}{\lambda}\right)^3$$

$$+ (-1.155 \cdot 10^{-4} \cdot T_u{}^2 - 1.523 \cdot 10^{-1} \cdot T_u - 46.477) \cdot \left(\frac{1}{\lambda}\right)^2$$

$$+ (-1.185 \cdot 10^{-5} \cdot T_u{}^2 + 1.922 \cdot 10^{-2} \cdot T_u - 24.82) \cdot \frac{1}{\lambda} \tag{A-3}$$

$$+ (6.75 \cdot 10^{-6} \cdot T_u{}^2 - 9.55 \cdot 10^{-3} \cdot T_u - 5.185)$$

$$d = 0.45 \tag{A-4}$$

A.2 Determination of the Laminar Burning Velocity in a CVCC

The governing equations for evaluating the laminar burning velocity in the constant volume combustion chamber are energy, mass conservation, volume and ideal gas law equations.

Energy equation of unburnt (index u) and burnt (index b) zone (parameters without an index are global):

$$\frac{dU_u}{dt} = \dot{Q}_u + \dot{W}_u - \dot{m}_u \cdot h_u \tag{A-5}$$

$$\dot{m}_u \cdot u_u + \dot{m}_u \cdot \frac{du_u}{dt} = \dot{Q}_u - p \cdot \frac{dV_u}{dt} - \dot{m}_u \cdot h_u \tag{A-6}$$

$$\frac{dU_b}{dt} = \dot{Q}_b + \dot{W}_b - \dot{m}_b \cdot h_b \tag{A-7}$$

$$\dot{m}_b \cdot u_b + \dot{m}_b \cdot \frac{du_b}{dt} = \dot{Q}_b - p \cdot \frac{dV_b}{dt} - \dot{m}_b \cdot h_b \tag{A-8}$$

The parameters are:

m: Mass   h: Specific enthalpy

$\dot{m}$: Mass flow   p: Pressure

U: Internal energy $\dot{Q}$: Heat flux (neglected)

u: Specific internal energy $\dot{W}$: Change in volume work

t: Time

Mass conservation equation:

$$\dot{m}_u = -\dot{m}_b \tag{A-9}$$

Volume equation:

$$V = V_u + V_b \tag{A-10}$$

$$\dot{V}_u = -\dot{V}_b \tag{A-11}$$

Ideal gas law:

$$p \cdot V_u = m_u \cdot R_u \cdot T_u \tag{A-12}$$

$$p \cdot V_b = m_b \cdot R_b \cdot T_b \tag{A-13}$$

R stands for the gas constant of the respective zone.

The two energy equations can be written as follows:

$$T_u(c_{vu} + R_u) \cdot \frac{m_b}{dt} - p \cdot \left(1 + \frac{c_{vu}}{R_u}\right) \cdot \frac{dV_u}{dt} \tag{A-14}$$

$$= -c_{vu} \cdot \frac{V_u}{R_u} \cdot \frac{dp}{dt} - \dot{Q}_u$$

$$(-c_{vb} \cdot T_b - h_{ub} + u_b) \cdot \frac{m_b}{dt} - p \cdot \left(1 + \frac{c_{vb}}{R_b}\right) \cdot \frac{dV_u}{dt} \tag{A-15}$$

$$= -c_{vb} \cdot \frac{V_b}{R_b} \cdot \frac{dp}{dt} - \dot{Q}_b$$

This leads to 2 equations and 2 unknowns V_u and m_b. After solving the equation system, the laminar burning velocity can be calculated under assuming a spherical flame front according to Eq. (4-1).

A.3 Overview of Test Bed Setup of Engine II

Figure A-1 shows the test bed setup of engine II including measuring points.

1: Throttle
2: Compressor
3: Bypass valve
4: Heat exchanger
5: Water storrage
6: Water pump
7: Condensation trap
8: Filter

9: Plenum
10: Hot-film air-mass meter
11: Thermal mass flow meter
12: Gas valve
13: Venturi gas-mixer
14: 3-way valve
15: Generator
16: Encoder

17: Oxidation catalyst (dummy used)
18: Exhaust gas heat exhcanger
19: Muffler
20: Water pump
21: Water storrage
22: EGR cooler
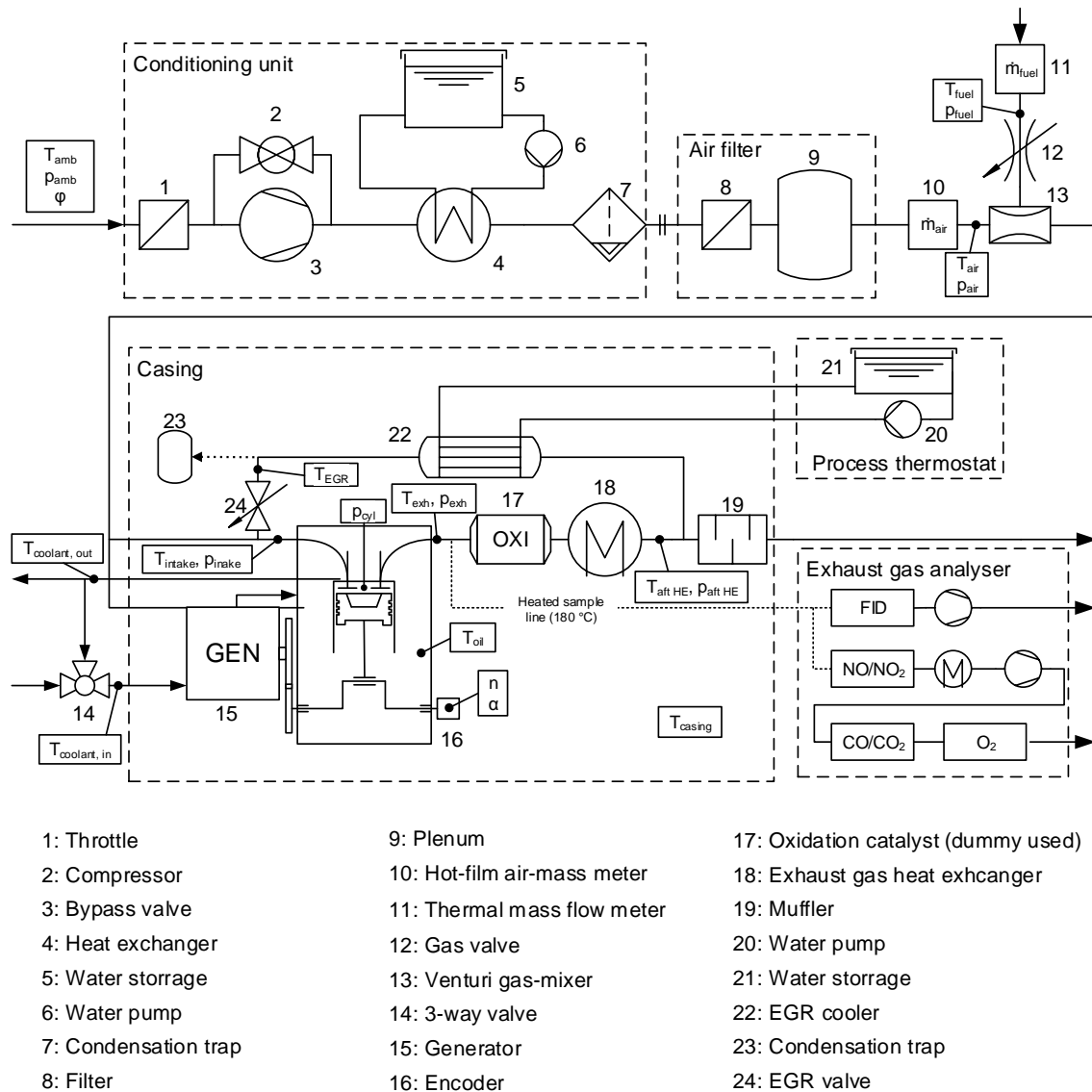23: Condensation trap
24: EGR valve

Figure A-1: Overview of the test bed setup of engine II

A.4 Flow Bench Testing

In order to build up an 1D CFD engine model that accurately predicts the gas dynamic flow behaviour and to apply the residual gas fraction model described in [7, 71], the flow coefficients of the intake and exhaust port needed to be determined as function of the valve lift curve. This was conducted for both test bed engines using a flow bench at Konstanz University of Applied Sciences (see Figure A-2). The setup includes a torque meter that allows determining the swirl number after Tippelmann, which is an input parameter of the Woschni wall heat transfer model used for 1D simulation but also in-cylinder pressure

analysis in this thesis.

The flow coefficient C_D is defined as ratio of the actual mass flow $\dot{m}$ and the theoretical mass flow $\dot{m}_{th}$ through a reference cross-section (here the inner valve seat diameter) at a certain pressure difference as given in Eq. (A-16):

$$C_D = \frac{\dot{m}}{\dot{m}_{th}} \tag{A-16}$$

The theoretical mass flow is calculated as follows

$$\dot{m}_{th} = A_{seat} \cdot \frac{p_0}{\sqrt{\gamma \cdot R_{air} \cdot T_0}} \cdot \frac{2 \cdot \gamma}{\gamma - 1} \left[\left(\left(\frac{p_1}{p_0} \right)^{\frac{2}{\gamma}} - \left(\frac{p_1}{p_0} \right)^{\frac{\gamma + 1}{\gamma}} \right) \right]^{1/2} \tag{A-17}$$

where A_{seat} stands for the cross-section area of the inner valve seat diameter, R_{air} the gas constant of air, T_i its temperature and p_i its pressure. The air is assumed to flow from index i = 0 to i = 1, which governs the pressure and temperature that is to insert into Eq. (A-17). The case given in Figure A-2, for instance, would lead to $p_0 = p_{amb}$, $p_1 = p_{cyl}$ and $T_0 = T_{amb}$, whereas trials where the mass flow exits the cylinder via the intake port would result to $p_0 = p_{cyl}$, $p_1 = p_{amb}$ and $T_0 = T_{cyl}$. All trials were conducted at a constant pressure difference of 50 mbar.

p_{amb}: Ambient pressure

p_{cyl}: Pressure before Torque meter

T_{amb}: Ambient temperature

T_{cyl}: Cylinder temperature

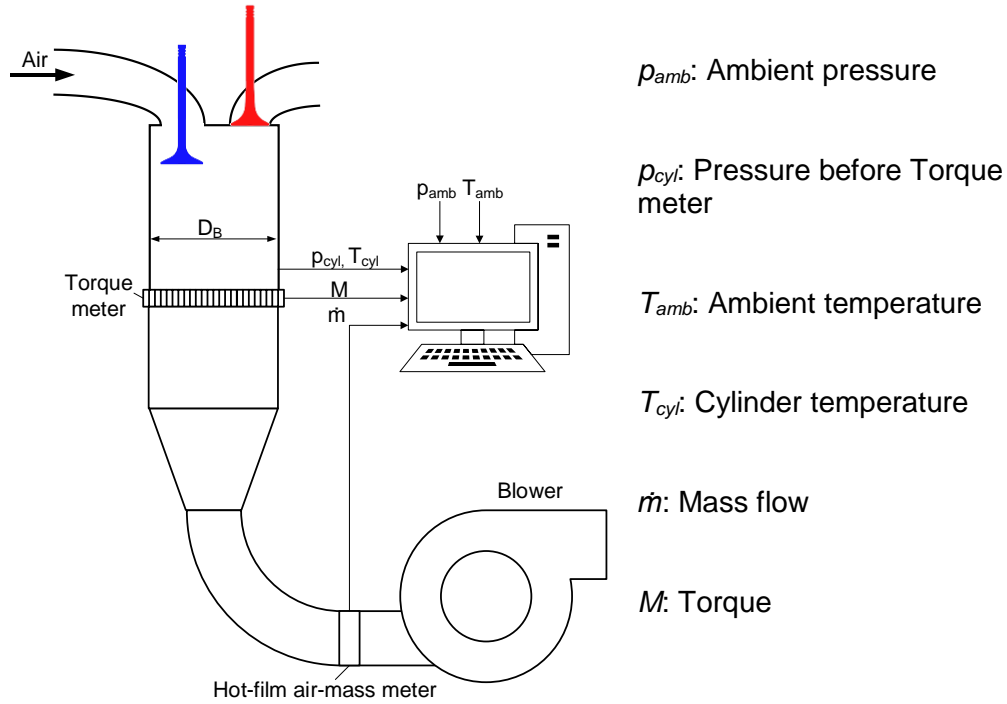$\dot{m}$: Mass flow

M: Torque

Figure A-2: Schematic setup of the flow bench test-rig

After passing the intake valve, the air flow is straightened by the torque meter. The occurring change in angular momentum of the flow applies a torque M, which is measured

through a load cell. Along with the cylinder bore diameter D_{cyl}, the gas constant of air R_{air}, the pressure and temperature within the cylinder and the mass flow, the swirl coefficient C_s for each valve lift can be calculated as follows:

$$C_s = M \cdot \frac{D_{cyl}}{2} \cdot \frac{p_{cyl}}{\dot{m}^2 \cdot R_{air} \cdot T_{cyl}} \tag{A-18}$$

This method was postulated by Tippelmann in 1978 [159]. With the data obtained, a mean swirl coefficient can be calculated, which is described more in detail in literature [85, 86, 119, 159].